

**Design and optimization of a small compressed air energy storage system for isolated
applications**

by

© Hanif SedighNejad

A Thesis submitted to the

School of Graduate Studies

In partial fulfillment of the requirements for the degree of

Master of Engineering

Faculty of Engineering and Applied Science

Memorial University of Newfoundland

May 2022

St. John's

Newfoundland

ABSTRACT

In this study, a variety of practical and theoretical CAES systems are reviewed in order to show the current status of the available CAES systems. Then a small scale compressed air energy storage for small isolated wind based hybrid energy system is introduced and discussed.

In order to develop a cost-effective renewable based hybrid energy system, this research investigates the optimization of each component of the system from the wind turbine to the load to deliver the required energy in the most efficient way. After finding the general control strategy for energy harvesting from the wind, the control strategy based on predictive initial working condition of the air vane motor is investigated through practical tests. A control path is developed using the implemented air motor steady state operation based on its manufacturer datasheet, and it is used to supply a fixed amount of power to the grid.

A new criterion for evaluation of different energy storage system with identical power rating and storage capacity is proposed and examined during a case study and the performance of pumped hydro, battery and compressed air energy systems are compared based on the total shortage time and total fuel consumption of backup diesel generators. The Monte Carlo simulation was used in order to regenerate the wind speed data with 10 minute resolution to represent more accurate variable wind speed. The proposed Harvested Energy Index (HEI) showed the ability of energy storage systems with low efficiency in utilizing excess wind energy and reach their storage capacity. Based on the obtained results, a novel general control concept for such systems is proposed and its steady state simulation results are discussed.

ACKNOWLEDGEMENTS

I would like to express my gratitude to all who supported this research financially, my supervisors, Professor John Quaicoe and Professor Tariq Iqbal, WESnet (Wind Energy Strategic network), and school of graduate studies at MUN.

I should acknowledge my supervisors supports, in reviewing this thesis and for their constructive comments and feedbacks in different stages of this research. In addition, I would like to thank Greg O'Leary for providing me with technical support; and Professor Benjamin Jeyasurya, Lester Marshal and Dr. Faisal Khan for their consultation and guidance.

Finally, my deepest gratitude goes to my family for their unflagging love and spiritual support throughout my whole life; specifically my wife, Sahar Vakili, who always supported me and stood by me through my graduate studies.

Table of Contents

ACKNOWLEDGEMENTS.....	iii
Table of Contents	iv
List of Tables	viii
List of Figures	ix
List of Symbols, Nomenclature or Abbreviations	xvii
Chapter 1 Introduction.....	19
1.1 Renewable energy options for off grid applications	19
1.2 Energy storage systems benefits	20
1.3 Current Status of Energy Storage Technologies	21
1.4 Comparison of Energy Storage Systems	23
1.5 Thesis Outline.....	29
Chapter 2 Compressed Air Energy Storage System	30
2.1 Principle of CAES Energy Conversion	31
2.2 Overview of Existing and Developing CAES Technologies	34
2.2.1 First Generation of CAES Systems (Classic CAES).....	34
2.2.2 Second Generation of CAES Systems	37
2.2.3 Third Generation CAES Systems (Adiabatic CAES).....	41
2.2.4 Hybrid Diesel-CAES Systems	42
2.2.5 Liquid Piston Based CAES Systems	46

2.3	Proposed Small Scale CAES System for isolated hybrid power system application.	49
2.4	Research objectives	51
2.5	Summary	51
Chapter 3	Hybrid Power System Components and Their Models	53
3.1	Proposed hybrid power system structure	53
3.2	System component modeling.....	55
3.2.1	Wind Turbine.....	56
3.2.1.1	Wind Turbine static modeling	56
3.2.1.2	Dynamic Modeling	60
3.2.2	CAES System	62
3.2.2.1	Compressor	62
3.2.2.2	High Pressure Reservoir	69
3.2.2.3	Air Motor	71
3.2.2.3.1	Steady state model	72
3.2.2.3.2	Dynamic model.....	78
3.2.2.4	Rectifier unit	88
3.2.2.5	The Grid connected inverter unit	89
3.2.2.6	The Synchronous Generator for the CAES system.....	95
3.2.3	Back up Diesel Generator	100
3.2.3.1	Dynamic model of the diesel generator	101
3.2.4	Supervisory Control Unit.....	103

3.3	Other Components	105
3.4	Interactive dynamic load model.....	105
3.5	Experimental Setup.....	109
3.5.1	Air motor simplified model	110
3.5.2	Flow rate control valve	112
3.5.3	Output power control of the CAES system setup	117
3.6	Summary.....	122
Chapter 4	Hybrid Power system sizing, design and optimization	123
4.1	Monte Carlo simulation of wind speed.....	124
4.1.1	Wind speed data analysis.....	124
4.1.2	Wind speed data regeneration methodology.....	128
4.2	General Criteria for a Hybrid Wind-CAES Energy System Design.....	131
4.2.1	Selection and Sizing of Wind Turbines based on their energy output.....	132
4.2.2	Efficiency of a Pneumatic Storage System.....	137
4.2.3	Energy Density of Pneumatic Storage System	139
4.3	Proposed criterion for energy storage capability assessment	141
4.3.1	Using Harvested Energy Index for storage system sizing	143
4.3.2	The HEI impact on the overall performance of a HPS in a case study.....	146
4.3.2.1	Determination of the HEI for the case study	149
4.3.2.2	Control strategy based on tracking the maximum HEI.....	151
4.3.2.3	Proposed compression configuration to maximize HEI	152

4.3.2.4	Average value of the HEI for the case study	153
4.3.2.5	Impact of the maximum tracking HEI control strategy on the fuel consumption of the diesel generator	155
4.3.3	Harvested Energy Index calculation in different storage technologies.....	159
4.3.3.1	Harvested Energy Index for Battery storage systems	161
4.3.3.2	Harvested Energy Index for Pumped hydro energy storage system	168
4.3.3.3	Harvested Energy Index for CAES system.....	169
4.3.3.4	Energy storage system performance comparison.....	172
4.4	Summary.....	180
Chapter 5	Conclusions, and Suggested future work	182
5.1	Conclusions and Contributions.....	182
5.2	Suggested Future Work	185
References	186
Appendix 1	Wind turbine specifications.....	204
Appendix 2	Simulation parameters values	205
Appendix 3	wind box interface and inverter specifications	208
Appendix 4	Full bridge diode Rectifier	210

List of Tables

Table 1-1: Energy storage characteristics comparison	28
Table 2-1: Summary of Performance and Estimated Price Data for Various CAES Plant Concepts.....	40
Table 2-2: The compressed air supercharging system comparison [69].....	45
Table 2-3: Cost evaluation for 60kWh-10kW storage for three storage technologies [76].	48
Table 3-1: The Gaussian equation parameters for the Bergey Excel R wind turbine C_p approximation	58
Table 3-2: The measurement results and corresponding valve flow coefficients	114
Table 4-1: Characteristics of the 6 different wind turbines under study.....	133
Table 4-2: The total shortage duration in different compression control strategies.....	157

List of Figures

Figure 1-1: Energy storage systems with different storage capacity [18].....	24
Figure 1-2: Energy storage comparison based on efficiency and life cycle.	26
Figure 2-1: Compression and expansion cycle with isothermal, adiabatic and polytropic paths [38].....	31
Figure 2-2: a): Schematic of a typical first generation CAES system [47], b): Diagram of the Iowa Stored Energy Park [7].....	35
Figure 2-3: The schematic of a typical CAES-AI system [58].	38
Figure 2-4: Typical schematic of a CAES-AI with the HP Expander concept [60].	38
Figure 2-5: Typical schematic of: a) CAES-AI-BCE and b) CAES-BCE-IC concept [61].	39
Figure 2-6: Typical schematic of a CAES-AI with the HP Expander concept [60].	40
Figure 2-7: Schematic of a typical adiabatic CAES system [64].....	41
Figure 2-8: The configuration of the direct connection of the turbine to the air turbine (a), and two stages turbocharger system (b) [69] and [70].....	43
Figure 2-9: The configurations of a) Direct admission of compressed air in the compressor of the turbocharger, and b) Direct admission of compressed into the engine [69].....	44
Figure 2-10: Two types of liquid piston concepts: a) BOP-A; b) BOP-B [73].....	47
Figure 3-1: Schematic of the proposed hybrid system.....	54
Figure 3-2: Manufacturer’s wind turbine power curves: (a) Bergey Excel-R & Excel-S [86], (b): Wisper 500 [87], (c): Skystream 3.7[88], (d): Eoltec Scirocco E5.6-6 [89].	57
Figure 3-3: Calculated and approximated C_p values for the Bergey Excel-R wind turbine.	58
Figure 3-4: Obtained power curve using approximated C_p equation compared with Bergey Excel-R wind turbine datasheet.	59

Figure 3-5: Simplified Wind turbine dynamic model based on its drive train [90].	60
Figure 3-6: Excel-R wind turbine response for nominal condition (Wind Speed 13 m/s).	62
Figure 3-7: Dynamic response of simplified compressor model for 8 cycles of compressions.	66
Figure 3-8: Change in air temperature with different compression stages	68
Figure 3-9: Change in (a) required work and (b) efficiency with different compression stages.	69
Figure 3-10: Tank size for isothermal and polytropic energy-conversion	71
Figure 3-12: (a): 4AM-FRV-36A GAST vane type air motor; (b): Air consumption-speed curves;	73
Figure 3-13: Calculated Torque-Speed characteristic comparison to its datasheet values.	76
Figure 3-14: Static model of Power speed characteristic of the air motor in comparison to its datasheet.....	76
Figure 3-15: The obtained values for the quadratic equation coefficients from the air motor datasheet is compared to their calculated values. (a): C_{AF2} , (a): C_{AF1} , (a): C_{AF0}	77
Figure 3-16: The calculated air consumption curve comparison to its datasheet values.	78
Figure 3-17: Schematic of a 4 vane air motor.....	79
Figure 3-18: Drive and driven chamber volume variation.....	82
Figure 3-19: Flow rate correction factor to model the choked flow condition.	84
Figure 3-20: The dynamic response of the air motor speed to a fixed 7 bar input compressed air.	85
Figure 3-21: The output torque of the air motor for a fixed 7 bar input compressed air	85
Figure 3-22: The dynamic response of the air motor output power to a fixed 7 bar input compressed air	86

Figure 3-23: Air consumption of the modeled air motor for a fixed 7 bar input compressed air	87
Figure 3-24: Equivalent circuit of the rectifier unit.	88
Figure 3-25: Rectifier current block diagram	89
Figure 3-26: The Aurora inverter block diagram.....	90
Figure 3-27: A typical Schematic of a single phase grid connected inverter.....	91
Figure 3-28: Block diagram of a typical single phase grid connected inverter with filter.....	91
Figure 3-29: The bode diagram of the inverter with line filter: a) with no compensator, b): with Lead-Lag compensator.....	93
Figure 3-30: The response of the compensated inverter system with line filter	94
Figure 3-31: A separately excited single phase synchronous generator block diagram	96
Figure 3-32: Open circuit voltage of the SESPSG as a function of field current and speed.....	98
Figure 3-33: Open circuit flux of the SESPSG as a function of the field current for different speeds.....	98
Figure 3-34: Open circuit flux measurement comparison to the approximated equation.....	99
Figure 3-35: The applied load variation.....	99
Figure 3-36: The simulated SESPSG response to the load variation: (a) The terminal voltage and (b) and the speed variation of the generator respectively.....	100
Figure 3-37: The fuel consumption profile of a 6.5 kW Diesel Generator [3].	101
Figure 3-38: The DG dynamic model block diagram.....	102
Figure 3-39: The step response of DG dynamic model	103
Figure 3-40: Block diagram of the proposed hybrid system.....	104
Figure 3-41: The load – power system interaction	106

Figure 3-42: Dynamic load model.	107
Figure 3-43: The dynamic interactive load model. (a) The parallel R-L model for lagging power factor and (b) The parallel R-C model for leading power factor.	108
Figure 3-44: The load variation on the first day of January.....	108
Figure 3-45: experimental setup of small scale CAES system	110
Figure 3-46: The air motor speed response to variable input pressure. (a): 40 Psi and (b): 60 Psi	112
Figure 3-47: The dynamic response of modeled air motor to different input pressures.	112
Figure 3-48: GAST air motor Air Consumption vs. Speed characteristic	113
Figure 3-49: Calculated C_f values by increasing working pressure	114
Figure 3-50: The C_f value error variation by increasing working pressure	115
Figure 3-51: Reference PWM signals for flow rate control vale for (a): 650 rpm, (b): 1000rpm.	116
Figure 3-52: Flow rate valve actuating signals for reference values (a): 650 rpm, (b): 1000rpm.	116
Figure 3-53: Air motor speed control for reference values (a): 650 rpm, (b): 1000rpm.....	117
Figure 3-54: Response of CAES system in delivering 100W power to the grid in no load mode.	118
Figure 3-55: Steady state performance of the CAES system in delivering 100W power to the grid.	118
Figure 3-56: The synchronous generator excitation current and its output current in no load condition.	119

Figure 3-57: The synchronous generator, rectifier unit and inverter output voltage waveform of the CAES system in delivering 100W power to the grid.	120
Figure 3-58: The output waveforms of the delivered voltage, current and power to the grid.	120
Figure 3-59: The output waveforms of the delivered voltage, current and power to the grid.	121
Figure 3-60: Steady state performance of the CAES system in delivering 100W power to the grid.	122
Figure 4-1: The wind speed distribution frequency for (a): 12:00am - 1:00am, (b): 12:00pm - 1:00pm	126
Figure 4-2: The obtained Weibull probability density function for (a): the first hour (12:00am – 1:00 am) and (b): the thirteenth hour (12:00pm – 1:00pm).	127
Figure 4-3: The hourly Weibull distribution of the wind speed probability during a day.	127
Figure 4-4: The approximated CDF for the first hour (12:00am – 1:00 am) with its corresponding measured values from the wind speed data base.	129
Figure 4-5: Proposed method for producing wind speed profile with desired resolution.	130
Figure 4-6: Four produced sample wind speed profiles for the first hour (12:00am – 1:00 am)	130
Figure 4-7: Generated wind speed profile for January, 1 st , 7 th and 14 th , for the first 3 hours.	131
Figure 4-8: Approximated C_p values as a function of wind speed for six the different wind turbines.....	134
Figure 4-9: (a): The annual average power production of the 6 different wind turbines, and (b): their total annual energy production.	135
Figure 4-10: The performance index comparison for the 6 wind turbines under study.	136
Figure 4-11: Energy conversion efficiency variation for different pressure ratios	138

Figure 4-12: Variation of CASES energy density based on the number of stages and the storage pressure.....	140
Figure 4-13: Energy density ratio variation as a function of number of stages.	141
Figure 4-14: The wind power and demand power curve in minute time scale	143
Figure 4-15: Harvested Energy index for different energy storage capacity	144
Figure 4-16: An example of compression system with capability of working in series/parallel configuration.	145
Figure 4-17: The calculated harvested energy index at different working pressures.....	150
Figure 4-18: The HEI at different working pressures and their maximum HEI point track...	151
Figure 4-19: A 4-stage design of the CAES system based on harvested energy index	152
Figure 4-20: Change in average HEI in a day time scale considering only constant working pressure for the compressor	154
Figure 4-21: The maximum HEI point track of a continuous compression system in comparison with various fixed pressure compression systems.	154
Figure 4-22: The tank pressure variation in different compression control strategies.....	156
Figure 4-23: The DG fuel consumption in Standby and On-Off mode of operations.	157
Figure 4-24: The DG fuel consumption comparison in different compression control strategies.	158
Figure 4-25: The resultant power balance curve for a one year period.	160
Figure 4-26: The resultant power balance characteristic for the first day.....	161
Figure 4-27: The battery voltage variation to several load currents	162
Figure 4-28: The change in the state of the charge of 1kWhr system during the first day	163
Figure 4-29: The SOC for several storage capacities during 4 consecutive days.	164

Figure 4-30: The stored power, the delivered and the rejected power profile for the 1kWhr storage system during the first day	164
Figure 4-31: The fuel consumption and the shortage power profile for the 1kWhr storage system during the first day	165
Figure 4-32: The instantaneous VS continuous HEI for the 1kWhr storage system during the first day	166
Figure 4-33: The annual HEI for battery storage systems with different storage capacities ..	167
Figure 4-34: Total annual fuel consumption in battery based energy storage systems with different power rating.....	167
Figure 4-35: The annual HEI for pumped hydro storage system with different storage capacities.....	169
Figure 4-36: Total annual fuel consumption in pumped hydro energy storage system with different capacities.	169
Figure 4-37: Required tank volume as a function of the power rating and the compressor pressure.	170
Figure 4-38: The reservoir pressure variation in five consecutive days.	171
Figure 4-39: The variation of the calculated continuous HEI for several CAES systems with different power rating.....	172
Figure 4-40: The total fuel consumption of several CAES systems with different compression ratios.....	172
Figure 4-41: The annual CHEI of three energy storage technologies with different storage capacities: (a): 1kWh & 2kWh, and (b): 5kWh & 10kWh.....	174

Figure 4-42: The annual averaged value of CHEI for three storage technologies with different ratings.....	175
Figure 4-43: Compressor efficiency variation as a function of its working pressure.	175
Figure 4-44: The annual shortage profile and the total fuel consumption of the three storage systems under study.	177
Figure 4-45: the variation of the daily shortage power to the excess power ratio over a period of a year for a battery storage system with 1kWhr storage capacity.....	178
Figure 4-46: The annual shortage to the excess power ratio variation as a function of the storage capacity for three different energy storage technologies.....	179

List of Symbols, Nomenclature or Abbreviations

Symbol	Description	Unit
V_w	Wind speed	m/s
A_r	Cross section area swept by rotor	m^2
R_r	Rotor Radius	m
ω_R	Turbine rotor angular speed	rad/s
C_p	Power coefficient	
ρ	Air density (1.225)	kg/m^3
λ	Tip speed ratio	
n_G	Gearbox transfer ratio	
B_T	Wind turbine shaft damping	Nms/rad
J_T	Wind turbine moment of inertia	$kg.m^2$
T_{mw}	Wind turbine mechanical torque	N.m
ω_T	Wind turbine angular speed	rad/s
B_{we}	Wind turbine generator shaft damping	Nms/rad
J_{we}	Wind turbine generator moment of inertia	$kg.m^2$
T_{we}	Wind turbine electrical torque	N.m
ω_{we}	Wind turbine angular speed	rad/s
B_{TLS}	equivalent shaft damping referred to the low speed side	Nms/rad
J_{TLS}	equivalent inertia referred to the low speed side	$kg.m^2$
V_{nWT}	Wind turbine nominal speed	m/s
m_r	Wind turbine rotor weight	kg
γ	Heat capacity ratio or adiabatic index	
n	Polytropic exponent	
c_p	Heat capacity at constant pressure	J/K
c_v	Heat capacity at constant volume	J/K
P_{in}	Input pressure	Pa
P_{out}	Output pressure	Pa
PR	pressure ratio	
Q_{Comp}	Compressor volumetric flow rate	m^3/s
N_{cs}	Number of compression stages	
R	Gas constant	
m	Air mass	kg
T	Temperature	K
ω_{r-Comp}	Compressor crank shaft rotational speed	Rpm
J_{T-Comp}	Equivalent Compressor inertia	$kg.m^2$
B_{T-Comp}	Equivalent Compressor damping	Nms/rad
p_s	Storage pressure	Pa
σ_r	Maximum reservoir allowed stress	
s_{res}	Reservoir thickness	m

D_{res}	Reservoir diameter	m
\dot{m}_{v-HL}	Mass flow rate through the valve from higher toward lower pressure	kg/s
C_V	Valve coefficient	
A_V	Valve cross sectional area	m^2
p_H	High pressure	Pa
p_L	Low pressure	Pa
ρ_H	Air density at the higher pressure	kg/m^3
r_o	Orifice radius	m
r_B	Ball radius	m

Chapter 1 Introduction

1.1 Renewable energy options for off grid applications

Electrical loads that are not connected to the electrical power grid are generally dependent on diesel generators. Diesel generators can be portable, modular, or stationary depending on the electrical load size; and have a high power-to-weight ratio, which makes them an ideal power source for such systems. The utilization of diesel generators as the main power generation for off-grid applications comes with its implicit disadvantage in terms of high cost of diesel-based power generation as well as having a negative environmental impact due to high CO₂ emission per kWh consumed [1], [2].

Until recently, conventional fossil fuel power plants have been used to meet the increasing energy demands. According to Environment Canada, 18% of Canada's greenhouse gas emissions are created by burning fossil fuels to generate electricity [3]. Renewable resources, such as hydro, wind, solar or geothermal energy are considered as clean energy sources. Hydropower is a cost attractive possibility; however, geological constraint, long term planning horizons and negative environmental impact on site especially flooding land are the main disadvantages of this energy source [4]. Solar energy as another source of clean energy is still facing high cost of installation and maintenance; also the potential in Canada is not very promising as a comprehensive solution. Due to geographical limitations, the geothermal energy application is limited to specific locations. Wind as a source of energy can be the best option due to its environmentally friendly nature, and also considering the fact that a wind farm can be

established quickly with low negative environmental impact, if the proper site with reasonable wind potential is available. Therefore, wind is considered as the main source of energy in this study.

Wind energy technologies can help to reduce the utilization of diesel generator in remote areas by converting the abundant wind energy to electricity; which results in less fuel consumption, lower operational cost, and less greenhouse gas emissions. Although wind as a renewable energy source is being widely used due to its availability, ease of installation, maintenance and operation, and competitive cost [5], the wind speed fluctuations make the electrical energy output of a purely wind based electrical system very unreliable. Therefore, a combination of different energy sources is required to provide stable and reliable energy system for off grid applications. A typical Hybrid Energy System (HES) often includes some other power source such as wind, solar, or hydropower [6], a diesel generator, energy storage system and a control unit.

1.2 Energy storage systems benefits

Energy storage systems in conjunction with renewable energy sources can provide many environmental, technical and financial benefits to a power system. For instance, energy storage technologies can reduce the overall greenhouse gas emissions and enhance the reliability and economic performance of renewable power generation systems [7] and [8].

The uncertainty of wind forecast is independent of load forecast, and will result in more uncertainty of energy balance in a power system. As a solution, electricity storage

with the capability to decouple the energy production and consumption times and to damp the fluctuations of the wind farms output power, can increase the reliability and flexibility of the system, and make it less dependent on the accuracy of the renewable source forecasting [9], [10] and [11].

In wind farm design, it is more economically desirable to use a site with higher wind speed to provide more energy production, and increase the financial benefit from certain amount of investment [9], [12]. Therefore, developing a cost effective storage system can lower the electricity production cost in energy production based on wind scenario [13]. Furthermore, most of the currently online wind farms are working without storage, and it may become more economically attractive if the output characteristics can be improved using storage systems. The main advantage for these utilities could be accepting small installation cost for cost-effective storage system to increase the capacity factor of an existing wind farm instead of adding more expensive wind turbines to a wind farm [13]. Recent studies have shown that storage can reduce the costs for wind energy even at relatively low penetration levels where the generation capacity is limited [14], [15].

1.3 Current Status of Energy Storage Technologies

Energy can be converted to different forms of energies, including chemical, mechanical and thermal as well as electrical and then be stored to be transformed back to electrical energy when it is needed. Electrical energy is usually stored in three steps. Initially, the electrical power is converted into a storable form. In the second step the storage medium (e. g. compressed air, hydrogen) remains in its rest cycle. Finally, the

storage medium releases the stored energy and transforms it back into electrical energy, when it is needed.

Different storage technologies can be classified considering various technical and economic criteria, as well as their applications and levels of development [16] and [17]. Based on the physics of energy conversion, storage systems can be divided into four categories: mechanical, electrochemical, electrical, and virtual storage [18-20].

Mechanical energy storage systems are the oldest and well developed storage methods and include Pumped Hydro Storage (PHS) [19], Flywheel Energy Storage (FWES) System [21], Compressed Air Energy Storage (CAES) system [22], and Thermal Energy Storage (TES) systems [23].

There are two types of electrochemical storage systems: Accumulators and fuel cells. Accumulators known as batteries are currently the most cost-effective available options in the market [24] and the most commonly used batteries include lead-acid [19], Nickel-Cadmium (Ni-Cd) [24], Lithium ion [25], Sodium-Sulfur (NaS) [26], Zinc-Bromine flow [22], Vanadium Redox Flow [27] batteries. Hydrogen energy storage system use fuel cells to convert chemical energy from hydrogen and oxygen reactions to electricity [28].

The main characteristic of Electrical storage technology is its high power energy density and suitability for transient compensation and power quality applications where fast response is required. The Superconducting Magnetic Energy storage (SMES) [29], and Electrochemical double layer capacitors (EDLC) (also known as super or ultra-capacitor) [30], are two main storage technologies in this category.

In virtual storage theory, the energy consumption trend is controlled by “demand side management” in order to balance the energy production and demand in a power system instead of decoupling the energy consumption time from its production in conventional energy storage systems. For example, unnecessary loads in private or industrial sections can be shut down during the peak time in order to reduce the required energy in demand side management. Ground water pumping, electrical heater and cooler are some of these unnecessary loads which can be used in light load regimes. This load management needs an intelligent control system with capability of active interaction with consumers and power system known as smart grid. Smart grids as advanced communication and control technologies can enhance the flexibility of power systems in order to be compatible to modern energy management policies with acceptable level of effectiveness, reliability and investment [31] and [32].

1.4 Comparison of Energy Storage Systems

At the moment, different energy storage technologies are available to match various applications. The performance of these storage systems can be evaluated considering a variety of parameters. In general efficiency, life cycle, cost (including initial and operational costs) and energy/power rating are the most important factors in choosing a storage system for a given application. Some applications require specific characteristics of the storage system to meet some technical constraints such as high energy density for limited space conditions or transportability for portable applications. Energy storage technologies have been compared based on different parameters in variety of research

[18]-[33]. Some of the parameters in addition to the factors mentioned above include capacity, depth of discharge (an important factor in batteries), autonomous operation capability, adaptability to various applications and renewable energy sources, self-discharge rates, reliability, environmental aspects, and the simplicity of the system for isolated community application. Two main comparison approaches can be considered in the choice of a storage system for a given application. In the first approach, the storage system can be selected based on its capability to provide energy for long or short time. Such a comparison is shown in Figure 1-1.

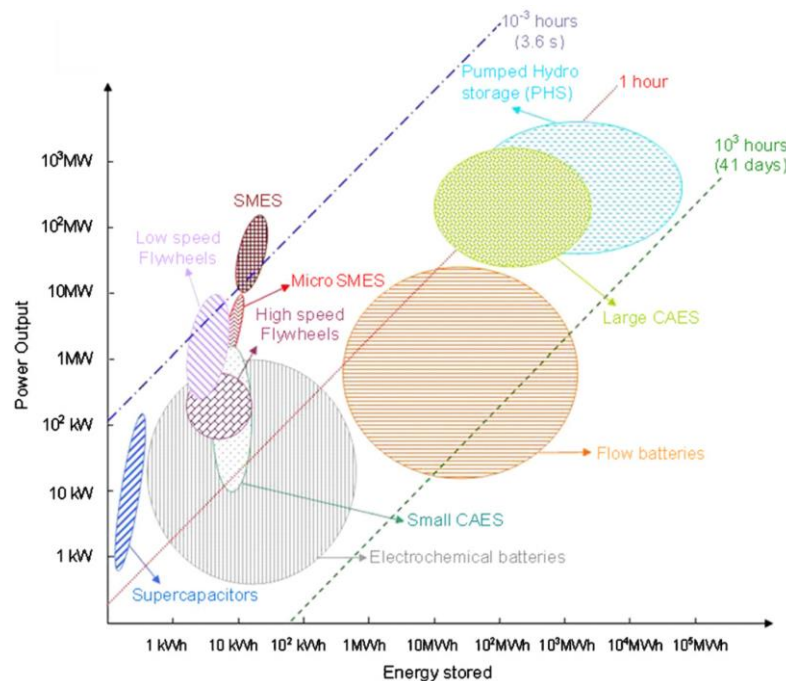


Figure 1-1: Energy storage systems with different storage capacity [18]

The figure shows that for long term or short term energy storage applications corresponding to a specified energy or power delivery requirement, suitable storage technologies can be selected. As shown in Figure 1-1, CAES system can be used either in

large scale or small scale based on energy storage requirements. Such a scalability characteristic is one of the main advantage of CAES over other storage systems.

The second approach is based on the efficiency and life cycle comparison of energy storage systems. Efficiency of a storage system can be formulated as discharged energy divided by stored energy either in a specific working condition as single point or in variable working condition during a time scale as overall efficiency. A storage system should have reasonable overall efficiency. In a variable working condition, maximum efficiency corresponding to each condition can be obtained by controlled energy transfer rate and loss. On the other hand, life cycle of an energy storage system is another important characteristic because it is directly related to the maintenance and replacement cost of the storage system. This comparison approach is suitable for economical evaluation of the possible options, special application with limited available energy source, and high number of cycling requirement. Such a comparison is shown in Figure 1-2. In this illustration, energy storage systems are arranged based on increasing efficiency.

One possible option is to calculate the required investment to produce certain amount of output power/energy of different energy storage systems in a single cycle. Obtaining such an index requires the cost for producing specific quantity of power/energy, a good approximate value for the overall efficiency of the storage system and number of cycles which cannot be found easily for all storage technologies. Social cost of energy production can be defined as amount of investment for producing certain amount of energy considering all the side effects of a power plant on environment. This cost usually

is not considered for financial evaluation of storage systems, while including social cost will add more value to establish a clean energy system with nonpolluting storage system; however, the economic assessment of storage system is not one of the objectives of this study.

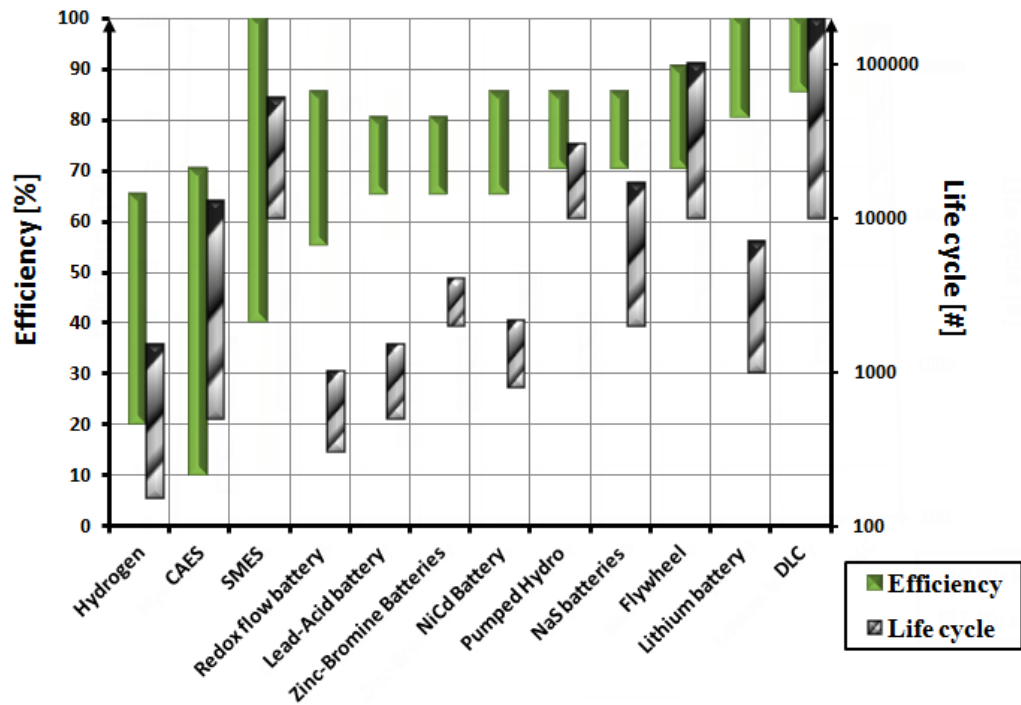


Figure 1-2: Energy storage comparison based on efficiency and life cycle.

Note: The Figure 1-2 was obtained by using nominal efficiency and life cycle information available in [18]-[33] for each energy storage system.

Considering the storage capacity of different storage systems shown in Figure 1-1, proper energy storage system can be selected using comparison chart based on efficiency and life cycle shown in Figure 1-2. As it is shown in this figure, CAES system has high life cycle with 500 to 12000 cycle-ability, and efficiency of 10 to 70 percent. The scalability of CAES and high number of life cycle makes it an attractive nonpolluting energy storage system for a wind based energy system for remote communities with great

wind potential. It can be a promising energy storage system if the overall efficiency of the energy system can be increased to a reasonable value, and make it economically attractive in comparison to other storage alternatives. In a wind based energy system emphasis on high values of efficiencies can be reduced by considering the fact that the stored energy will be provided by replenish abundant source of energy: *The wind*.

Each energy storage technology has some advantages and disadvantages, with characteristics suitable for particular application. Table 1-1, is presented to provide a summary of the characteristics, performance and applications of the various energy storage technologies.

Considering information provided in this chapter, a comparative evaluation of different energy storage systems is summarized in Table 1-1. CAES system has been chosen in this study for energy storage system because of its long term and short term storage capability, scalability, low initial and maintenance cost, good energy density, excellent life cycle, low self-discharge rate, high depth of discharge capability, high reliability and environment friendly characteristic. Table 1-1, is arranged based on available criteria in the literature and based on the unique characteristic of the CAES on capturing excess energy, a novel criterion will be introduced and discussed in chapter 4. Another objective of this study is to compare the impact of using different storage technologies on the fuel consumption of an isolated hybrid energy system.

Table 1-1: Energy storage characteristics comparison

Energy storage technology characteristics	Pumped hydro	Flywheel Energy storage system	CAES system	Thermal Energy storage system	Lead-acid battery	Nickel-cadmium battery	Zinc-bromine flow battery	Vanadium Redox flow battery	Lithium ion battery	Sodium-sulfur (NaS) battery	Hydrogen-based fuel cells	SMES	EDLC
Technology	Mature	Developing	Developing	Developing	Mature	Mature	Early stage	Early stage	Developing	Mature	Developing	Developing	Developing
Initial Cost	High	High	Low	Low	Low	High	High	High	High	High	High	High	High
O&M Cost	High	High	Low	Low	High	High	High	Medium	Good	High	High	High	Good
Energy density	Good	Excellent	Good	Poor	Poor	Excellent	Excellent	Excellent	Excellent	Excellent	Low	Low	Low
Efficiency	Good	Good	Poor	Good	Good	Good	Good	Good	Excellent	Good	Poor	Good	Excellent
Life cycle	Excellent	Excellent	Excellent	Poor	Poor	Poor	Poor	Poor	Good	Excellent	Poor	Excellent	Excellent
Self-discharge rate	Low	High	Low	High	Low	Medium	Medium	Low	Low	Medium	High	Low	High
Depth of discharge	Excellent	Excellent	Excellent	Excellent	Poor	Good	Excellent	Excellent	Good	Excellent	Excellent	Good	Good
Discharge time	Poor	Excellent	Poor	Poor	Excellent	Excellent	Excellent	Excellent	Excellent	Excellent	Good	Excellent	Excellent
Reliability	High	Medium	High	Low	Medium	Poor	Poor	Medium	Poor	Medium	High	Medium	Medium
Transportability	Poor	Good	Excellent	Poor	Good	Good	Poor	Poor	Excellent	Poor	Excellent	Poor	Excellent
Environmental aspect	Good	Excellent	Excellent	Good	Poor	Poor	Poor	Poor	Poor	Good	Good	Good	Poor
Major Application*	EM	PQ	EM	EM	UPS& EV	UPS & EV	EM & UPS	EM & UPS	EV	EM	EV	PQ	PQ

Major Application*: Energy Management (EM), Power Quality (PQ), Uninterrupted Power Supply (UPS), Electric Vehicle (EV)

1.5 Thesis Outline

The thesis is organized in five chapters as follows. The second chapter is dedicated to working principle of CAES and a review of existing configurations. Then the proposed CAES system configuration is proposed and discussed. The research objective and questions are presented at the end of the chapter 2.

In the third chapter, first, the proposed hybrid power system structure, and the required components for such system are listed, and then the physical structure of the components and their modified models are presented in different sections. Simulation results and different analysis results are explained in each section. Then, the experimental setup and test results are presented.

In Chapter 4, a typical hybrid power system for isolated application is simulated. The procedure for predictive wind and load data regeneration using Monte-Carlo simulation, and novel approach to evaluate different wind turbine performance in the desired location are presented. The performance of different energy storages is evaluated by introducing new criterion based on the system capability on capturing excess wind energy when the storage capacity is not limited. Then three different storage technologies are investigated through case studies, and their sizing and design impact on total fuel consumption of diesel generators are investigated. Finally, the last chapter is dedicated to conclusions and future work.

Chapter 2 Compressed Air Energy Storage System

Energy can be stored by compressing abundant air and expanding it later. As described in the previous chapter, pumped hydro and compressed air storage systems are the only two options for bulk energy storage. The geological constraint and huge initial investments associated with the pumped hydro system is a major drawback for its implementation. On the other hand, compressed air with lower initial cost and the option of mixing with natural gas in a conventional gas turbine is becoming an interesting option. This can be more economically attractive when wind energy is used to provide the required compressed air instead of using energy produced by fossil fuel based power plants. Extensive studies have been conducted to investigate the financial benefit of Compressed Air Energy Storage (CAES) system implementation in a power grid [7, 9, 10], [14], [34], [17], [22] and [35].

Also research aimed at improving the energy conversion efficiency and extending its application range has been successively conducted, resulting in excellent characteristics and advantages of the CAES system [36]. Considering the availability of air, high pressure tank and compressors can be used to eliminate the geographical constraint and also increase the energy density of CAES system [37]. In this chapter, the energy conversion principle in a CAES system is discussed in more detail and the current status of CAES system development is presented.

2.1 Principle of CAES Energy Conversion

In order to understand the viability of compressed air energy storage system, it is important to understand both the process of compression and expansion. In a CAES system, the energy storage and extraction processes are thermodynamic cycles, therefore the overall performance of a CAES system depends on the path of the energy conversion cycles. Energy can be stored and extracted in three different processes namely, isothermal, adiabatic and polytropic paths, as shown in Figure 2-1.

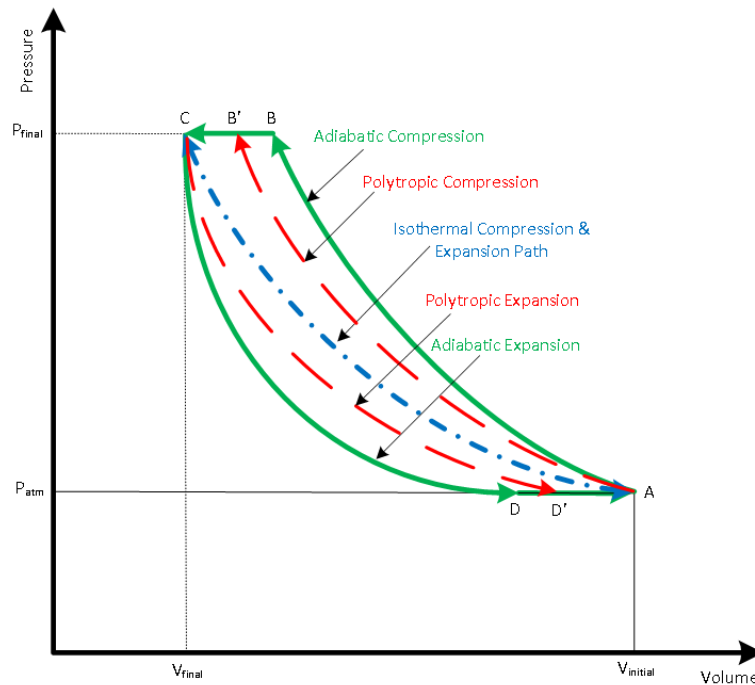


Figure 2-1: Compression and expansion cycle with isothermal, adiabatic and polytropic paths [38].

According to the first law of thermodynamics, the change in internal energy is the sum of the change in external work done on the system and change in heat content of the system ($dU=dW+dQ$, where U , W and Q represent internal energy, work and heat content of a system respectively). In an isothermal energy conversion process ($dU=0$), and the air temperature is assumed to remain constant. In this case the input-output rate of heat and

work is identical. In a real system, it is impossible to achieve this condition for the energy conversion despite the implementation of highly efficient, well designed and complicated heat exchangers. The energy conversion for both isothermal compression and expansion path lies in the middle of Figure 2-1 (Path A-C) [39] and [38].

According to the ideal gas equation in an isothermal process: $P_1V_1=P_2V_2$ [40] and [41]. The required work to compress air from (P_1, T_1) to $(P_2, T_2=T_1)$ in an isothermal process can be calculated by the following equation:

$$W_{isothermal} = -\int_{V_1}^{V_2} P dV = -\int_{V_1}^{V_2} \frac{nRT}{V} dV = nRT \ln\left(\frac{V_1}{V_2}\right) = P_1V_1 \ln\left(\frac{P_2}{P_1}\right) \quad (2-1)$$

Where P is the pressure, T is the absolute temperature, and V is the volume.

Heat exchange during an adiabatic energy conversion cycle is zero ($dQ=0$), and applying mechanical energy during the compression will increase the internal energy of the thermodynamic system, resulting in the rise of the system temperature and pressure. This concept has been used in advanced adiabatic CAES systems to increase the overall energy conversion efficiency. The produced heat during the compression stage is stored and used later to preheat the compressed air before the expansion cycle. Such a system is only practical in a well isolated system with short intervals between compression and expansion [42]. The compression and expansion cycle is shown by A-B and C-A respectively in Figure 2-1.

In practice, heat transfer occurs between the system and environment due to imperfect insulation. As a result, the temperature does not remain constant during a thermodynamic cycle, and the energy conversion path fits between the isothermal and adiabatic paths,

referred to as polytropic energy conversion cycle. This path is shown by dashed lines (A-B' & C-D') in Figure 2-1. For a polytropic compression/expansion, the ideal gas equation can be written in a general format as [43]:

$$PV^n = nRT \quad (2-2)$$

$$W_{Polytropic} = \frac{nPV_1}{n-1} \left[\left(\frac{V_1}{V_f} \right)^{n-1} - 1 \right] = \frac{nPV_1}{n-1} \left[\left(\frac{P_2}{P_1} \right)^{(n-1)/n} - 1 \right] \quad (2-3)$$

Where n is polytropic exponent (c_p/c_v), R is the universal gas constant, V_f is the final volume and N is the number of moles of gas. The polytropic exponent value for air can change from 1 for an isothermal process to 1.4 in an adiabatic process, based on the heat transfer characteristics of the heat exchanger. In multistage compression or expansion, intermediate pressure and temperature can be calculated using the following equations respectively:

$$P_2 = P_1 \left(\frac{V_1}{V_f} \right)^n \quad (2-4)$$

$$T_2 = T_1 \left(\frac{V_1}{V_f} \right)^{(n-1)/n} \quad (2-5)$$

The presented thermodynamic anatomy and equations for a compression cycle are also valid for an expansion cycle. The compression efficiency can be obtained by dividing the required work to compress certain amount of air to desired pressure in an isothermal process by the same required work in a polytropic process. In an expansion cycle, the polytropic exponent value is close to its adiabatic value (1.4 for air) as the energy conversion is instantaneous. The multistage expansion with proper heat exchanger can increase the expansion efficiency which is critical in small scale storage systems with limited storage capacity [40].

$$\eta_{Compression} = \frac{W_{isothermal}}{W_{Comp-Polytropic}} \quad (2-6)$$

$$\eta_{Expansion} = \frac{W_{Exp-Polytropic}}{W_{Isothermal}} \quad (2-7)$$

A typical CAES system works on the basis of one of the processes described above. Different energy conversion paths and application based on different implementation of the basic principle have been proposed and developed, resulting in various types of CAES systems. The current status of some of the CAES systems is presented below.

2.2 Overview of Existing and Developing CAES Technologies

In this section an overview of the different CAES systems is presented in a chronological order to show their technical progress and extended application. This provides the current and future interest in developing such a storage system in order to create other possible future applications. These brief descriptions of CAES technologies provide a basis for defining the status and objective of this thesis.

2.2.1 First Generation of CAES Systems (Classic CAES)

Classic or conventional CAES systems, as first generation systems, are currently the only well developed and available CAES system at the commercial stage. The basic principle of this type of system is to combine air with natural gas in order to reduce the fuel consumption of the gas turbines. Two third of fuel in a gas turbine is consumed to compress the air and super-charge the gas turbine. The required compressed air can be produced and stored in off peak hours and used later. In this type of storage system, the

compression cycle time is decoupled from the combustion time to enhance the power output and fuel consumption profile of the power plant. Such a storage system is suitable for energy management, load leveling and peak energy support applications for bulk energy storage when cheap excess energy is available [44-46]. The emission from this type of energy system is lower than conventional gas turbine based power plant as a result of the decrease in fuel consumption; however, it is not a zero emission power plant.

The elementary idea of this concept goes back to the 1960s, while the first implementation of such a storage system, a 290 MW plant for 3 hours storage capacity, has been operational in Huntorf, Germany since 1979 [32] and [47]. The second example of this system, a 110 MW unit designed for 26 hours of generation at full power, was established in McIntosh, Alabama in 1991.

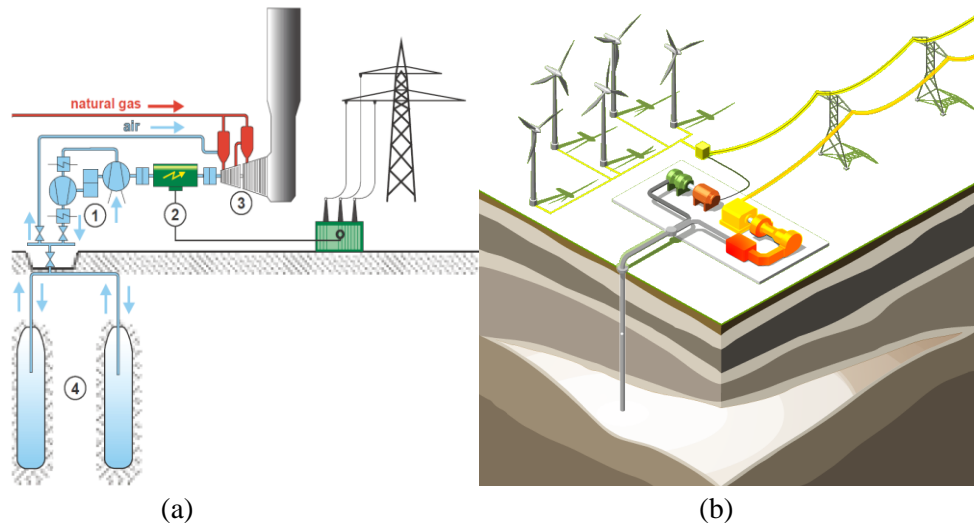


Figure 2-2: a): Schematic of a typical first generation CAES system [47], b): Diagram of the Iowa Stored Energy Park [7]

The schematic of a typical classic CAES system is shown in Figure 2-2(a). It consists of the following components [47]:

1. The air compression equipment, which includes air compressor and might be in single or multi-stage configuration; air filter to remove the particles and moisture; and heat exchanger to cool the compressed air.
2. Electrical motor/generator to drive the compressor in storage cycle.
3. Low pressure and high pressure turbines and recuperator.
4. Underground reservoir

Several studies have been conducted to evaluate the technical and economic aspects of applying a bulk CAES system to the electric grid [45], [48] and [49]. As a result of these studies, this type of storage system is available for large scale (100 to 1000 MW), long duration (more than 8 hours to even seasonal storage) application in load shifting and support for wind farms, and it is less complex and cheaper to construct and operate than a combined cycle which is used in thermal power plants in order to capture the exhaust heat to reproduce steam [7] and [50].

Further technical developments have resulted in the application of CAES system in large scale systems for peak shaving and energy management. Consequently, more future CAES systems have been planned to be established in the US power network [51].

The Iowa Stored Energy Park located in Dallas Center, Iowa is going to be the first CAES system coupled to a wind farm (Figure 2-2b) [7]. The Iowa Association of Municipal Utilities (IAMU) is planning to establish a 268 MW CAES plant, using an aquifer to support a 75-100MW wind farm integration to their electrical grid [52].

High wind potential in Texas has attracted attention to wind farm development; however, limited available transmission capacity with a few interconnection points is the

main constraint for such a development because the excess wind energy cannot be used or transmitted [7]. Existing salt domes in the Texas State and also the financial and technical benefit of CAES system implementation in Huntorf and McIntosh have created incentive for CAES development. As a result of supporting research [53], [54], Ridge Energy Storage & Grid Services L.P. have started to design and develop several CAES projects (4x135MW units) in Texas state [55]. In a carbon restricted scenario, this type of storage system is one of the best options for the bulk storage in wind integration application to increase its capacity factor; although, its emission can be considered as another disadvantage [56] and [57].

2.2.2 Second Generation of CAES Systems

Second generation of CAES systems are similar to the first generation systems, with a different design in order to reduce the relatively high initial costs, provide flexible rating for different applications and reduce the emissions. These technologies could have 15MW to 600MW capacity, and their lower initial cost is related to using standard components, simple structure and fast establishment (within 2 years). In addition, environmental consideration in their design has led to lower emission in comparison to the classic CAES systems [58] and [59]. The theoretical efficiency of the second generation CAES systems is approximately 54%, 4% more than the classic CAES systems of the same rating [45].

Various hybrid designs have been developed based on existing gas turbine modification. Energy storage and power corporation (ESPC) is the pioneer in this technology and have patented different CAES systems concepts [60]. The first developed

concept is the CAES-Air Injection (CAES-AI) concept based on the direct injection of the preheated stored air into the compressor discharge plenum of a gas turbine (GT) to increase its power output. Figure 2-3 shows the illustration of a typical CAES-AI system.

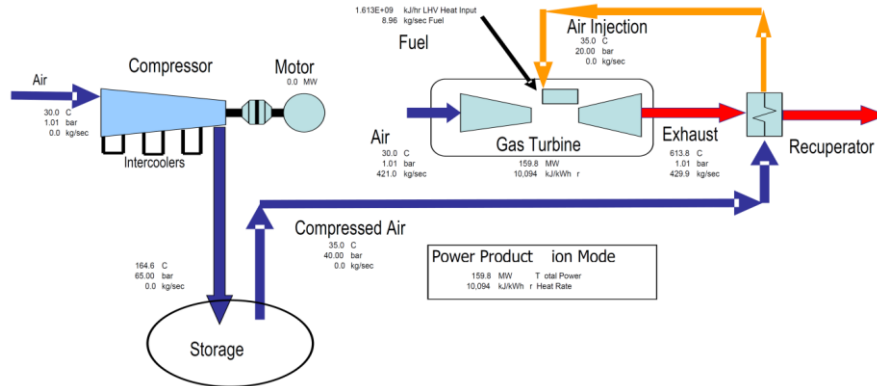


Figure 2-3: The schematic of a typical CAES-AI system [58].

ESPC has proposed another CAES concept known as CAES-AI with HP Expander Concept (CAES-AI-HPE) by adding a high pressure expander to utilize the available pressure difference between the preheated stored air and the air injected to the Gas turbine. A typical CAES-AI with the HP Expander concept schematic is shown in Figure 2-4.

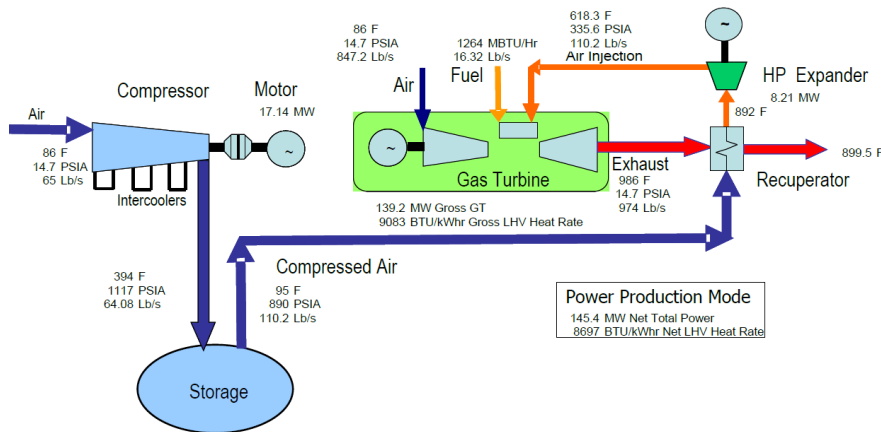


Figure 2-4: Typical schematic of a CAES-AI with the HP Expander concept [60].

Another CAES-AI concept developed by ESPC utilizes the pressure difference between pre heated stored air and ambient air using two HP and LP expanders as shown in Figure 2-5a. This technology referred to as CAES-AI with the Bottoming Cycle Air

Expander (CAES-AI-BCE) has higher power rating in comparison to the previously proposed CAES systems.

In a CAES system with the Bottoming Cycle Air Expander and Inlet Chilling (CAES-BCE-IC), another patented technology by ESPC, as shown in Figure 2-5b, the HP expander output is fed through the combustion turbine. The main characteristics which make this CAES concept different from previous designs are firstly the expander exhaust air flow is equal to the GT input air flow; and secondly its temperature is usually less than ambient temperature [61] and [62].

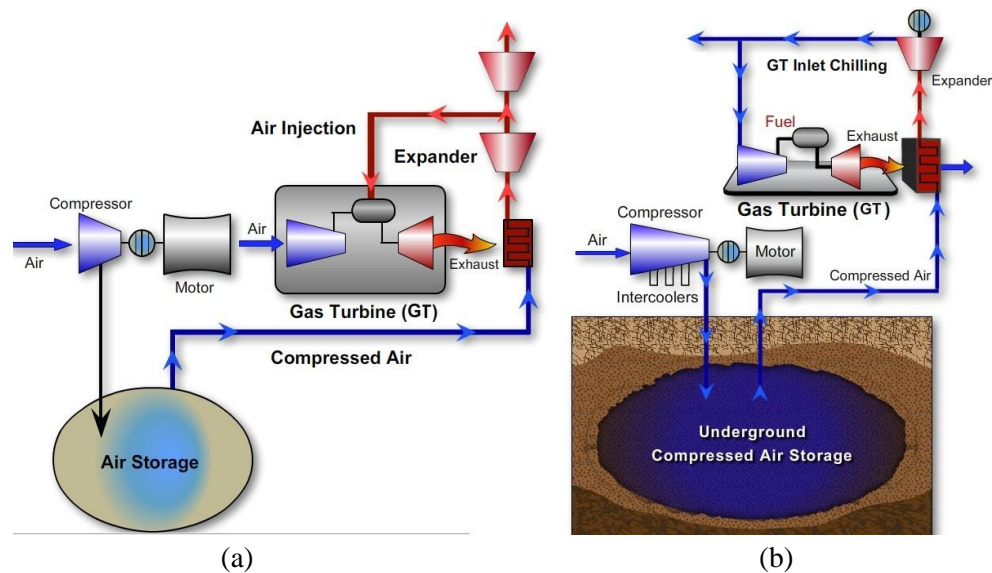


Figure 2-5: Typical schematic of: a) CAES-AI-BCE and b) CAES-BCE-IC concept [61].

Another variation of the second generation CAES concept, which includes components similar to other second generation, is the CAES systems with Bottoming Cycle Air Expander (CAES-BCE). Its schematic is shown in Figure 2-6. The air expander can have various sizes due to its independent operation from the GT and the outlet-inlet air requirement is not limited in this configuration.

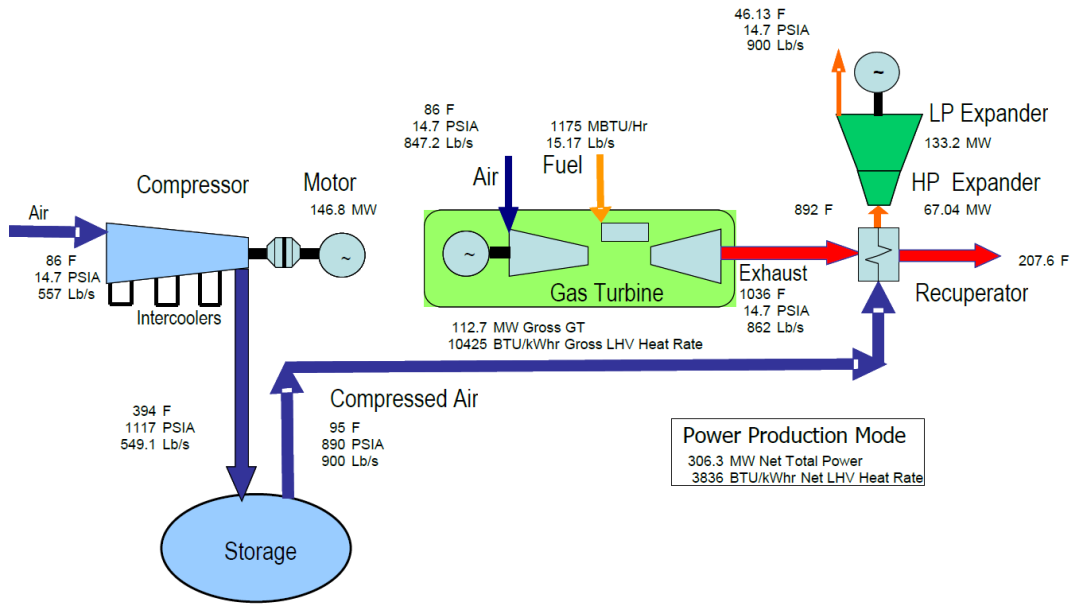


Figure 2-6: Typical schematic of a CAES-AI with the HP Expander concept [60].

A summary of the second generation CAES systems with their characteristics are presented in Table 2-1 to facilitate their comparison. The specific cost has been calculated based on the market price for the required components in 2006 [60] and [61]. The Plant power in Table 2-1 shows the nominal gas turbine power without using CAES, and The CAES power includes both the Gas turbine power increase due to compressed air injection and the multi stage high pressure expander power.

Table 2-1: Summary of Performance and Estimated Price Data for Various CAES Plant Concepts

Characteristics	CAES type					
	Classic	AI	AI-HPE	AI-BCE	BCE-IC	BCE
Plant Power, MW	110	137	145	333	327	306
CAES Power, MW	110	25	33	221	215	194
Off-Peak Compressor Power, MW	81	16	17	147	142	147
Total Power Fuel Related HR, Btu's/kWh	3970	9355	8700	3800	3940	3696
Relative Cavern Volume	5.7	1.5	1.5	5.45	5.3	5
Approximate Specific Capital Cost, \$/kW	850	495	480	550	520	560

As can be deduced from Table 2-1, CAES-AI and CAES AI-HPE concepts have lower specific capital cost and required cavern volume. On the other hand, CAES-BCE has the lowest heat rate in Table 2-1, and it can be the best environmental friendly option with a reasonable capital cost. This category of CAES systems is currently under development and no CAES system has been established based on this concept.

2.2.3 Third Generation CAES Systems (Adiabatic CAES)

The third generation of the CAES systems attempts to achieve quasi adiabatic energy conversion path for both air compression and expansion cycles by storing the produced heat during compression and using it later to preheat the air in the expansion cycle. A general configuration of such a system is shown in Figure 2-7. As illustrated in this figure, an adiabatic CAES includes air filters, high temperature ($\sim 650^{\circ}\text{C}$) and pressure (~ 10 to 20 MPa) compressor, high and low temperature heat storage equipment, multistage expanders, and power conditioning devices [63].

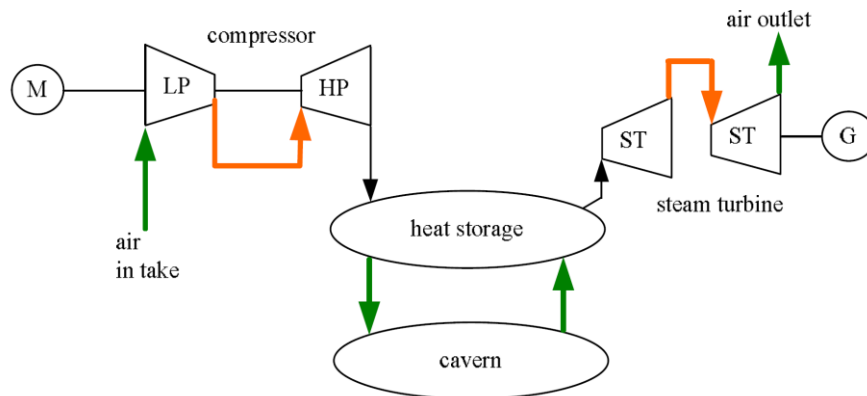


Figure 2-7: Schematic of a typical adiabatic CAES system [64].

Thermal storage unit in adiabatic-CAES has significant effect on the overall efficiency of the storage system. This well insulated unit should be able to exchange heat with air

during compression and expansion cycles in relatively high and adjustable rate depending on the operational condition. In addition such a system should have reasonable cost. Solid and liquid based thermal storage systems are currently more attractive due to their high energy density and insulation characteristics [64]. The use of large heat transfer surface in order to have direct heat exchange between the thermal storage and the air, results in lower heat loss through the medium and consequently higher efficiency. Thermal energy storage technology, high-temperature insulation material, and active cooling concept are currently in their development stage, and will increase the adiabatic-CAES system share in energy storage systems [65] and [66].

The main advantage of this type of storage system is its emission free characteristics because it does not use any fossil fuel in its energy conversion cycles. The capacity of adiabatic CAES is smaller, and its efficiency is higher than the first or second generation CAES technologies [67] and [68]. High initial costs and early stage technology are the main constraints in the implementation of this type of CAES system [45]. This type of storage system is suitable for isolated application where fuel consumption is a challenging concern and the energy should be provided by renewable sources. This technology is currently in its research and development stage, and at the moment no practical operational system has been found in the literature.

2.2.4 Hybrid Diesel-CAES Systems

A new concept similar to the second generation CAES system has been introduced by Hussein Ibrahim, et al in [69] and [70]. In this system, the gas turbine is replaced with

diesel generators and compressed air is used for supercharging the engine in order to increase its specific power. As a result, the diesel engine consumes less fuel to produce the same power. The excess energy can be converted to compressed air and stored in a high pressure tank to be utilized later for engine supercharging. This strategy can reduce the fuel consumption while overcharging the diesel engine with high pressure air, leading to lower reliability and life time which results in higher cost for engine replacement and maintenance. The main motivation for the development of such a system can be attributed to its potential applications in isolated power supply systems which currently employ diesel generators. In these implementations, available renewable energy source can be used to supercharge the diesel generator to reduce the fuel consumption.

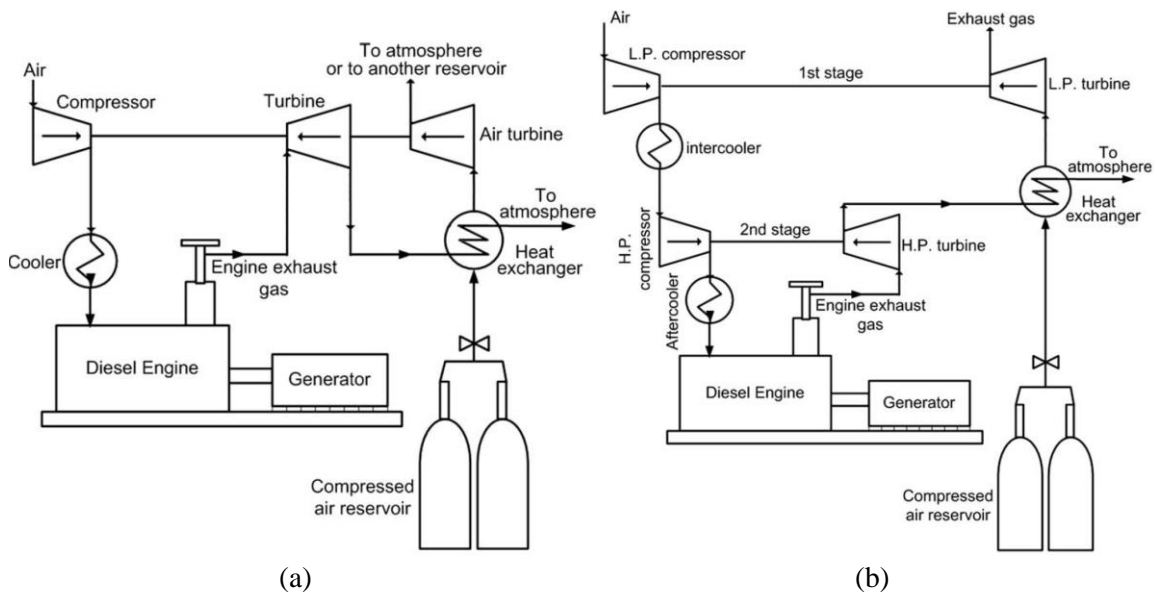


Figure 2-8: The configuration of the direct connection of the turbine to the air turbine (a), and two stages turbocharger system (b) [69] and [70].

Similar configuration to the second generation CAES has been proposed as hybrid diesel-CAES system and a brief description of the different configuration for

Direct admission of compressed air into the diesel engine is another possible concept in hybrid-diesel CAES system. The schematic of such a system is shown in Figure 2-9b. The compressed air is injected to the engine after being heated in heat exchanger by the engine exhaust gas. This system requires an intake system modification and reduces the engine life time [69] and [70].

Different parameters such as efficiency, simplicity, adaptability, cost, control system complexity, and reliability, can be used to investigate the performance and practicality of the described hybrid-diesel generator concepts. Applying weighted score method for each criterion, the overall score of each system has been calculated in order to determine the optimum concept in [69]. A weight factor between 0.1 and 0.225 has been associated in Hussein Ibrahim, et al's study [69] to each criterion based on its importance level. Three different score values, 0, 0.5 and 1, were assigned to each factor based on its performance as poor, good and excellent respectively. Using these factors the different presented supercharging configurations are compared in Table 2-2.

Table 2-2: The compressed air supercharging system comparison [69].

Criteria	Weight coefficient	Config. #1	Config. #2	Config. #3	Config. #4
Efficiency	0.2	0.8	0.7	0.6	0.7
Simplicity	0.225	1.125	0.675	1.2375	0.5625
Adaptability with the diesel engine	0.225	1.125	0.9	1.0125	0.5625
Cost	0.125	0.625	0.5	0.6875	0.25
Control system	0.125	0.5625	0.375	0.625	0.125
Reliability	0.1	0.45	0.45	0.3	0.1
Total	1	4.6875	3.6	4.4625	2.3
Rank	NA	1	3	2	4

According to Table 2-2 the direct connection of the turbine to the air turbine Configuration #1) is the best option for supercharging the diesel engine. Using these

values for performance assessment is subject to question where no technical or financial data was provided in [69]; however, it can be used as a primary decision table. The proposed method was abandoned later due to reduced lifetime and safety concerns of the diesel generators as they were not designed to operate at the supercharged condition.

2.2.5 Liquid Piston Based CAES Systems

In a thermodynamic system, especially in relatively high pressure systems, deviation from isothermal energy conversion path will lead to poor efficiency. Having a cost effective heat exchanger, in order to keep the compression and expansion cycles at ambient temperature, can increase the overall efficiency of a CAES system. In a liquid piston based CAES system, also known as accumulator energy storage system, a mixture of two compressible (air) and incompressible (water, oil) fluids is used to achieve high pressure and proper heat transfer characteristics. In this method, an incompressible fluid is pumped into a tank including a gas-liquid interface which increases the gas pressure. The energy is stored in a combination of compressed gas and potential energy of certain amount of liquid in higher elevation [39] and [71]. The incompressible fluid can be used to run a liquid based turbine or pump utilizing the stored energy in liquid piston. The main advantage of this method is its quasi-isothermal energy conversion cycle, and the required heat for both compression and expansion cycles can be provided by ambient. The storage tank can be installed in ground level or higher elevation in order to benefit more from gravitational potential energy [72].

High efficiency can be achieved using liquid based machines considering the fact that charging time of an accumulator is much higher than required heat transfer time constant. The slow charging rate of an accumulator leads to an isothermal energy conversion where the system has enough time to exchange heat with the surrounding environment. The oil/hydraulic motors/pumps have the advantages of lower leakages, losses and noise in comparison to air motors. Two possible configurations shown in Figure 2-10 can be used for the liquid-air interface. They are known as Batteries with Oil-hydraulics and Pneumatics (BOP) type A (Figure 2-10a) and type B (Figure 2-10b) [73].

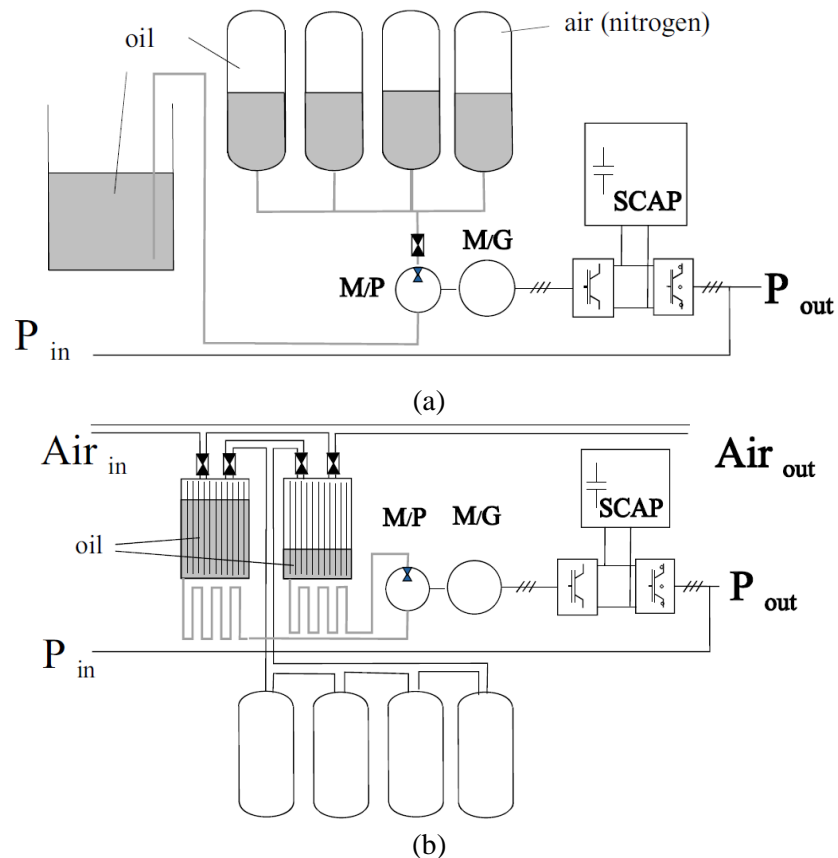


Figure 2-10: Two types of liquid piston concepts: a) BOP-A; b) BOP-B [73].

BOP-A is based on industrial liquid/gas interface accumulator where a membrane separates the liquid from gas. This technology has limited energy density due to fixed amount of gas working in a closed loop, and additional reservoir is needed for the liquid supply. The energy density of the system can be improved by applying this concept in type-B configuration where the air works in an open cycle and additional required air can be supplied from outside. However the liquid piston concept implementation has some practical issues mainly related to the liquid-air interface [74] and [75].

A cost analysis has been done in [76] to compare the required investment for three different storage systems for a 10kW-60kWh application. A lead acid batteries system, a BOP-A system and a BOP-B system were compared and the results are summarized in Table 2-3. The BOP-B storage system has the lowest energy cost, while the BOP-A energy cost is as high as the lead acid based system due to low energy density and high cost of the accumulator [76].

Table 2-3: Cost evaluation for 60kWh-10kW storage for three storage technologies [76].

60kWh - 10kW		Lead Acid	BOP-A	BOP-B
Techn ology	Storage	€ 18'000	€ 60'000	€ 4'500
	Conversion	/	€ 15'000	€ 18'000
	Total	€ 18'000	€ 75'000	€ 22'200
Operation & Maintenance		30% € 5'500	20% € 15'000	20% € 6'000
Total Cost		€ 23'500	€ 90'000	€ 28'000
Life cycle		3'500 or 210'000 kWh	15'000 or 900'000 kWh	15'000 or 900'000 kWh
Energy Cost /kWh		€ 0.11 / kWh	€ 0.1 / kWh	€ 0.03 / kWh

2.3 Proposed Small Scale CAES System for isolated hybrid power system application.

Remote communities which are not connected to the electrical power grid are generally dependent on diesel generators, a polluting, inefficient (especially in partial loads) and relatively expensive electricity production option. In northern isolated communities, additional transportation difficulties for supplying fuel during winter months make electricity production by diesel generators unreliable. Considering the large number of these communities in Canada [77], an attractive market is available for developing hybrid power system based on renewable energy sources. Such a system is more attractive when great wind potential is available in such areas. As result, some wind-diesel projects were installed in few remote communities in Canada, but most of them are not operational or still suffering from low wind penetration in their hybrid power system [77]. Consequently, isolated communities still depend on diesel generator, and their fuel consumption profile has not improved even after wind turbine installation. This issue can be related to insufficient funding, non-optimum wind turbine selection and installation, lack of an effective energy storage system to increase the wind energy share in electricity production, and mainly as a result of modifying existing power system instead of integrated design of a hybrid power system with proper study [77], [78]. Therefore, cost effective, safe and efficient energy storage is the missing link in renewable energy power generation infrastructure especially for remote communities.

Based on the literature review of the current status of CAES technologies, there is a great potential for research on the possibility of using pure pneumatic energy storage

system where air is the sole medium in both energy storage and expansion cycles. Considering an isolated community with great wind potential, a pure pneumatic storage system can be installed to store the wind turbine excess energy during high wind speed regimes, and deliver stored power when the wind turbine output power is not sufficient to meet the demand.

Considering the significant demand for a hybrid power system for isolated application or communities, a small scale pure pneumatic CAES system is proposed in this study. In this proposed system, both charge and discharge cycles as a thermodynamic processes happen at ambient temperature. The heat can be exchanged through both compression and expansion cycles with the environment naturally. This pure pneumatic CAES system can operate with much more simple heat exchanger configuration and heat transfer requirements. As a result, the number of system components and required control equipment will be reduced, resulting in a simple system. Moreover, maintenance requirement will be less than liquid piston based CAES system. However, this storage system has lower energy density in comparison with a liquid piston based CAES system, requiring higher storage volume than a liquid piston system. Therefore, the possibility of using a pure pneumatic system, as an inexpensive storage system with flexible and expandable size; reasonable energy density; low complexity; and low maintenance characteristics is explored for isolated applications.

In this study, the required energy for the air compression will be provided by a properly designed wind farm; while in conventional CAES systems, fossil fuel is consumed to produce required energy for air compression. This change in main energy

source provides free excess energy for CAES system in compression cycle and can be considered as compensation for its low efficiency because the additional energy required for the CAES system losses is supplied by the wind energy rather than burning fossil fuel in traditional systems. As a result more energy can be stored and injected to the load in order to reduce the diesel generator fuel consumption, and make CAES system more economically attractive.

2.4 Research objectives

Considering the main objective of this research on increasing wind energy penetration in electricity generation for an isolated application, the following research questions can be introduced:

1. How incorporating wind energy and compressed air energy storage system can reduce the diesel fuel consumption for electricity generation in remote areas?
2. How we can ensure that energy system designers produce only correct and reliable designs, using proper wind turbines and storages system?
3. What are the factors that have impact on design and implementation of a RES based electricity generation system for remote areas

2.5 Summary

In this chapter, an overview of existing and developing CAES technologies has been presented. After explaining the energy conversion in thermodynamic compression and expansion cycles, the required energy to compress certain amount of air mass has been formulated. Three different generations of CAES systems were presented in a

chronological order to show their technical progress and extended application. Also a brief overview of some operational CAES systems was introduced. In addition, Different configurations of hybrid diesel based CAES system for isolated community was presented because of its application similarity to the objective of this study. Pure pneumatic CAES system flexibility in scaling and establishment for different applications including a small scale CAES without geographical constraint was the main motivation to select this type of CAES system in this study.

Chapter 3 Hybrid Power System Components and Their Models

There are different types of storage techniques, which are theoretically and operationally available to remedy the RES fluctuations. Due to technical and economic advantages wind - gas turbine configuration is used in large scale applications [79-81], this research explores the feasibility of small scale CAES system with possible upgrade to medium scale. This system selection is suitable storage option for different future applications including small and medium scale wind integration. In this research a hybrid power generation system which includes compressed air energy storage (CAES) is developed. The excess wind energy is stored in a pressurized tank as compressed air, and it is fed through an expander to produce electricity via a synchronous generator when it is needed.

In this chapter, a small scale CAES system for possible implementation in a wind based energy system for an isolated community is introduced. After presenting the overall schematic of the hybrid energy system, the main components in the energy conversion process are modelled. The chapter also includes the general design considerations, simplifications and simulations of the hybrid power system components.

3.1 Proposed hybrid power system structure

The focus of this work is to develop a reliable and efficient source of electricity which combines a small wind energy generation system with a compressed air energy storage system for isolated customers. When the output energy of a wind turbine is more than the

energy demand at the load side, the excess energy is converted into a mechanical form using high pressure compressors and stored in a high pressure reservoir as potential energy. In the case that the wind turbine cannot deliver the required energy at the load side, the stored mechanical energy is converted to electrical energy through an air motor, synchronous generator and a power conditioning unit consisting of a rectifier, and a grid connected inverter. The schematic of the proposed hybrid system is shown in Figure 3-1.

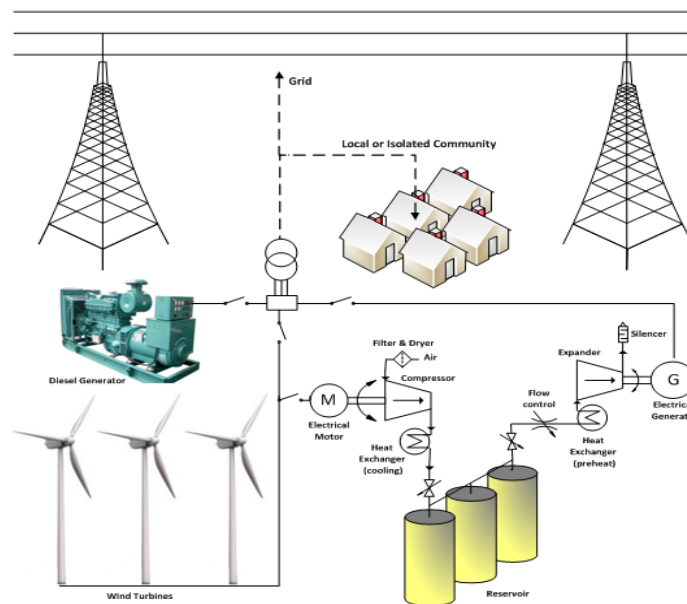


Figure 3-1: Schematic of the proposed hybrid system.

To ensure reliable supply of electricity to an isolated community, it is assumed that the existing diesel generators can be utilized as backup system. The preliminary design of the proposed hybrid system includes the existing diesel generators, wind turbines, CAES system, and supervisory control unit for dynamic energy management. The objective of such an implementation is to reduce the diesel generator total fuel consumption. It is

expected that the CAES system will reduce the operation time of the diesel generator and result in a stable and cost effective operation of the diesel generator.

The energy dispatch control unit performs a supervisory role. Based on the wind speed and demand data, the dispatch control unit defines the energy production share of each of the generation units, i.e. the wind turbine, diesel generator and CAES system. The operating condition of each power component, including the compressor, storage tank pressure, air motor, and synchronous generator is controlled in a way that achieves the stable operation of the system with maximum possible efficiency. Each component is optimized to ensure optimum performance of the hybrid power system. The control unit for each component defines the optimum operating condition of the device. The different components of the proposed hybrid energy system along with their selection criteria and mathematical modeling are presented in the following section.

3.2 System component modeling

The static and dynamic behavior of a system and its control system can be investigated by using the MATLAB software [82] to simulate the different physical system performance under several working conditions. Power system toolbox includes a comprehensive collection of power system components including wind farm, transmission line, electrical machines, power electronic switching devices and other electrical components. These components in combination with digital and analog devices can be used to develop an accurate simulation model of the proposed hybrid system.

However, explicit analytical modeling of each component and using numerical integration to solve the resulting equations might result in significant long simulation time. In addition, this explicit analytical modeling and the nonlinear nature of different elements of the system, would not guarantee simulation convergence. For these reasons, simplified analytical models are developed for each component and implemented in MATLAB -Simulink to simulate the hybrid power system.

3.2.1 Wind Turbine

The performance of a wind based power system depends on the wind turbine characteristics. The main goal of this research is the development of a reliable wind based power system with an effective energy storage system. Such a system can enhance the wind energy penetration in an isolated community or application. The energy production capability of wind turbine is critical in wind-based power systems. Therefore, in order to assess the wind turbine performance in the hybrid system, the static and dynamic models of the wind turbine are developed. The models are presented in the next subsections.

3.2.1.1 Wind Turbine static modeling

The wind turbine output power depends on the produced aerodynamic force of the wind on the wind turbine blades. The steady state output power of a typical wind turbine can be determined using the following equation [83-85]:

$$P_{wind\ Turbine} = 0.5 C_p(\lambda) \rho A_r V_w^3 \quad (3-1)$$

$$\lambda = \frac{R_r \omega_r}{V_w} \quad (3-2)$$

where A_r is the cross section area swept by rotor, and V_w is the wind speed. The air density ρ can be taken as 1.225kg/m^3 . C_p is the wind power coefficient and is a function of λ known as tip speed ratio. Considering (3-2) and Comparing (3-1) with the provided manufacturer power curve shown in Figure 3-2, it can be concluded that the C_p value depends on the wind speed.

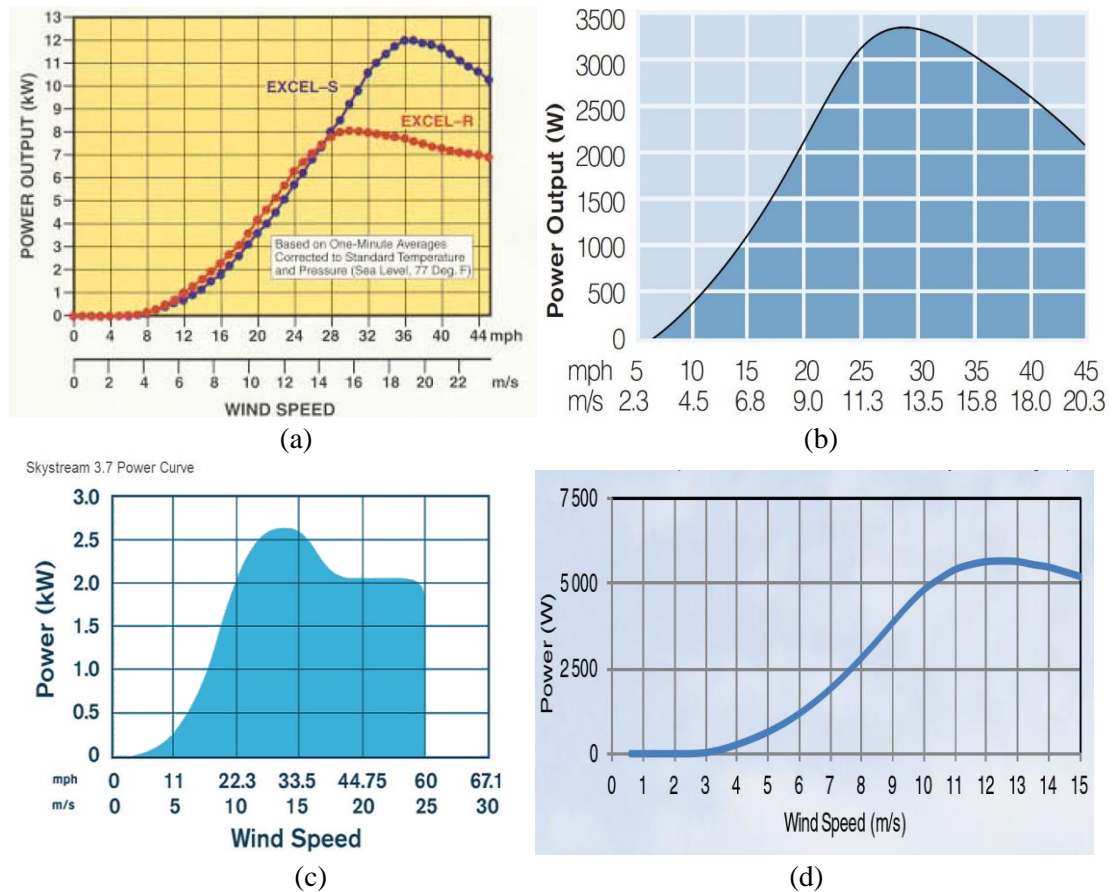


Figure 3-2: Manufacturer's wind turbine power curves: (a) Bergey Excel-R & Excel-S [86], (b): Wisper 500 [87], (c): Skystream 3.7[88], (d): Eoltec Scirocco E5.6-6 [89].

In order to find the corresponding C_p curve as a function of the wind speed, the output power of each wind turbine manufacturer provided power curve was divided by the calculated output power using (3-1) at the identical wind speed. At the next step, the calculated C_p value for each wind turbine was fitted with an equation in MATLAB curve

fitting toolbox to find its mathematical representative. Gaussian equation with four terms was the best fit for the calculated C_p values as a function of wind speed. Equation (3-3) is an example of the Gaussian equation for the Bergey Excel-R wind turbine.

$$C_p(V_w) = a_1 e^{-\frac{(V_w - b_1)^2}{c_1}} + a_2 e^{-\frac{(V_w - b_2)^2}{c_2}} + a_3 e^{-\frac{(V_w - b_3)^2}{c_3}} + a_4 e^{-\frac{(V_w - b_4)^2}{c_4}} \quad (3-3)$$

where V_w is the wind speed. All the parameters in the equation are provided in Table 3-1.

Table 3-1: The Gaussian equation parameters for the Bergey Excel R wind turbine C_p approximation

Parameter	Value	Parameter	Value	Parameter	Value
a_1	0.1787	b_1	8.564	c_1	2.956
a_2	0.0154	b_2	21.5	c_2	4.056
a_3	0.1271	b_3	12.21	c_3	3.669
a_4	0.2121	b_4	5.577	c_4	1.977

The same procedure can be applied to several wind turbine power curves in order to find their mathematical representative of C_p values as a function of wind speed. This method simplifies the wind turbine static modeling for its performance assessment in a variable wind speed working condition. In order to show the accuracy of the proposed approximation method, the calculated C_p value from the Bergey Excel-R wind turbine datasheet is compared with its approximated value using the Gaussian equation is shown in Figure 3-3.

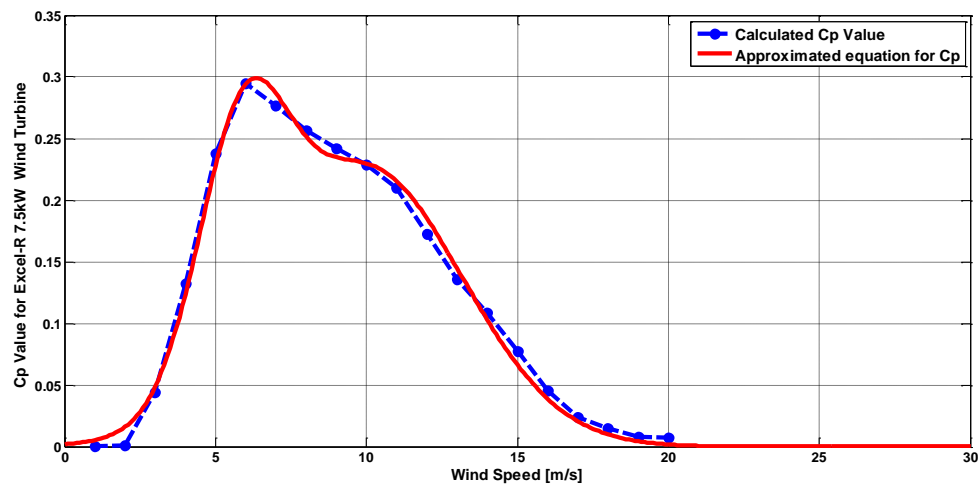


Figure 3-3: Calculated and approximated C_p values for the Bergey Excel-R wind turbine.

The C_p equation for the Bergey Excel-R wind turbine was applied to (3-1), and its output power as a function of wind speed was obtained. Figure 3-4 shows the comparison between the calculated power curve using the approximated C_p equation and the Bergey Excel-R wind turbine datasheet. The comparison shows that the calculated power curve is almost identical to the manufacturer's power curve for wind speeds lower than 20 m/s. It should be noted that most of the small scale wind turbines in this study have either cut-off speed or power curve for speed ranges lower than 20m/s. In addition, this approximation is sufficient for wind farms located at sites where the average value of the wind speed is less than 16m/s, which is the case for the site considered in this study. For higher wind speed ranges and different accuracy of curve fitting, one can use higher order Gaussian equation or other approximated equation.

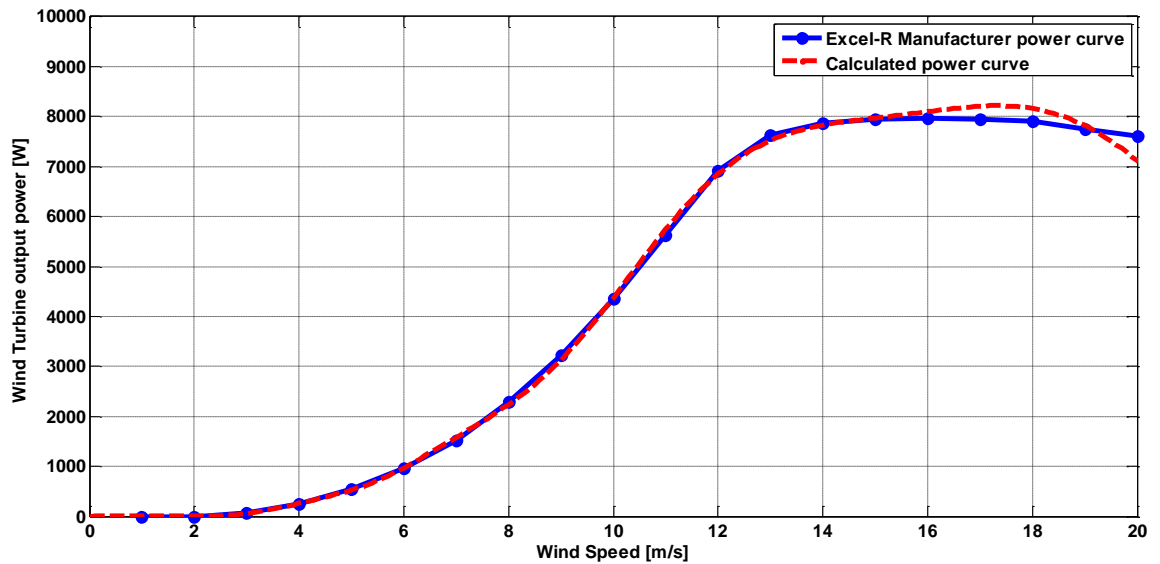


Figure 3-4: Obtained power curve using approximated C_p equation compared with Bergey Excel-R wind turbine datasheet.

3.2.1.2 Dynamic Modeling

Dynamic performance assessment of a wind turbine requires a reasonable dynamic model. In addition, a simple dynamic model assists the analysis of a plant for control design purposes and simulations. The drive train of a wind turbine can be simplified as a lumped model shown in Figure 3-5 [90], [91]. The wind turbine drive train includes all the rotating parts in the wind turbine: low speed shaft, gear box and high speed shaft. J_a in Figure 3-5 represents the rotor moment of inertia, J_e represents the generator moment of inertia; B_T is the wind turbine shaft damping; B_e is the generator shaft damping; and n_G is the gearbox speed transfer ratio. The rotor blades' moment of inertia has a significant higher value in comparison to the generator moment of inertia. As a result, it prevents variation of the rotor speed during both acceleration and deceleration modes.

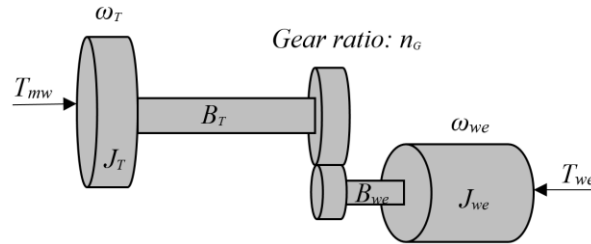


Figure 3-5: Simplified Wind turbine dynamic model based on its drive train [90].

Note: The Figure 3-5 was reproduced by information available in [90].

The dynamic model can be described as below after referring all the parameters to the low speed side of the drive train [90], [91]:

$$T_{wm} - n_G T_{we} = J_{TLS} \frac{dw_{TLS}}{dt} + B_{TLS} w_{TLS} \quad (3-4)$$

$$B_{TLS} = B_T + n_G^2 B_{we} \quad (3-5)$$

$$J_{TLS} = J_T + n_G^2 J_{we} \quad (3-6)$$

where B_{TLS} and J_{TLS} are equivalent shaft damping and inertia referred to the low speed side respectively. The inertia value can be experimentally obtained using the natural time constant of a wind turbine which corresponds to the required time for a wind turbine to reach its rated rotational speed [92]. On the other hand, the total inertia of a body with multiple mass can be calculated using the following equation [91]:

$$J = \sum m_i r_i^2 \quad (3-7)$$

where r_i is the radial distance from the center of the mass for m_i particle. It can be assumed that the mass middle point of a wind turbine blade is approximately located at 1/3 of its radius [91], [92]. Then using equation (3-8), and provided wind turbine specifications available in Appendix 1, the nominal values for the three blade wind turbine inertia and the gearbox transfer ratio can be determined as follows:

$$J_T = \frac{1}{9} m_r R_r^2 \quad (3-8)$$

$$n_G = \frac{\pi R_r \omega_{we}}{30 V_{nWT}} \quad (3-9)$$

where m_r is the mass of the whole rotor including the three blades, R_r is the rotor radius, V_{nWT} is the wind turbine nominal speed in m/s and ω_{we} is the generator nominal speed in rpm. The generator moment of inertia and its shaft damping was chosen in a way that the step response of wind turbine transfer function reaches its steady state value in 15 seconds. This settling time for the wind turbine time constant is selected in order to reduce the overall simulation time. Other simulation parameters are listed in Appendix 1. The Excel-R wind turbine dynamic response in nominal condition is shown in Figure 3-6.

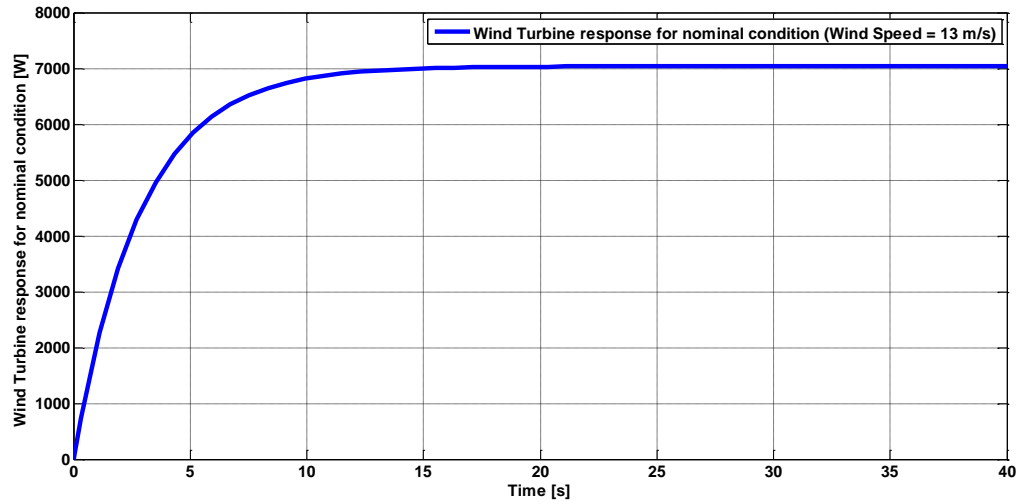


Figure 3-6: Excel-R wind turbine response for nominal condition (Wind Speed 13 m/s).

3.2.2 CAES System

A typical CAES plant includes the following power components: compressor(s), expander(s) and generator. In addition it needs a reservoir to store the energy. Air refinement equipment can also be used to improve the working condition of the CAES plant. In the following subsections the CAES system components are presented and the modeling approach for each component is explained.

3.2.2.1 Compressor

The compressor in the CAES system has the responsibility of converting the excess energy of the wind farm to high pressure compressed air. The high pressure air flow is stored in a high pressure tank. The compression ratio should be high enough in order to decrease the required storage volume. Considering the variability of the available excess energy, reciprocating compressors with variable discharge rate are appropriate in this study. They are inexpensive, operate at low speeds, and provide good performance

throughout the speed range of operation. In addition, they can be used in multistage configuration to achieve high compression ratios. Intercoolers can be used between each stage to increase the energy conversion efficiency by having a polytropic thermodynamic cycle close to isothermal cycle [47]. An electric motor converts the electric energy into the potential energy of the compressed air through the reciprocation motion of a piston.

The energy conversion in a compressor consists of three different physical processes: electrical torque generation in electric motor; mechanical movement of the crank shaft, piston and valves; and fluid process including compressing the air in a cylinder and air flow through the outlet valve. Although, for an accurate dynamic modeling of a compressor all the components and their mathematical equations should be included in the final model [93] and [94], the model can be simplified by ignoring the valve motion effect on the final build up pressure in the cylinder. A combination of the static model and dynamic model can be obtained by considering the step response of the compressor in each compression cycle. The static performance of the compressor defines the amount of outlet compressed air which is stored in a high pressure tank for future use.

The amount of work required to compress certain amount of air from atmospheric pressure to a desired pressure, in a polytropic process and isothermal process can be expressed as (3-10) and (3-11) respectively as [85]:

$$W_{Comp} = \left(\frac{\gamma}{\gamma-1} \right) \cdot P_{in} V_{in} \left[PR^{\left(\frac{\gamma}{\gamma-1} \right)} - 1 \right] \quad (3-10)$$

$$W_{Comp} = P_{in} V_{in} \ln(PR) \quad (3-11)$$

$$\gamma = \frac{c_p}{c_v} \quad (3-12)$$

$$PR = \frac{P_{out}}{P_{in}} \quad (3-13)$$

where γ is the heat capacity ratio or adiabatic index which can be replaced by n where the process is a polytropic one; c_p is the heat capacity at constant pressure; c_v is the heat capacity at constant volume; P_{in} and P_{out} are the input and output pressure in the compression cycle respectively; and PR is the pressure ratio.

The required power of a single stage compressor can be calculated by deriving the work equation (3-10) with respect to time. Considering the fact that the input pressure of the compressor is atmospheric pressure and has a constant value, the pressure ratio also can be assumed to be constant when the output pressure of the compressor is constant. This condition can be obtained by keeping the polytropic index constant through good heat exchange with environment. Therefore, the required power as a function of the volumetric flow rate (Q_{Comp}) in a polytropic process can be obtained from (3-14) for single stage and (3-15) for multistage operation [95] and [96]:

$$P_{Comp} = \left(\frac{n}{n-1} \right) P_{in} Q_{Comp} \left[PR^{\left(\frac{n-1}{n} \right)} - 1 \right] \quad (3-14)$$

$$P_{Comp-Nstage} = \left(\frac{nN_{CS}}{n-1} \right) P_{in} Q_{Comp} \left[PR^{\left(\frac{n-1}{nN_{CS}} \right)} - 1 \right] \quad (3-15)$$

where N_{CS} is the number of compression stages. The power rating and flow rate requirement of the compressor can be calculated using (3-14). Applying the available excess electrical energy of wind turbine to the compressor, the volumetric flow of high pressure air at the compressor output can be calculated as follows:

$$Q_{Comp} = \frac{(n-1)P_{Comp-Nstage}}{nN_{CS}P_{in} \left(PR^{\left(\frac{n-1}{nN_{CS}} \right)} - 1 \right)} \quad (3-16)$$

The above compression equations are valid for a closed-system with a constant air mass; while, the desired storage system in this study should work in an open cycle interacting with the storage tank and the environment. One possibility for considering this condition in modeling could be to represent the process with several time steps in terms of successive closed compression system with specific inlet air mass. Each compression cycle is defined as one crank shaft rotation. Each time step consists of certain number of cycles based on the required accuracy. In each time step, compressed air with certain amount of mass enters the tank, and high pressure compressed air accumulates in the reservoir. The stored energy can be calculated based on the reservoir volume and the final pressure of the stored air at the end of each time step.

Using this method a quasi-dynamic model for the compressor can be obtained using its static performance. The dynamic response of the compressor in each cycle can be approximated by a first order system, where the total rotating components' inertia (J_{T-Comp}) and their damping (B_{T-comp}) are included in the model as follows:

$$P_{comp-out}(s) = \frac{K_{Comp}}{J_{T-Comp}s + B_{T-Comp}} P_{in}(s) \quad (3-17)$$

where K_{Comp} represents the compressor pressure ratio in each time step. Considering nominal values for the compressor output pressure, its nominal rotational speed and cylinder volume provided by the manufacturer, the output flow rate of a compressor can be presented as a periodic train of step response of the compression cycle as shown in Figure 3-7, where 8 consecutive compression cycles are shown.

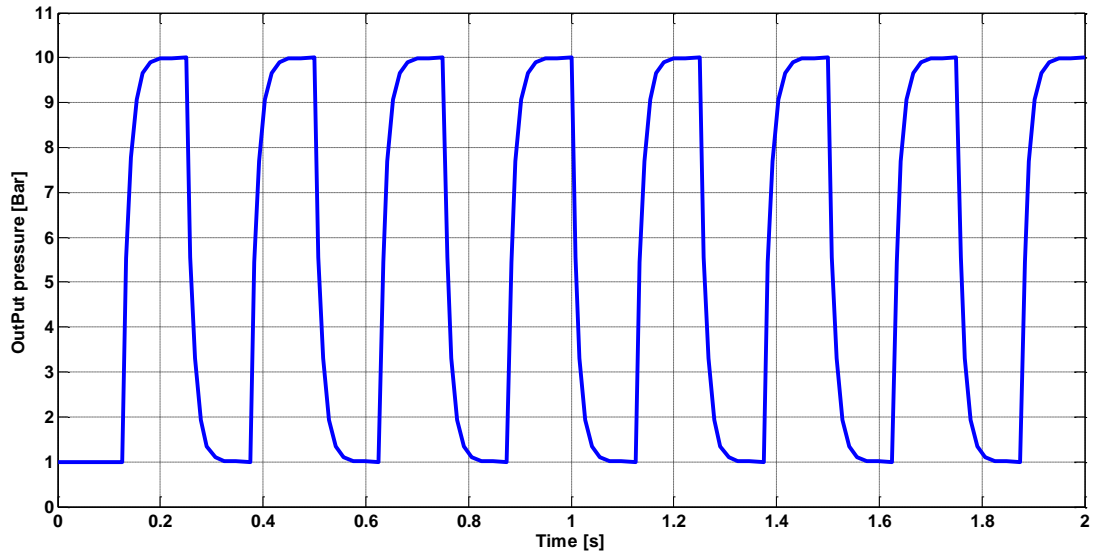


Figure 3-7: Dynamic response of simplified compressor model for 8 cycles of compressions.

The average output flow rate of the compressor can be calculated as a function of the shaft rotational speed and the applied power to the compressor using (3-16). Assuming a polytropic process for the compression cycle, the polytropic exponent of air for the compression process can be considered 1.45 for compression and 1.36 for expansion [68]. The compressor output air mass which enters the high pressure reservoir can be calculated as follows:

$$m_{out-Comp} = \rho \cdot \int Q_{Comp} \cdot dt \quad (3-18)$$

The pressure of the tank will increase depending on the amount of the air mass in the reservoir based on the following equation:

$$P \cdot V^n = mRT \quad (3-19)$$

where R is the gas constant and T is the working air temperature. The change in the compressed air mass stored in the reservoir depends on the available power for the high pressure compressor and it can be formulated using (3-10) to (3-19).

In this study, a flexible power rating was assumed for the compressor unit. The assumed compressor unit consists of several individual compressors with controllable valves which enable series or parallel configuration. In a high power regime, the parallel configuration of the compressors provides high flow rate at the early charge stage of the storage. The compressors could be reconfigured into series connection when the air pressure stored in the tank increases to the set point, and the compressors work in multi-stage configuration to reach higher compression ratios. Low efficiency for single stage compression and expansion is the limiting factor of a very high pressure system. In multistage compression or expansion, the intermediate pressure and temperature can be calculated as follows:

$$P_2 = P_1 \left(\frac{V_1}{V_f} \right)^n \quad (3-20)$$

$$T_2 = T_1 \left(\frac{V_1}{V_f} \right)^{\frac{n-1}{n}} \quad (3-21)$$

where V_i is the initial air volume, V_f is the final air volume and T_1 , T_2 are the corresponding air temperature. Changes in air temperature for different compression stages are shown in Figure 3-8, where N is the number of compression stages.

As shown in Figure 3-8, the air temperature in 5-stage compression will drop to approximately half of the compressed air temperature in a single-stage configuration. This leads to lower required work for compressing the same amount of air to the desired pressure. On the other hand, there is no significant air temperature reduction when the compression stage is increased from 6 to 10 as illustrated in Figure 3-8.

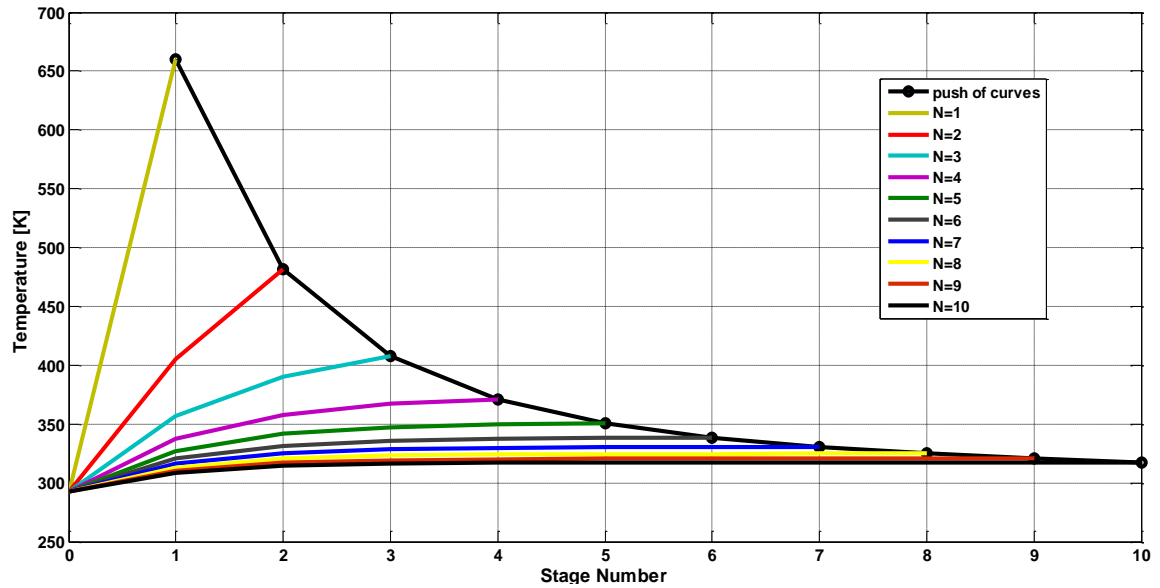


Figure 3-8: Change in air temperature with different compression stages

The required work to compress certain amount of air to the desired pressure with different compression ratios is shown in Figure 3-9(a). As shown in the figure, the required work to compress certain amount of air is reduced by increasing the number of compression stages. The change in efficiency of the compression cycle as a function of the number of compression stage is shown in Figure 3-9(b). As illustrated in the figure, the efficiency can be increased using more compression stages. This can help the performance of the CAES system in cases where the excess energy is available for short durations. Using high pressure compressors can help to improve the energy density and performance of the proposed CAES system, which is shown in design consideration for a CAES system in the next chapter.

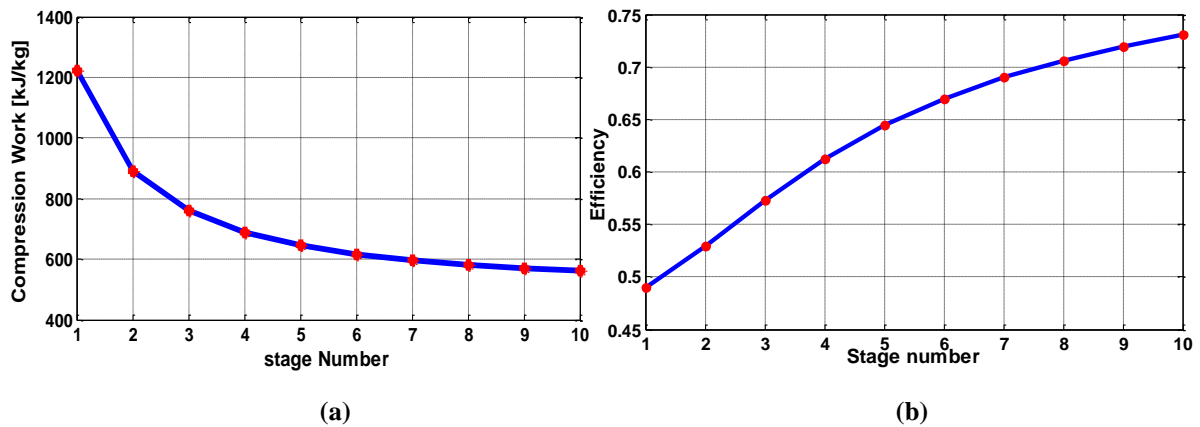


Figure 3-9: Change in (a) required work and (b) efficiency with different compression stages.

3.2.2.2 High Pressure Reservoir

Storing air in a reservoir with constant volume is the next step in storing the excess energy of the wind farm. Various possible methods for storing compressed air are as follows [68], [70] and [96]:

- store in caverns or cavities excavated in rocks,
- store in abandoned mines, salt domes
- store in old oil or gas reservoirs,
- store in underground storage aquifers,
- store in cryogenic liquid form,
- store in pressure accumulator,
- store in underground pipes,
- store in underwater pipes or vessels,
- store in metal tanks, and
- Store in polymeric high pressure tanks.

For the small scale size of the CAES system considered in this research, the metal tank can be an efficient option. Current metal tanks, available commercially, can withstand high pressures up to 500Bar. If a special reservoir is needed for storage, the following equation can be used to determine the spherical tank size and design parameters [68]:

$$\frac{s_{res}}{D_{res}} = \frac{p_s}{4\sigma_r} \quad (3-22)$$

where p_s is the storage pressure, σ_r is the maximum allowed stress, s_{res} is the tank thickness and D_{res} is the reservoir diameter. Using material with high values of σ_r/p_s results in thinner storage tanks with specific diameter and leads to reduction in reservoir weight or higher energy density. The tank storage capacity can be defined as a function of the required energy storage capacity. The required work can be estimated using the product of the required power and the duration. The amount of input air volume (V_{in}) that can produce the required energy can be obtained from the following equations for polytropic and isothermal processes respectively.

$$V_{in-Polytropic} = \frac{W_{Comp}}{P_{in} \cdot (PR^{\frac{\gamma}{\gamma-1}} - 1)} \left(\frac{\gamma-1}{\gamma} \right) \quad (3-23)$$

$$V_{in-Isothermal} = \frac{W_{Storage}}{P_{in}} \ln\left(\frac{P_{out}}{P_{in}}\right) \quad (3-24)$$

The tanks volume size can be calculated from the required input air volume as follows:

$$V_{tank-Polytropic} = V_{in} \sqrt[\gamma]{\frac{1}{PR}} \quad (3-25)$$

$$V_{tank-Isothermal} = V_{in} \frac{P_{in}}{P_{out}} \quad (3-26)$$

The size of a tank that provides a required energy of 4kWh for isothermal and polytropic energy conversion is shown in Figure 3-10 as a tank sizing example. It

observed that the required tank volume for certain required amount of energy is a function of the working pressure and the energy conversion process.

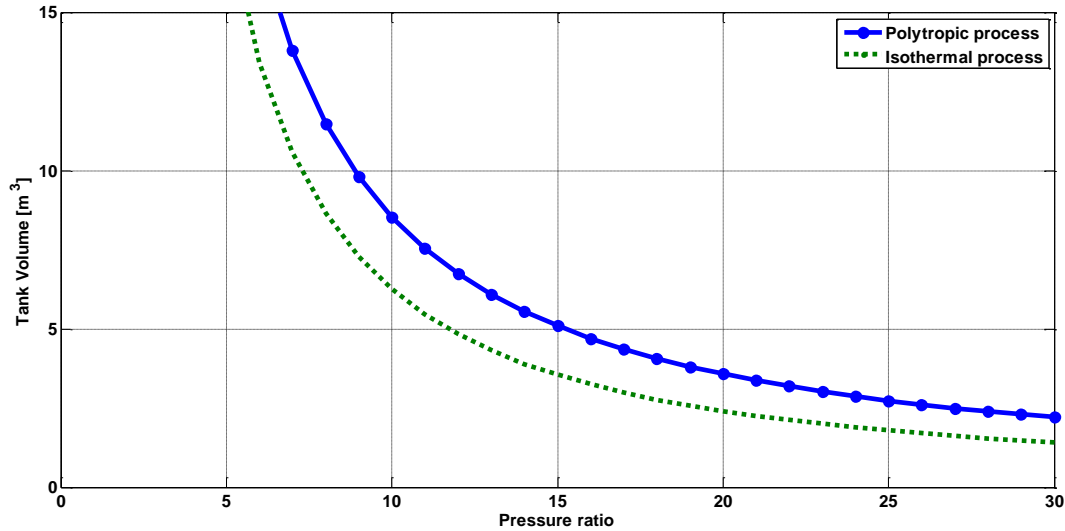


Figure 3-10: Tank size for isothermal and polytropic energy-conversion

3.2.2.3 Air Motor

The air motor is a mechanical device which can be used as prime mover for the alternator in order to extract the stored energy in compressed air format and transform it into electrical energy. A vane type air motor is considered in this research. The main advantage of the vane type air motor is its ability to operate at low speeds in the 1000-3000 rpm range, eliminating gearbox requirement, and as a result, increasing efficiency and reliability. The vane type air motor also gives relatively constant control volumes in comparison to reciprocating type air motors [97].

The rotor is the only moving part and the energy conversion takes place in moving chambers when their volumes change with rotation. The chambers are separated by a freely sliding rectangular vane that moves outward as a result of centrifugal force. The

pressure difference between the inlet and outlet air produces the required torque to rotate the rotor. For a counter clockwise rotation, the air will expand in the left hand side of the air motor and leave the vane motor in the right hand side chambers as shown in **Error! Reference source not found.**(b) [98] and [99].

As a result of the compressibility of air and the friction between the vane and the internal surface of the air motor stator, the air motor is highly nonlinear. Attempts have been made by researches to develop a dynamic or steady state model for controller design in servo application [100-105]. The proposed nonlinear model of the air motor usually include high number of parameters, some of which can be determined through experimental tests [102] and [103]. The complicated and time consuming method to find these parameters has led to other approximation approaches [99-101] and [104]. Although these approaches are acceptable for both speed and position control in servo applications of the air motor, some dynamic models are only valid for specific speed ranges. Therefore, the limitation of the adopted model shall be taken into the consideration. The static and dynamic modeling of an air motor used in this research is presented in the following sections.

3.2.2.3.1 Steady state model

In this research, a simplified model based on the speed-torque and speed-air consumption curves provided by the manufacturer are developed to represent the steady state operation of the air motor. The air motor used in this study is the industrial 4AM-FRV-36A GAST vane type air motor. The motor is rated at 1.3kW maximum power at 7

Bar. Figure 3-11, shows the vane-type air motor and its datasheet characteristics including air consumption, output torque and power.

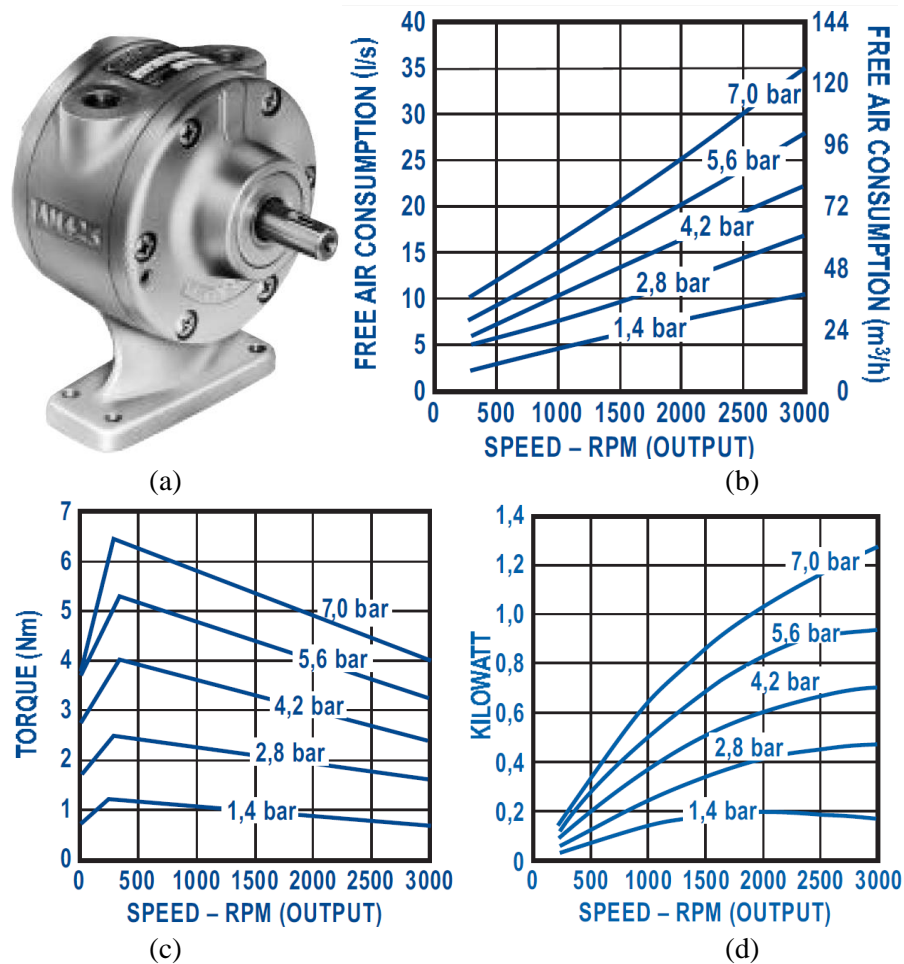


Figure 3-11: (a): 4AM-FRV-36A GAST vane type air motor; (b): Air consumption-speed curves; (c): Torque-speed curves; (d): power-speed curves;

The torque acting on the rotor shaft is created from the air pressure difference, resulting in rotation toward the higher volume chamber. The torque output of the air motor is approximated from the manufacturer data sheet using the following linear equation [106] and [75] for the speed values higher than 250 rpm, where the torque characteristic as a function of the air motor speed has a negative slope as shown in Figure 3-11(c).

$$T_{AM} = f(n_{AM}) = T_{0AM} \left(1 - \frac{n_{AM}}{n_{fAM}}\right) \quad (3-27)$$

where T_{0AM} is the initial torque at the speed of 250 rpm, n_{AM} is the air motor speed, and n_{fAM} is the free rotational speed of the air motor. This piecewise selection of the torque curve is acceptable considering the low output power and air consumption profile for the low speed regime of the air motor shown in Figure 3-11 (b and d).

The mechanical power of this air motor can be described as the product of the motor speed and its torque as follows:

$$P_{mAM} = g(n_{AM}) = \frac{\pi}{30} n_{AM} T_{AM} = \frac{\pi}{30} T_{0AM} \left(\frac{n_{AM} n_{fAM} - n_{AM}^2}{n_{fAM}}\right) \quad (3-28)$$

Based on an extensive analysis of the power curve by the manufacturer, a quadratic equation is found to provide an accurate match in comparison to (3-28). Therefore, the power speed equation of the air motor is modified and represented by:

$$P_{mAM}(n_{AM}, p_{AM}) = C_{PW2}(p_{AM})n_{AM}^2 + C_{PW1}(p_{AM})n_{AM} + C_{PW0}(p_{AM}) \quad (3-29)$$

where C_{PW2} , C_{PW1} , C_{PW0} are the polynomial coefficients and they are dependent on the p_{AM} . Similarly, the air consumption of the air motor is approximated by a quadratic equation as:

$$Q_{VAM}(n_{AM}, p_{AM}) = C_{AF2}(p_{AM})n_{AM}^2 + C_{AF1}(p_{AM})n_{AM} + C_{AF0}(p_{AM}) \quad (3-30)$$

where Q_{VAM} is the required air flow rate, C_{AF2} , C_{AF1} , C_{AF0} are the polynomial equation coefficients and p_{AM} is the working pressure of the air motor. Considering the air motor characteristics provided by the manufacture as shown in Figure 3-11, it can be concluded that the output torque, power and air consumption of the air motor depends on the working pressure. Hence, in (3-29) and (3-30) the coefficients ($C_{PW2} \dots C_{AF2}$) are functions of the working pressure. In order to obtain a general equation to represent the variable

pressure performance of the air motor, modification coefficients based on MATLAB simulations are applied to the air motor air consumption as well as the output torque and power equation. As a result of these simulation, the variation of the proposed coefficients in (3-28) to (3-30) as a function of working pressure can be fitted to a set of polynomial equations for each characteristic. Considering the torque characteristic, its equation can be presented as a function of the air motor working pressure as:

$$T_{AM}(n_{AM}, p_{AM}) = C_{T1}(p_{AM})n_{AM} + C_{T0}(p_{AM}) \quad (3-31)$$

where,

$$C_{T1}(p_{AM}) = -\frac{T_{0AM}(p_{AM})}{n_{JAM}(p_{AM})} \quad (3-32)$$

$$C_{T0}(p_{AM}) = T_{0AM}(p_{AM}) \quad (3-33)$$

where C_{T0} and C_{T1} coefficients are interpolation constants obtained using curve fitting toolbox in MATLAB software. The best polynomial fit for (3-32) and (3-33) is found to be a linear equation expressed as:

$$C_{T1}(p_{AM}) = C_{T11}p_{AM} + C_{T10} \quad (3-34)$$

$$C_{T0}(p_{AM}) = C_{T01}p_{AM} + C_{T00} \quad (3-35)$$

The general torque equation as a function of rotational speed and the air motor working pressure is obtained as:

$$T_{AM}(n_{AM}, p_{AM}) = (C_{T11}p_{AM} + C_{T10})n_{AM} + (C_{T01}p_{AM} + C_{T00}) \quad (3-36)$$

Applying the correction factors to the approximated output torque will result in modified equation for variable pressure operation. The torque-speed characteristic of the air vane motor is shown in Figure 3-12, where the calculated characteristics obtained from (3-36) are shown as straight lines and the characteristics from the manufacturer

datasheet are shown as dots. The results show the accuracy of the steady state modeling of the air motor output torque as function of variable speed and working pressure.

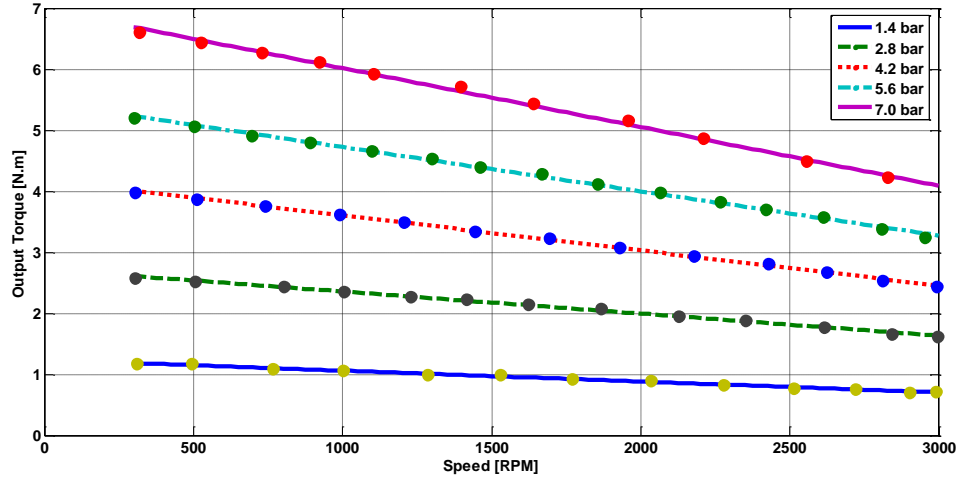


Figure 3-12: Calculated Torque-Speed characteristic comparison to its datasheet values.

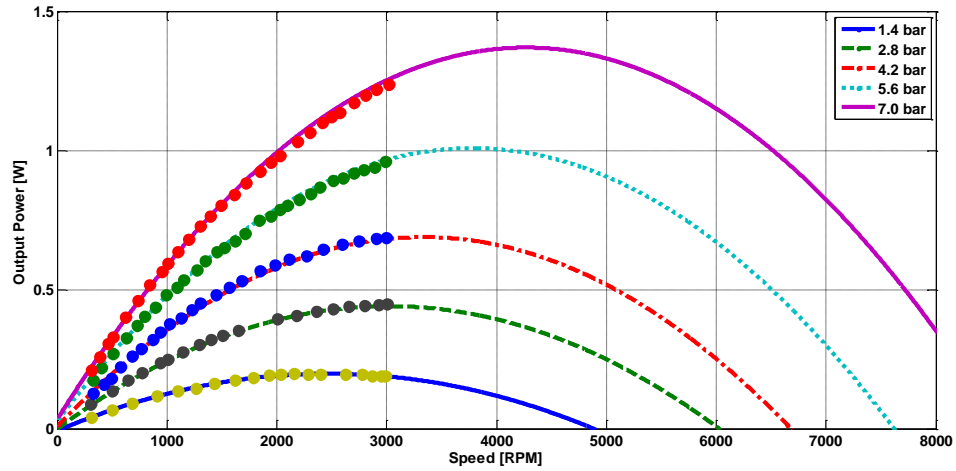


Figure 3-13: Static model of Power speed characteristic of the air motor in comparison to its datasheet.

Similar methodology is used to find the best fitted general representative of the air motor power (3-29). The coefficients of the quadratic are obtained as follows:

$$C_{PW2}(P_{AM}) = C_{PW22}P_{AM}^2 + C_{PW21}P_{AM} + C_{PW20} \quad (3-37)$$

$$C_{PW1}(P_{AM}) = C_{PW12}P_{AM}^2 + C_{PW11}P_{AM} + C_{PW10} \quad (3-38)$$

$$C_{PW0}(P_{AM}) = C_{PW02}P_{AM}^2 + C_{PW01}P_{AM} + C_{PW00} \quad (3-39)$$

The values of the coefficients are listed in Appendix 2. Similar to the air motor torque, the output power of the air motor can be described as a function of its rotational speed and its working pressure. Figure 3-13 shows the static model of the power-speed characteristic of the air motor in comparison with its datasheet characteristic. The proposed methodology yields the following coefficients for the quadratic equation that represents the air consumption characteristic.

$$C_{AF2}(p_{AM}) = C_{AF24}p_{AM}^4 + C_{AF23}p_{AM}^3 + C_{AF22}p_{AM}^2 + C_{AF21}p_{AM} + C_{AF20} \quad (3-40)$$

$$C_{AF1}(p_{AM}) = C_{AF14}p_{AM}^4 + C_{AF13}p_{AM}^3 + C_{AF12}p_{AM}^2 + C_{AF11}p_{AM} + C_{AF10} \quad (3-41)$$

$$C_{AF0}(p_{AM}) = C_{AF04}p_{AM}^4 + C_{AF03}p_{AM}^3 + C_{AF02}p_{AM}^2 + C_{AF01}p_{AM} + C_{AF00} \quad (3-42)$$

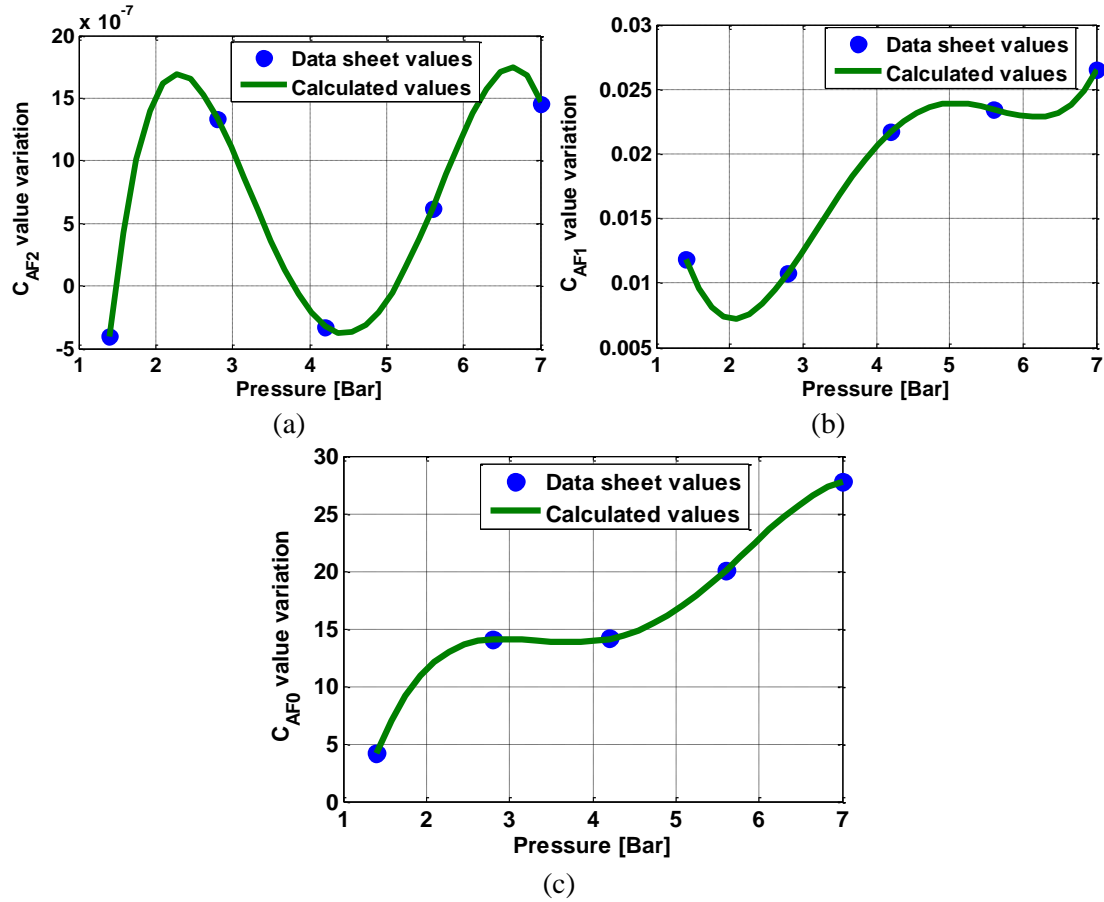


Figure 3-14: The obtained values for the quadratic equation coefficients from the air motor datasheet is compared to their calculated values. (a): C_{AF2} , (a): C_{AF1} , (a): C_{AF0} .

The values of the coefficients are given in Appendix 2. The calculated values of the coefficients of the quadratic equation are compared with the values from the datasheet shown in Figure 3-14(a), (b), and (c). The results of the air consumption-speed characteristics based on the proposed methodology compared with the datasheet values are shown in Figure 3-15.

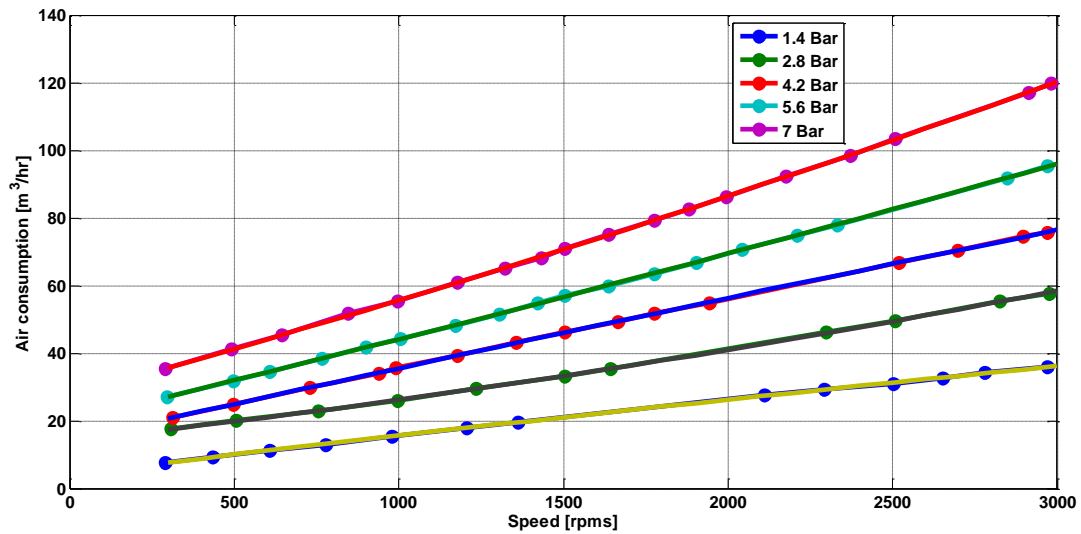


Figure 3-15: The calculated air consumption curve comparison to its datasheet values.

3.2.2.3.2 Dynamic model

Pneumatic actuators demonstrate nonlinear performance as a result of nonlinear flow through the valve, air compressibility, friction, valve characteristics, leakage between chambers, time delay and attenuation in piping system, which should be carefully considered in deriving a theoretical nonlinear dynamic model [107]. Several techniques have been investigated for modeling pneumatic actuators [97, 99-110]. One of the commonly used approaches for obtaining the steady state and dynamic models is based on mathematical representations of the physical construction of pneumatic motors. This

model incorporates a combination of thermodynamics, fluid dynamics, heat transfer and the dynamics of the motion. At the beginning, the mass flow rate passing through the valve is calculated. The pressure, volume and temperature variation in a chamber is then determined. Finally, the output torque-speed characteristic based on the load dynamics is defined [98], [103] and [107-110].

Among all the available mathematical models the model developed by Wang et.al [103], [109] and R.Pandian et.al [108] are the two most commonly used in dynamic modeling of vane motors. Therefore, their dynamic mathematical model based on the air motor geometry is adopted in this research and presented here.

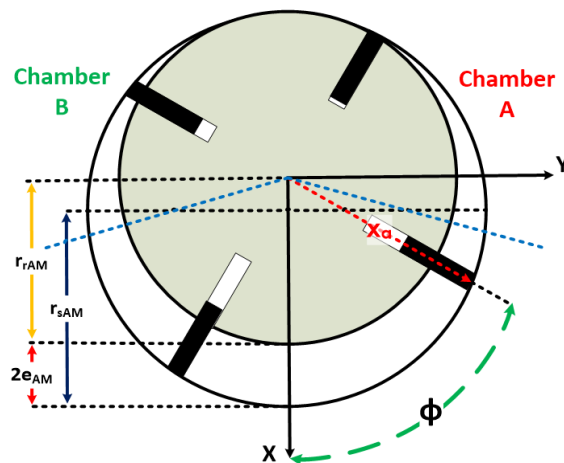


Figure 3-16: Schematic of a 4 vane air motor

Figure 3-16, shows the sketch of a 4 vane air motor. An air motor is driven by the torque created as a result of the pressure difference between chamber A and B from the leading vane in each working chamber toward the next chamber with lower pressure. The pressure difference between the drive and driven chambers creates a force on the vane area between these two chambers and the resultant drive torque can be written as:

$$T_{AM} = (P_a - P_b)A_{ab}l_T \quad (3-43)$$

where A_{ab} is the working area of each vane between the drive and driven chambers, and l_T is the torque arm. In order to calculate the net torque equation in a vane type air motor, the pressure in each chamber, the torque arm and working vane area should be calculated as a function of shaft rotation angle considering the geometry of the motor shown in Figure 3-16. Assuming the XY coordinate system shown in Figure 3-16, the vane working radius (x_a) can be described as:

$$x_{xa} = x_a \cos \phi \quad (3-44)$$

$$y_{xa} = x_a \sin \phi \quad (3-45)$$

where ϕ is the air motor shaft rotation. The circular equation of the stator can be written as:

$$(x_{xa} + e_{AM})^2 + y_{xa}^2 = r_{sAM}^2 \quad (3-46)$$

where e_{AM} is the eccentricity of the stator circle center with respect to the rotor circle center shown in Figure 3-16, and r_{sAM} is the air motor stator radius. The number of unknown variables in (3-46) can be simplified by substituting (3-44) and (3-45) in (3-46). Solving the second order resultant equation results in a mathematical relation for the vane working radius as a function of the air motor shaft rotation as:

$$x_a(\phi) = e \cos \phi + \sqrt{r_{sAM}^2 - e_{AM}^2 \sin^2 \phi} \quad (3-47)$$

The working radius of the vane motor is the most important parameter required to develop the motor behavior in each rotation. Other physical features of the air motor such

as the volume of the drive and driven chambers; the active vane area; and torque arm can be determined as a function of the shaft rotation once the working radius of the vane motor is obtained. The exposed area of the vane to the pressure difference between the chambers can be written as follows:

$$A_{AV} = L_{AM}(x_a - r_{rAM}) \quad (3-48)$$

where r_{rAM} is the air motor rotor radius, and L_{AM} is the air motor length. The torque arm (r_T) is the distance from the rotor center to the midpoint of the active vane where the force is applied, and from Figure, the torque arm can be calculated from the following equation:

$$r_T = x_a - \frac{x_a - r_{rAM}}{2} = \frac{x_a + r_{rAM}}{2} \quad (3-49)$$

The vane motor chamber is divided into drive (V_a) and driven (V_b) chambers and their variable volume as a sinusoidal function of rotational speed is obtained after integrating the differential section of the chambers as a function of the shaft rotation as follows [103] and [109].

$$V_{a,b} = L_{AM} \left(\int_{\phi-\pi/2}^{\phi} \frac{x_a^2}{2} d\phi - \frac{\pi r_{rAM}}{4} \right) \quad (3-50)$$

$$V_a(\phi) = \frac{1}{2} L_{AM} (r_{sAM}^2 - r_{rAM}^2)(\pi + \phi) + \frac{1}{4} L_{AM} e_{AM}^2 \sin 2\phi + L_{AM} e_{AM} r_{sAM} \sin \phi + c \quad (3-51)$$

$$V_b(\phi) = \frac{1}{2} L_{AM} (r_{sAM}^2 - r_{rAM}^2)(\pi - \phi) - \frac{1}{4} L_{AM} e_{AM}^2 \sin 2\phi - L_{AM} e_{AM} r_{sAM} \sin \phi + c \quad (3-52)$$

where

$$c = -\frac{1}{4} L_{AM} \left(e_{AM} r_{sAM} + \frac{\pi}{2} (r_{sAM}^2 - r_{rAM}^2) \right) \quad (3-53)$$

The variation of the drive and driven chambers variation as a function of the shaft rotation is shown in Figure 3-17. The shaft speed in this simulation was assumed to be 300 rpm, and the air motor active volume variation is shown in 5 full rotations of the shaft.

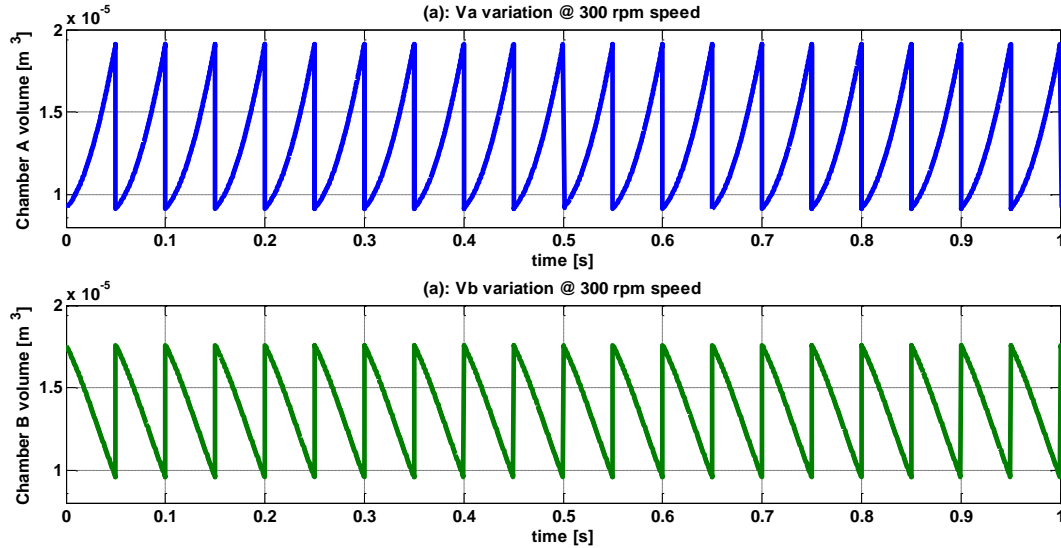


Figure 3-17: Drive and driven chamber volume variation

In this study, it is assumed that air enters at an angle of -60° , and leaves the air motor at an angle of $+60^\circ$ with respect to its X axis. The drive chamber starts at $\phi_{AStart} = -120^\circ$, and works as a driven chamber at $\phi_{AEnd} = -30^\circ$, the driven chamber starts at $\phi_{BStart} = -30^\circ$ and ends at $\phi_{BEnd} = +60^\circ$. As a result, the chambers exchange their function from drive to driven chamber at $\phi_{BStart} = \phi_{AEnd} = -30^\circ$. The mathematical model of the chamber volumes exhibits high frequency fluctuations as shown in Figure 3-17, as a result of the discrete nature of the active volume of the chambers. The fluctuation frequency is directly related to the finite number of vanes. The modeled air motor has 4 vanes, therefore each chamber acts as a drive chamber for a quarter of a full rotation; and as a result, the frequency of the

drive and driven chambers is four times the air motor shaft rotation frequency. As shown in Figure 3-17, by rotating toward the outlet port, the volume of the chamber “A” increases and the that of chamber “B” decreases, which creates a variable volume based on the air motor working principle.

The pressure variation in each chamber is required for the net developed torque calculation. The pressure change in each chamber can be calculated as follows [109], [111], and [112]:

$$\frac{dm}{dt} = \frac{P}{RT_s} \frac{dV}{dt} + \frac{V}{\gamma RT_s} \frac{dp}{dt} \quad (3-54)$$

$$\frac{dP_a}{dt} = \frac{RkT_s}{V_a} \frac{dm_a}{dt} - \frac{kP_a}{V_a} \frac{dV_a}{dt} \quad (3-55)$$

$$\frac{dP_b}{dt} = \frac{RkT_s}{V_b} \frac{dm_b}{dt} - \frac{kP_b}{V_b} \frac{dV_b}{dt} \quad (3-56)$$

The mass flow rate formula can be described by the following equation by assuming standard orifice theory [113]:

$$\frac{dm}{dt} = \frac{C_d C_0 A P_u}{\sqrt{T_u}} f(P_r) \quad (3-57)$$

$$P_r = \frac{P_d}{P_u} \quad (3-58)$$

$$f(P_r) = \begin{cases} 1 & ; P_r \leq C_r \\ C_k \sqrt{P_r^{\frac{2}{k}} - P_r^{\frac{k+1}{k}}} & ; C_r < P_r \leq 1 \end{cases} \quad (3-59)$$

where the values of k , C_0 , C_r and C_k can be determined from their corresponding equations listed in Appendix 2. The flow rate correction coefficient variation as a function of downstream to upstream pressure ratio is obtained using (3-59), and shown in Figure 3-18 to model the choked flow condition of the air motor.

After determining the volume of the chambers, the working vane radius and the mass flow rate the pressure in each chamber can be obtained using (3-55) and (3-56). The developed torque can be obtained using (3-43). The working area of each vane between the drive and driven chambers can be calculated as follow:

$$A_{ab} = (x_a - r_{rAM})L_{AM} \quad (3-60)$$

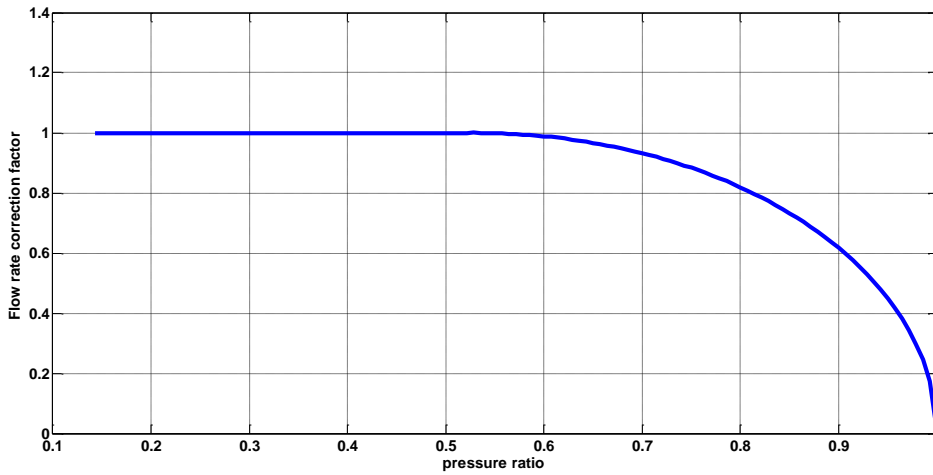


Figure 3-18: Flow rate correction factor to model the choked flow condition.

The torque arm in (3-43) can be written as a function of the air motor rotor radius and the vane working radius as follows:

$$l_T = x_a - \left(\frac{x_a - r_{rAM}}{2}\right) = \frac{x_a + r_{rAM}}{2} \quad (3-61)$$

Replacing (3-60) and (3-61) in (3-43), the developed torque equation can be written as:

$$T_{AM}(P_a, P_b, \phi) = (P_a - P_b)(x_a^2 - r_{rAM}^2) \frac{L_{AM}}{2} \quad (3-62)$$

The speed of the air motor can be obtained using its drive train as follow:

$$J_{AM} \frac{d\omega}{dt} + B_{AM} \omega = T_{AM} - T_d \quad (3-63)$$

Where J_{AM} is the inertia of the air motor rotating parts, and B_{AM} is its friction coefficient. The air motor dynamic performance was simulated using the equations provided in this section for a fixed tank pressure of 7 bar. Figure 3-19 shows the dynamic performance of the rotational speed of the air motor.

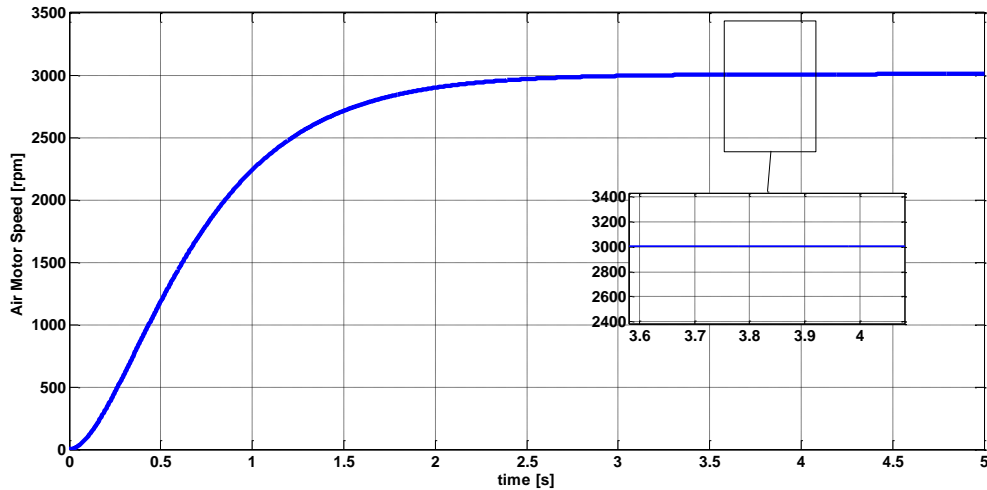


Figure 3-19: The dynamic response of the air motor speed to a fixed 7 bar input compressed air.

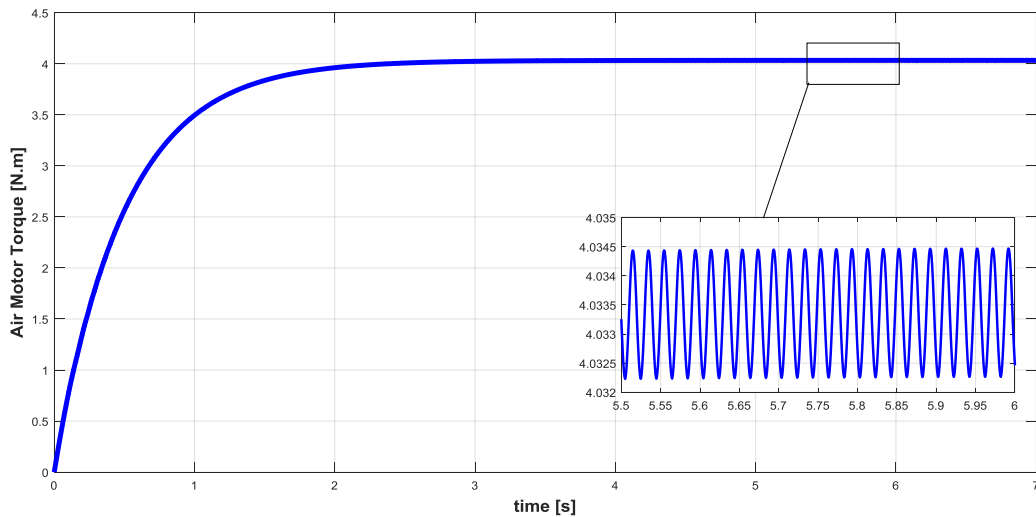


Figure 3-20: The output torque of the air motor for a fixed 7 bar input compressed air

The output torque of the air motor is shown in Figure 3-20, which at its steady state condition is approximately identical to the manufacturer datasheet shown in Figure 3-11

where the developed torque at 3000rpm and 7 bar equals to 4.03N.m. The fluctuation of the response is related to the infinite number of the vanes which results in fluctuation in the volume of drive and driven chambers.

The output power of the modeled air motor for a fixed 7 bar input compressed air was calculated as a product of the developed torque and the speed, and shown in Figure 3-21. The steady state value of the calculated value is identical to the manufacture power curve shown in Figure 3-11(d) with 1274W value for the output power in 3000 rpm and 7 bar operation condition.

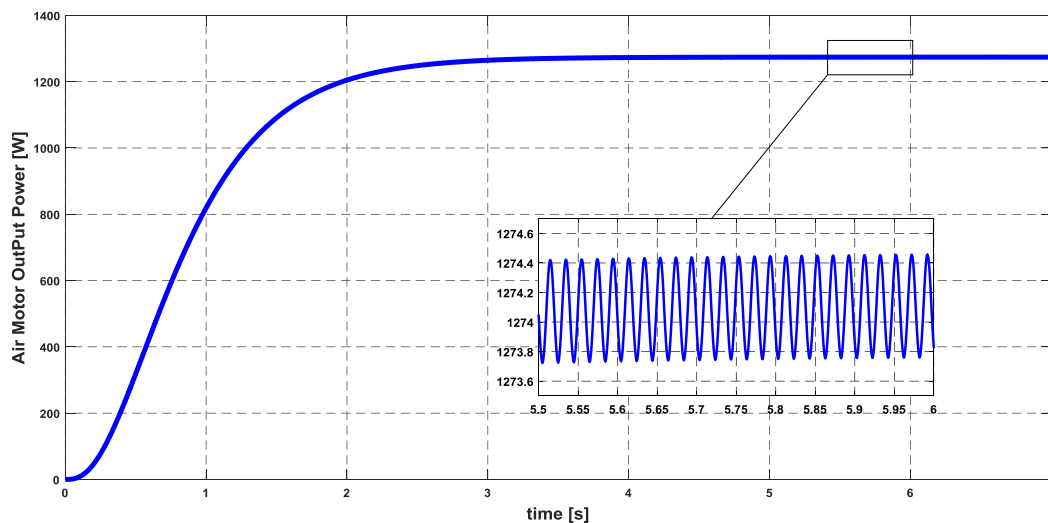


Figure 3-21: The dynamic response of the air motor output power to a fixed 7 bar input compressed air

The result of air motor air consumption simulation is shown in Figure 3-22. The result is obtained by assuming of constant supply and exhaust pressure in order to compare the predicted results with the manufacturer datasheet. The simulated air consumption has a value of 118 [m³/hr], which is close to the value from the manufacturer datasheet (119 [m³/hr]) considering very small simulation time step (1ns).

The convergence of the mathematical model depends on the coefficients and parameter values in the active volume of the drive and driven chambers, the pressure variation, flow rate and developed torque equations. Identification techniques can be implemented to obtain the required parameters using system identification toolbox in MATLAB-Simulink environment. In addition, Kalman filtering method [114], the design of experiment (DOE) technique [115] and neural network model [116] can be adopted to obtain accurate estimates of the system parameters for the models.

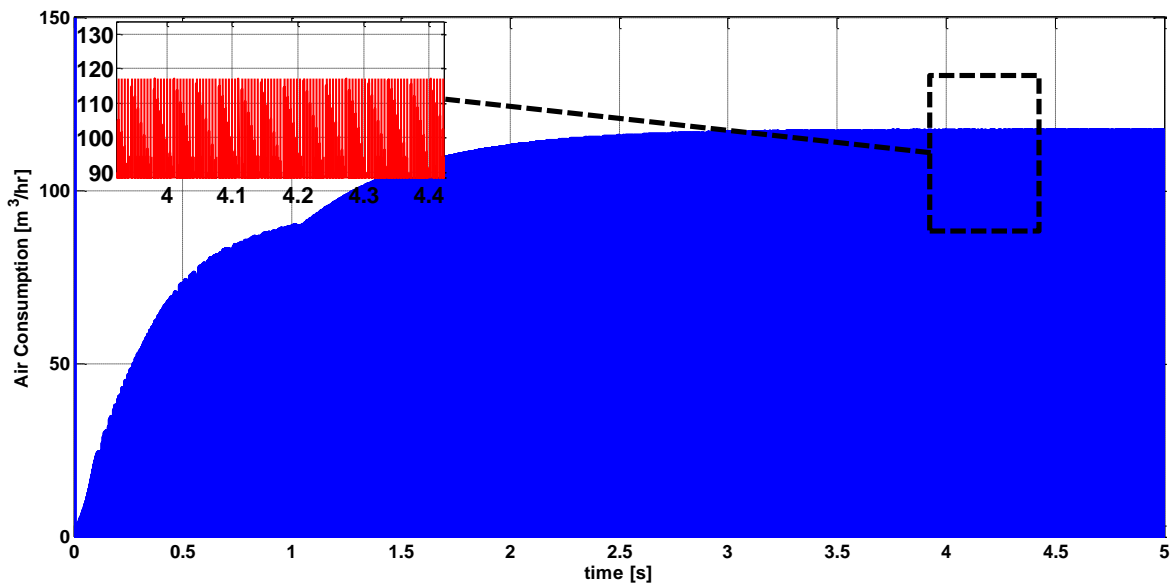


Figure 3-22: Air consumption of the modeled air motor for a fixed 7 bar input compressed air

The efficiency of the pneumatic actuator depends on its operation condition and control strategy, which increase the necessity of having an approximate model with reasonable error [117]. These models usually include a large number of parameters which require excessive practical tests to obtain all of the parameters, the final model should be modified in order to provide accurate match with manufacturer product specification catalog.

3.2.2.4 Rectifier unit

In the proposed CAES system the synchronous generator output voltage was converted to DC voltage using a full bridge diode rectifier model PVI-7200-WIND-INTERFACE. The unit consist of line filter; regulating capacitor; high power module (TBR1500) with forward voltage drop $V_f=0.7$ for each diode, and its manufacturer specification is listed in Appendix 4 The simulation model for this unit was obtained by calculating the average dc voltage of the bridge taking into account the diode voltage drop and assuming ideal sinusoidal waveform for the input as follows:

$$V_{dc} = \frac{2V_m}{\pi} - 2V_f \quad (3-64)$$

where V_m is the magnitude of the generated voltage. In order to model the impact of the DC load current on the rectifier current and voltage, its equivalent circuit can be considered as Figure 3-23, where the capacitor bank, the line filter and their internal resistances are included .

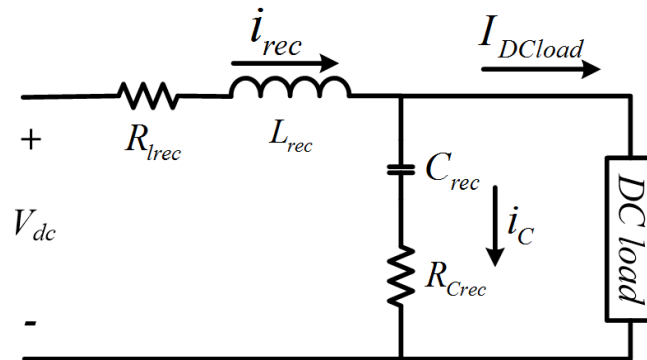


Figure 3-23: Equivalent circuit of the rectifier unit.

The rectifier current can be written as:

$$I_{rec}(s) = \frac{1}{L_{rec}s + R_{lrec}} [V_{dc}(s) - V_c(s)] \quad (3-65)$$

The equivalent block diagram can be obtained after writing the required KVL and KCL equations as Figure 3-24. The dc bus voltage and the rectifier unit current response to the DC load current and input voltage disturbances can be obtained using the developed dynamic model.

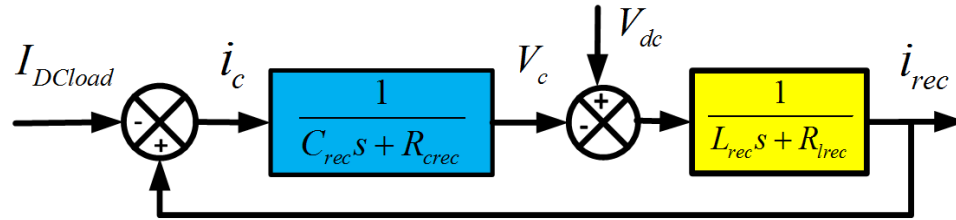


Figure 3-24: Rectifier current block diagram

3.2.2.5 The Grid connected inverter unit

The final step in the energy extraction process of an energy storage system is using a grid integration unit to deliver the stored energy to the local distribution system. This unit includes a voltage source inverter, current limiter for protection and output power control purposes, and a line filter [118], [119]. In this study, the Aurora wind inverter (PVI-3600-OUTD) was used for grid connection. The inverter includes an output filter in order to remove the switching harmonics and prevent their injection to the grid. This inverter can be connected to a PC for data logging and power curve programming purposes.

The desired power curve of the inverter as a function of input DC voltage level can be entered as a look up table in programming mode of the inverter prior to connection to the grid. The output power control and grid connection procedure is performed by the Aurora inverter embedded controller module, and its power curve is the only controllable feature

of this inverter. Therefore, the inverter input DC voltage value is the only parameter that defines the output power of inverter. Considering this limitation of the inverter, the output power of the whole CAES system will be limited to the definition of the proper power curve for the inverter and control the generated DC voltage level.

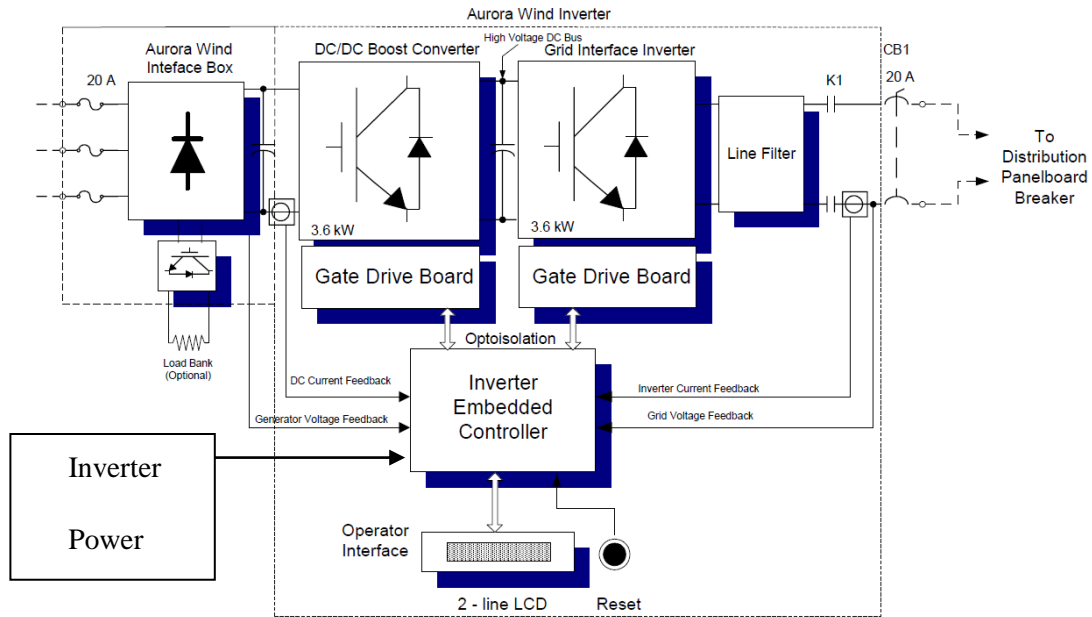


Figure 3-25: The Aurora inverter block diagram.

The structure of the Aurora inverter used in this research, is shown in Figure 3-25, where it includes DC/DC boost converter, grid interface inverter and a line filter. In general, the inverter controller structure includes two controller loop: DC voltage control loop for the boost converter and current control loop for the grid interface inverter. Utilizing different time constants for the inner current regulator loop and the outer voltage regulator loop, the dynamic behavior of the two control loops can be decoupled. This can be achieved by providing significant higher sampling frequency (more than 10 times) for the inner current regulator loop [118] and [120]. The output power of the inverter can be

adjusted by programming its lookup table. The desired output current of the inverter is estimated using the power curve of the inverter. This current is compared to the actual measured current to produce the actuating signals for the inverter switches.

Although the control strategy of the inverter was not accessible, its dynamic performance affects the general response of the system. Therefore, its model and dynamic behavior should be considered in the simulation and system performance studies. In order to obtain a dynamic model of the inverter, an average switch model can be combined with its electrical analytical model, and the Aurora inverter characteristics and its controller structure. It is assumed that the output current of the inverter has no harmonics as a result of the output filter. A typical schematic of a single phase grid connected inverter is shown in Figure 3-26, and its corresponding block diagram is shown in Figure 3-27.

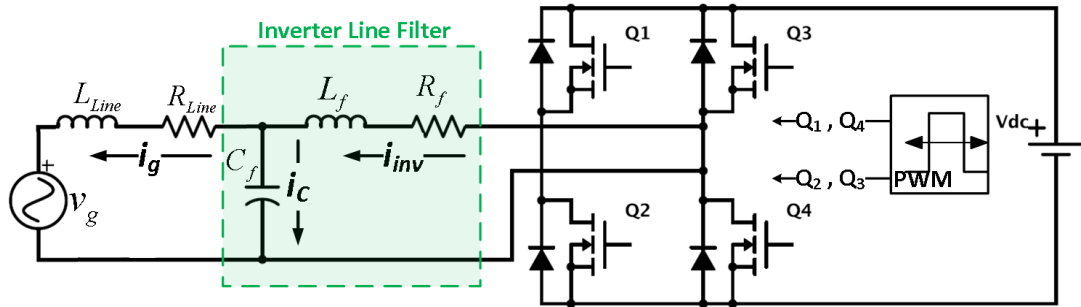


Figure 3-26: A typical Schematic of a single phase grid connected inverter

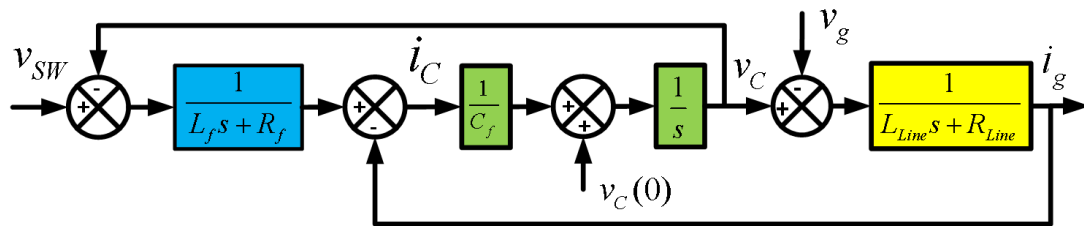


Figure 3-27: Block diagram of a typical single phase grid connected inverter with filter.

Assuming a line filter between the inverter output and the grid [121] as shown in

Figure 3-26, the inverter output current can be written as follows:

$$L_f \frac{di_{inv}}{dt} = v_{sw} - v_C - R_f i_{inv} \quad (3-66)$$

where L_f is the line filter inductance, v_C is the voltage across the line filter capacitor and v_{sw} is the output voltage of the inverter switches over a PWM period given by the following equation:

$$v_{sw} = D \times V_{DC(AV)} \quad (3-67)$$

where D stands the PWM duty ratio over a PWM period and $V_{DC(AV)}$ is the inverter input DC bus voltage provided by the boost converter. The output current of a grid connected inverter is the key parameter that controls the output power of the inverter. This current has two components: i_C and i_G , as shown in Figure 3-26.

$$i_C = C \frac{dv_C}{dt} \quad (3-68)$$

$$L_{Line} \frac{di_g}{dt} = v_C - v_g - R_{Line} i_g \quad (3-69)$$

$$i_g = i_{inv} - i_C \quad (3-70)$$

Using (3-66) to (3-70)(3-69), the state space model of the grid integration unit can be derived as follows:

$$\frac{dx}{dt} = Ax + Bu \quad (3-71)$$

$$A = \begin{bmatrix} \frac{-R_f}{L_f} & 0 & \frac{-1}{L_f} \\ 0 & \frac{-R_{Line}}{L_{Line}} & \frac{1}{L_{Line}} \\ \frac{1}{C_f} & \frac{-1}{C_f} & 0 \end{bmatrix}, \quad B = \begin{bmatrix} \frac{1}{L_f} & 0 \\ 0 & \frac{-1}{L_{Line}} \end{bmatrix}, \quad x = \begin{bmatrix} i_{inv} \\ i_g \\ v_C \end{bmatrix}, \quad u = \begin{bmatrix} v_{sw} \\ v_g \end{bmatrix} \quad (3-72)$$

The grid integration unit transfer function can be found by solving the state space matrices and using (3-67). The output current transfer function can be described as a function of input duty cycle ratio and input DC voltage as the following equation:

$$i_{Line} = \frac{1}{\Delta} v_{SW} - \frac{C_f s(L_f s + R_f)}{\Delta} v_G \quad (3-73)$$

$$\Delta = C_f R_f L_{Line} s^3 + C_f (R_f L_{Line} + R_{Line} L_f) s^2 + (C_f R_f L_{Line} + L_{Line} + L_f) s + (R_f + R_{Line}) \quad (3-74)$$

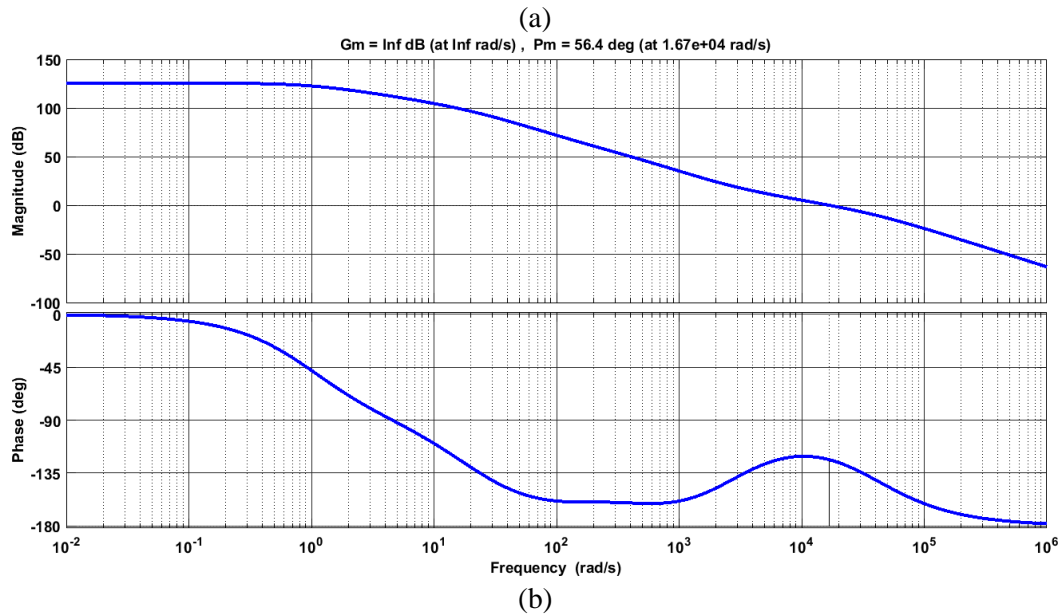
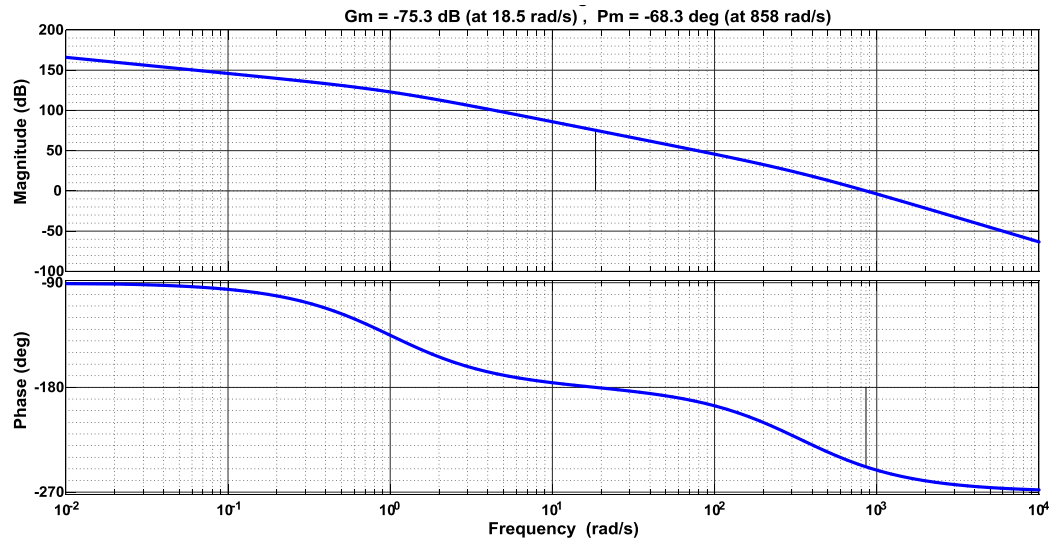


Figure 3-28: The bode diagram of the inverter with line filter: a) with no compensator, b): with Lead-Lag compensator.

Using the inverter parameters provided in Appendix 2, the bode diagram of the uncompensated closed loop system shows an unstable behavior as it is shown in Figure 3-28(a). Therefore a lead-lag compensator is added to the system to make the system stable and improve the system transient performance to disturbances. Figure 3-28(b) shows the bode diagram of the compensated system with phase margin value of 56.4 deg.

The response of the system with a Lead-Lag compensator the three different reference current values is shown in Figure 3-29.

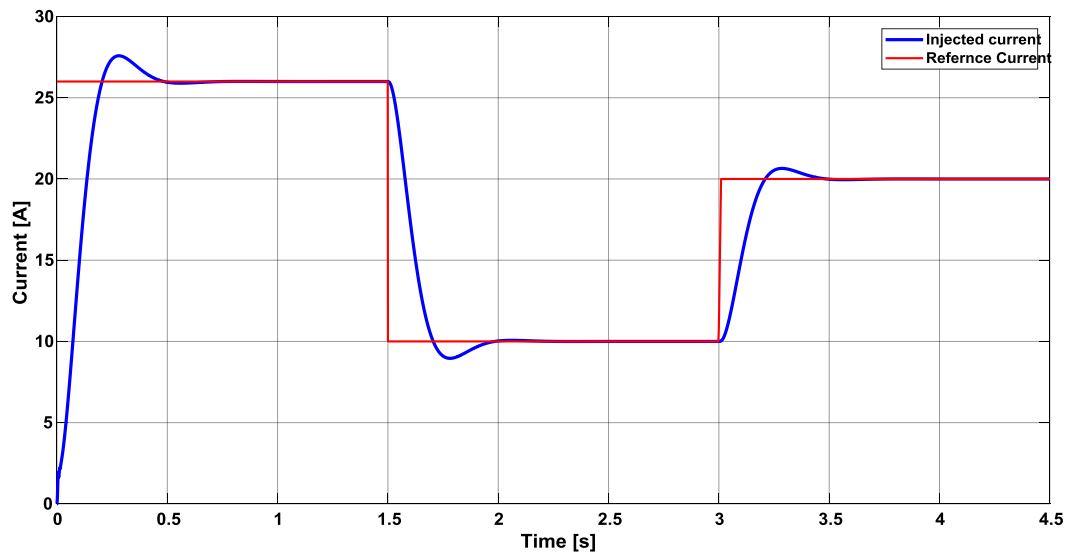


Figure 3-29: The response of the compensated inverter system with line filter

As it can be concluded from Figure 3-28 and Figure 3-29, adding a lead-lag controller improves the performance of the inverter by making the system stable, removing its steady state error, increasing the phase and gain margin of the closed loop system, and reducing the system response settling time by placing the system poles in the left half plane far away from imaginary axis.

3.2.2.6 The Synchronous Generator for the CAES system

The implemented synchronous generator to convert the developed mechanical torque into electrical energy is a separately excited single phase machine. A simple single phase model is developed for the separately excited single phase synchronous generator in this study. The following assumptions are made in the development of the single phase model:

- Space harmonics in the air-gaps are neglected.
- Air-gap reluctance has a constant component.
- Eddy current and hysteresis effects are neglected.
- Presence of damper windings are not considered
- Saturation is neglected although it can be taken into account by parameter changes.
- Because the mechanical systems have high time constant, the current variation around its average value has sufficiently small effect on the generator motion performance.

A permanent magnet and excitation windings can produce similar EMF, and there is no difference between the stator of the PMSG and the wound rotor synchronous generator (SG). The presented mathematical model can be used for both permanent magnet and wound rotor synchronous machines [122]. Assuming the DC machine analogy for separately excited single phase synchronous generator, the electromagnetic torque produced by the drive train of the rotor shaft can be written as:

$$J_{SG} \frac{d\omega_{re}}{dt} + B_{SG}\omega_{re} = T_{mech} - T_{em} \quad (3-75)$$

$$T_{em} = K_{SG}\phi(I_f)I_{SG} \quad (3-76)$$

where J_{SG} and B_{SG} are the synchronous generator inertia and the friction coefficient respectively, and ω_{re} is the electrical rotational speed of the rotor. Using simplified model for a synchronous generator connected to a rectifier unit presented in [123] and [124], the electrical circuit equation for the stator phase windings can be written as:

$$V_{TSG} = -(L_{SG}s + R_{SG})I_{SG} + E_{SG} \quad (3-77)$$

where L_{SG} is the stator winding inductance; R_{SG} is the stator winding resistance; V_{TSG} is the synchronous generator terminal voltage; and E_{SG} is the no load generated voltage which is a function of rotational speed. The field current can be written as:

$$E_{SG}(I_f, \omega_{re}) = K_{SG}\phi(I_f)\omega_{re} \quad (3-78)$$

Using (3-75) to (3-78), the dynamic model of a separately excited single phase synchronous generator (SESPSG) can be represented by the block diagram as shown in Figure 3-30.

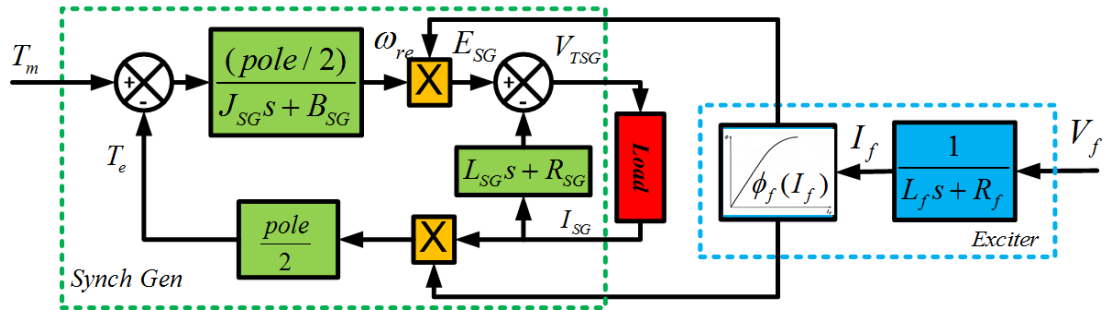


Figure 3-30: A separately excited single phase synchronous generator block diagram

The synchronous generator parameters can be determined from experimental tests. In order to obtain the stator resistance (R_{SG}) and the field winding resistance (R_f) values, a

dc voltage test would result in acceptable values for small machines. The average value of the resistance was calculated after averaging 20 different measurements. The average value of R_f and R_{SG} were obtained 52.8Ω and 0.218Ω respectively. A reasonable compensation for skin and temperature effects of the stator winding is achieved by applying a coefficient [124] and [125].

$$R_{SGdc} = \frac{R_{SG}(234.5 + t_{mc})}{234.5 + t_{rm}} \quad (3-79)$$

$$R_{SGac} = 1.25 \times R_{SGdc} \quad (3-80)$$

where t_{mc} is the machine temperature and t_{rm} is the room temperature, and their nominal values are listed in the Appendix 3. Considering (3-78), the magnetic flux linkage variation as a function of the field current can be calculated after conducting several sets of practical tests at the desired speed. The open circuit voltage of the synchronous generator was logged at different speeds, while the field current was maintained constant in each set. Figure 3-31 shows the open circuit voltage output variation of the SESPSG as a function of the field current and speed.

The open circuit flux of the SESPSG can be obtained by dividing (3-78) by the corresponding speed. The resulting relationship includes the electrical machine constant (K_{SG}). The variation of the open circuit flux is shown in Figure 3-32 as a function of its corresponding field current for different speeds.

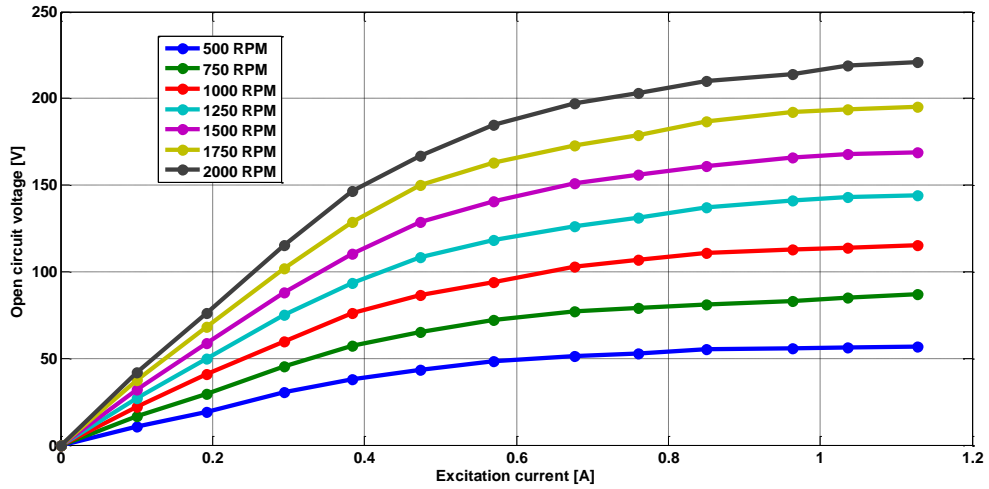


Figure 3-31: Open circuit voltage of the SESPSG as a function of field current and speed.

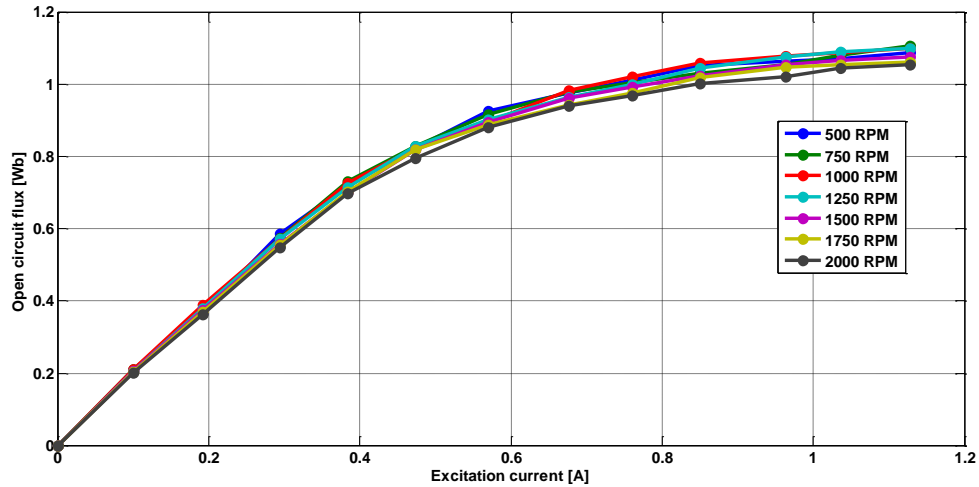


Figure 3-32: Open circuit flux of the SESPSG as a function of the field current for different speeds.

In order to represent the resulting curve as a mathematical equation, the average of derived curves for each field current was calculated and is shown in Figure 3-33. The resulting curve is approximated by a cubic polynomial equation as follows:

$$\phi(I_f) = 0.4545(I_f)^3 - 1.911(I_f)^2 + 2.554I_f - 0.01824 \quad (3-81)$$

The derived relationship is compared to the measurement curves in Figure 3-33. The comparison shows a good fit between the measured and predicted values.

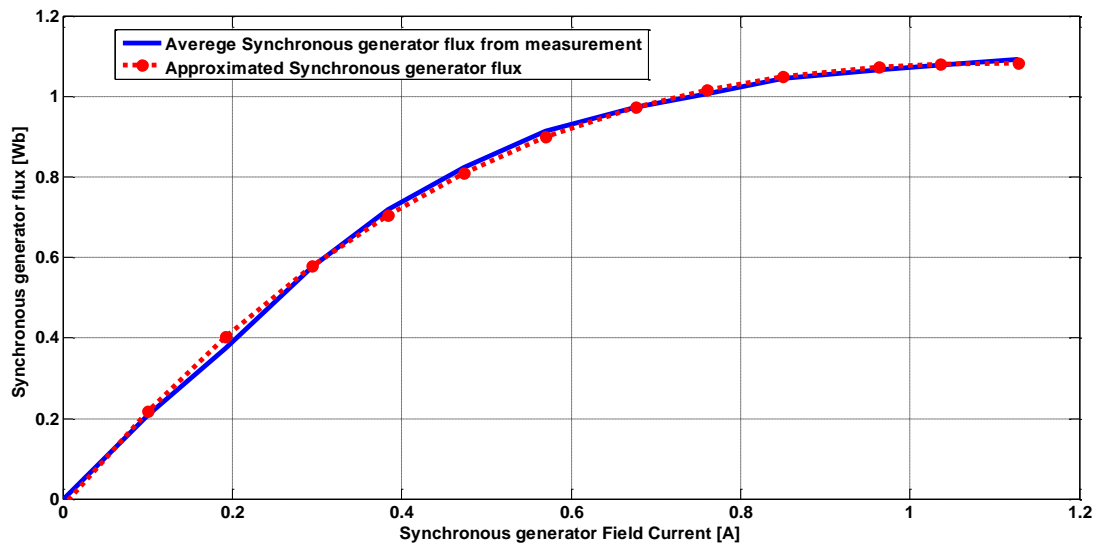


Figure 3-33: Open circuit flux measurement comparison to the approximated equation

The synchronous inductance can be calculated using the open circuit and the short circuit characteristic of the stator windings by changing the field current. The stator inductance was determined as 188 mH. The developed block diagram for SESPSG was simulated using MATLAB-Simulink. In this simulation, the applied load was changed in 3 steps as shown in Figure 3-34: the no-load condition at the start, 232W load applied at $t=4.01s$, and 800w load applied at $t=8.01s$.

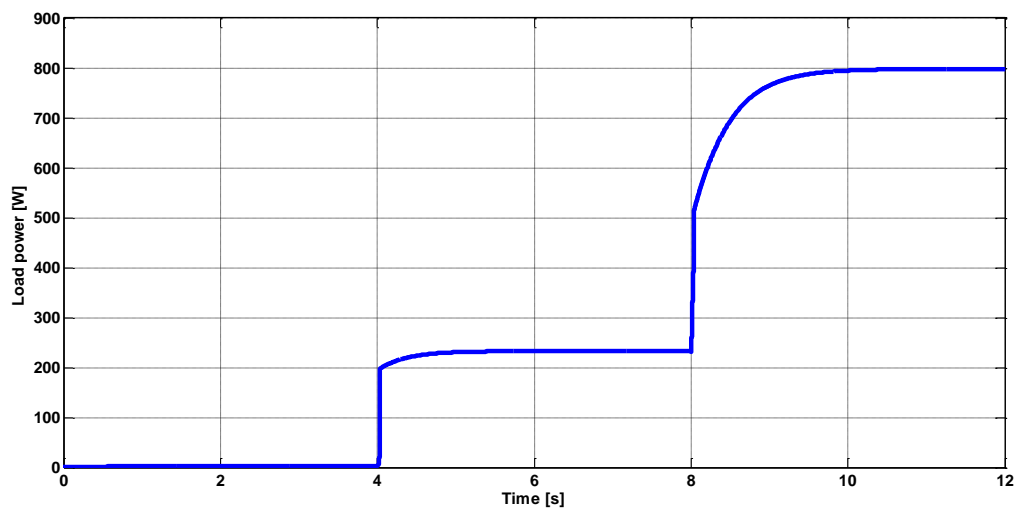


Figure 3-34: The applied load variation

Figure 3-35 shows the change in terminal voltage and speed variation of the generator in response to the applied load power respectively, with constant field current and applied mechanical torque.

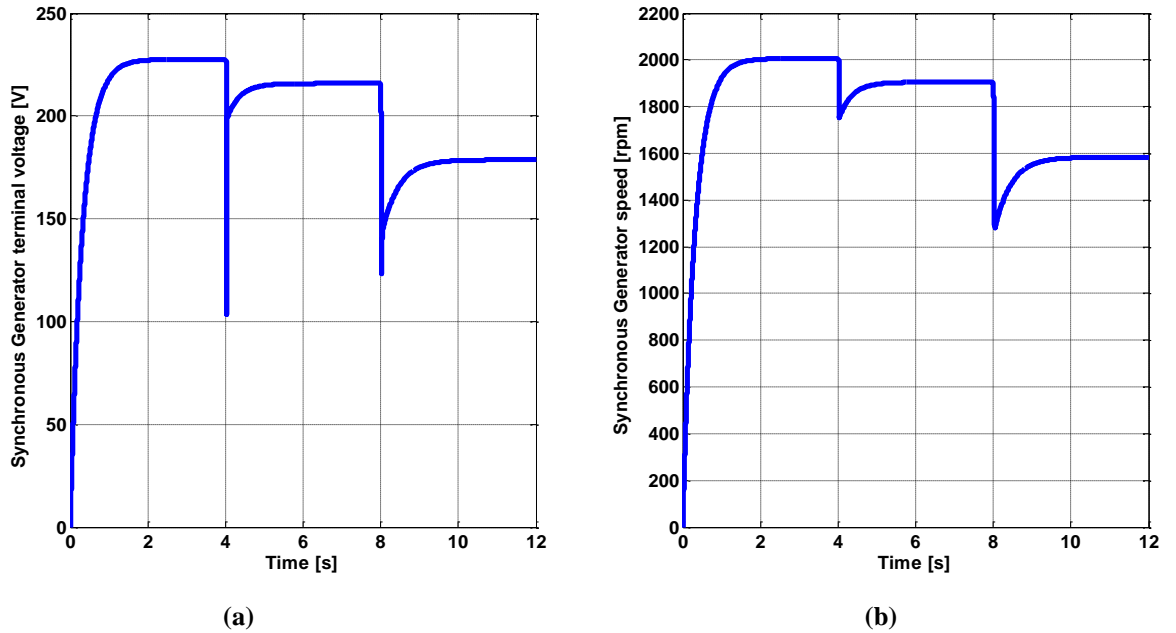


Figure 3-35: The simulated SESPSG response to the load variation: (a) The terminal voltage and (b) and the speed variation of the generator respectively

3.2.3 Back up Diesel Generator

In this study, a four stroke Yanmar Powered 6.5 kW DG is considered. Using available data in the manufacturer datasheet [1], the fuel consumption of the considered DG unit can be approximated as a function of its real power output by the following quadratic polynomial:

$$FC_{DG} = (2.15 \times 10^{-8})P_{DG}^2 + (6.29 \times 10^{-5})P_{DG} + 0.8782 \quad (3-82)$$

where P_{DG} is the DG power in Watts and FC_{DG} is the DG fuel consumption in L/hr.

The DG fuel consumption profile obtained based on (3-82) was compared with a DG with

identical power rating in Homer energy software [3] and shown in Figure 3-36. The fuel consumption profile obtained from Homer energy software is shown with a straight line.

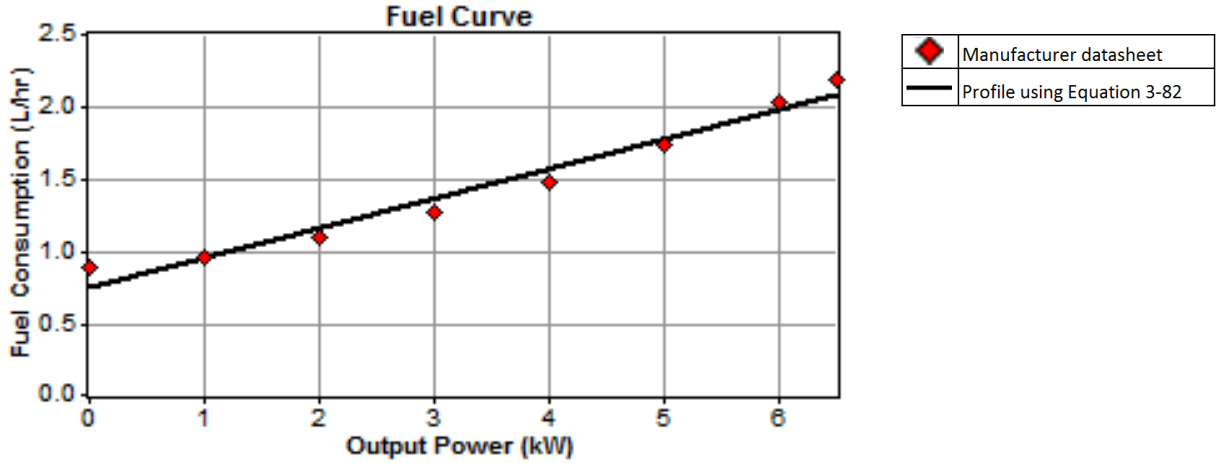


Figure 3-36: The fuel consumption profile of a 6.5 kW Diesel Generator [3].

3.2.3.1 Dynamic model of the diesel generator

The diesel prime mover in a diesel generator has a higher time constant in comparison with the synchronous generator (SG) connected to a common shaft. In order to simplify the dynamic model of the DG, the SG dynamics are neglected, and it is assumed that the output voltage amplitude is kept constant using an automatic voltage regulator (AVR) unit. Therefore the DG model can be presented as follows [126] and [127]:

$$T_{mDG}(s) = \frac{k_e}{\tau_e s + 1} e^{-t_d s} u_c(s) \quad (3-83)$$

$$u_c(s) = k_p \left(1 + \frac{1}{\tau_i s} + \tau_d s \right) (\omega_{rDG_ref} - \omega_{rDG}(s)) \quad (3-84)$$

where T_{mDG} is the developed mechanical torque of the DG, k_e and τ_e are the fuel injection system gain and time constant respectively; t_d is the engine dead time and is equal to delay in torque production; u_c is the control signal from the governor system; k_p ,

τ_i and τ_d are the PID controller parameters for the fuel injection system in the DG governor; and ω_{rDG} is the DG shaft rotor speed. The drive train of the DG can be written as follows:

$$\omega_{rDG}(s) = \frac{1}{J_{DG}s + B_{DG}} [T_{mDG}(s) - T_d(s)] \quad (3-85)$$

where T_d is the disturbance torque produced at the common shaft; B_{DG} is the total DG damping coefficient; J_{DG} is the lumped inertia of the rotating parts and can be calculated based on the DG rating as follows [128], [129]:

$$J_{DG} = \frac{2p^2 H_{DG} S_{DG}}{\omega_{nDG}^2} \quad (3-86)$$

where p is the number of the generator poles; H_{DG} is the inertia time constant; ω_{nDG} is the nominal rotational speed of the generator; and S_{DG} is the DG nominal power rating. Figure 3-37 shows the DG dynamic model block diagram. The step response of DG dynamic model in this study to a provide 3kW for active power balancing purpose is shown in Figure 3-38. The model parameters are listed in Appendix 2. As shown in Figure 3-38, the diesel generator is able to follow the desired rotational speed within reasonable response time.

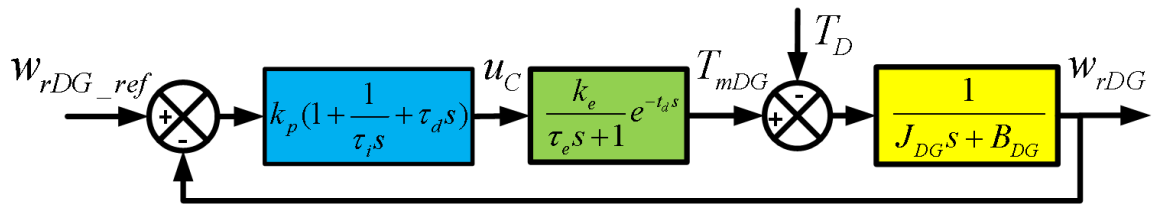


Figure 3-37: The DG dynamic model block diagram

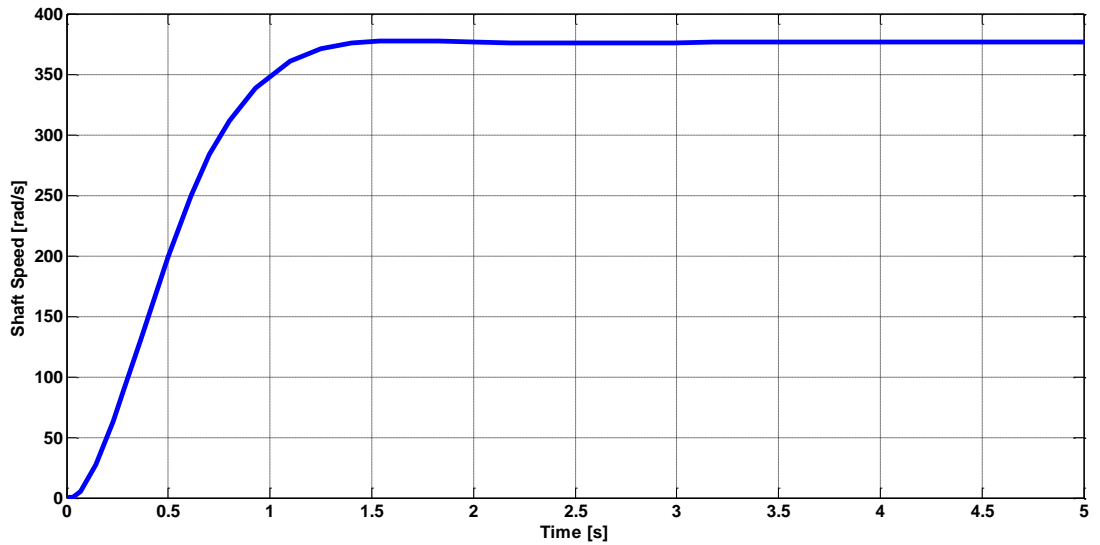


Figure 3-38: The step response of DG dynamic model

3.2.4 Supervisory Control Unit

The control unit in a hybrid wind system is the key component in controlling the wind penetration in energy production of the energy system by reducing the diesel generator total fuel consumption. In this study a supervisory control unit as shown in Figure 3-39 is proposed to control the energy transfer management.

This unit is responsible to produce and send required control signals including the activation or deactivation commands and the reference values of the controllers to different hybrid system components. These signals are generated based on the measurement signals from different sensors and predefined control scheme. For example, the proposed supervisory control unit collects the stored compressed air pressure in the tank in order to calculate the available stored energy and decide in case of excess energy it shall be stored or dumped. On the other hand, during a discharge operational regime, the supervisory control activates the air motor to deliver the required power.

The diesel generators will only operate when the pressure sensors indicate insufficient remaining stored energy to meet the demand. Two different modes of operation can be considered for the diesel generators in a wind based HPS: Standby and On-Off mode of operation. In a standby mode of operation, diesel generator is always on and operates in no load mode, while in an on-off mode of operation, the energy storage system eliminates the no load operation of the diesel generator and results in more economical operation of the diesel generator.

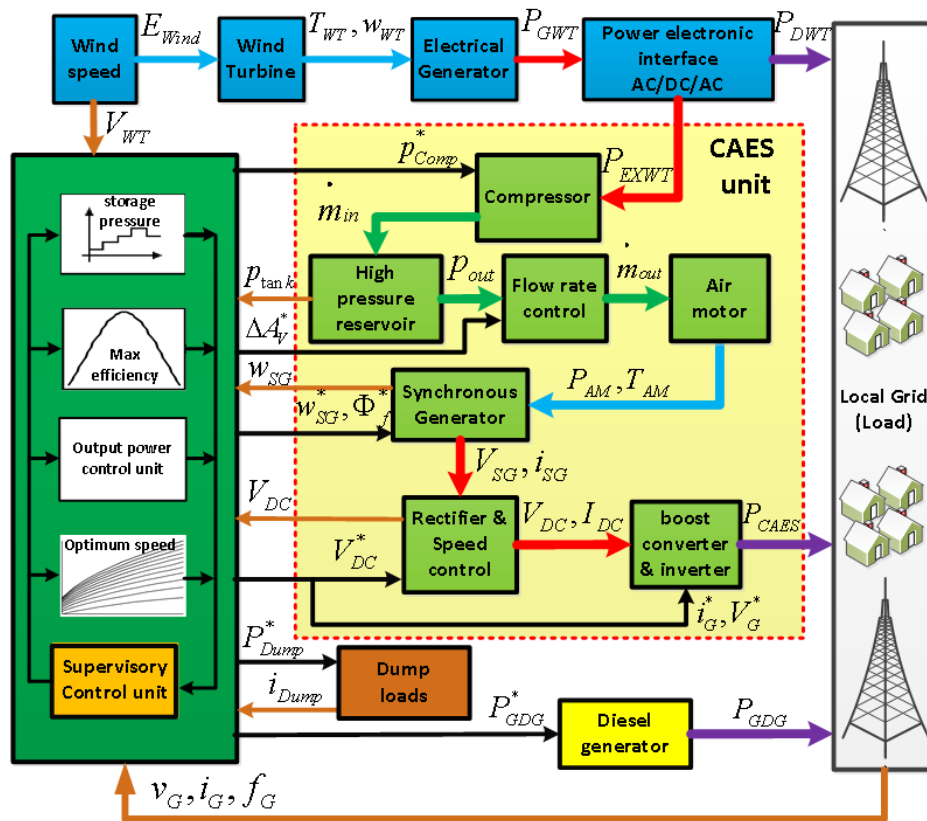


Figure 3-39: Block diagram of the proposed hybrid system.

The control scheme in the hybrid system is divided into two main categories: Overall control scheme and system level control approach. Overall control scheme, which usually

happens during the charging cycle, is based on available excess energy working condition of compressors. The flow rate and compression ratio is controlled in a way that maximum possible energy can be harvested from the wind. On the other hand, the system level control scheme defines the working condition of each component in the CAES system to increase the overall efficiency of the discharge cycle.

3.3 Other Components

In addition to the main power units, the CAES system needs dump load and proper controller to provide stable condition for the connected loads, piping to provide the path for compressed air to and from the reservoir. Air filter and dryer are also needed at the compressor and air motor inlet to refine the air. In addition, a muffler is used at the air motor outlet to reduce the noise.

3.4 Interactive dynamic load model

In reality, the grid load impedance changes during a day based on the different types of industrial or residential loads with variable amount of active and reactive power. This change in active and reactive power affects the required energy produced by the power system. Therefore using a dynamic load model that can accurately represent the change in the grid load impedance is essential in this study.

A number of modeling techniques have been applied to model the load for different applications [130-133]. A summary of basic load modeling concepts and definitions is available in [134]. In these studies, the efforts have been devoted to the development of static load models as well as dynamic and time-varying models in synchronous generator

modeling for control purposes. Static load models are divided into 3 categories [132]: Constant impedance (Z) , Constant current (I), and Constant power (P).

In many studies a balanced fixed resistive load has been considered to represent the load behavior. This model is not adequate because it does not include the reactive power variations and unbalanced load conditions.

In this study, a dynamic load model is developed based on a combination of constant impedance and constant power models. The interaction of the load and power system can be modeled as a feedback path. Disturbances in produced power result in the bus voltage variation based on its transfer function. As a result, the bus voltage variations create the load current disturbances that affect the power delivered to the load as shown in Figure 3-40 [131].

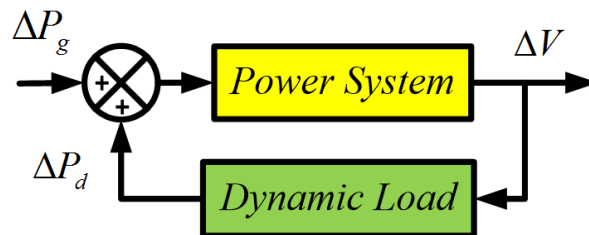


Figure 3-40: The load – power system interaction

The dynamic load impedance is obtained using the required active and reactive power during the specific time duration. In this model, a load is represented as a parallel R-L or R-C equivalent circuit as shown in Figure 3-41 with the same nominal active and reactive power.

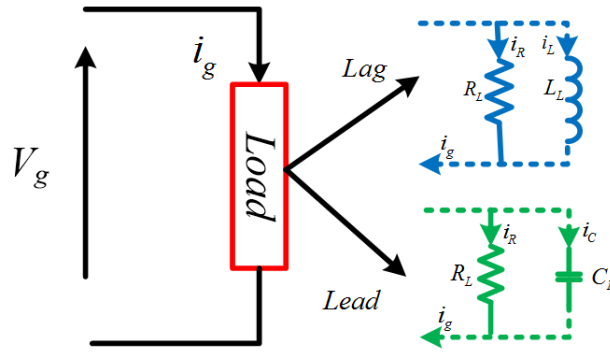


Figure 3-41: Dynamic load model.

The equivalent impedance or admittance can be calculated from the following equation:

$$\frac{1}{G_L + jB_{L(or C)}} = \frac{V_n^2}{S_L^*} \quad (3-87)$$

where V_n is the rated output voltage, and S_L is the load complex power ($S_L = P + jQ$)

which can be used to define R_L , L_L or C_L values for simulation. For loads with lagging power factors the parallel R-L equivalent circuit parameters can be found using the following equations:

$$V_g = i_R R_L = (i_g - i_L) R_L \quad (3-88)$$

$$i_L = \omega_{ref} B_L \int V_g dt \quad (3-89)$$

$$L_L = \frac{1}{\omega_{ref} B_L} \quad (3-90)$$

With similar approach the R-C equivalent circuit parameters can be calculated for loads with leading power factors.

$$V_g = \omega_{ref} B_C \int \left(i_g - \frac{V_g}{R_L} \right) dt \quad (3-91)$$

$$C_L = \frac{1}{\omega_{ref} B_C} \quad (3-92)$$

The MATLAB representation of the R-L and R-C equivalent circuits are shown in Figure 3-42(a) and (b) respectively.

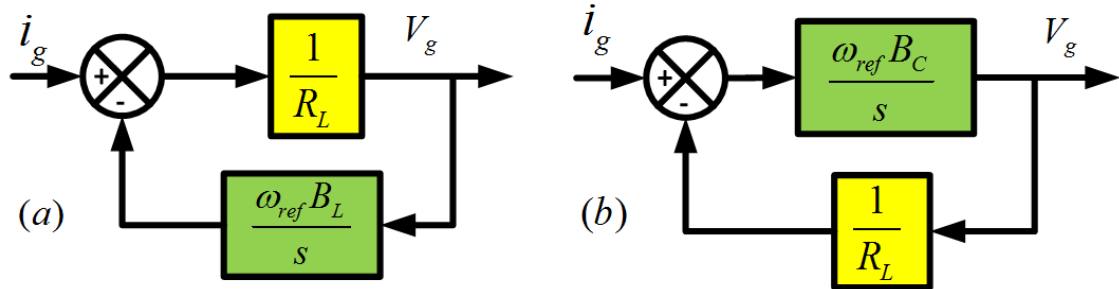


Figure 3-42: The dynamic interactive load model. (a) The parallel R-L model for lagging power factor and (b) The parallel R-C model for leading power factor.

In order to include a practical load variation profile in this study, the load profile of a domestic residence was logged over a year with 1HZ sampling frequency. The load variation in first day of January is shown in Figure 3-43.

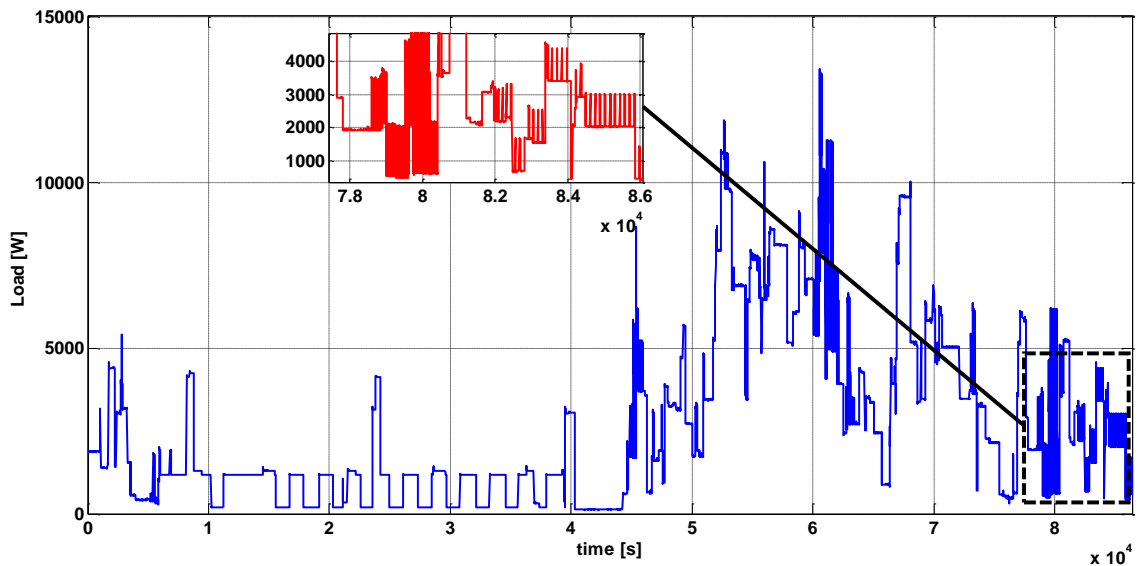


Figure 3-43: The load variation on the first day of January

The load profile is used in Monte-Carlo simulation with random uniform distribution for power factor between (-1 to -0.7) and (0.7-1) to generate the corresponding load impedance using the proposed interactive load model. As a result a variable impedance

model with 1 sec resolution is created to model the load variation that is used in later chapters for the system performance assessment.

3.5 Experimental Setup

In this section the experimental setup of a small scale compressed air energy storage system is presented. The experimental setup is developed to validate the air motor model, obtain the flow rate valve control flow coefficient and investigate the technical challenges related to the implementation of a small scale CAES system. Figure 3-44, shows a picture of the test bench, and includes an air filter, a compressor, an air tank, pressure regulator, a PSI 200GAI136/4.5 V pressure sensor, an analog pressure transducer, a flow rate control valve, a tachometer and an EXTECH 451104 vane type anemometer. A low pass filter can be added the speed measurement system to eliminate the high frequency fluctuation of the signal caused by the finite number of vanes.

The compressed air provided by a compressor and small storage tank with support of a 10 bar compressed air supply line from the MUN engineering facility is fed to an air motor via a flow rate control valve and the mechanical output of the air motor is converted to electrical energy using a synchronous generator. Then the AC power is converted and modified by a rectifier and inverted with a predefined power curve. The generated electricity then is fed to a fixed load and grid.

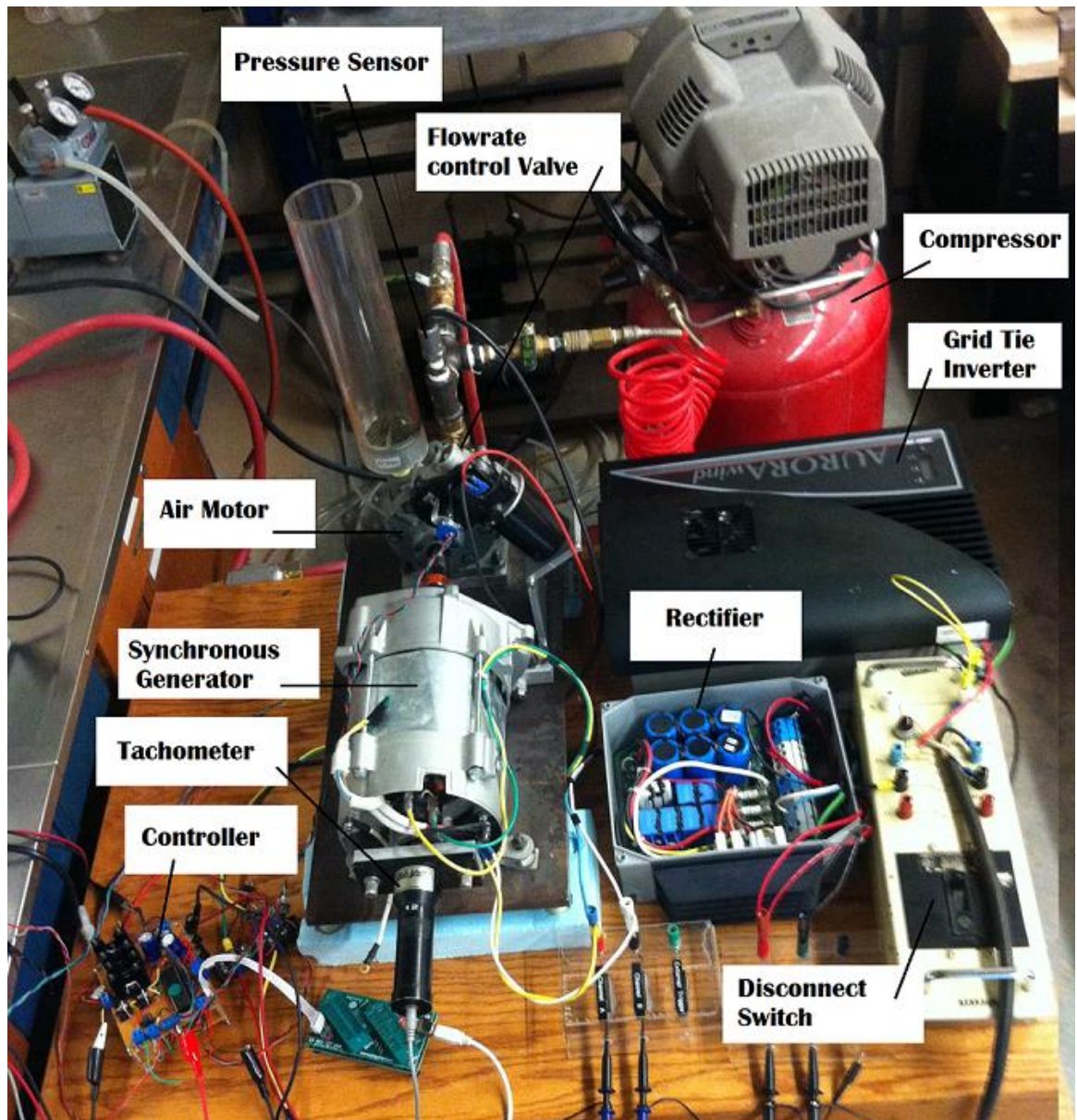


Figure 3-44: experimental setup of small scale CAES system

3.5.1 Air motor simplified model

The relationship between speed and pressure is one of the main characteristics of an air motor, and it can define the output power/torque of the motor. This relationship should correspond to the manufacturer datasheet, which can be implemented in control scheme

of the air motor. Based on the results in mathematical modeling provided in 3.2.2.3, the air motor transfer function can be approximated by a first order system. The system gain (k) and its time constant (T) can be easily derived from practical test of the prototype. As a result of friction, low pressure and flow rates cannot provide sufficient torque/power to rotate the air motor shaft, which creates non-linearity in its operation. In our study it has been assumed that the input pressure and flow rate are more than the minimum required to rotate the air motor shaft.

The system response to various inlet pressures can be measured using a pressure regulator at the air motor inlet port and recording the corresponding speed using a tachometer connected to the motor shaft. The proposed simplified model based on some simple practical experiments can provide a valuable representative for dynamic performance of an air motor, and it can be implemented to develop control strategies without the need for mathematical models and excessive tests to find a large quantity of parameters. In order to investigate the effectiveness and overall performance of the proposed model, some experiments have been conducted and the required parameters for the transfer function were calculated.

Figure 3-45 (a), and (b) show the air motor speed for input pressure of 40 and 60 Psi respectively which correspond to output speed of 1350 and 1600 rpm. Using the oscilloscope measurement for the air motor speed, the system time constant is obtained as 0.75 s and the system gain is 0.075. The air motor speed for constant working pressure of 40, 50 and 60 Psi has been simulated in MATLAB-Simulink environment and Figure 3-46 shows the simulation result. .

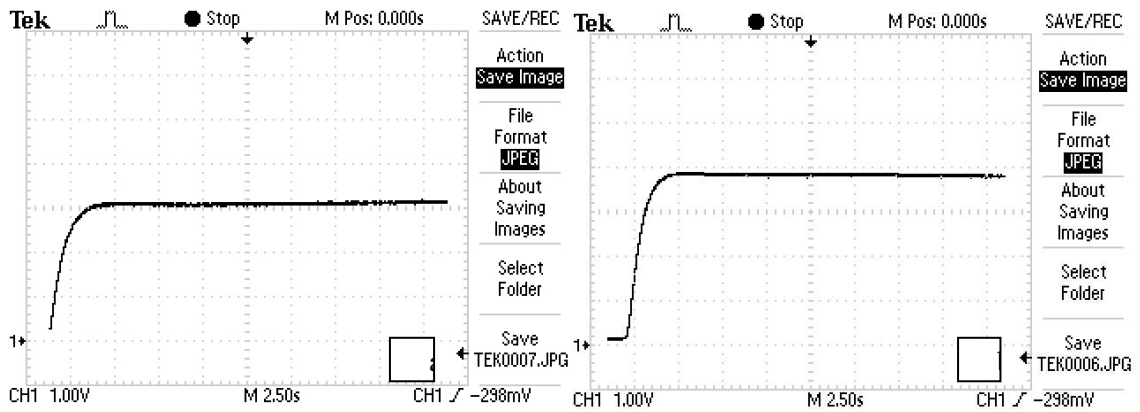


Figure 3-45: The air motor speed response to variable input pressure. (a): 40 Psi and (b): 60 Psi

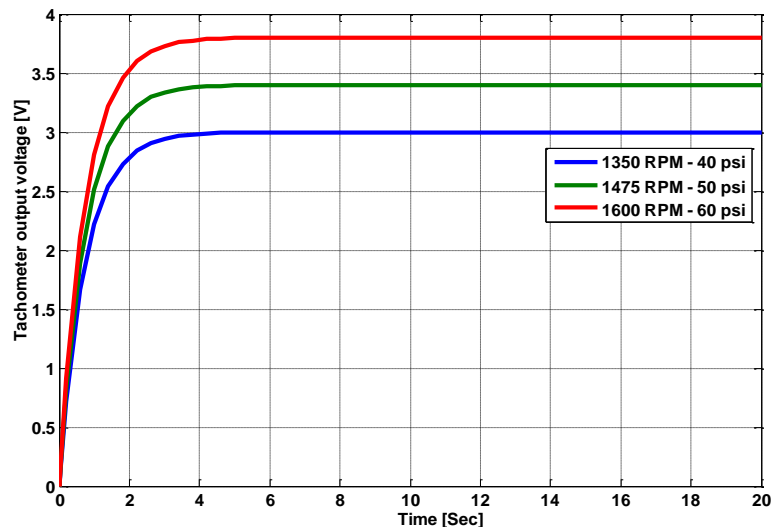


Figure 3-46: The dynamic response of modeled air motor to different input pressures.

The simulation results have been verified by careful experimental work, and it has been found that the results give a high degree of agreement. Experimental results demonstrate the ability of the model to predict the speed-torque characteristics of the air motor.

3.5.2 Flow rate control valve

After modeling the air motor speed response to pressure variation, the next important task was to find the valve flow coefficient. The air flow profile after passing through the

valve is quite complex and in practice a flow coefficient (C_f) is introduced to the equation to represent the effective area. The final equation can be simplified as follows [111]:

$$Q = C_f A_o \sqrt{\frac{2\Delta P}{\rho}} \quad (3-93)$$

Where A_o is the area of the orifice. The flow coefficient C_f can be obtained from experiments. The inlet compressed air pressure can be calculated from (3-93) (3-68) and having the C_f , A_o , ρ values and assuming sufficient flow rate to provide required torque according to manufacturer datasheet. The pressure drop across the valve can be measured using two properly installed pressure transducers and by using (3-93), the valve flow coefficient can be calculated.

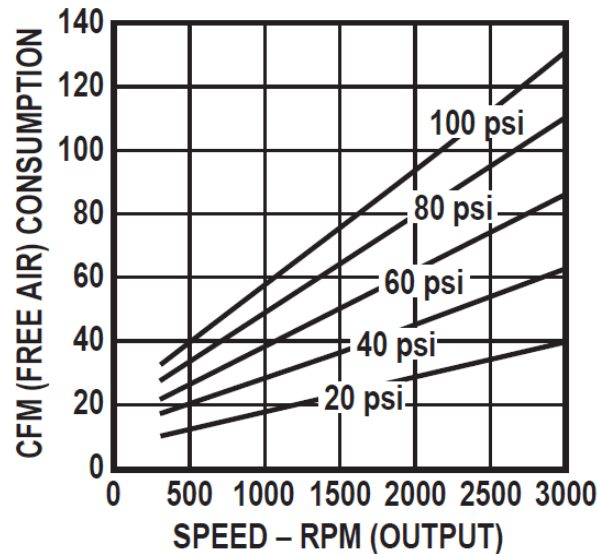


Figure 3-47: GAST air motor Air Consumption vs. Speed characteristic

In order to investigate the effectiveness of the proposed model, some experiments have been conducted and the required parameters for the valve flow coefficient have been calculated. In order to measure the valve flow coefficient under various operating conditions, the pressure drop across the valve, shaft speed and output air speed were

recorded for different working pressures and valve condition. The measurement results and corresponding valve flow coefficients are presented in Table 3-2, including the air motor air consumption at the related speed based on manufacturer data sheet Figure 3-47. In addition, the C_f value has been calculated and presented in Table 3-2 based on P_1 and P_2 pressure difference with respect to the atmosphere pressure at the air motor output.

Table 3-2: The measurement results and corresponding valve flow coefficients

P_1 (Psi)	35	40	50	60
P_2 (Psi)	28.200	31.560	35.860	42.275
Speed (rpm)	1150	1350	1475	1600
Output Flow rate (CFM)	30.448	35.301	42.879	49.195
Air consumption based on Datasheet (CFM)	29	34	42	50
Error (%)	4.992	3.825	2.094	1.610
C_f value based on $\Delta P=P_1-P_2$	0.410	0.416	0.401	0.411
C_f value based on $\Delta P=P_1-P_{atm}$	0.236	0.245	0.253	0.256
C_f value based on $\Delta P=P_2-P_{atm}$	0.289	0.303	0.326	0.328

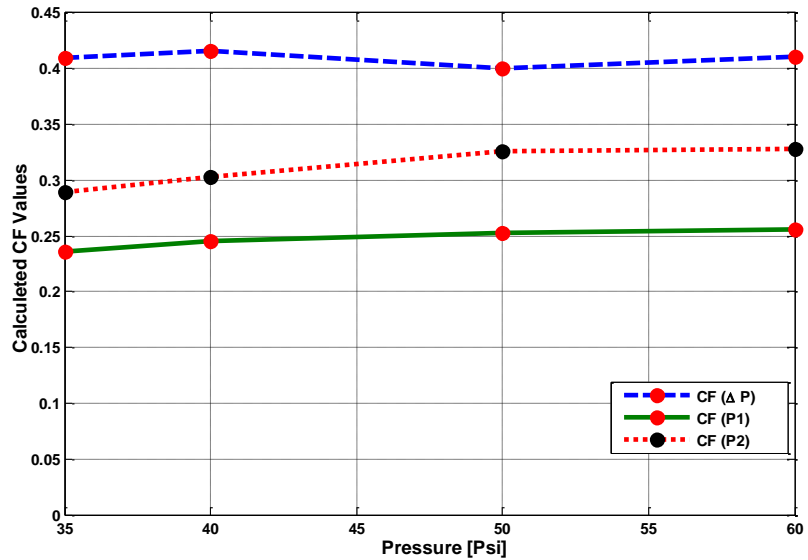


Figure 3-48: Calculated C_f values by increasing working pressure

The three different obtained values of C_f for different operational pressures are shown and compared in Figure 3-48. It can be observed that the C_f values calculated based on $\Delta P = P_1 - P_{atm}$ has low variation over increasing pressure working condition, and therefore by using only one pressure sensor for the air motor inlet pressure, reasonable approximation of the C_f value can be obtained. Considering a constant C_f for variable input pressure condition creates error in comparison to the reference air consumption chart provided by the manufacturer. This error, as it is shown in Figure 3-49, decreases by increasing the working pressure; as a result, the C_f value can be considered as a constant value $C_f = 0.256$ by accepting 2% error over the working pressure of 50 to 100 psi.

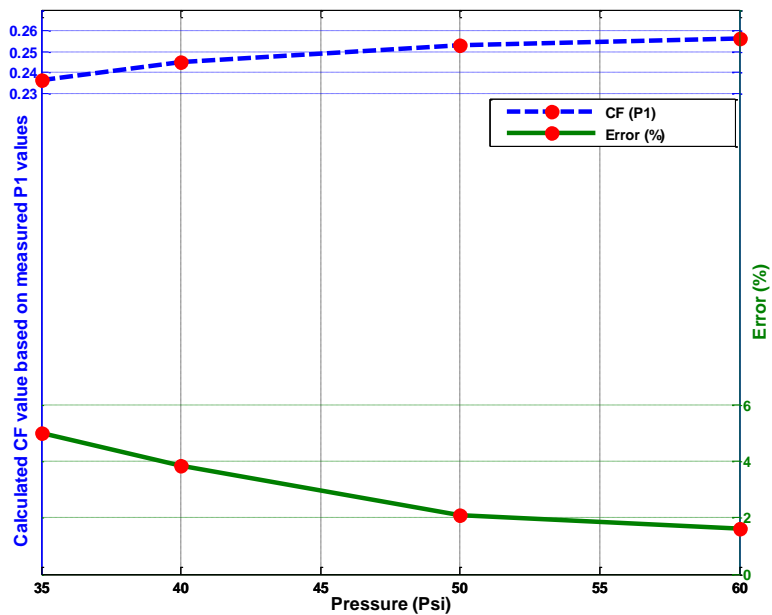


Figure 3-49: The C_f value error variation by increasing working pressure

The approximated C_f value was used in flow rate control valve to estimate the initial value of the required cross section for delivering the desired flow rate. The PWM control reference signals and the valve actuating signals are shown in Figure 3-50 and Figure

3-51 correspondingly, and the corresponding air motor speeds are shown in Figure 3-52.

The test result shows the capability of the control system to follow the reference speed variations.

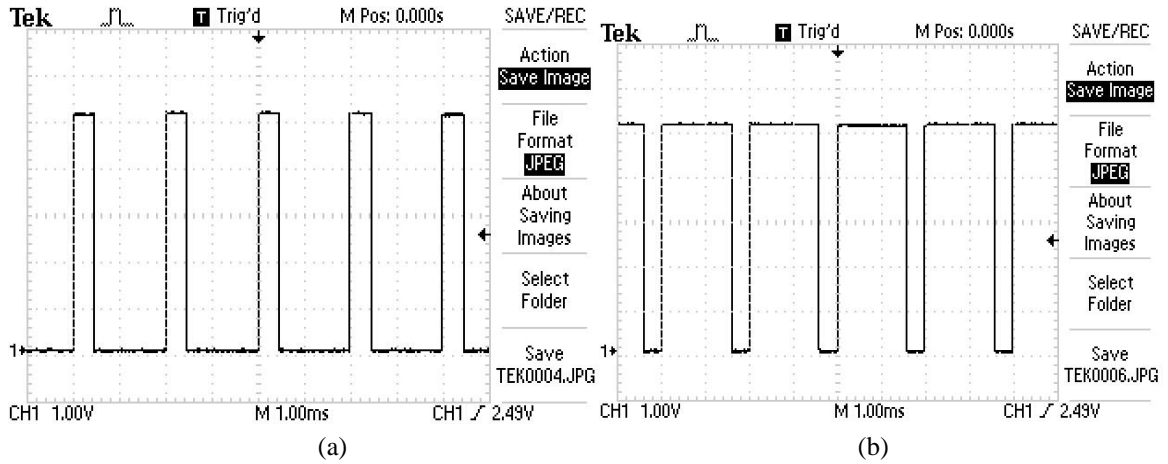


Figure 3-50: Reference PWM signals for flow rate control vale for (a): 650 rpm, (b): 1000rpm.

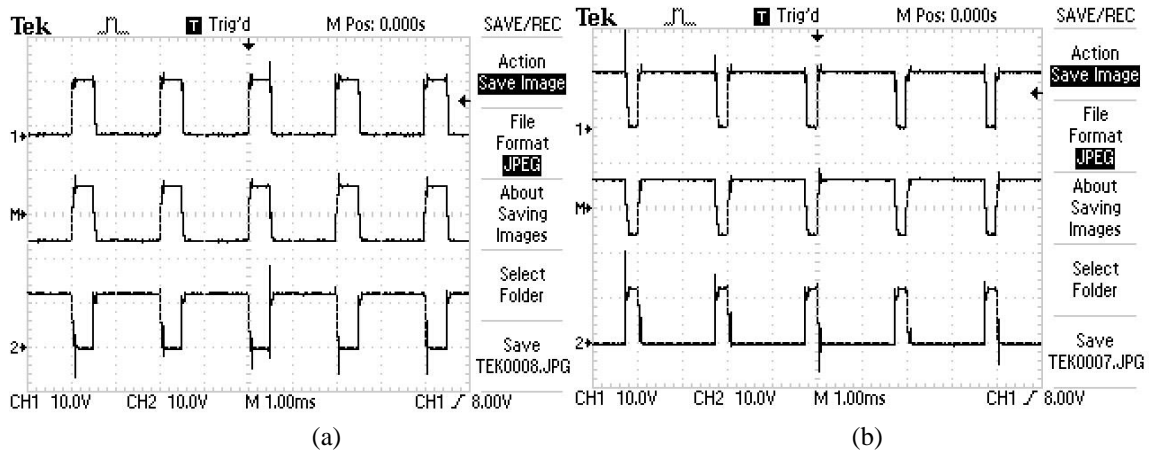


Figure 3-51: Flow rate valve actuating signals for reference values (a): 650 rpm, (b): 1000rpm.

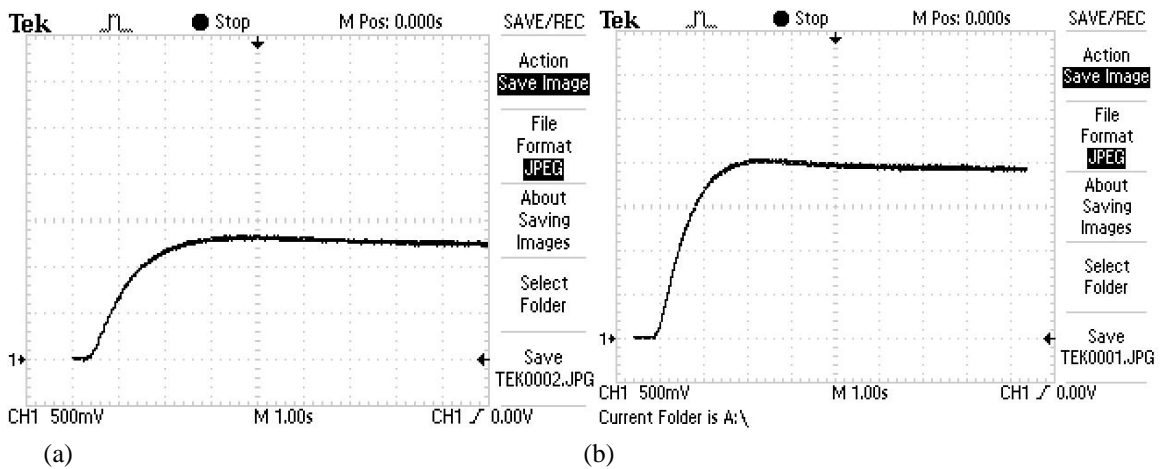


Figure 3-52: Air motor speed control for reference values (a): 650 rpm, (b): 1000rpm.

3.5.3 Output power control of the CAES system setup

In the next step, the power delivery operating mode of the test CAES system in delivering power to a constant load is examined. In this control strategy, the CAES system is responsible to deliver a fixed amount of power to the grid. The air vane motors power curve is shown in Figure 3-11 and Figure 3-13; and the working trajectory of the air motor path can be obtained by mapping the power and pressure points of Figure 3-13 in speed-pressure plane. This trajectory can be approximated with a quadratic equation as a function of the input pressure and desired output power and the reference speed is calculated and applied to the speed control of the air motor. Figure 3-53, shows the response of the CAES system to 100W output power and 7 bar working pressure of the air motor when the disconnect switch is off and CAES works in no load mode. Channel 1, shown in yellow color shows the synchronous generator – air vane motor coupling speed, channel 2, in blue color, shows the input pressure of the air motor and channel 3, in purple color, shows

the synchronous generator output voltage. Figure 3-54, shows the same waveform with different time scale (0.1s/div) to show detail with better resolution.

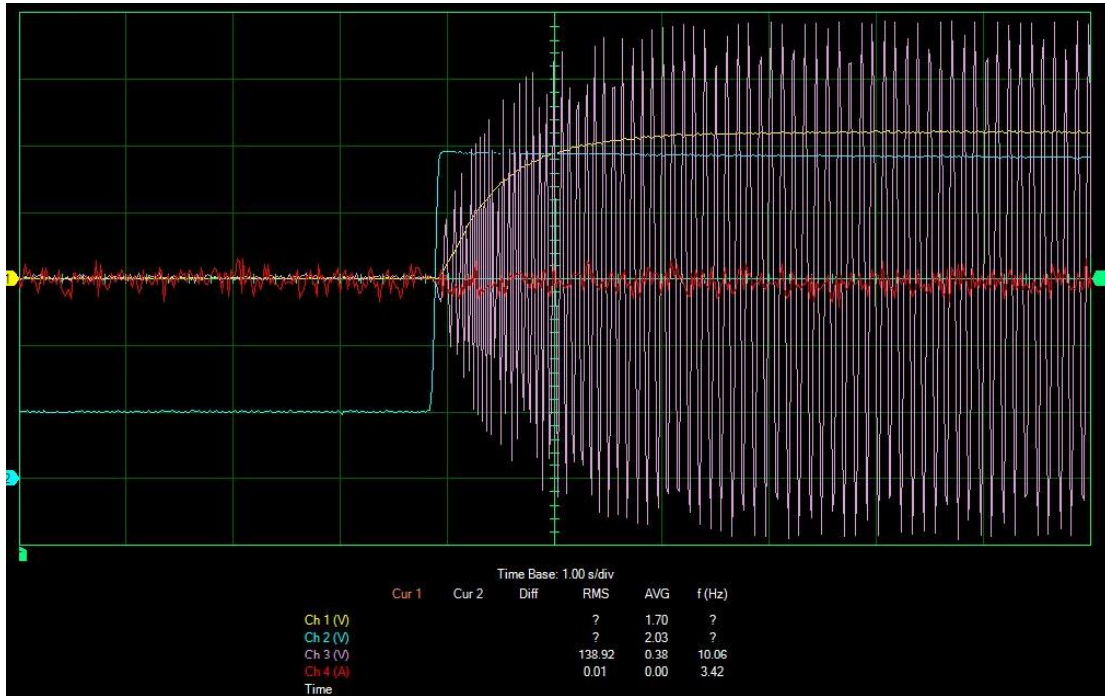


Figure 3-53: Response of CAES system in delivering 100W power to the grid in no load mode.

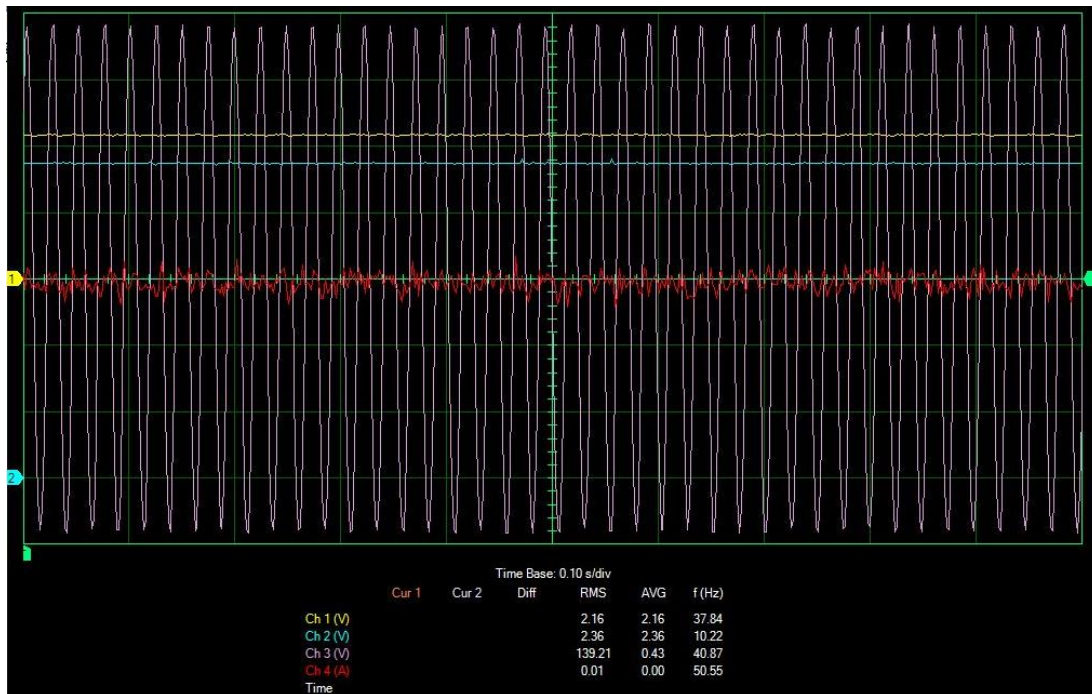


Figure 3-54: Steady state performance of the CAES system in delivering 100W power to the grid.

The synchronous generator excitation current and the generator output currents in no load condition are shown in Figure 3-55. When the disconnect switch is connected to the grid, the CAES system is able to inject the power to the grid and its loading condition for 100W can be obtained. Figure 3-56, shows the synchronous generator voltage output, the rectifier voltage and the output voltage waveforms of the inverter in the loaded condition.

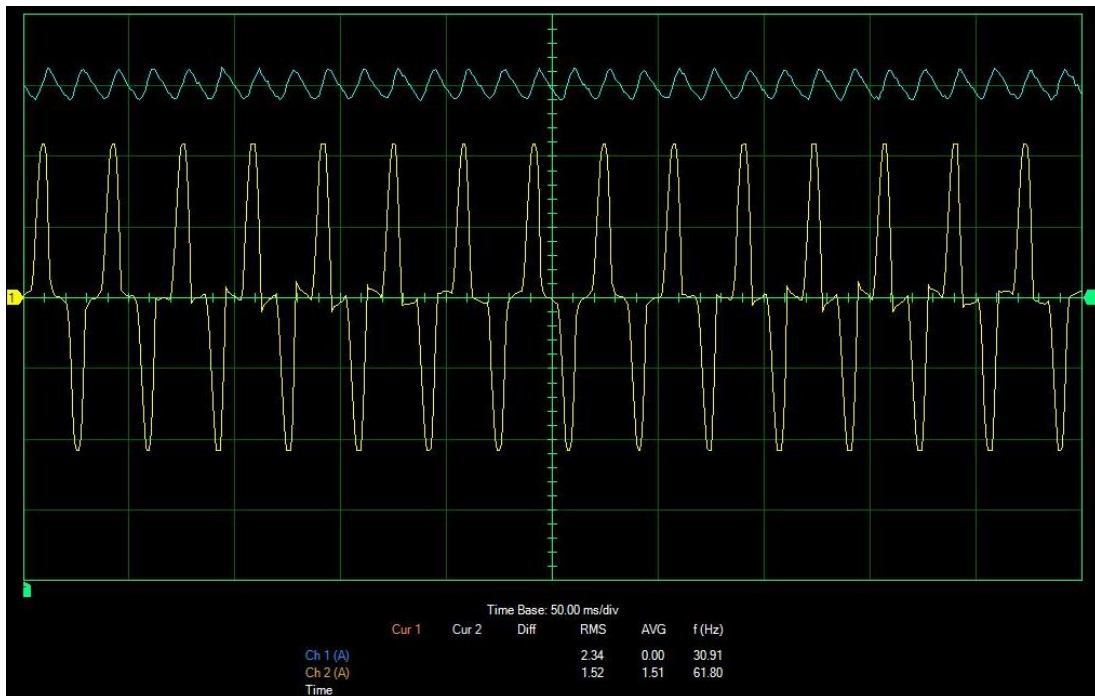


Figure 3-55: The synchronous generator excitation current and its output current in no load condition.

As it shown in this figure, the output voltage of the synchronous generator is deviated from pure sinusoidal waveform compared to no load condition shown in Figure 3-54, due to current harmonics injected by the current loop controller of the inverter. The inverter used in this study had a block dedicated to mitigate current harmonics and therefore the current harmonic mitigation was not considered in this study. In addition, the power rating of the inverter is 3kW with input voltage of 215Vdc, and its power curve was needed to be adjusted for the power rating of 100W and input voltage of 80V which falls

in low efficiency range shown in figure 28, Appendix 4. The output waveforms of the delivered voltage, current and power by the inverter is shown in Figure 3-57.

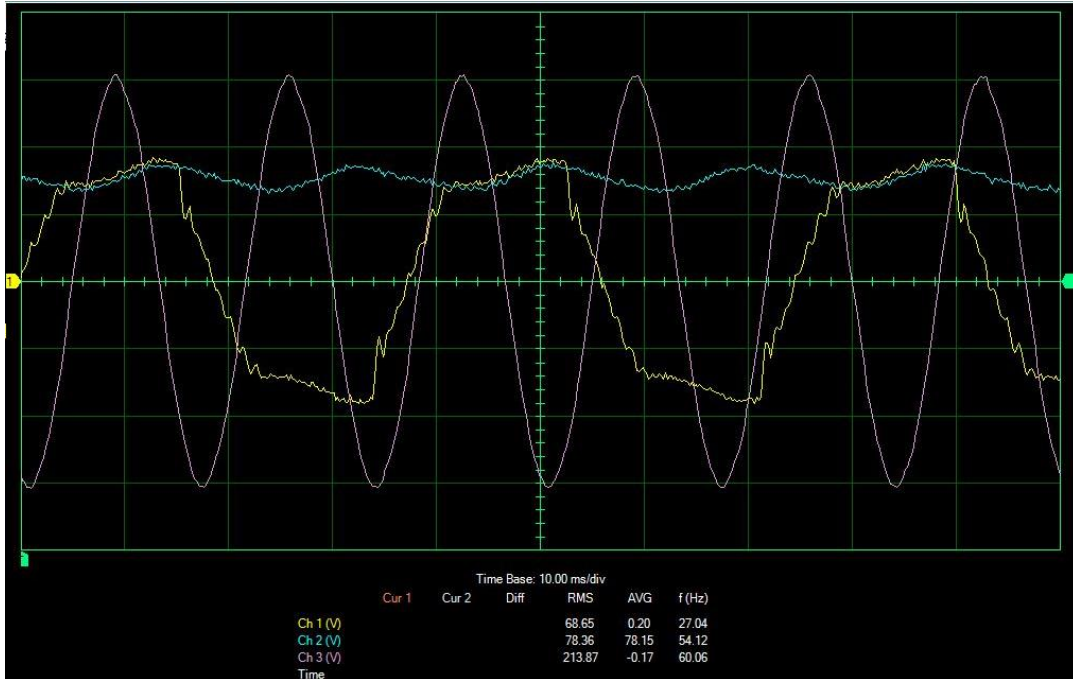


Figure 3-56: The synchronous generator, rectifier unit and inverter output voltage waveform of the CAES system in delivering 100W power to the grid.

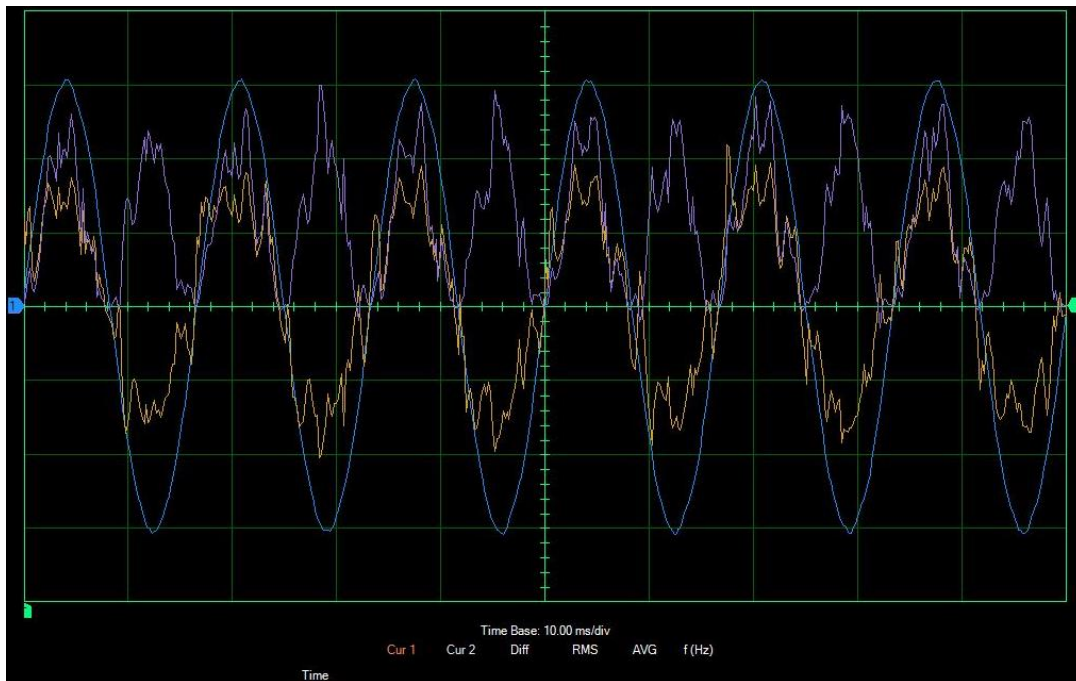


Figure 3-57: The output waveforms of the delivered voltage, current and power to the grid.

The CAES system response in loaded condition is shown in Figure 3-58, where the air vane speed and the compressed air supply's pressure drop is stabilized by adjusting the opening of the flow rate control valve.

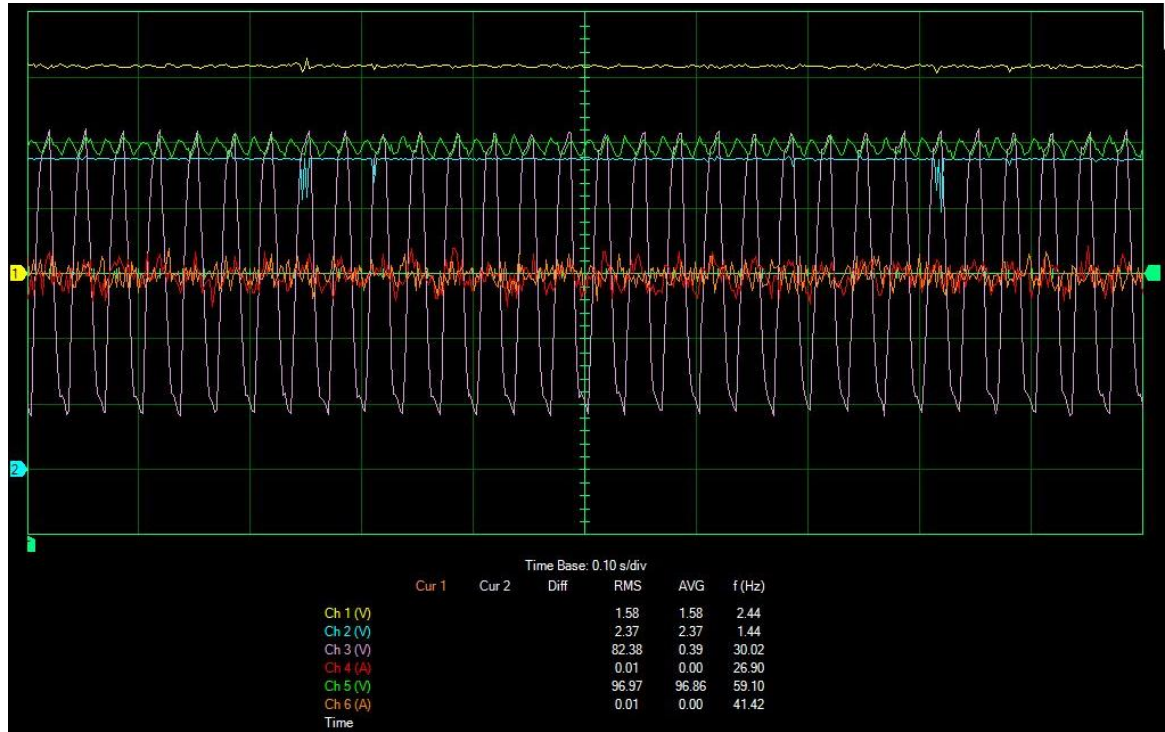


Figure 3-58: The output waveforms of the delivered voltage, current and power to the grid.

Figure 3-59, shows the synchronous generator, rectifier and inverter output power waveforms, and as it shown in purple waveform the CAES system was able to deliver 98.55W to the grid while the air vane more speed and the input pressure drop was negligible by adjusting the flow rate control valve opening. In addition as it can obtained from this waveform, the inverter efficiency dropped to 70% due to working in output power and input voltage rating different from its nominal ratings, which shows the importance of the proper sizing of CAES system components.

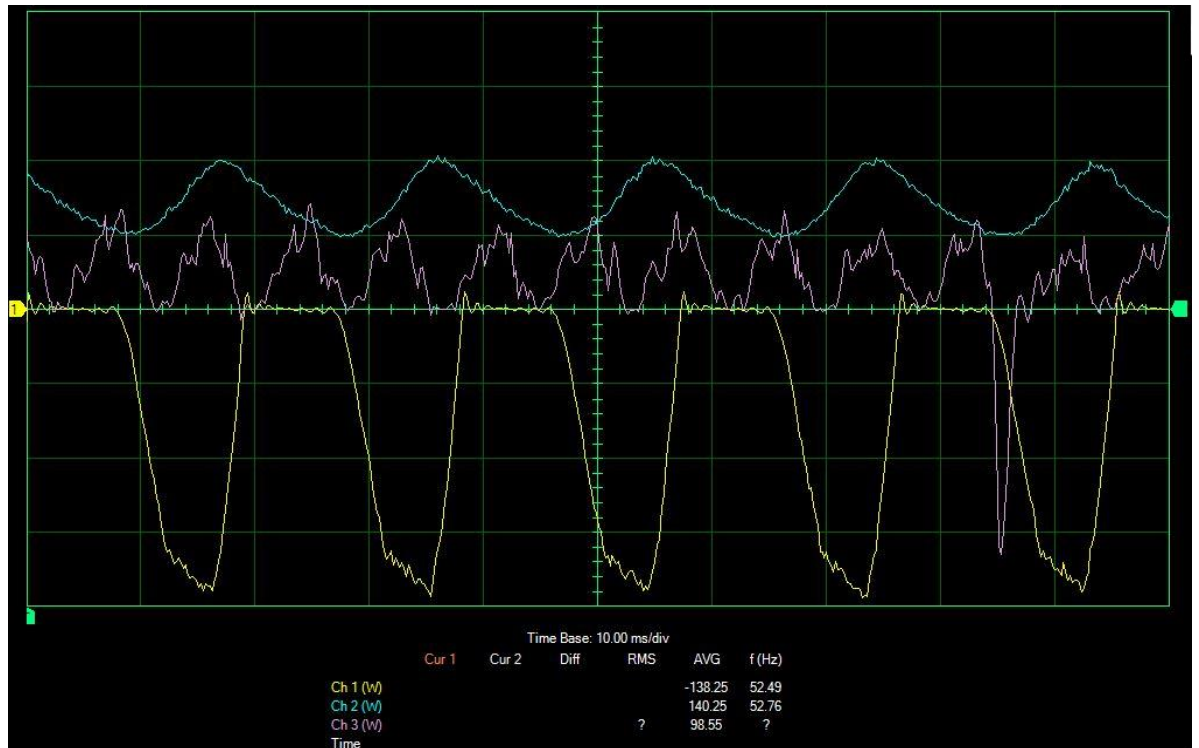


Figure 3-59: Steady state performance of the CAES system in delivering 100W power to the grid.

3.6 Summary

In this chapter, the proposed hybrid power system structure was described. The system was divided into four main categories: Wind turbine as the main energy harvesting equipment; CAES system to increase the wind energy penetration; Diesel generator unit for backup and improved reliability purpose; the supervisory control unit; and the system load. The steady state and dynamic modeling of individual components of the systems was presented, then two simplified models for air motor and flow rate valve was presented and validated through some experiments. Then using initial working condition obtained from the steady state models, the performance of the CAES system in expansion mode to deliver 100W power to the grid was explored.

Chapter 4 Hybrid Power system sizing, design and optimization

In a wind-based power system, the general design of the system is focused on increasing the wind energy share in energy production in a cost effective manner. The random nature of the wind speed highlights the necessity for an energy storage system. While a storage system can smooth the energy output characteristics of a wind turbine, the wind penetration rate can only be increased by storing a large quantity of wind energy during overproduction periods and restoring it during underproduction regimes.

The increase in wind penetration is directly related to the amount of the stored energy. A storage system capability is limited by its energy conversion rate and predefined maximum capacity for most of storage system presented in chapter 2 and 3. One possible option is to overdesign of the storage system in order to increase the wind penetration in electricity generation; however, this might not be a proper approach due to stochastic nature of the available RES and financial constraints. In addition, having a huge storage capacity does not guarantee that the storage system can harvest the available excess energy in a limited duration of time. This chapter focuses on three approaches to increase the wind penetration: choosing the most suitable wind turbine based on the local wind speed profile; design an effective storage configuration for the storage system and develop an overall control scheme of storage strategy with high energy harvesting capability.

4.1 Monte Carlo simulation of wind speed

The availability of high resolution wind speed data is essential to increase the accuracy of the estimated output power of a wind farm [135, 136]. Such data can be used to estimate the annual energy production and compare the performance of different wind turbines on the targeted or proposed installation site.

The average wind speed for a region can be found in a wind map [137, 138]. This mean value is calculated based on the average wind speed during a year and its accuracy and resolution is very limited [139]. Therefore, using such a data for establishing a wind farm will lead to a high level of uncertainty. The wind speed frequency distribution is another way for estimating the wind speed average for a specific location. However, the availability of such a distribution depends on the existence of anemometer and recorded data on a site.

The aim of the first part of this chapter is to present a statistical model capable of generating wind speed data with desired time scale resolution. The generated wind speed data will be used to assess the performance of different commercial wind turbines in order to either compare the performance or choose the proper size of the wind turbine.

4.1.1 Wind speed data analysis

Statistical analysis of available wind speed data can be executed in order to predict the wind speed variation trend in desired time scale resolution. The result of such analysis can be utilized to produce suitable wind speed data. In this study, available wind speed data measured at airport weather reporting stations for 7 years with 1 hour resolution have

been used [137]. The measurements of wind speed at airports are done with the anemometer located at standard 10m level. On the other hand, the direction of the wind has the least concern in a wind farm design since it is assumed that prospective wind turbines are fully equipped with yaw control system. For this reason, the direction of the wind is not considered here, and it is assumed that wind farm layout has been selected to minimize the wind shadow.

In this study standard approaches including wind speed distribution modeling and statistical analysis are combined in order to generate the required wind speed data. The first step of this study is to gather wind data. The proposed approach is based on the frequency of the wind speed. As a result, the wind speed data is independent of the sampling rate of the wind speed. Consequently, the approach allows available wind data from different sources to be combined. Considering significant amount of data from various resources such as Atmospheric Environment Service (AES) Canada [137] or National Climatic Data Center [140], the accuracy of the generated wind speed data can be increased by using a large quantity of input data. However, a compromise is necessary between the level of accuracy and the data processing time.

In this study, hourly wind speed data from National Climatic Data Center database from 2006 to 2013 was used and adjusted for the desired elevation. The Environment Canada wind speed data base for each hour during 7 years has been collected and classified in 10 different wind speed ranges. The total number of the collected data for each hour is 2557 ($7 \times 365 + 2$ days in the leap days 2008 and 2012), and its frequency

distribution for the first hour (12:00am – 1:00 am) and the thirteenth hour (12:00pm – 1:00pm) are shown in Figure 4-1.

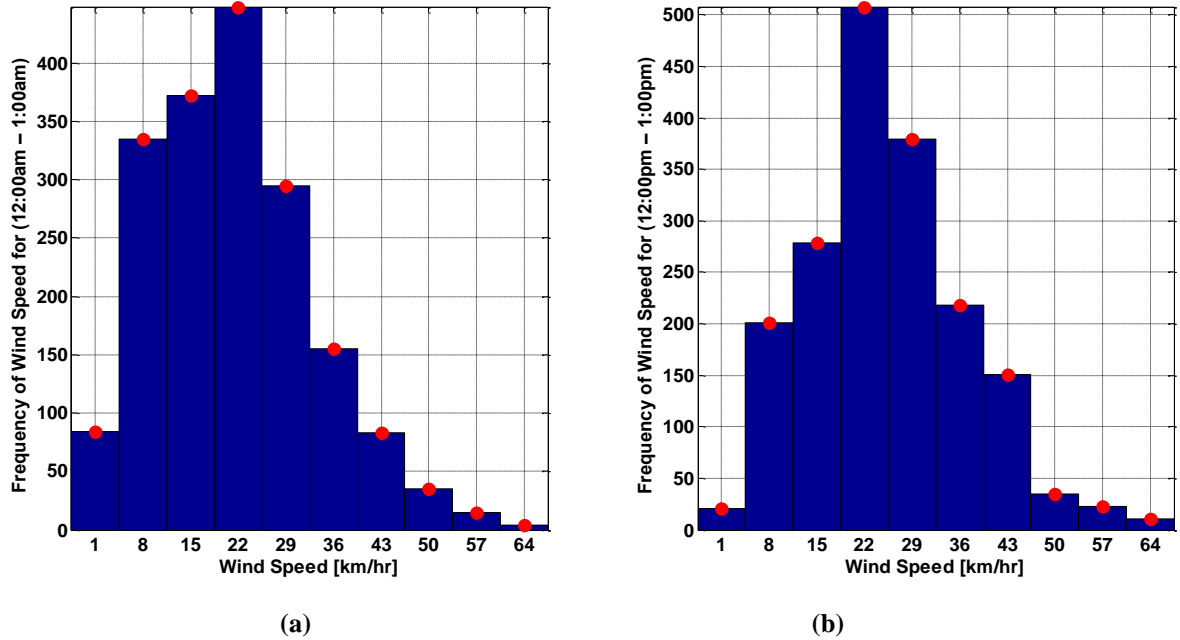


Figure 4-1: The wind speed distribution frequency for (a): 12:00am - 1:00am, (b): 12:00pm - 1:00pm

As shown in Figure 4-1, the frequency of the wind speed varies during a day, and this fact can be used to develop individual mathematical representation of the distribution for each hour. Different probability distribution can be applied to the wind speed frequency database in order to represent its probability. Weibull function is the most common distribution in wind speed distribution studies, because it has been proven to provide a good fit to the wind speed data [136], [141] and [142]. The wind speed frequency distribution can be found from the following Weibull equation:

$$f(V) = \frac{k}{C} \left(\frac{V}{C}\right)^{k-1} e^{-\left(\frac{V}{C}\right)^k} \quad (4-1)$$

where $f(V)$ is the Weibull probability density function, C is the Weibull scale factor and, k is the wind speed distribution shape factor. Figure 4-2 shows the obtained Weibull

probability density function for the first hour (12:00am – 1:00 am) and the thirteenth hour (12:00pm – 1:00pm).

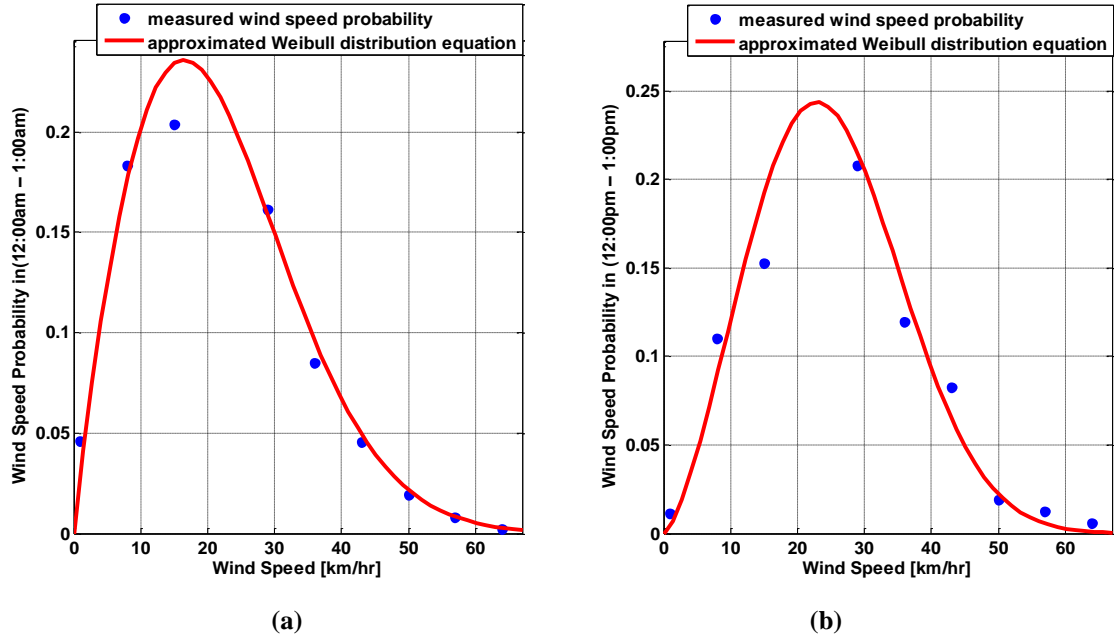


Figure 4-2: The obtained Weibull probability density function for (a): the first hour (12:00am – 1:00 am) and (b): the thirteenth hour (12:00pm – 1:00pm).

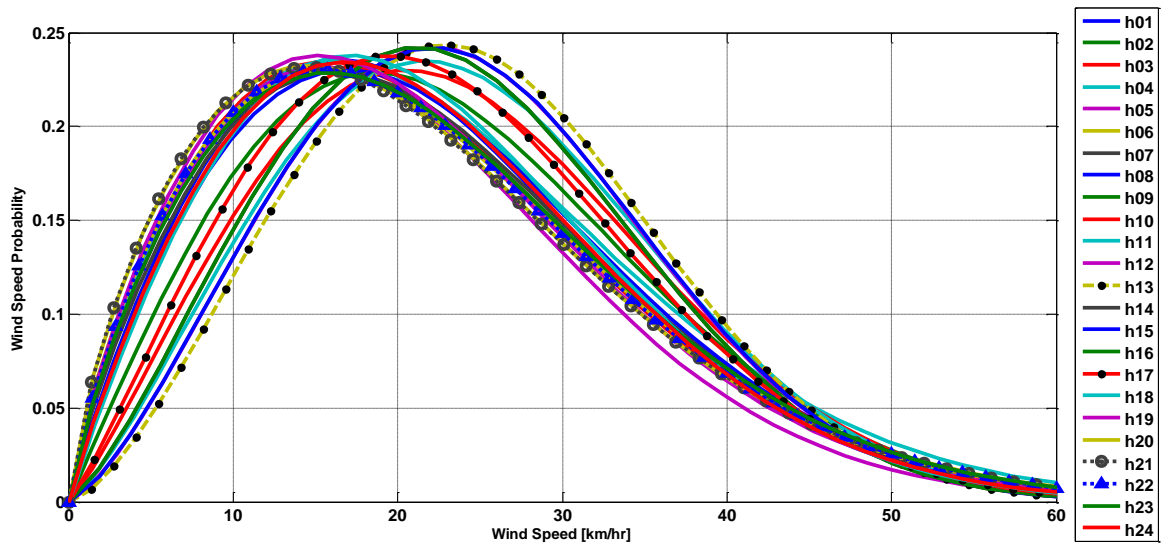


Figure 4-3: The hourly Weibull distribution of the wind speed probability during a day.

The wind speed data was categorized based on its hourly measurement time, and the obtained frequency distribution was fitted to a most accurate Weibull distribution in MATLAB curve

fitting toolbox for each hour. The hourly Weibull distribution is provided in Appendix 2. The estimated wind speed frequencies obtained using the hourly Weibull distribution is shown in Figure 4-3. As shown in Figure 4-3, the high wind speed probability at 13:00 pm is higher than the other hourly wind speed profiles. The high wind speed probability trend increases from 12:00am until it reaches its maximum value at 13:00pm, and returns to the low speed probability from 14:00 pm to 12:00 am.

4.1.2 Wind speed data regeneration methodology

Monte Carlo simulation method which is a statistical and mathematical method can be used to generate stochastic wind profile according to the provided wind speed database [143]. This method is based on an iteration process, which generates random variables considering their distribution functions [144-146].

A combination of direct sampling method and Monte Carlo simulation was utilized in this study to achieve random data generation with specific frequency distribution. The simulation error of the Monte Carlo method can be approximated by $1/\sqrt{n}$, where n is the number of applied samples in a simulation. To achieve less than 3% error in a Monte Carlo based simulation, the number of data should be more than 1000. To meet such a high accuracy in wind speed data generation, a set of 1500 uniformly distributed numbers between [0-1] was produced and applied to the inverse of the Weibull Cumulative Distribution Function (CDF) of each hour in order to generate the wind speed data for the corresponding hour. Then based on required resolution, a certain amount of samples were randomly chosen from the generated wind speed data base for each hour.

The wind speed generation is made through a code developed in MATLAB, based on the Monte Carlo simulation method. In this study, the hourly CDF can be obtained by integrating the Weibull distribution for each hour wind speed data set. The obtained CDF from the measured data was approximated with a fifth degree polynomial equation for each hour. This approximated equation is given in Appendix 2. Figure 4-4, compares the approximated CDF for the first hour (12:00am – 1:00 am) with its corresponding measured values from the wind speed data base.

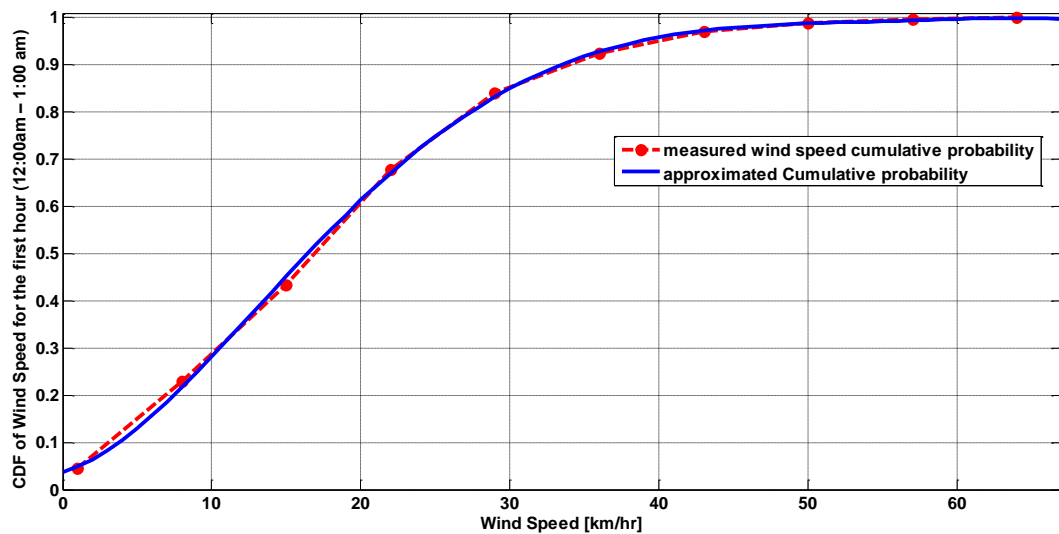


Figure 4-4: The approximated CDF for the first hour (12:00am – 1:00 am) with its corresponding measured values from the wind speed data base.

The resultant hourly CDF is used in Monte Carlo simulation in order to produce the wind speed profile with predefined time scale resolution. The structure of the proposed method is shown in Figure 4-5, and four produced sample wind speed profiles for the first hour (12:00am – 1:00 am) are shown in Figure 4-6.

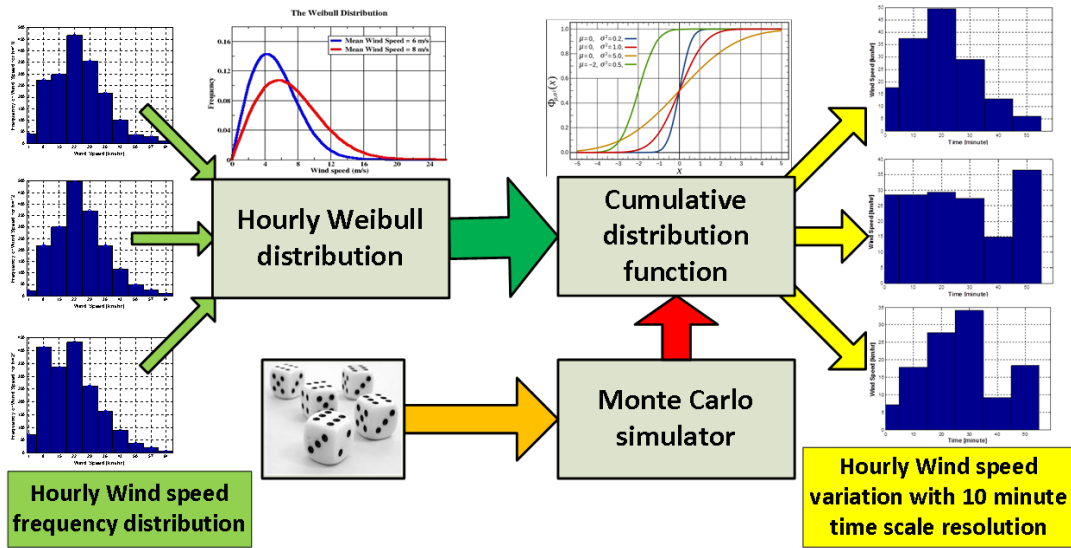


Figure 4-5: Proposed method for producing wind speed profile with desired resolution.

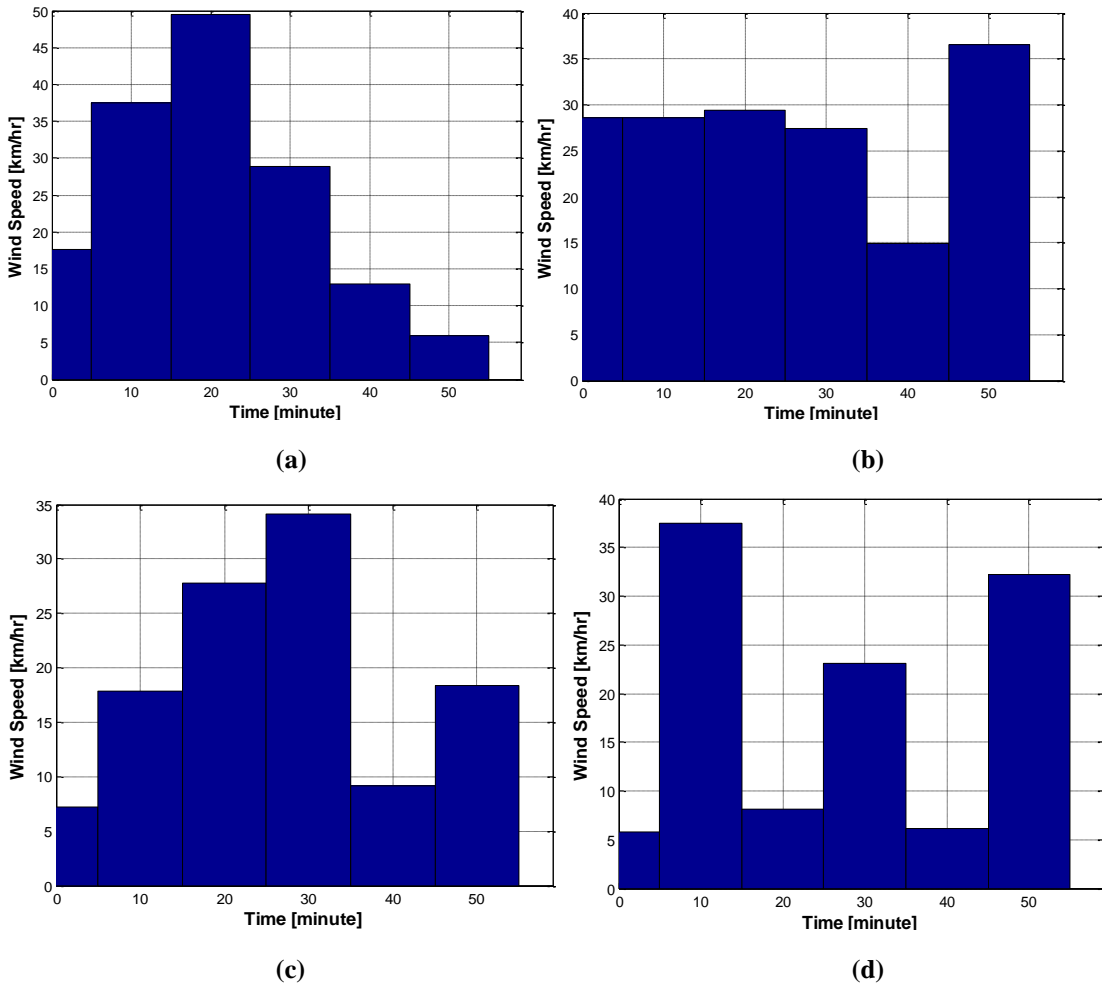


Figure 4-6: Four produced sample wind speed profiles for the first hour (12:00am – 1:00 am)

Produced sample wind profile for an hour can be appended to the next hour profile in order to generate daily wind speed profile. An example of the generated wind speed profile for the first 3 hours (12:00 am – 3:00 am) in 3 days (1st, 7th and 14th) in January with 10 minute resolution (6 samples per hour) is shown in Figure 4-7.

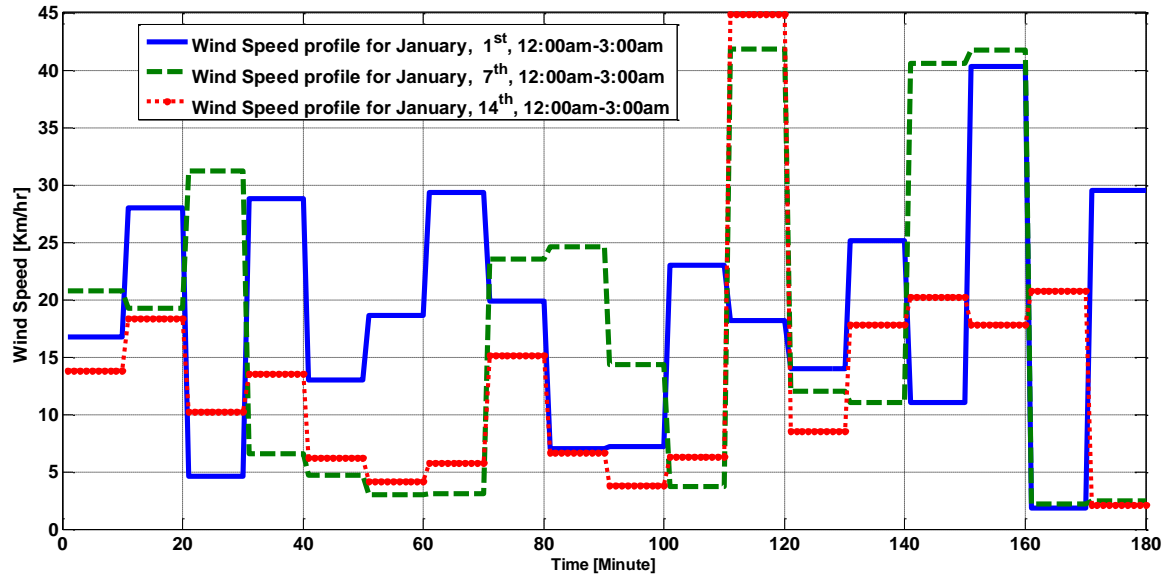


Figure 4-7: Generated wind speed profile for January, 1st, 7th and 14th, for the first 3 hours.

4.2 General Criteria for a Hybrid Wind-CAES Energy System Design

Stochastic variation of the wind speed increases the uncertainty of wind farm design, and as a result the working performance of selected components in a wind farm is not known in advance [83].

The reliability and economical feature of the produced wind energy can be improved by proper design of wind based energy systems and its integration to the electricity grid [8, 147]. Choosing an effective wind turbine for a specific site will increase the harvested energy from the available wind energy, and as a result the economic benefit of installed equipment will be higher. In addition, more energy is available for cost-effective energy

storage systems to store the excess wind energy during off-peak or over production time and restore it later during peak time or low production regime, and as a result the wind energy penetration will increase [8, 147, 148].

A primary general design can be obtained using the general criteria for maximum wind energy exploitation with realistic optimum energy conversion efficiency. The general design of a hybrid wind–CAES based energy system is divided into three stages: first, choosing the most suitable wind turbine with maximum annual output power, second, a design that achieves reasonable energy conversion efficiency by selecting the proper number of compression stages and the compression ratio; and third, finding the most effective configuration and control strategy to extract maximum energy.

4.2.1 Selection and Sizing of Wind Turbines based on their energy output

The performance of different wind turbines can be evaluated and compared using the generated wind speed profile at a desired location, and the turbine with maximum power output can be chosen. Variable speed control could be assumed for the wind turbine to have more energy production even in low wind speed regimes in comparison to the fixed speed wind turbines [149]. The average wind speed at the desired site is also another factor in wind turbine selection, and the 5 to 18 m/s wind speed range is usually considered ideal as most commercially available wind turbines work in the same wind speed range. Some additional factors, such as wind average direction (known as wind rose plots), availability of land for proper spacing between the wind turbines, availability of power grid (for a grid connected system), accessibility of site, soil/ground roughness,

frequency of lightning strikes, should be considered for the wind farm site location selection [150]. Performances of 6 different wind turbines is assessed in this study. The wind turbine models, their power rated, rotor diameter and required tower height are listed in Table 4-1.

Table 4-1: Characteristics of the 6 different wind turbines under study.

Wind turbine model	Rated Power [kW]	Rotor Diameter [m]	Tower Height [m]	Survival Wind Speed [km/hr]
Sky Stream	2.4	3.72	13.7 (zone 3)	226.8
Wisper 500	3	4.5	13.7	198
Excel-5	5	6.2	24	216
Scirocco	6	5.6	24	216
Excel-R	7.5	7	24	201
Excel-S	10	7	24	201

The capacity factor, C_p shows the ability of the turbine to extract power from the kinetic energy available in the air flow. In order to find the corresponding C_p curve as a function of the wind speed, the output power from each wind turbine manufacturer provided power curve was divided by the calculated output power at the identical wind speed based on the methodology described in section 3.2.1.1. Figure 4-8, shows the approximated C_p values as a function of wind speed for the six different wind turbines.

Considering the result obtained from the calculated C_p values as function of wind speed shown in Figure 4-8, it can be concluded that each wind turbine has different behavior in different wind speed regimes. Wind turbine datasheet provides the nominal wind speed for its rated output power, which is not an accurate measure to choose a wind turbine for a specific site. In this section, the performance of 6 different wind turbines is compared using the generated wind speed data. The purpose of this study is to find the most effective wind turbine to provide a required energy demand.

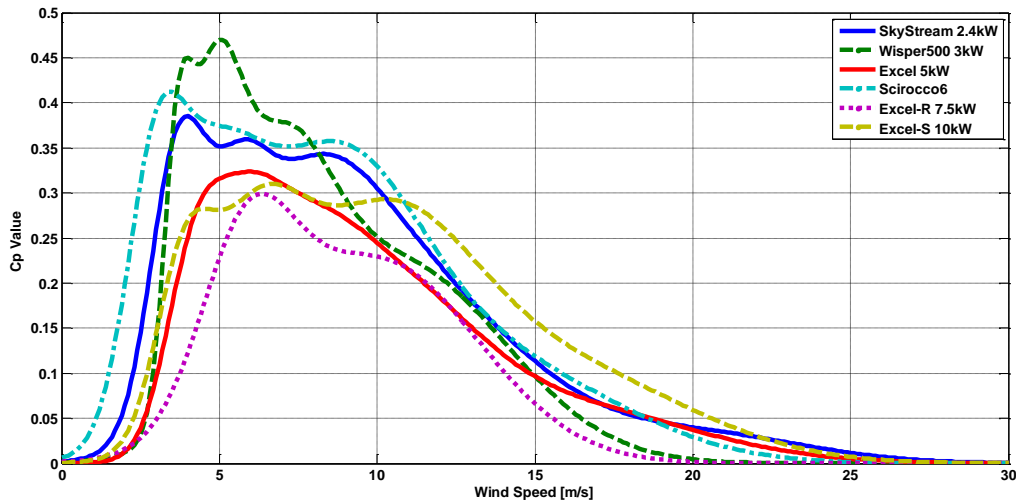


Figure 4-8: Approximated C_p values as a function of wind speed for six the different wind turbines.

The wind data analysis is usually performed on available databases which have been created for general purpose use. Based on the logging techniques for such a data, the collected data might not be suitable for wind energy assessment studies. Considering the fact that measurement techniques over long periods of time might be subject to change, it is satisfactory to accept a reasonable level of error in a statistical analysis. The error sources include: incompleteness of the anemometer logged data, change in measurement techniques with incorrect calibration, measurement at different elevations, missing data and other sources of errors. Although it is almost impossible to avoid all of the above mentioned errors, the data should be corrected by applying proper adjustment.

The wind speed data for our desired location was available for 1 hour frequency measurement, which was converted to 10 minute frequency using Monte Carlo simulation explained in the section 4.1. This time scale resolution is acceptable in this analysis considering its steady state nature. The available wind power during a day can be calculated using the average wind speed data with specific time scale resolution. The

wind speed at a desired height of the wind turbine tower (h_2) can be calculated by applying the wind speed power law:

$$V_2 = V_1 \left(\frac{h_2}{h_1} \right)^\alpha \quad (4-2)$$

where V_2 , in m/s, is the adjusted wind speed at a height of h_2 in m, using the measured speed V_1 at a height of h_1 , and α is the wind speed power law exponent. Its value for ideal condition has been found to be 1/7 based on practical test values [136]. In order to expose each wind turbine to wind speed at its tower height, the wind speed adjustment was applied to each wind turbine based on its tower height (Table 4-1).

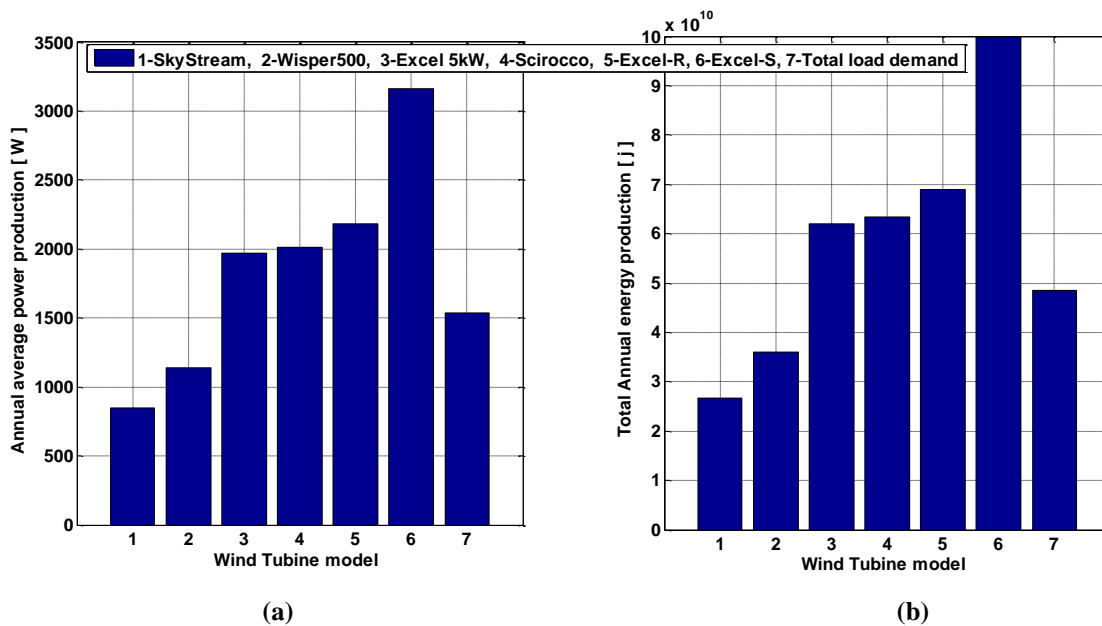


Figure 4-9: (a): The annual average power production of the 6 different wind turbines, and (b): their total annual energy production.

The generated annual wind speed profile with 10 minute time scale resolution was applied to the six selected wind turbines, whose total annual energy production and annual average power production are shown in Figure 4-9. The average annual load

demand is also included in Figure 4-9(a) and (b) as reference for evaluating the wind turbine performance in producing the required power and energy.

As shown in Figure 4-9(a), SkyStream and Wisper 500 wind turbines could not meet the average load demand (#7 in Figure 4-9(a)), although their manufacturer provided power rating (Table 4-1) is higher than the average load demand. On the other hand, Excel-S with 10 kW rated power produces two times the rated load which is considered an overdesign for the subject wind farm site. Excel-5, Scirocco and Excel-R are able to meet the demand and their excess energy can be utilized in a typical energy storage system in order to remedy the wind speed fluctuation.

To choose the optimum wind turbine based on its performance, the average power production of each wind turbine was divided by its rated power to give the results shown in Figure 4-10.

$$\text{Wind Turbine Performance index} = \frac{\text{Average Annual output Power}}{\text{Rated output Power}} \quad (4-3)$$

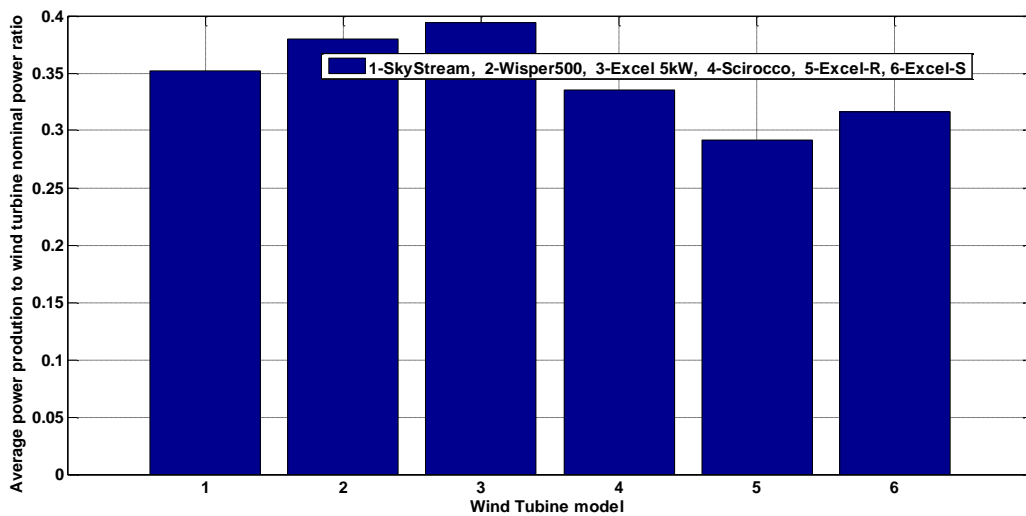


Figure 4-10: The performance index comparison for the 6 wind turbines under study.

Based on the performance index results shown in Figure 4-10, Excel-5 wind turbine has the highest value and it can deliver the required power to the load. SkyStream and Whisper 500 wind turbines have high performance index values close to the Excel-5 wind turbine performance index value, but based on results shown in the Figure 4-9, they cannot provide the required load demand. Based on this criterion, Excel-5 is the smallest size of the wind turbine that can meet the load requirement and has the highest performance index value. Using the proposed methodology, the wind farm designer can avoid overdesigning a wind farm and choose the most effective wind turbine with the highest possible performance index for a desired location. The smallest size of the wind turbine that can provide the load demand can be found using the proposed assessment methodology.

4.2.2 Efficiency of a Pneumatic Storage System

The efficiency of CAES systems has been considered as the main drawback in many studies [18], [35], [151]. Low efficiency for single-stage compression and expansion is the limiting factor of a very high pressure system. However, an efficient design of such a system can lead to an enhanced performance of a CAES system. Highly efficient heat exchangers for after compression cooling and pre heating between expansion stages can be utilized to overcome this limitation. In addition, compressing air in multi-stages instead of one stage can improve the overall energy conversion efficiency. As the Figure 3-9 illustrates, the efficiency can be increased using more compression stages. As a result,

the challenge is to establish a compromise between the performance, complexity and the operational cost of a CAES system.

The efficiency of an energy conversion process in a pneumatic storage system can be investigated by considering both the multistage configuration of the compressors to determine a cost effective number of stages and the optimum compression ratio to determine the working pressure of the compressors. Changes in efficiency of the compression cycle with different compression stages are shown in Figure 3-9. For finding the optimum working pressure, rewriting the compression efficiency equation presented in Chapter 2, 2.1 can be simplified as follows:

$$\eta = \frac{1 - \left(\frac{P_f}{P_i}\right)^{\frac{1-n}{n}}}{\left(\frac{P_f}{P_i}\right)^{\frac{n-1}{n}} - 1} \quad (4-4)$$

Figure 4-11 shows the variation of the energy conversion efficiency for different pressure ratios and polytropic exponent coefficients.

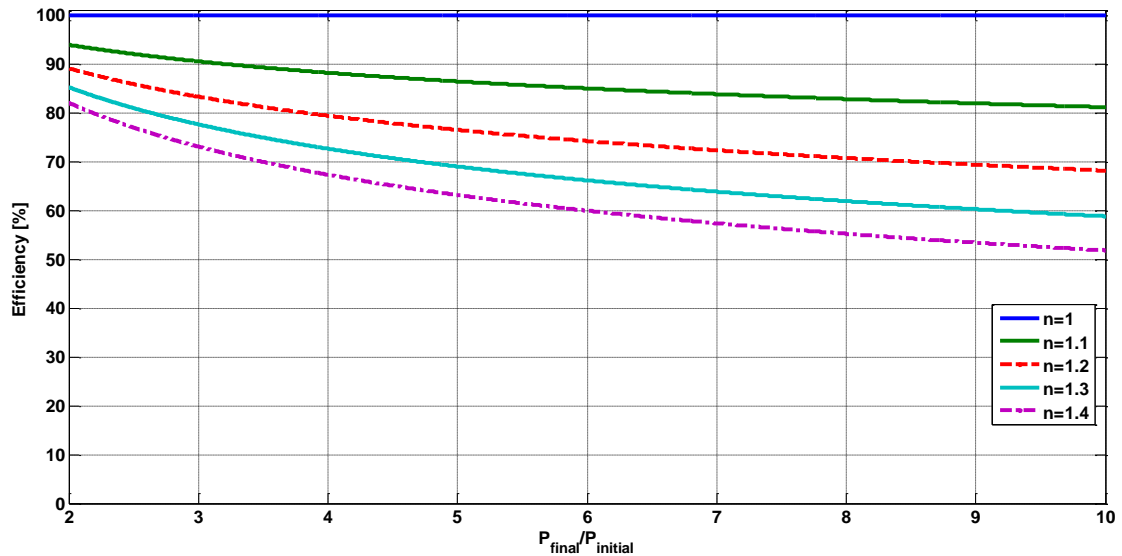


Figure 4-11: Energy conversion efficiency variation for different pressure ratios

Although, the compression efficiency in a system with ideal heat exchanger can theoretically reach 100% efficiency as shown in Figure 4-11, this efficiency will decline in an experimental setup. This efficiency drop depends on the quality of the heat exchanger and heat storage capability, and can be modeled as a change in air constant from 1 to 1.45. In addition, high compression ratios in a non-isothermal process result in efficiency drop as shown in Figure 4-11. Therefore, choosing lower compression ratios has the priority over aiming to reach a high energy density at the beginning of the charging cycle in a CAES system when the reservoir is empty. For example, in a system with $n=1.4$, the compression efficiency of 73% can be obtained using pressure ratio of 3, while this efficiency will drop to 52% for a compression ratio of 10 as shown in Figure 4-11.

4.2.3 Energy Density of Pneumatic Storage System

The energy density of the storage system is a critical parameter, especially for applications with limited space allocation. The energy storage density (w) in kWh/m³ can be expressed by the following equation:

$$w = \frac{nNP_f}{3600(n-1)} \left(1 - \left(\frac{P_a}{P_f} \right)^{\frac{n-1}{nN}} \right) \quad (4-5)$$

where n is the polytropic coefficient, N is the number of stages, P_a is the atmospheric pressure and P_f is the final pressure. Figure 4-12 shows the variation of the pneumatic CAES storage energy density with changes in the number of energy conversion stages and working pressure.

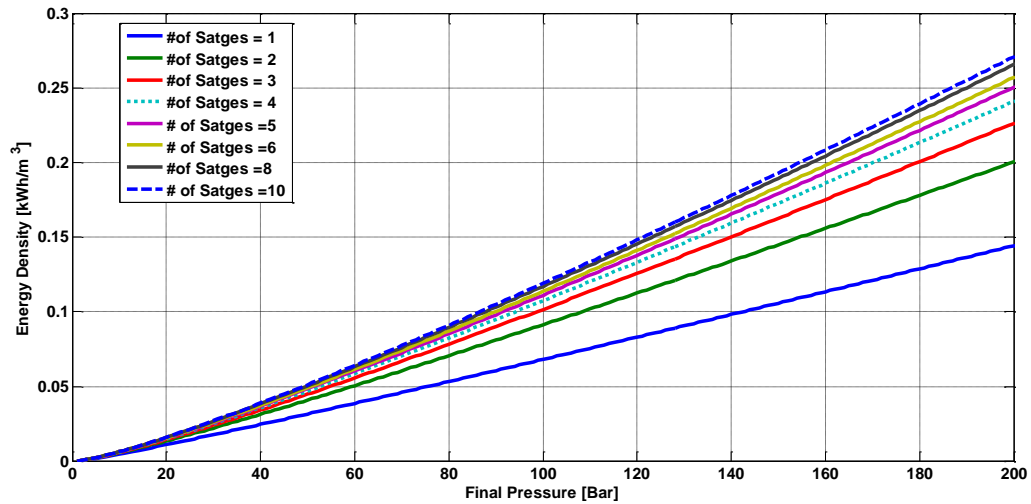


Figure 4-12: Variation of CASES energy density based on the number of stages and the storage pressure

It can be observed from Figure 4-12 that it is essential to increase the maximum pressure in the tank in order to increase the energy density of the storage system. In addition, increasing the number of stages can improve the energy density characteristics of the storage system. However the effect of increasing the number of stages on the energy density decreases for number of stages higher than 5. In order to highlight the impact of number of stages on the energy density, the energy density ratio of the results shown in Figure 4-12 is obtained by normalizing their values for each final pressure.

Figure 4-13 shows the energy density ratio variation as a function of number of stages for the worst case scenario at 200Bar final pressure, where there is the highest difference occurs between the system energy density with single stage and another one with 10 stages. As it shown in Figure 4-13, the energy density ratio for a four stage is 1.69, while this value for a 10 stage compression reaches 1.9 with cost of higher complexity including adding 3 more stages and controllers and as a result more investment to obtain only 0.21 more energy density ratio. This result should be considered in the general

design of a CAES system in order to define the optimum number of stages and its working pressure.

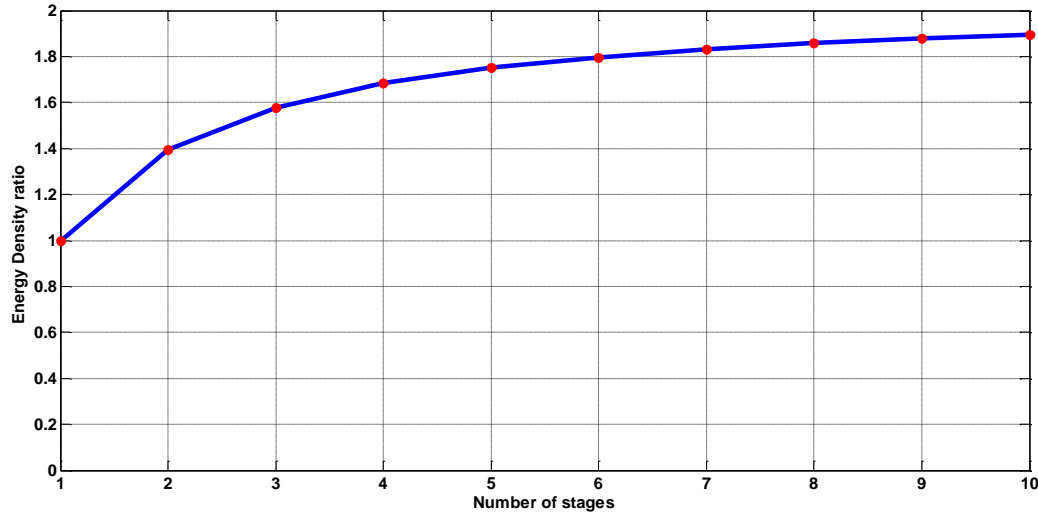


Figure 4-13: Energy density ratio variation as a function of number of stages.

4.3 Proposed criterion for energy storage capability assessment

When a typical storage system is charged to its nominal capacity, it is not possible to store more available excess energy from a wind farm. In this study, rejected energy is considered to be the amount of energy that a storage system could not harvest from a RES because of its limited capacity. In an isolated, this extra energy is usually applied to a dump load to maintain the power system stability. In a fully controlled wind farm the wind turbine blades are controlled in such a way that the energy production is limited to the load demand and power system stabilizer capacity. In other words, sometimes the energy system cannot extract the full capacity of available wind energy. This condition can be more significant when a large amount of energy is available in a short time duration as a result of high wind speed, and the storage system is not able to capture that energy due to either its limited storage capacity or low power rating. This phenomenon is

more critical when the frequency of wind speed fluctuation at the desired location is significant, and the high wind speed periods occurs in a short period of the time. As a result the storage system cannot extract the available excess energy and the total rejected energy becomes considerable.

Based on this logic, a performance index is proposed in this research to assess the capability of a storage system to extract as much of the available wind energy as possible in a given time period. This index is referred to as the Harvested Energy Index (HEI) and is expressed as the ratio of the total stored energy in a typical energy storage system to the total available excess wind energy during specific time scale:

$$HEI = \left(\int_0^{t_s} E_{stored}(t) dt \right) / \left(\int_0^{t_s} E_{excess}(t) dt \right) \quad (4-6)$$

where t_s is the total sample time, $E_{stored}(t_i)$ is the amount of stored energy at the time t_i and the $E_{excess}(t_i)$ is the amount of available excess energy. This new index has been introduced in consideration of the limited capacity of storage systems as a result of their physical limitation in energy conversion and storage. For example a battery cannot store more energy when it reaches its full charge, nor can a hydro storage system when the reservoir is full. On the other hand, in a CAES system air can be compressed to higher pressures during high excess energy regimes. This concept will be more attractive for locations that have non-uniform excess energy distribution during a given time scale (e.g. an hour time scale). In a non-uniform excess energy profile, the frequency of the high wind speed regimes is higher in a specific time duration while this frequency is low during the rest of the time. In this case the excess energy is available only for a short

duration of the time, and the storage system capability to capture this opportunity is critical in order to achieve high wind penetration.

To show the effect of the proposed performance index on the overall design of a wind based hybrid power system (HPS), the Harvested Energy Index (HEI) for different energy storage systems and different capacities is calculated. At the end, the analysis of the proposed HEI effectiveness is shown through a case study.

4.3.1 Using Harvested Energy Index for storage system sizing

One of the main challenges in a RES based HPS for a remote application is to design a storage system with proper sizing. Using equation (4-6), the harvested energy indices for different energy storage capacities can be calculated.

In order to show the impact of the proposed index in selecting the proper capacity for the storage system, a wind power profile and load demand for a single day based on Figure 4-14 is considered for the HEI calculation for different energy storage capacities.

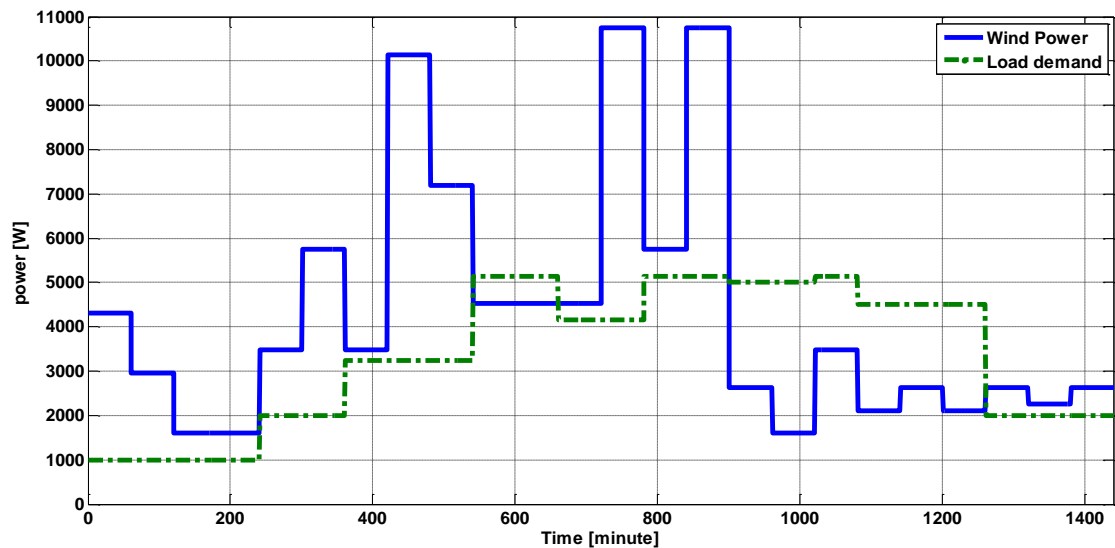


Figure 4-14: The wind power and demand power curve in minute time scale

Figure 4-15 compares the calculated HEI for different storage capacities.

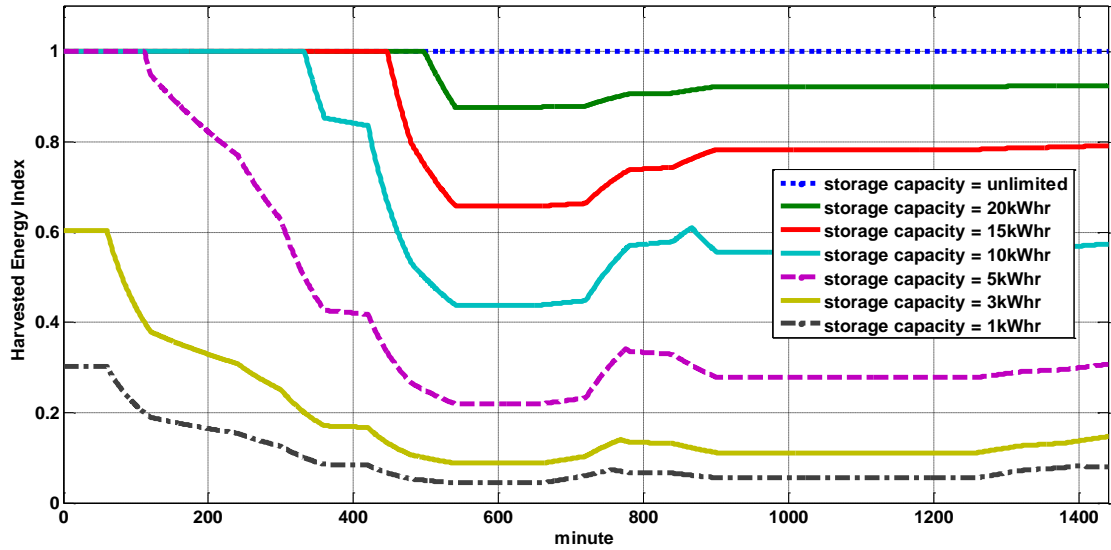


Figure 4-15: Harvested Energy index for different energy storage capacity

As shown in Figure 4-15, the storage system with lower capacities saturate faster in comparison with the systems with higher capacities. This behavior reveals the limitation of such systems in extracting available free wind energy which can improve the wind penetration profile of the HPS during the time duration in the case study. Among all the energy storage systems, the system with unlimited capacity is the only system that is able to harvest all the excess energy in the presented example. The corresponding HEI for such a system with 100% energy harvesting capability is shown in Figure 4-15 with a fixed value of 1. However, a storage system with unlimited storage capacity is not feasible, and compromise between the capital cost and the technical advantage of high capacity storage system should be established by the system designer. In this case study, all calculated indices are obtained by assuming that the energy conversion systems have the required power rating to convert the excess energy into the desired energy form.

As can be concluded from Figure 4-15, an energy storage system with limited energy storage capacity cannot benefit from the excess wind energy when it reaches its maximum capacity; and its HEI will decline from its maximum value. A CAES system capacity can be expandable using higher compression pressure considering the maximum permissible stress on the reservoir. The scalability characteristic of a CAES in light of HEI is one of the major advantages that the CAES system has over other types of the storage systems. Another advantage of the CAES system is its capability to work on series and parallel configuration. The CAES system compressors can be established in a configuration that with proper control valves they can operate in parallel mode at the beginning of the charging cycle when the tanks is empty, and work in series as multistage when the tank pressure reaches its predefined values.

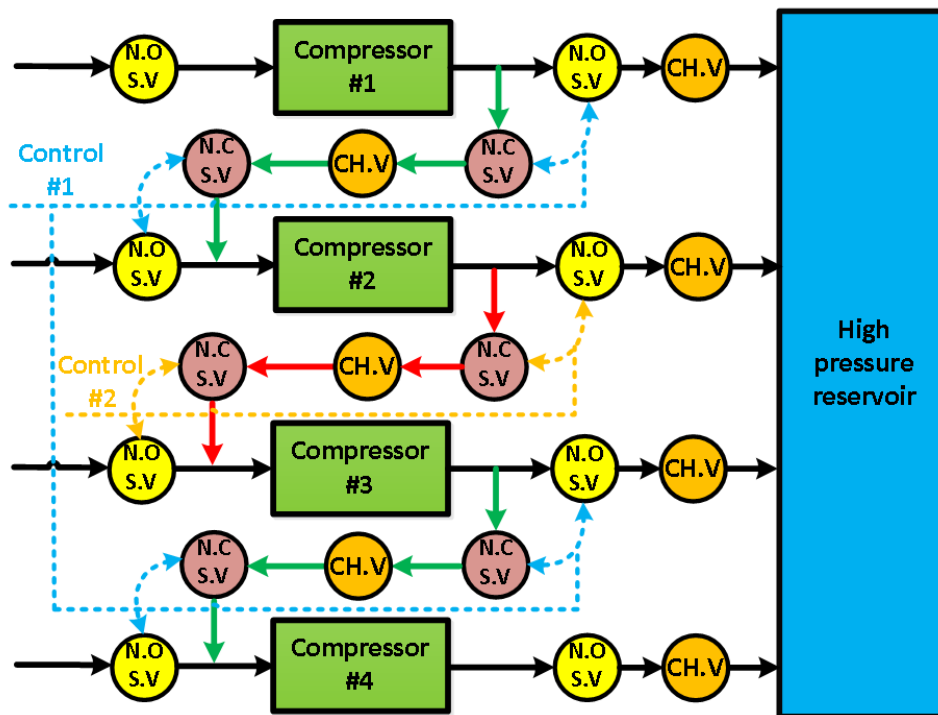


Figure 4-16: An example of compression system with capability of working in series/parallel configuration.

An example of such configuration is shown in Figure 4-16. This modification not only increases the storage efficiency, but also improves its energy harvesting capability, and makes it a unique alternative among all the energy storage technologies.

4.3.2 The HEI impact on the overall performance of a HPS in a case study

In order to investigate the effect of the HEI on the overall performance of an isolated HPS, the wind energy installation on Ramea Island in Newfoundland was considered as a case study. The wind speed at the wind farm during a day is applied to the modeled Bergey Excel-S 10 kW wind turbine and the load profile (Figure 4-14) of a single user is considered for modeling the variable load demand. In this case study, a CAES system was chosen because of its expandability characteristic.

The required power of the compressors is calculated by its work derivative with respect to time. All the working parameters of a compressor, except flow rate (Q), can be considered constant (assuming an efficient heat exchange with the environment). The power of the compressor can be obtained from:

$$P_{compressor} = (n/n-1) \cdot P_1 \cdot Q [PR^{(n-1/n)} - 1] \quad (4-7)$$

where PR is the ratio of the compressor output pressure to its input pressure (P_1). Assuming a polytropic process for both compression and expansion, the polytropic exponent of air for the compression process can be considered 1.45 for compression and 1.36 for expansion [49]. The pressure of the tank will increase depending on the air mass (m) entering to the reservoir based on (4-8), where the change in air mass during a limited time can be calculated using (4-9):

$$P.V^n=(m_0+ \Delta m) RT \quad (4-8)$$

$$\Delta m=\rho.fQ.dt \quad (4-9)$$

where R is the gas constant, m_0 is the available air mass in the tank, and T is the working air temperature. The change of the compressed air stored in the reservoir can be calculated and it depends on the available power for the high pressure compressor. The change in stored energy is formulated using (4-7) to (4-9). The available wind power output defines the working condition of the other components of the hybrid power system. Based on this value, the following scenarios were considered for the HPS:

A. The charging cycle: This condition happens when the output power of the wind turbine is more than the load, and the storage system has available storage capacity. In this condition, the excess power is applied to the compressor and the output flow rate of the compressor is calculated using (4-7). The total air mass that enters the high pressure tank can be obtained using (4-9), and the tank pressure can be obtained using (4-8). The tank pressure will continue to increase as long as excess power is available and the tank pressure is lower than its nominal value.

B. The rejection cycle: In this cycle, the energy storage is charged to its maximum capacity and any additional energy cannot be stored. Considering the fixed blade configuration for the wind turbine, this rejected energy will be consumed by the dump load in order to maintain the system stability.

C. The discharge cycle: The storage system starts to deliver power to the load, when the output power of the wind turbine is not sufficient to meet the demand. This cycle will be terminated when the storage system is fully discharged or the wind

speed increases and the wind turbine output power is sufficient to meet the load demand.

D. The shortage cycle: At this situation, the total power of the wind turbine and storage system is less than the required power for the load and the stored energy is not sufficient. The diesel generator will operate in this mode in order to compensate for the wind turbine output power. The fuel consumption of the diesel generator during this cycle can be calculated by using its power-fuel consumption equation.

In this study, a four stroke Yanmar Powered 6.5 kW diesel generator was chosen and its power-fuel consumption curve is provided as (3-82). The tank volume was considered 6.06 m^3 in order to store 5 kWhr at 16 bar working pressure. This value was chosen based on the obtained HEI for different energy storage capacities shown in Figure 4-15. As seen in this figure, the system with the 5 kWhr capacity is the first storage system which can reach 100 percent HEI, and has a capacity close to the maximum load. The working pressure of 16 bar was chosen for the base working pressure of the system by considering 4 stage compression shown in Figure 4-16 assuming that each compressor has a compression ratio of two. As previously shown, this selection has reasonable energy density (Figure 4-12) and efficiency (Figure 3-9b). It was assumed that the compressor unit has the ability to change its configuration to reach the required flow rate and the working pressure. This assumption was made in order to assess the impact of the working pressure on the performance of the HPS. In practice, a system with working pressure of 3,

9, 27, 81 can be obtained using the 4-stage compression and compression ratio of 3 for each stage to reach higher energy densities.

4.3.2.1 Determination of the HEI for the case study

In order to show the importance of considering the HEI concept in an energy storage system design and control strategy development, and based on the proposed procedure, in each time step (one minute in this study) excess energy, stored energy, change in the tank pressure, rejected energy, delivered energy and the shortage energy is calculated. The excess energy and the stored energy is used in (4-6) to calculate the HEI value for each time step. The shortage power is provided by the diesel generator, and its value in each time step determines the diesel fuel consumption.

Figure 4-17 shows the calculated HEI for a CAES system at different working pressures. The HEI index for each working pressure increases when the storage system is able to capture the excess energy of the wind. This corresponds to the increment of the nominator value in (4-6). On the other hand, the HEI value will decline when the storage system has reached its saturation capacity and available excess energy on the wind turbine is rejected and applied to the system dump load. This situation corresponds to an increase in the denominator in (4-6) while its denominator is constant.

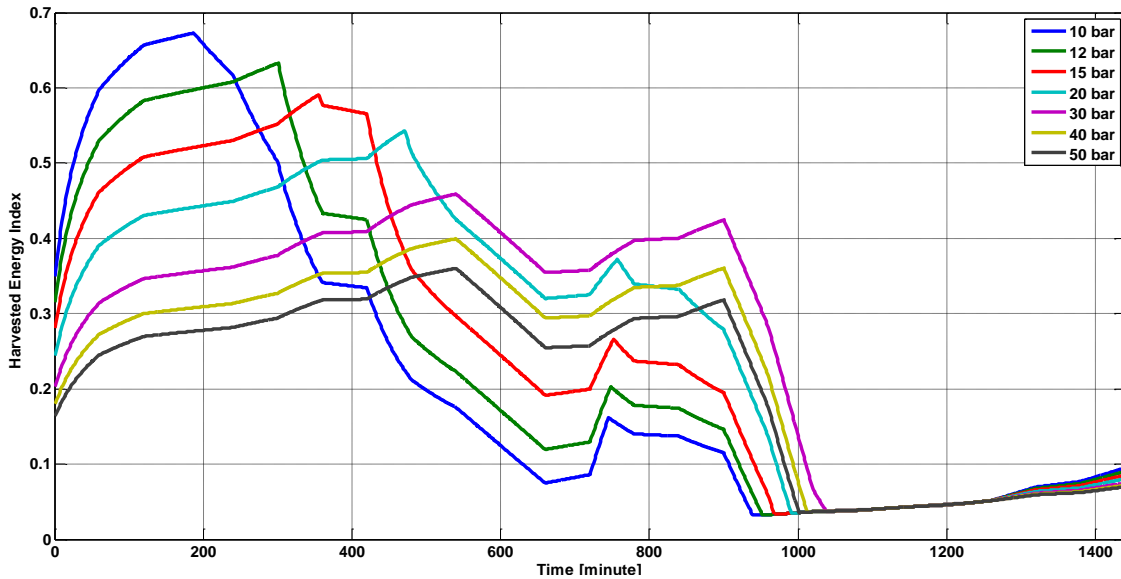


Figure 4-17: The calculated harvested energy index at different working pressures.

As seen in Figure 4-17, at the beginning of a charging cycle, the energy storage systems with low working pressure are able to reach higher HEI index in comparison with systems with higher working pressure. On the other hand, these low working pressure systems saturate faster, and the decline in their HEI values occurs earlier in comparison to high pressure systems. As an example, the CAES system working at a fixed 10 pressure ratio can reach the maximum HEI of 68% at time=187 minute, while this index will be 28% for a system working with a fixed 50 pressure ratio. On the other hand, the HEI value for a fixed 10 pressure ratio drops to 18% when a system with a fixed 50 pressure ratio reaches its maximum value (35%). In other words, at the beginning of a charging cycle, the system can harvest approximately twice the energy when it works at 10 bar in comparison to 50 bar, while this performance will be reversed at the end of the charging cycle where the higher pressure systems exhibit significant better performance in comparison to the systems with low working pressures.

4.3.2.2 Control strategy based on tracking the maximum HEI

Considering the proposed HEI and obtained results shown in Figure 4-17, an optimum control strategy based on the maximum HEI can be developed to increase the amount of stored wind energy. This control scheme goal is to maximize the HEI value by increasing the working pressure of the compressors, when storage system reaches its saturation point. As it is shown in Figure 4-17, the HEI starts to decline (shown by blue arrow in Figure 4-17) when the stored air pressure in the tanks reaches its preset nominal value while there is excess available energy. To store more energy, the working pressure of the compressors can be increased either by gradual increment in fixed steps or change in series-parallel configuration of the compressor connections to achieve high pressure ratios. This method is referred as maximum HEI tracking control. By increasing the compression pressure, the slope of the HEI curve will change from negative value to a positive value as it is shown by black arrows in Figure 4-18.

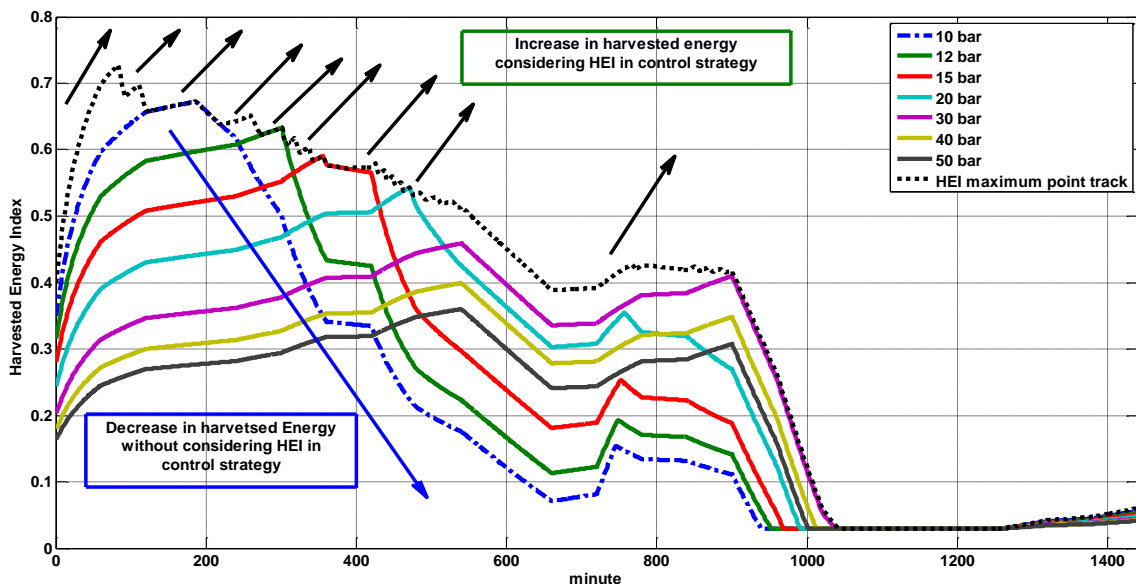


Figure 4-18: The HEI at different working pressures and their maximum HEI point track.

The resultant HEI maximum point track is shown in Figure 4-18 for a compression system capable of having continues increment in its compression pressure. Considering the fact that such a system is not feasible in practice, a modified system in proposed in the next section.

4.3.2.3 Proposed compression configuration to maximize HEI

Using suitable control approach and system configuration results in an increase in the electrical generation capability and penetration of the installed equipment, and add to financial benefits from specific amount of investment for a hybrid system. Considering the results obtained from HEI calculation, a possible configuration of the CAES system is proposed as shown in Figure 4-19.

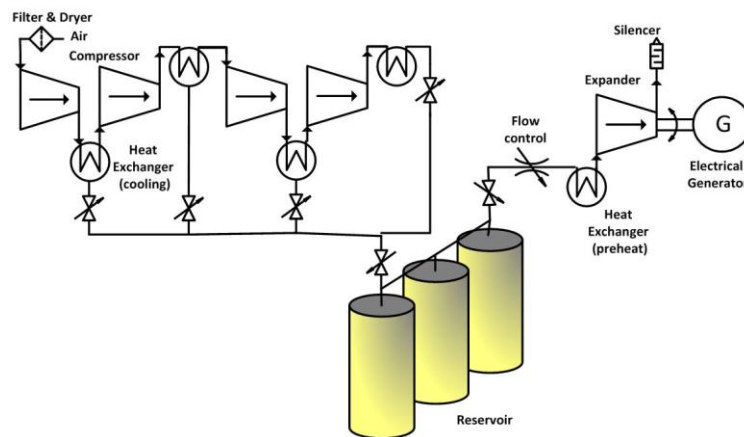


Figure 4-19: A 4-stage design of the CAES system based on harvested energy index

A four-stage compression has been chosen in this configuration by considering results obtained from Figure 3-9(b) and Figure 4-13. According to Figure 4-13, increasing the number of stages does not significantly impact on the energy density, and efficiency of 61.5 % can be obtained from a 4-stage configuration with less complexity and equipment in comparison to a 10-stage unit.

At the beginning of the storage cycle, the compressors can work in parallel mode with small pressure ratios to increase the storage speed and flow rate into the reservoir. Based on the pressure increment in the tank, the compressors can be switched to a series-parallel combination to increase the compression ratios. The working pressure of the compressor will change when the reservoir is fully charged to the optimum pressure based on the maximum HEI. This adjustable configuration of the multistage compressors enables the storage cycle to operate in variable capacity condition to increase the HEI. Compressing a certain amount of air to a high pressure can be done using gradually increasing working pressure to achieve an efficient energy conversion process. It takes less energy and time to compress air at low pressures compared to high pressures. Based on this, it is suggested to store energy in reservoirs at low pressure and gradually increase the working pressure of the compressors.

4.3.2.4 Average value of the HEI for the case study

An average daily HEI value for different working pressures can be calculated by integrating their stored energy during a day and dividing by the total available excess energy during the same day, which is identical to the area under their HEI curve in Figure 4-17. Figure 4-20, shows the average HEI variation as a function of different working pressures for a single day. The area was calculated only for the time duration with excess energy to concentrate on the harvesting capability of the system when it is available. Therefore, the integration was excluded during the shortage cycle.

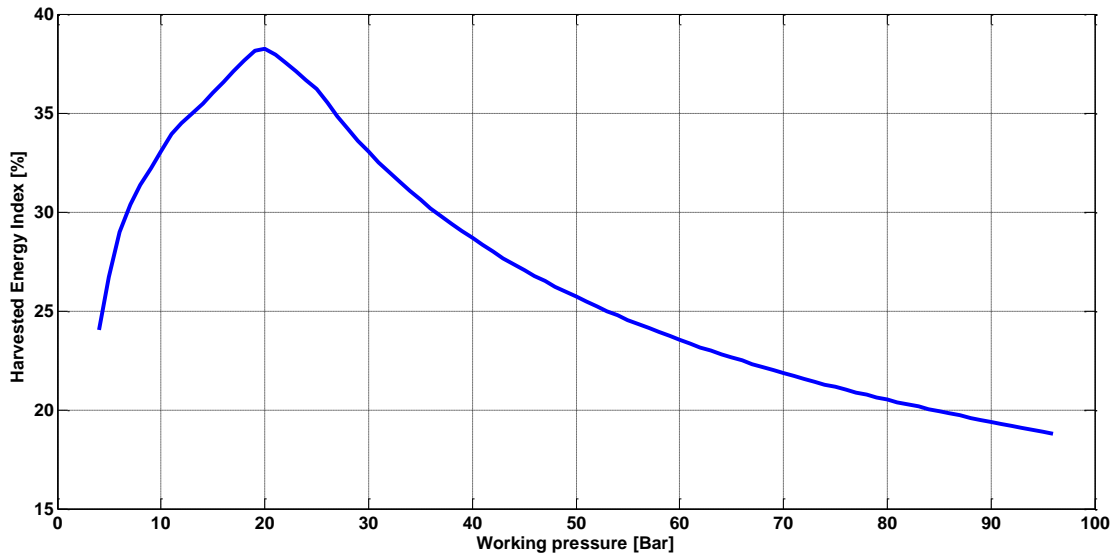


Figure 4-20: Change in average HEI in a day time scale considering only constant working pressure for the compressor

In Figure 4-20, the working pressure of each compressor was assumed to be constant as a result of not including the HEI in the control strategy. In order to compare the result with system with maximum HEI tracking algorithm, the calculated average HEI value of various systems are shown in Figure 4-21.

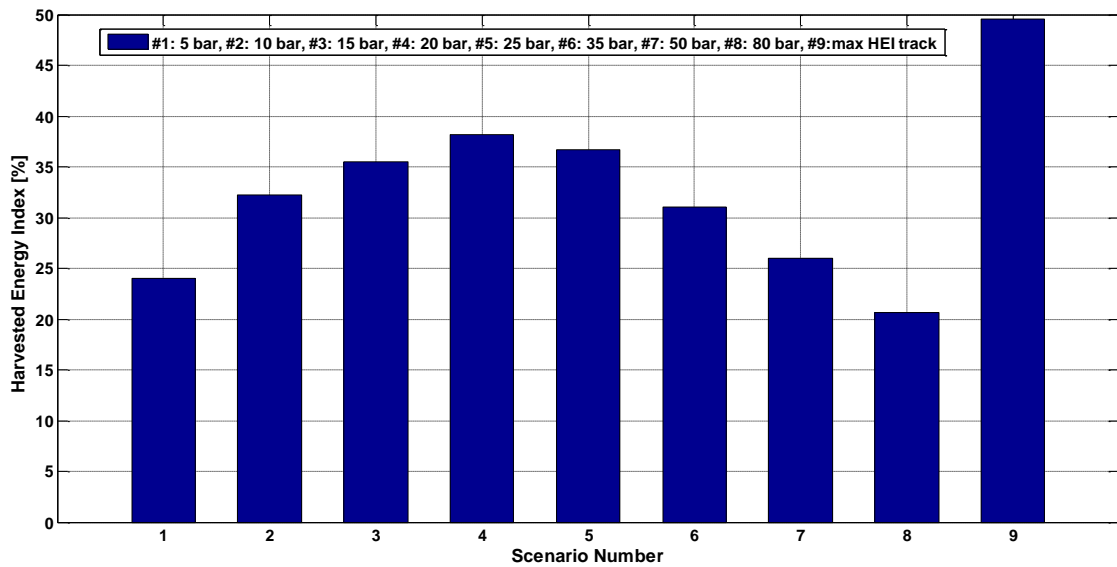


Figure 4-21: The maximum HEI point track of a continuous compression system in comparison with various fixed pressure compression systems.

As shown in Figure 4-20, a very high working pressure such as 90 bar can only harvest 18% of available excess energy during a day while the maximum value for the average HEI, which is 38.13 %, can be obtained at a fixed working pressure of 20 bar. On the other hand considering the HEI maximum tracking point control scheme in the compressor operation, its average daily HEI can reach up to 49.52% as shown in Figure 4-21 using the same calculation procedure. This result is more significant considering the low average HEI for very low or high working pressure with a fixed value, which results in less than 15% harvested energy from available excess wind energy.

4.3.2.5 Impact of the maximum tracking HEI control strategy on the fuel consumption of the diesel generator

In order to show the effectiveness of the proposed control method, the utilization impact of such a control strategy on the fuel consumption of the diesel generator is investigated. In this assessment, systems with different set of constant working pressures are compared to two systems with controllable working pressures based on the HEI concept. For the first control strategy based on the proposed maximum HEI tracking control strategy, the working pressure of the compressor is increased in 25 steps of 2 bar to the final working pressure of 50 bar. Although this control strategy increases the accuracy of the maximum HEI tracking, its complexity and cost might result in an impractical option for the control strategy. Therefore a 4-stage compression unit with controllable valve is considered a practical option for the HEI implementation. The second system has a 4-stage configuration with compression ratio of 3 for each stage.

Thus when each stage reaches the maximum working pressure of $3n$, it is connected to the previous compressor. Figure 4-22 shows the change in the tank pressure of the HPS with different working pressures for the compression system.

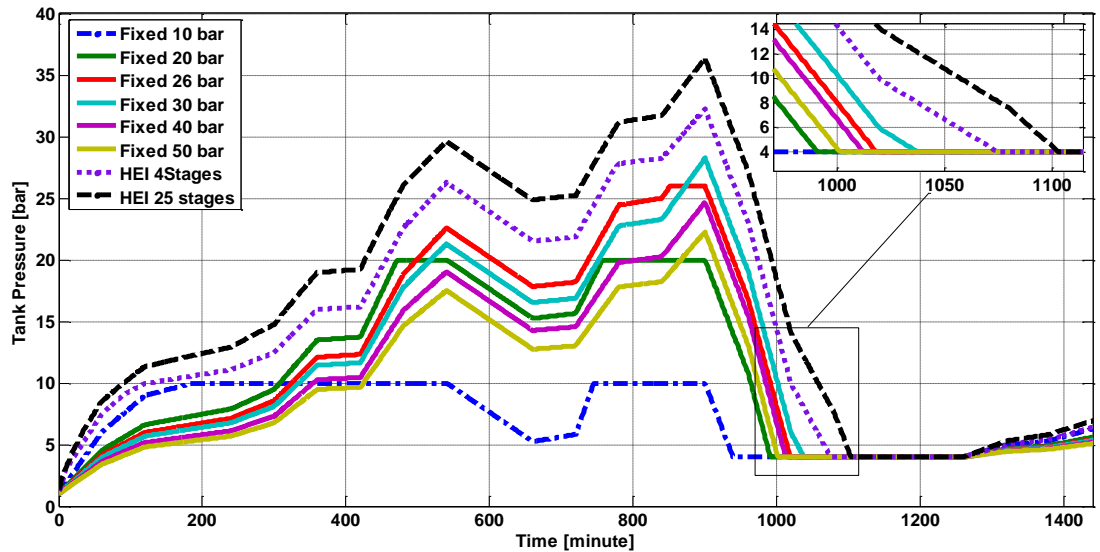


Figure 4-22: The tank pressure variation in different compression control strategies.

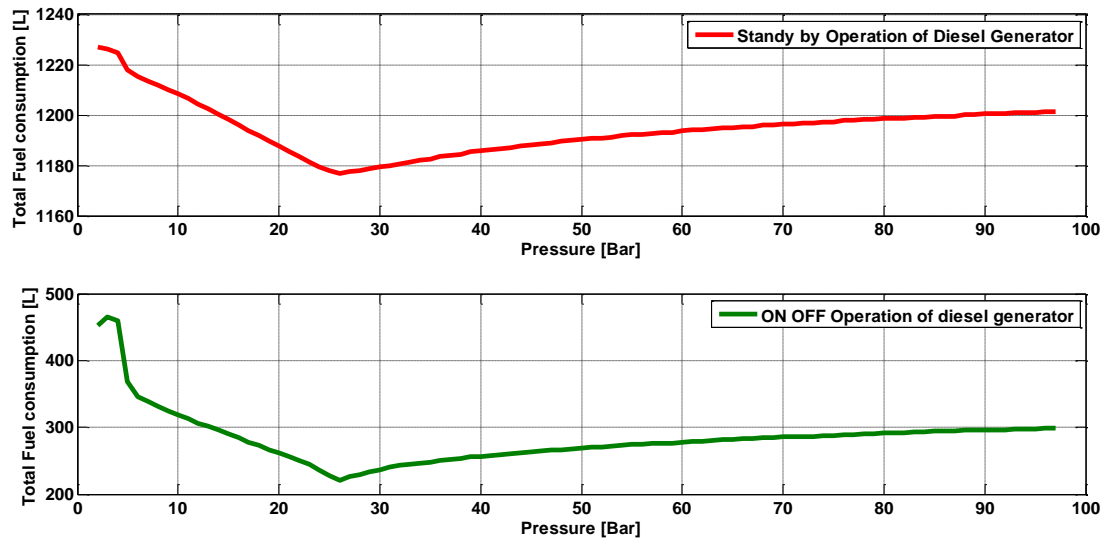
As seen in Figure 4-22, the HPS system with low compression ratios reaches its nominal working pressure faster than the higher working pressures, but it is unable to capture more wind energy. In the proposed case study, this condition occurs when the tank pressure profile maintain a constant value as shown in Figure 4-22 for a 10 bar and a 20 bar constant working pressure. Considering Figure 4-22, the HPS controlled with the proposed control strategy has higher tank pressure, and consequently higher stored energy in comparison to the systems working with fixed working pressures.

Using the proposed control strategy in the presented case study, the diesel generator (DG) operates in less time duration as it is shown in Figure 4-22, when the tank pressure reaches 4 bar. The total shortage duration in different compression control strategies is obtained from Figure 4-22 and listed in Table 4-2.

Table 4-2: The total shortage duration in different compression control strategies

Control method	Fixed 10 bar	Fixed 26 bar	HEI in 25 stages	HEI in 4 stages
Shortage Duration	326 [min]	225 [min]	163 [min]	192 [min]

The diesel generator (DG) fuel consumption in its backup mode can be calculated by applying the provided power by DG to its fuel consumption equation (3-82). Two scenarios were assumed for the diesel generator operation modes. For the first scenario, the DG operates in On-Off mode, and it will start only in shortage mode. In this scenario, it is assumed that the storage system control is fast enough and properly tuned to turn the diesel generator on. On the other hand, the second scenario assumes a standby mode of operation, and the diesel will be online during the shortage cycles and will work in no-load mode for the rest of the cycles. The total fuel consumption of the diesel generator in the standby and On-Off mode is compared in Figure 4-23.

**Figure 4-23: The DG fuel consumption in Standby and On-Off mode of operations.**

As shown in Figure 4-23, the On-Off mode of operation exhibits less fuel consumption for all the working pressures in comparison with the fuel consumption in standby mode of

operation. This big difference is related to the no load fuel consumption presented in (3-82). Although, the standby operation of the diesel generator provides a more reliable backup for the HPS, its fuel consumption is much higher than the diesel generator with an On-Off mode of operation. Therefore, the On-Off mode of operation is suitable for the HPS in an isolated application where benefits from high wind profile, where a storage system with the next commercially available storage size can be used to harvest more excess energy. On the other hand, the standby operation is preferred in locations with low wind speed profile and considerable fluctuations. In both modes a system with a fixed working pressure of 26 bar has the minimum fuel consumption. The total fuel consumption of the HPS based on the proposed control strategies are compared in Figure 4-24.

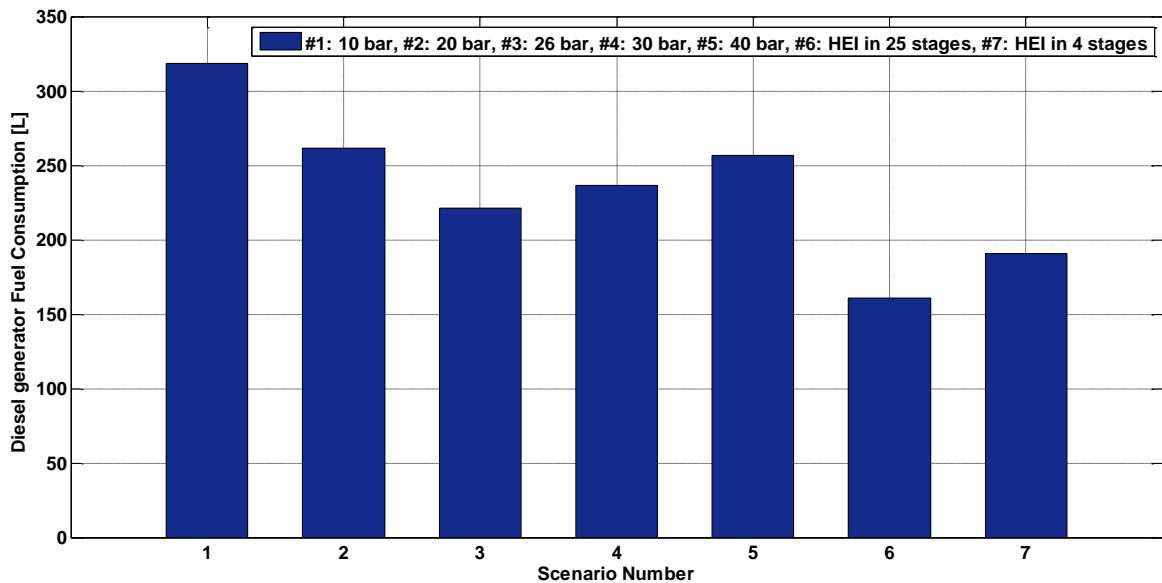


Figure 4-24: The DG fuel consumption comparison in different compression control strategies.

As shown in Figure 4-24, the total fuel consumption of the system is reduced to 161 Liters using the proposed the HEI index in compression pressure control. The minimum

value of the fuel consumption for the system with fixed working pressure is 221 Liters and belongs to a fixed 26 bar working condition. As a result of applying the HEI control strategy to a 4-stage compression unit, and performing a variable working pressure control instead of a fixed one, the total fuel consumption of 191 Liters is achievable in a practical configuration of the HEI implementation.

4.3.3 Harvested Energy Index calculation in different storage technologies

The energy storage capacity of each storage system can be calculated using a steady state representation of the energy conversion procedure. Based on their energy conversion process, three main categories of energy storage technologies are considered: Batteries, Pumped Hydro and CAES. These energy storage technologies have been chosen in this study in order to compare their performance based on the proposed HEI. In order to compare their energy storage capability, the required equations to describe the storage behavior of each energy storage system will be provided in the following subsections.

These energy equations assemble all the limiting parameters in each energy storage technology. Considering the energy capacity of each energy storage technology, it can be concluded that each storage system has physical limitations on the maximum storage capacity. For example, the volume of the reservoir in a pumped hydro system or CAES system is limited. This maximum capacity can be considered as a criterion for storage capability assessment of energy storage technologies, which is critical in a wind based energy system. Consequently, this constraint on energy storage capacity is the core focus

of this study in the evaluation of the performance of the selected energy storage technologies.

The load power over one year period that is generated based on the methodology described in section 3.4 is compared to the generated power of the wind speed profile that is obtained based on Monte-Carlo methodology in 4.1.2, and the resultant power balance curve is generated for each seconds. The resultant power balance characteristic for a one year period with 1s resolution is shown in Figure 4-25, and its first day curve is shown in Figure 4-26. Then this resultant power as available excess power is applied to the different energy storage systems with different storage capacities in the next subsections to evaluate their performance in capturing the available excess power.

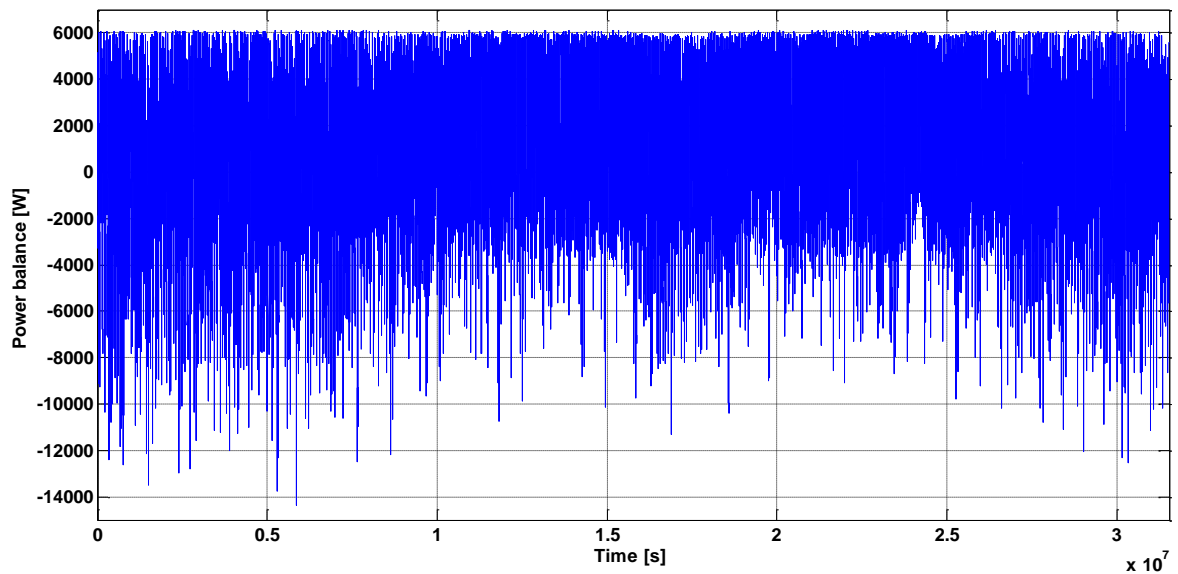


Figure 4-25: The resultant power balance curve for a one year period.

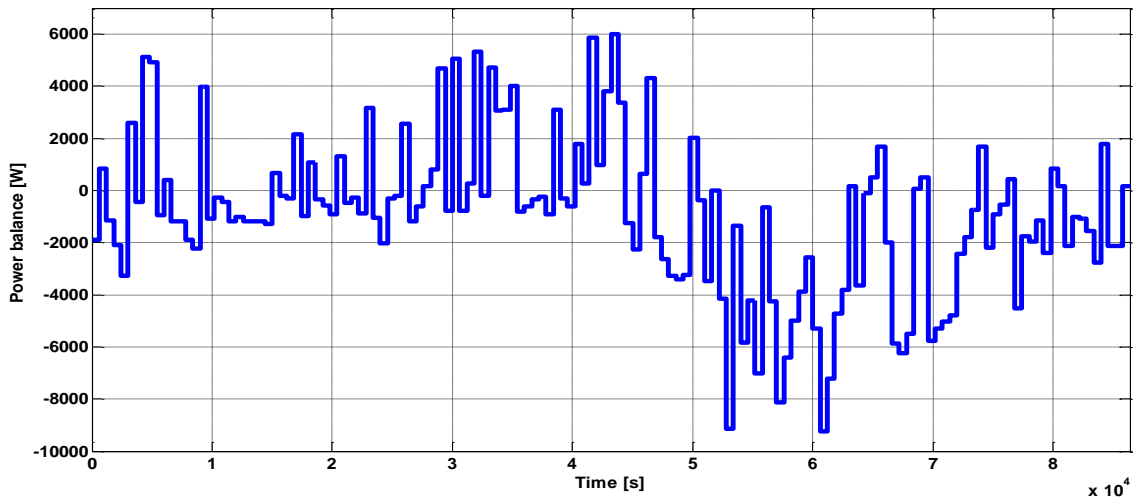


Figure 4-26: The resultant power balance characteristic for the first day.

4.3.3.1 Harvested Energy Index for Battery storage systems

The energy capacity of a battery is usually defined based on the product of the cell voltage and its nominal discharge current rate known as ampere-hours (Ahr), which is provided by the manufacturer. The charge and discharge characteristics of a battery can be examined utilizing a mathematical model. A comprehensive model of a typical battery comprises three sub-models: a thermal sub-model to represent the electrolyte temperature based on the thermal properties of the material and battery losses; the charge and capacity model to depict the state of the charge (SOC) and depth of discharge current (DOC); and an equivalent circuit to simulate the dynamic performance of the battery [152]. Although utilizing this model results in an accurate battery model, it requires a large number of parameters, for which obtaining their exact value can be a complicated and time consuming procedure. On the other hand, a generic battery model that represents a battery's performance during charging and discharging procedures can be satisfactory, and this only requires steady state analysis [153]. As a general description, its terminal

voltage can be approximated by an exponential mathematical equation as follows [153], [154]:

$$E = E_0 - K \left(\frac{Q_{rated}}{Q_{rated} - Q_{exchanged}} \right) + Ae^{-BQ_{exchanged}} \quad (4-10)$$

where E_0 is the battery constant voltage in Volts; K is the battery polarization voltage in Volts; Q_{rated} is the battery capacity in Ah; exponential zone amplitude (V); exponential zone time constant inverse $(Ah)^{-1}$. These parameters can be directly obtained from the manufacturer's datasheet. The exchanged electrical charges during charge and discharge cycles can be obtained by integrating its current.

$$Q_{exchanged} = \int idt \quad (4-11)$$

The battery capacity can be considered steady during the discharge hours by neglecting the effect of temperature on the discharge and output voltage characteristics. The battery voltage variation for several load currents is shown in Figure 4-27.

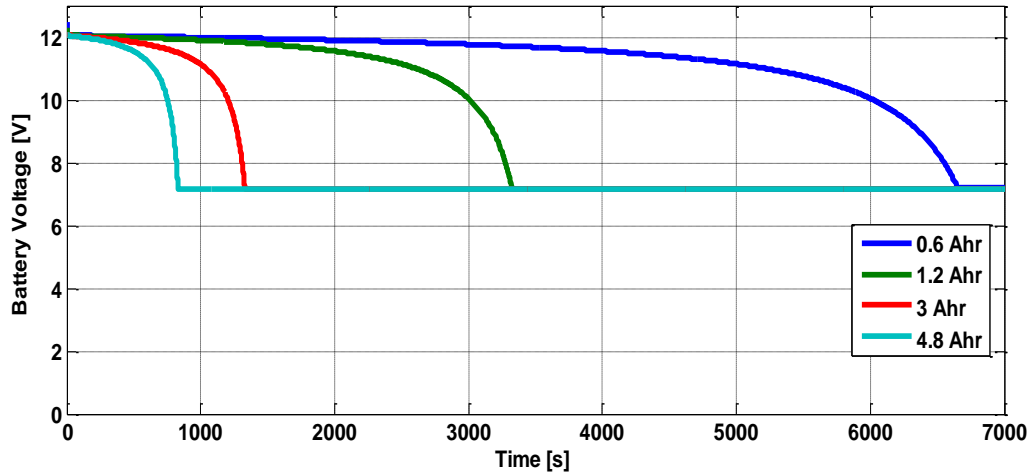


Figure 4-27: The battery voltage variation to several load currents

After applying the power balance of the system (Figure 4-25), the performance of the battery based energy storage system with different storage capacity was investigated by

calculating the HEI for each storage capacity. In this study, the energy conversion efficiency for battery storage system is assumed 99.5%, and the battery storage capacity was changed from 1kWhr to 10kWhr. Considering the nominal grid voltage as 120 volts, each battery column includes 10 batteries, and the required Ahr of the storage system can be obtained by using parallel set of battery columns. The depth of discharge (DOD) for the battery was assumed 30% to have reasonable life time for batteries. Figure 4-28 shows the change in the battery state of the charge (SOC) during the first day for a storage capacity of 1kWhr. As shown in Figure 4-28, for the 1kWhr system, the SOC rapidly drops to its minimum value due to low power rating and the system cannot deliver the required power. Using the same approach, the SOC for several storage capacities during four consecutive days is simulated and illustrated in Figure 4-29.

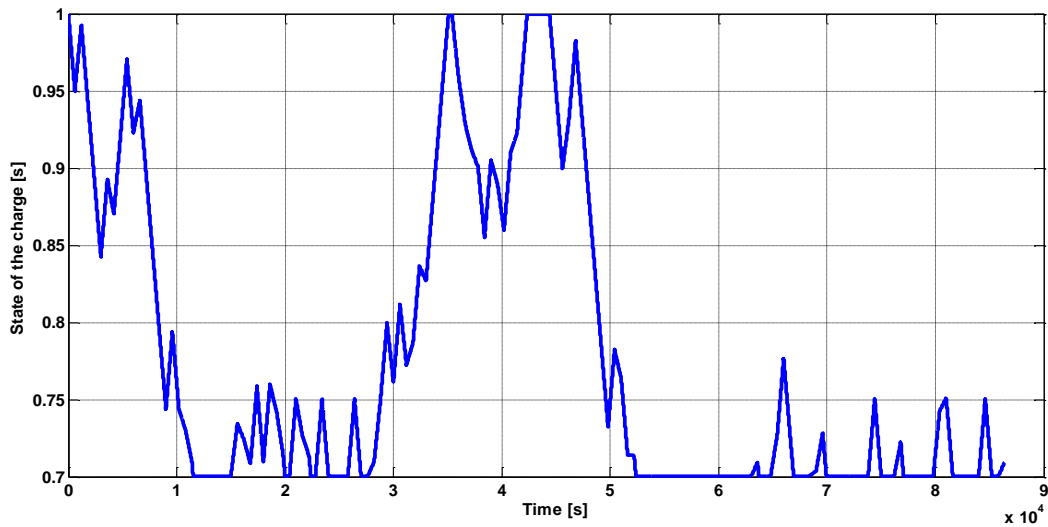


Figure 4-28: The change in the state of the charge of 1kWhr system during the first day

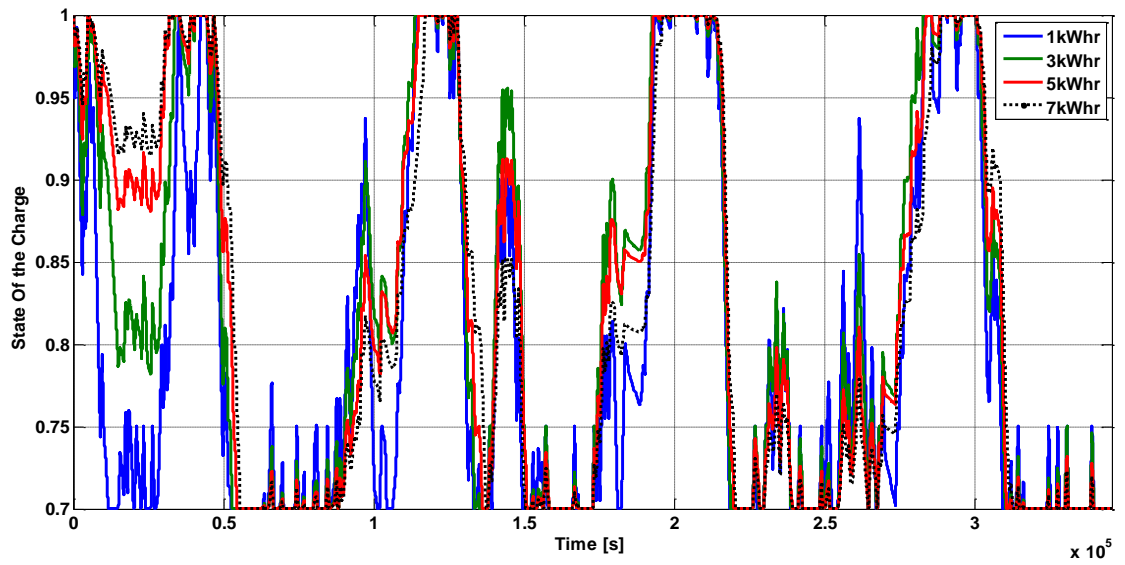


Figure 4-29: The SOC for several storage capacities during 4 consecutive days.

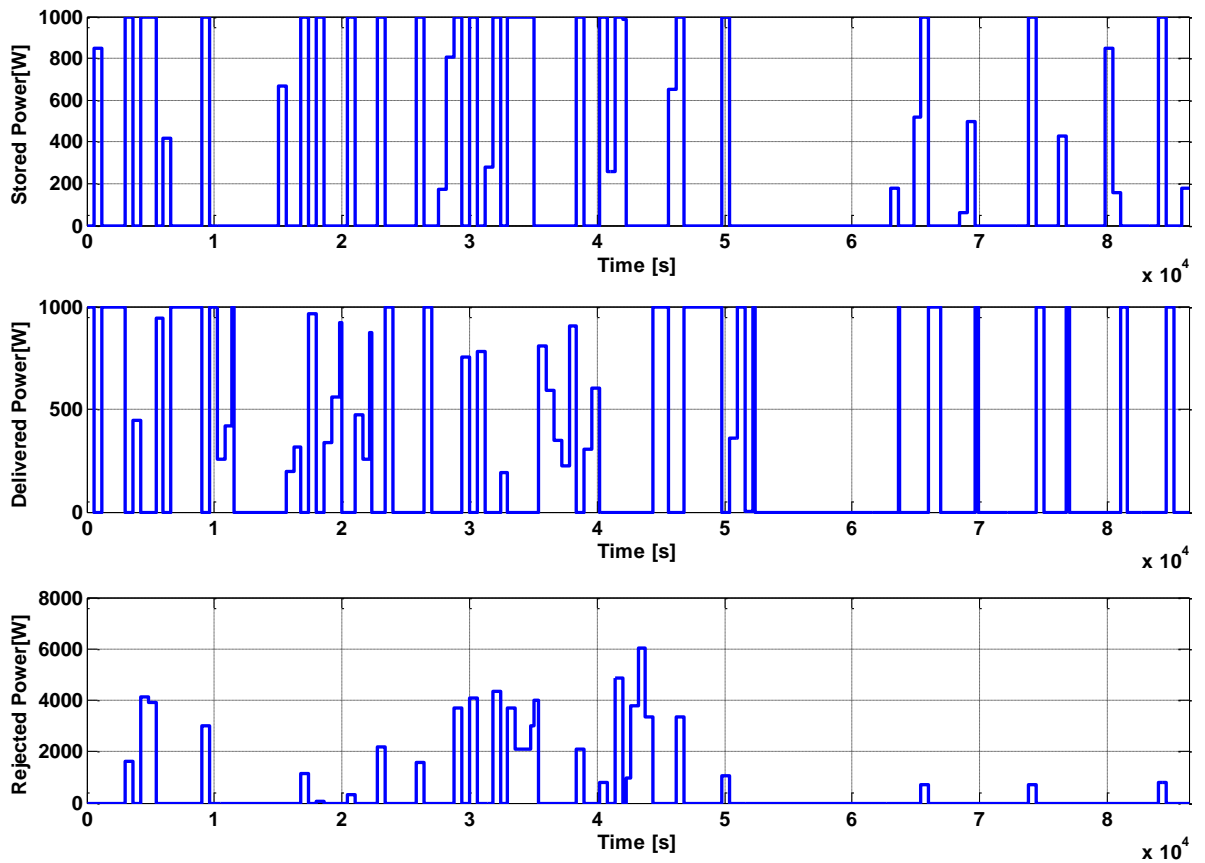


Figure 4-30: The stored power, the delivered and the rejected power profile for the 1kWhr storage system during the first day

Figure 4-30 shows the stored power, the delivered power and the rejected power profile for the battery storage system with 1kWhr capacity at the first day respectively. When the system reach its maximum storage capacity the excess energy cannot be stored, and it will be rejected.

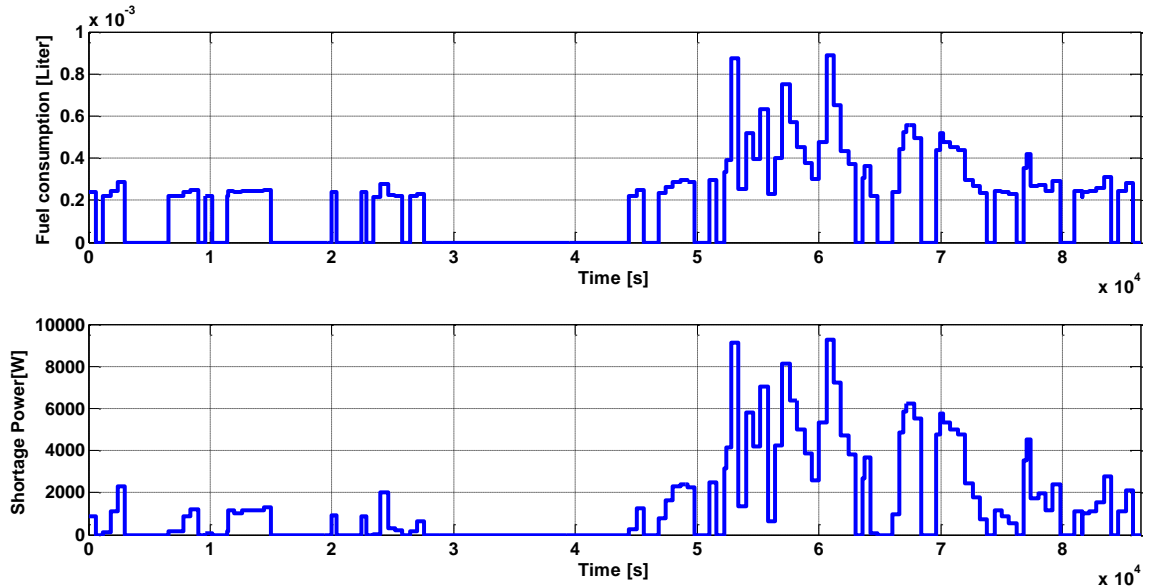


Figure 4-31: The fuel consumption and the shortage power profile for the 1kWhr storage system during the first day

The shortage power will be provided by the diesel generator (DG), and it happens when the total energy of the wind turbine and the remaining energy in the storage system is not sufficient to meet the load demand. Applying the shortage power to the fuel consumption profile of the diesel generator and considering ON-Off operation mode for the diesel generator, the fuel consumption profile of the DG can be obtained. Figure 4-31, shows the shortage power and the fuel consumption profile during the first day for a 1kWhr system.

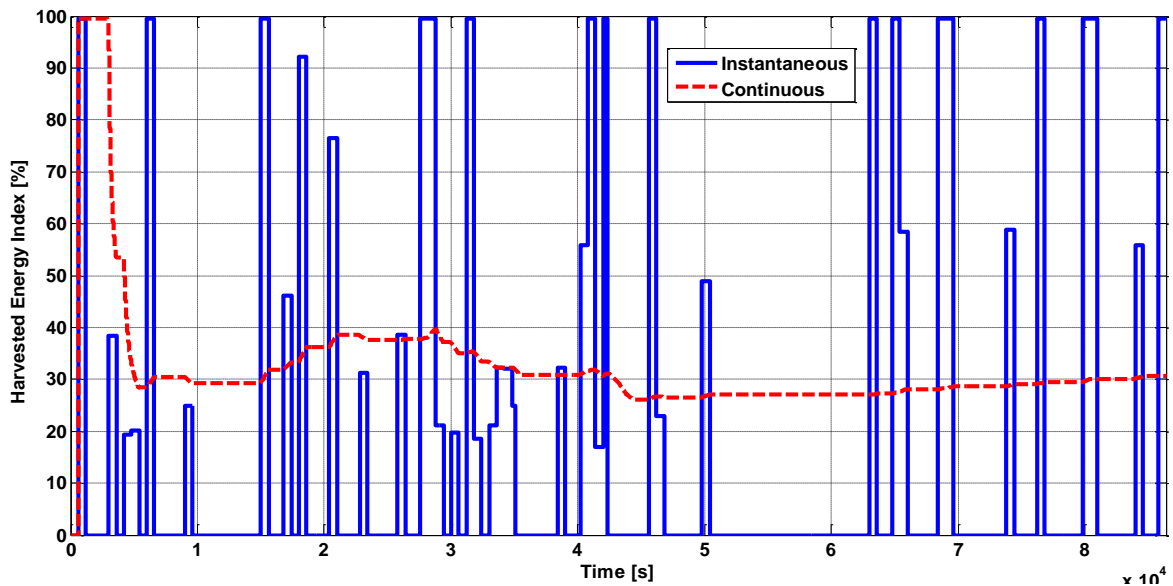


Figure 4-32: The instantaneous VS continuous HEI for the 1kWhr storage system during the first day

The instantaneous harvested energy index (IHEI) can be defined as the stored energy to available excess energy at time t_s , and the continuous harvested energy index (CHEI) can be described as the ratio of the total amount of the stored energy to the total available excess energy for a defined time duration. The CHEI value can be obtained by integrating the IHEI over required time duration. The IHEI shows the performance of the storage system in capturing energy on instantaneous basis and is useful for dynamic control of the system; while, the CHEI provides an overall perspective of the storage system for a longer time scale, which is more valuable in system design. Figure 4-32, shows the IHEI and the CHEI for the battery energy storage system at the first day. The storage system cannot capture energy when the system is full or the excess energy is not available.

In order to obtain the annual HEI value, the daily averaged CHEI can be calculated by averaging the value of the CHEI during a day. Figure 4-33, compares the annual HEI for different energy storage capacities.

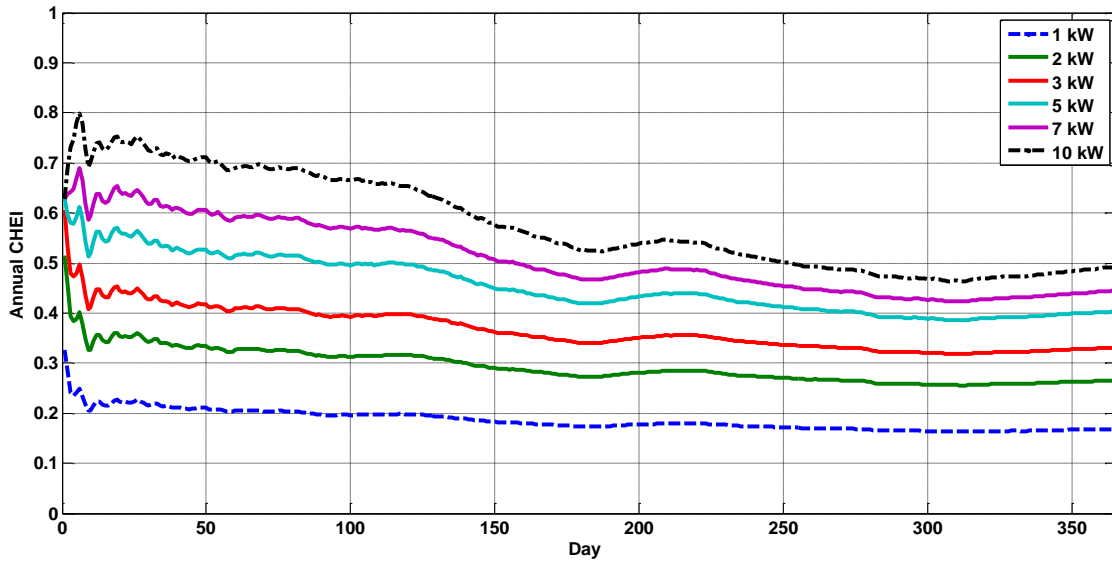


Figure 4-33: The annual HEI for battery storage systems with different storage capacities

In order to show the impact of the storage capacity of the battery storage system on the overall hybrid power system performance, the total fuel consumption of each storage system with different power rating is shown in Figure 4-34. As shown in Figure 4-34, the total fuel consumption can be reduced by increasing their power rating.

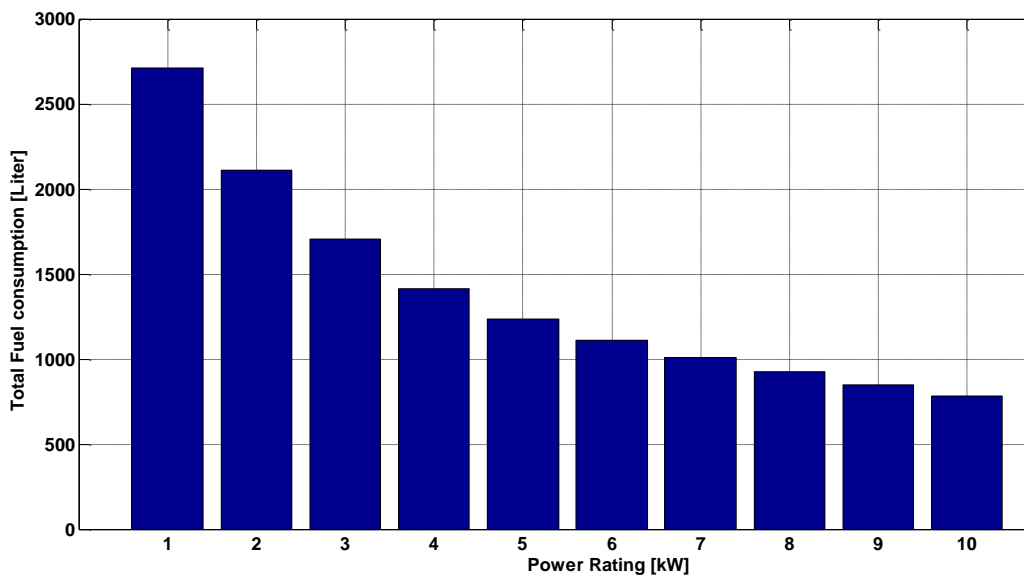


Figure 4-34: Total annual fuel consumption in battery based energy storage systems with different power rating.

4.3.3.2 Harvested Energy Index for Pumped hydro energy storage system

The pumped hydro energy storage system includes a pump-turbine, a higher reservoir and a lower reservoir. During low load demand periods, the excess energy from the wind farm is applied to pump water to a higher reservoir. The stored water will be released to a lower reservoir while the stored energy is delivered to the customers utilizing the hydro turbine. The mass power output of a pumped hydro energy storage system can be determined by the stored potential power in its reservoir using the following equation [151]:

$$P = \rho g Q H \eta_p \quad (4-12)$$

where ρ is density of water in kg/m³, g is the acceleration due to gravity in m/s², Q is the discharge through the turbines in m³/s, H is the effective head in meter and η_p is the efficiency of the pump. The delivered energy of a pumped hydro storage system can be determined by the product of the output power obtained in (4-12) and the time duration. The pump-turbine efficiency is assumed to be 90% in this study. The capacity of the pumped hydro is adjusted based on its power rating by changing the reservoir volume and the corresponding nominal flow rate of the pumped hydro storage system. Using similar power balance data (Figure 4-25), the performance of the pumped hydro storage system with different storage capacities is assessed. Figure 4-35, shows the annual HEI for the pumped hydro storage systems with different storage capacities. The fuel consumption of several pumped hydro energy storage system with different storage capacities is shown and compared in Figure 4-36.

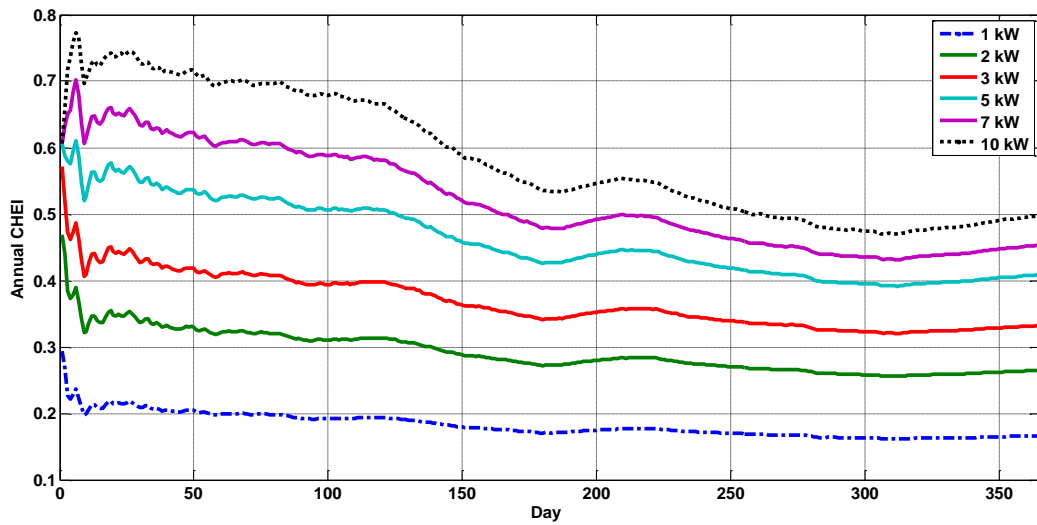


Figure 4-35: The annual HEI for pumped hydro storage system with different storage capacities.

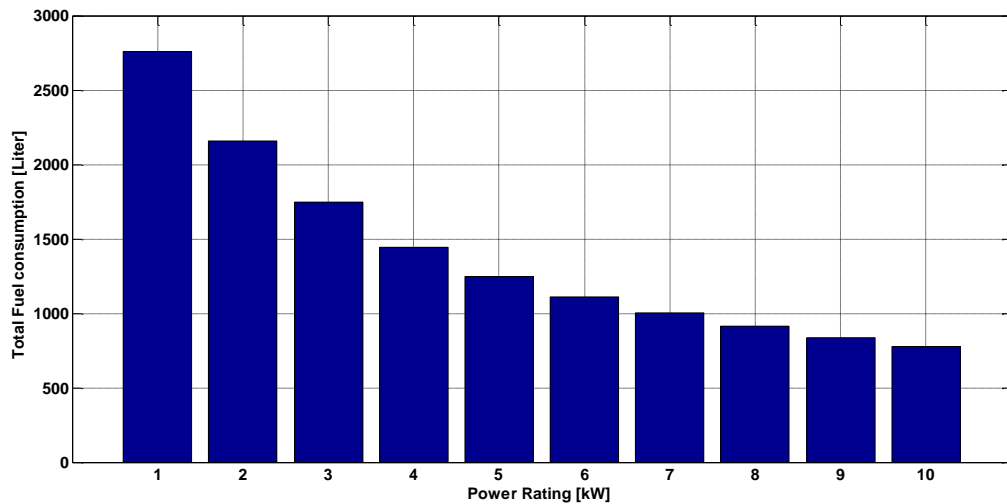


Figure 4-36: Total annual fuel consumption in pumped hydro energy storage system with different capacities.

4.3.3.3 Harvested Energy Index for CAES system

In a CAES system, energy can be stored as high pressure air in a high pressure reservoir by applying work to the compressor. The energy storage procedure in this technology follows the thermodynamic law of energy conversion for air. The stored energy depends on the reservoir volume, pressure, and type of the energy conversion

process, which can be isothermal, adiabatic or isentropic. Assuming a polytropic process for the CAES system in this study, the amount of work, in a polytropic process is expressed as [7] and [84]:

$$W = \frac{n}{n-1} (P_1 V_1) \left[\left(\frac{P_2}{P_1} \right)^{\frac{n-1}{n}} - 1 \right] \quad (4-13)$$

where n is the polytropic exponent (c_p/c_v), P_1 and P_2 are the atmospheric and the tank pressure in a compression cycle respectively. Considering a fixed working pressure for the air motor, the compressor rated power can be obtained as function of its working pressure. Using the rated energy capacity for the CAES system, the power rating of the system can be calculated. Then, for each working pressure and using (4-13), the required tank volume can be calculated. The relationship between the required storage volume and the system power rating can be presented in a 3D curve as a function of the compressor working pressure as shown in Figure 4-37, and it can be used to design the compressor rating as well as the tank size.

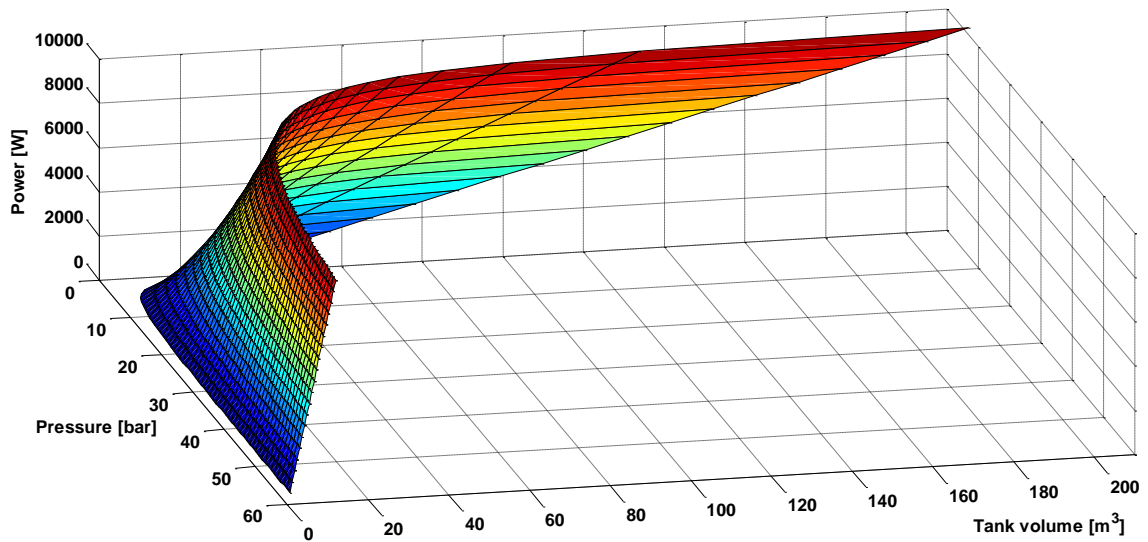


Figure 4-37: Required tank volume as a function of the power rating and the compressor pressure.

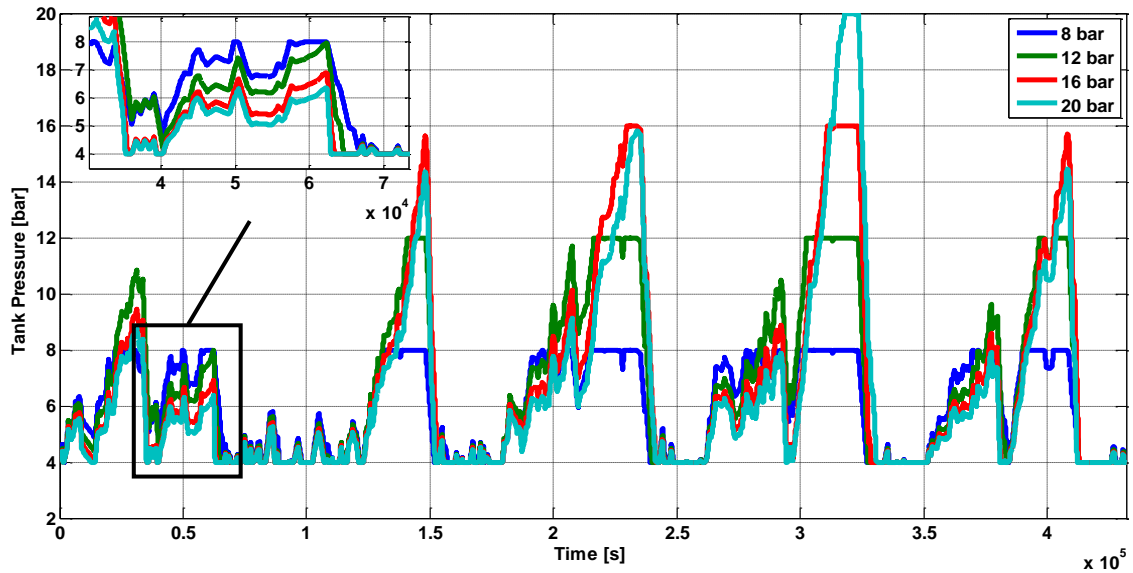


Figure 4-38: The reservoir pressure variation in five consecutive days.

The reservoir pressure variations in five consecutive days for four different CAES system with different fixed compression ratios are shown in Figure 4-38. As shown in Figure 4-38, the compressors with lower compression ratios are able to harvest the energy faster than the compressors with higher working pressure as result of higher energy conversion efficiency as it was discussed in 4.2.2. On the other hand, they will be saturated faster as a result of lower working pressure.

Figure 4-39, shows the variation of the calculated continuous HEI for several CAES system with different power rating. The total fuel consumption of each CAES system is separately calculated and shown in Figure 4-40. As seen in Figure 4-40, the fuel consumption reaches a minimum value at the working pressure of 16bar, and will increase by increasing the working pressure. The drop in energy conversion efficiency at high working pressures is the cause of this increase.

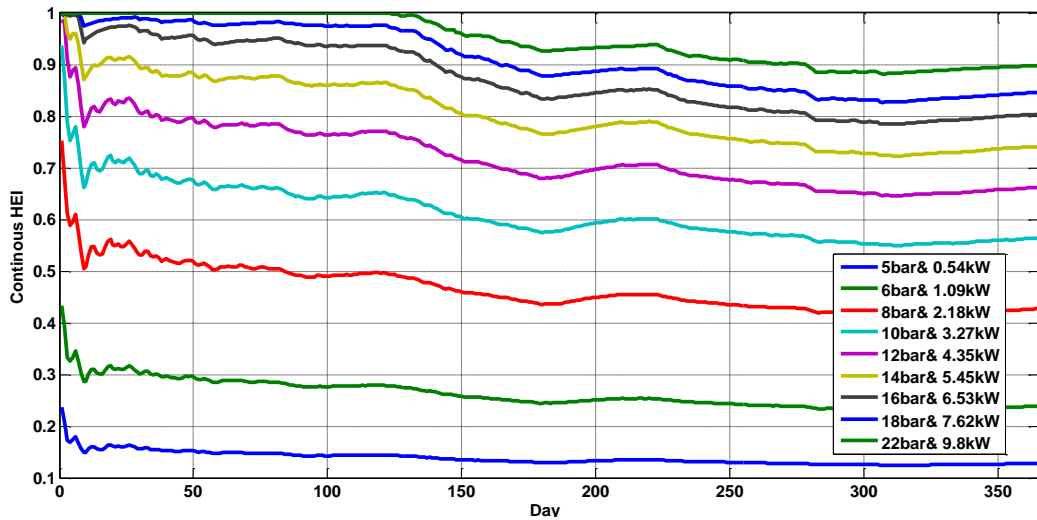


Figure 4-39: The variation of the calculated continuous HEI for several CAES systems with different power rating.

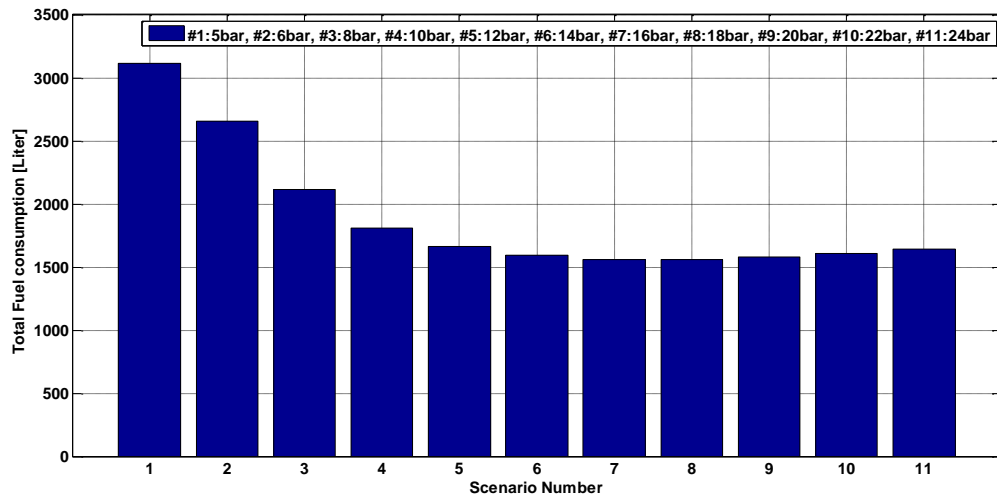


Figure 4-40: The total fuel consumption of several CAES systems with different compression ratios.

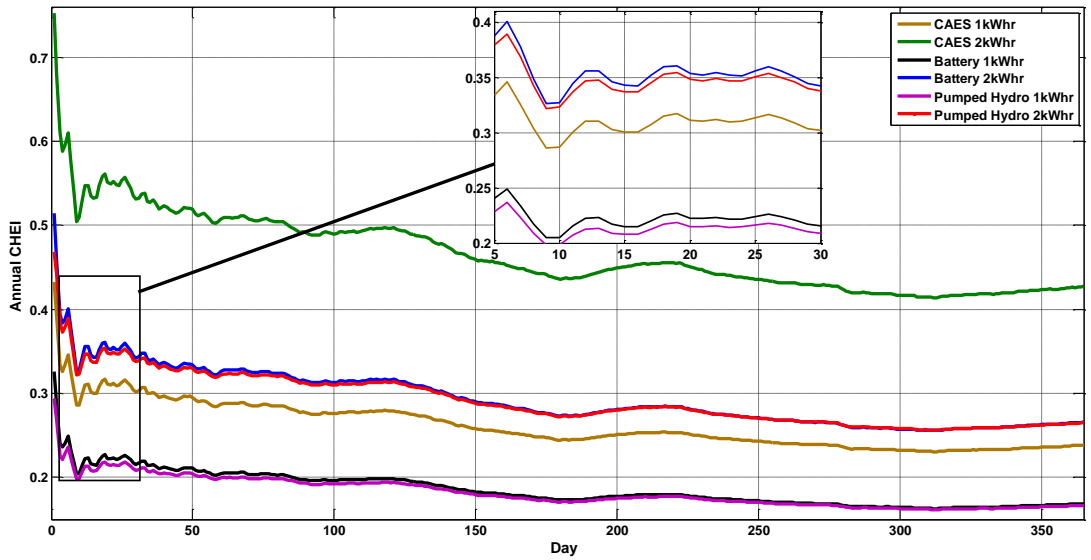
4.3.3.4 Energy storage system performance comparison

In order to choose a storage technology for an application, the geographical characteristics of the implementation site, the application size and the availability of RES are the key parameters that need to be considered. Therefore, a comprehensive economic and technical performance assessment is necessary for the energy storage comparison, and select the best storage technology for the desired application. In this chapter, a novel

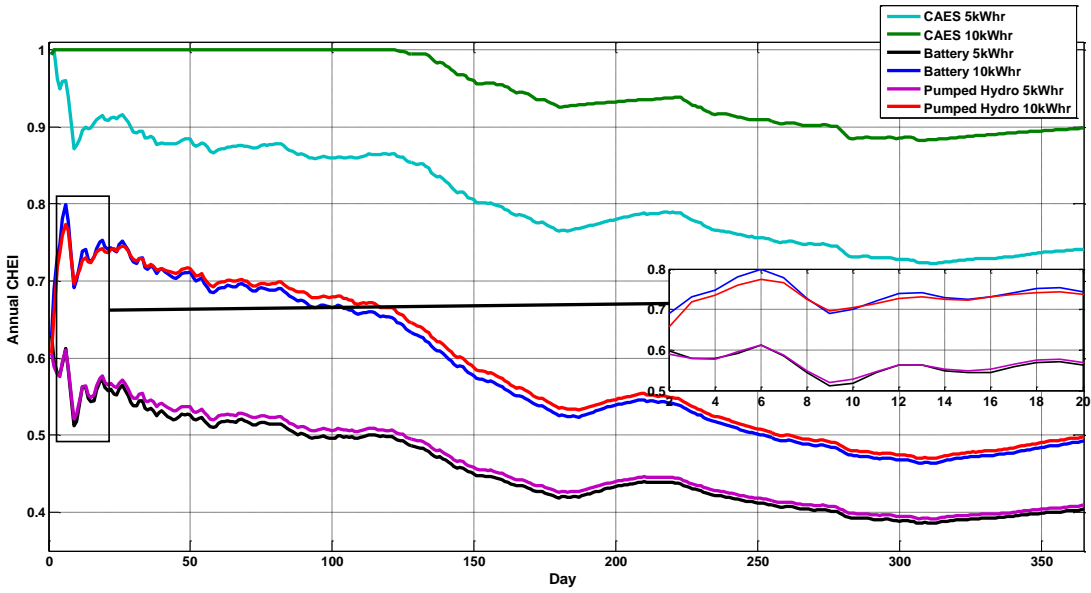
criterion for the assessment of an energy storage system (Harvested Energy Index) was proposed to enhance the accuracy of the performance investigation. This criterion targets the limited storage capacity of the energy storage system, and reveals its benefits in energy storage systems with expandable capacities such as CAES systems in locations with considerable renewable energy. The obtained results in each presented storage systems are compared in this section.

Figure 4-41, compares the annual CHEI for three energy storage technologies with different storage capacities. As shown in Figure 4-41, the CAES can utilize more excess energy in its energy conversion process in comparison with the pumped hydro and battery based energy storage systems. This higher value is related to the higher power requirement of the compressor in a CAES system. The average value of the continuous harvested energy for a time period of one year can provide a quantity representing the storage system capability in harvesting energy for a long term operation.

The annual averaged value of CHEI for three storage technologies with several storage capacities is shown in Figure 4-42. As shown in Figure 4-42, the storage system with higher capacities is able to extract more energy for future utilization. In addition, in all power ratings the CAES system absorbs more energy in comparison with the corresponding pumped hydro or battery storage system with the same storage capacities.



(a)



(b)

Figure 4-41: The annual CHEI of three energy storage technologies with different storage capacities: (a): 1kWh & 2kWh, and (b): 5kWh & 10kWh.

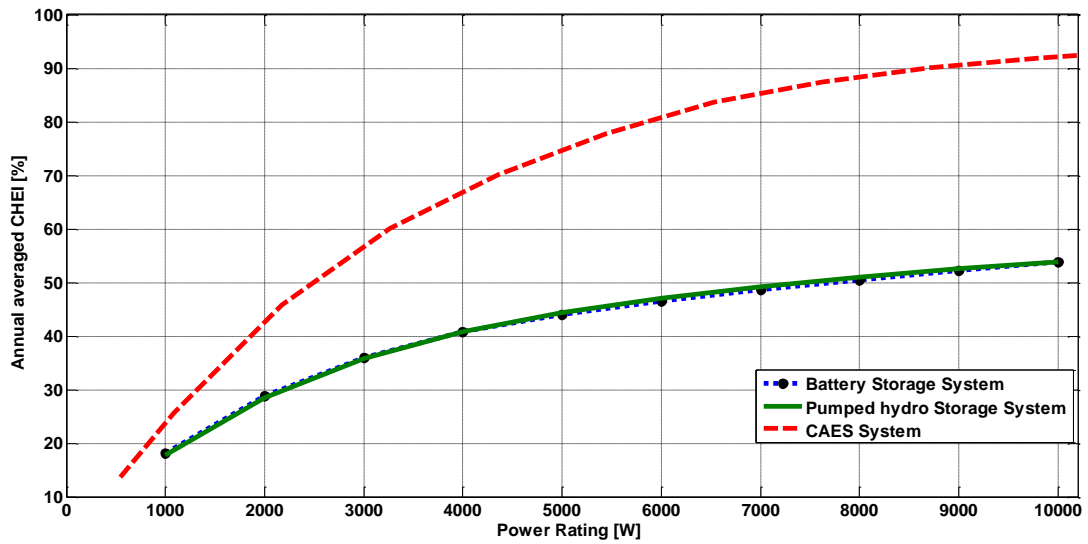


Figure 4-42: The annual averaged value of CHEI for three storage technologies with different ratings.

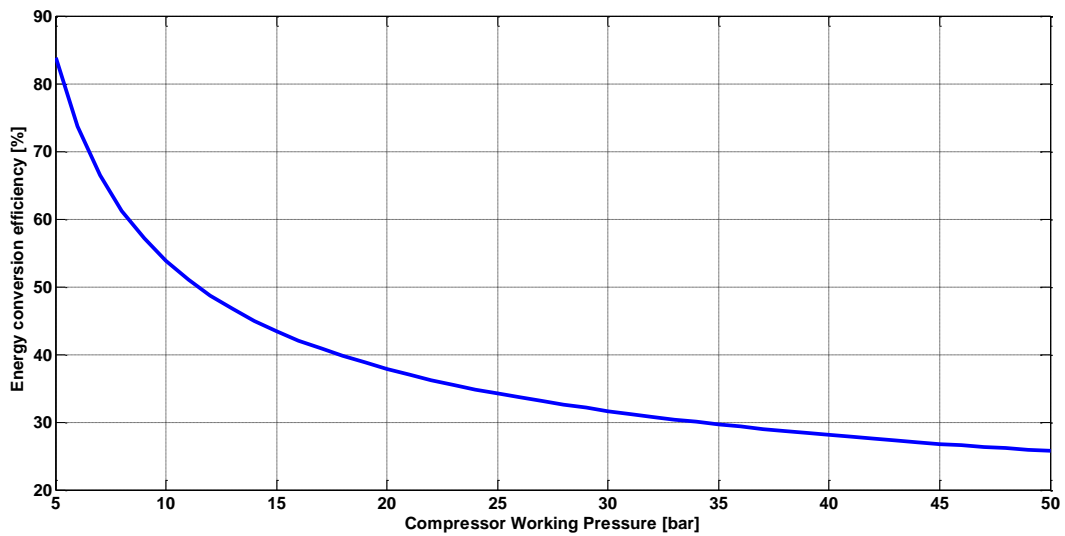


Figure 4-43: Compressor efficiency variation as a function of its working pressure.

The Figure 4-41 shows higher energy stored by a small scale CAES in comparison to battery and pumped hydro storage. For example the annual CHEI during 6th day for battery storage with 1kWhr capacity is 0.25 while the value for 1kWhr CAES is 0.35, which means the CAES has the ability to utilize 1.4 times more energy than battery during day 6. The working pressure of a 1kWhr small scale CAES as shown in Figure

4-39 is 6 bar; and by referring to the Figure 4-43, the efficiency of the compressor at 6 bar is around 70%. Multiplying 70% and 140% results in 98% which means the compressor of CAES is able to use 98% of available energy and store it. In the other word, the 70 % efficiency of 6 bar compressor is applied to higher amount of energy (1.4 times for day 6th) in a longer duration of the time and results in 98% utilization of the available excess wind energy.

In the traditional efficiency comparison, applying each system efficiency to a limited available energy results in the stored energy of each system. Lower energy conversion efficiency of CAES causes lower and slower stored energy but our argument is for the cases that there is still excess wind energy available and CAES or other less efficient systems can continue to store energy. In this case some energy will be wasted in CAES during compression cycle rather than wind turbine but results in a higher amount of stored energy.

In a hybrid renewable based energy system, the cost of storage system and increasing the size of it is much higher than increasing the size of the wind turbines or solar panels. By introducing HEI, we showed that instead of increasing the size of storage, the excess free renewable energy (wind turbine in our case) provides opportunity to the systems with lower efficiency to be able to reach their full capacity.”

In addition, considering the energy conversion efficiency curve shown in Figure 4-43, the higher working pressure of the compressor results in lower efficiency; as a result, the compressor power rating should be adjusted in order to meet the power rating of the CAES system.

In order to compare the performance of the three storage systems under study from the economic point of view, the annual shortage profile and the total fuel consumption is shown in Figure 4-44. In an energy system with higher storage capacity, the wind energy penetration is increased.

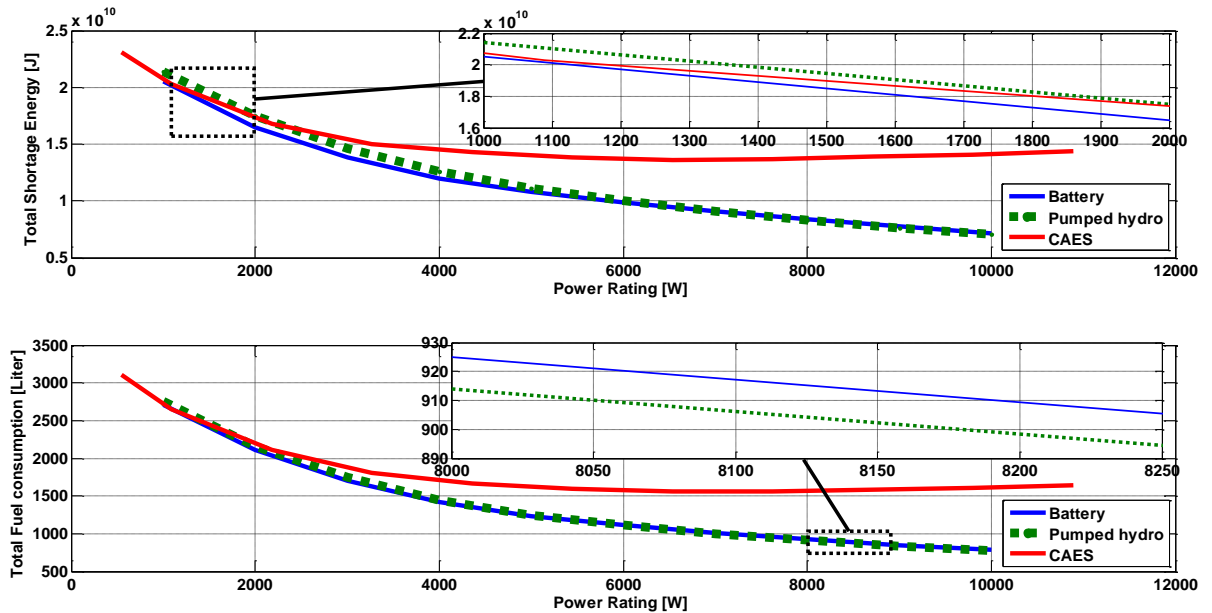


Figure 4-44: The annual shortage profile and the total fuel consumption of the three storage systems under study.

As illustrated in Figure 4-44, the total shortage energy, and consequently the total fuel consumption decreases by increasing the storage capacity in all three storage technologies. However, this reduction is less for the CAES system with power rating higher than 3kW, because of the low energy conversion efficiency for the CAES system with high working pressure and small reservoir size. The figure also suggests that for power ratings less than 3 kW, there is no difference between the fuel consumptions. This behaviour can be referred to the result shown in Figure 4-41, where, the CAES systems with lower power ratings harvest more excess energy in comparison with the battery

system and pumped hydro storage systems and compensate the low energy conversion efficiency of the compression cycle shown in Figure 4-43. The figure also suggests that for power ratings less than 3 kW, there is no difference between the fuel consumptions. On the other hand for ratings higher than 3 kW, the CAES system results in higher fuel consumption compared to the battery or pumped hydro systems. The high power profile of a CAES system can be improved by either using multistage compression or increasing the tank volume instead of increasing the working pressure in order to reach higher power rating.

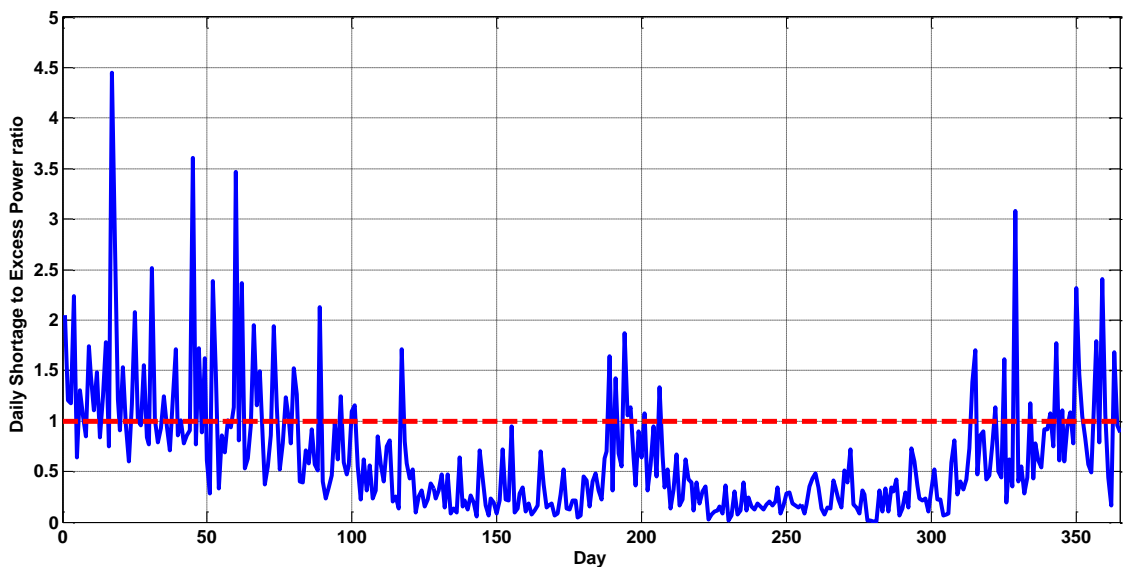


Figure 4-45: the variation of the daily shortage power to the excess power ratio over a period of a year for a battery storage system with 1kWhr storage capacity

In addition to the HEI, the shortage power ratio to the available excess power can be used to investigate the performance of the storage system in capturing the excess energy. Figure 4-45, shows the variation of the daily shortage power to the excess power ratio over a period of one year for a battery storage system with 1kWhr storage capacity. The dot dash line shown in Figure 4-45 represent the balance line for this parameter, when the

excess energy in a day is equal to the shortage energy during the same day. The values above the balance line cannot be compensated by the storage system as a result of the lack of available excess energy. On the other hand, the values below the balance line can be supplied by a properly designed storage system.

Figure 4-46, shows the annual shortage to the excess power ratio variation as a function of the storage capacity for three different energy storage technologies. As shown in Figure 4-46, the CAES system has higher value of the shortage to the excess power, representing the same trend obtained in total fuel consumption and total shortage energy (Figure 4-44). This result highlights the dominant impact of the energy conversion efficiency on the overall performance of the storage system, where the battery storage and pumped hydro storage system with efficiency close to 100% have better profile in comparison to a CAES system with the efficiency profile shown in Figure 4-43.

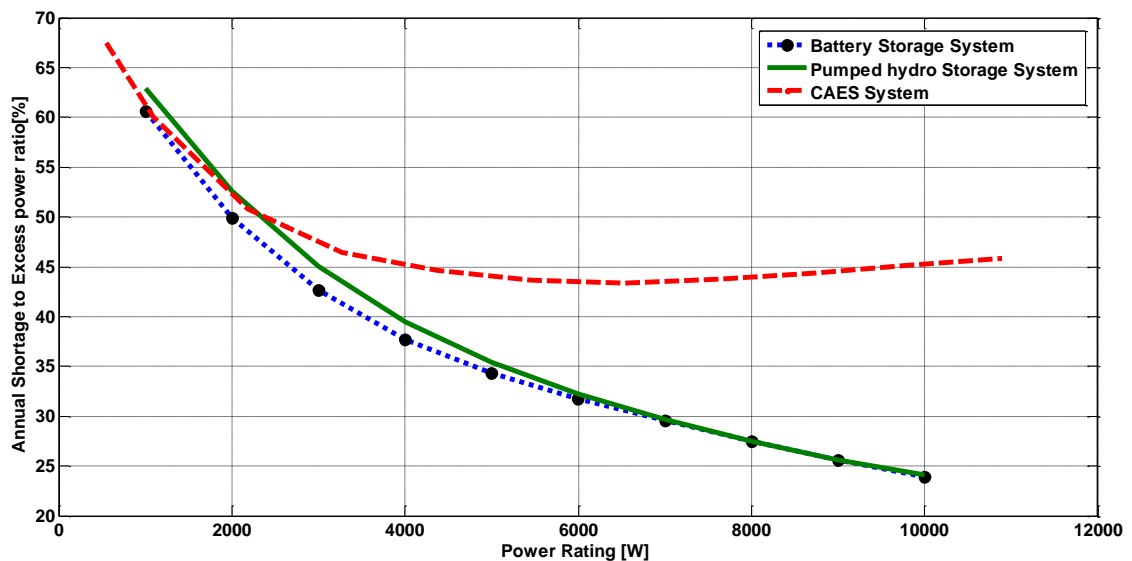


Figure 4-46: The annual shortage to the excess power ratio variation as a function of the storage capacity for three different energy storage technologies.

As it was shown in the proposed case study, despite the environmentally friendly nature, high life cycle and inexpensive configuration of a CAES system, the overall efficiency in a poorly designed CAES system can limit its application in energy related industries. It should be noted that, the maintenance cost after installing energy harvesting equipment is the only expense required by a RES based power system. It can benefit from a vast amount of free energy to compensate for its lower efficiency in comparison with other technologies. This enhancement can be more attractive considering the environmentally friendly nature of the CAES system, and its high durability. Proper design and developing suitable control strategy considering the physics of energy conversion in a CAES system can result in improved performance of a RES based power system.

4.4 Summary

In this chapter, a simple method to evaluate the performance of different wind turbines has been presented. At the first step, collected wind speed data from different sources was analyzed, and the wind speed frequency distribution was classified. Then a Weibull distribution function was obtained for each hour. In the next step, Monte Carlo simulation was performed based on inverse Weibull Cumulative Distribution Function (CDF) to produce wind speed profile with 10 minute time scale resolution. The generated wind speed profile was then used to assess the performance of candidate wind turbines. Considering the presented methodology for performance assessment of wind turbine at a

specific location, the optimum size of a wind turbine for a desired location can be determined.

A new criterion for energy storage performance assessment was introduced based on the ability to harvest and store the excess energy produced by a wind farm. The proposed index reveals the limitation on the storage capacity of various energy storage technologies, which is critical in RES-based power systems. In addition, a hybrid power system based on a wind farm is developed for possible application in an isolated electrical power grid to fulfill the demands of a remote community. Using a case study, the harvest energy indices for different energy storage capacities were calculated, and a variable working pressure control algorithm was proposed for the compression cycle. In order to demonstrate further the unique characteristics of CAES systems in capturing wind energy, this index was calculated for different fixed working pressure. Based on the results a practical 4-stages configuration of the CAES system was proposed, and the impact of the proposed control strategy on the total fuel consumption was presented.

Finally, the performance of three different energy storage systems, namely pumped hydro storage system, battery storage system and several CAES systems with different compression ratios which results in different energy storage capacities were investigated by calculating their continues HEI. Although, the performance of all three systems for power rating less than 3kW is similar, the CAES system performance degrades for higher power rating due to its low conversion efficiency in higher compression ratios. Moreover, the impact of the storage capacity on the total fuel consumption of a HPS was presented.

Chapter 5 Conclusions, and Suggested future work

5.1 Conclusions and Contributions

One of the challenges in the modeling of the pneumatic devices was the complexity of their mathematical model. A simplified model based on experimental tests was presented in order to represent the dynamic response of the air motor to specific pressure and input compressed air flow rate. It was shown that the air motor transfer function can be approximated with the first order system transfer function, while its parameters as a function of the input pressure can be obtained with simple tests. In addition, the flow rate response of the system to pressure variation has been modeled based on Venturi flow meter principle. The valve flow coefficient in this study has been obtained using measured pressure drop across the valve and output flow rate of the air motor. The experimental investigation provided an appropriate base aimed at testing the performances of the analytical model for several operating pressures and initial valve conditions. The simulation/experimental result comparisons showed the ability of the proposed model to provide an accurate dynamic response of the air motor speed. Then the power and air consumption of the CAES system was evaluated based on the manufacturer datasheet as a function of the working pressure and speed.

This research aimed to identify effective designs of a wind based small scale CAES system and proper control solutions that result in lower diesel fossil fuel consumption of the diesel generators that are currently supplying isolated loads. The energy conversion

efficiency analysis of a pneumatic was presented, and it was shown that in a system without any heat exchanger, the round trip efficiency of the compression and expansion cycles can drop to 25% for pressure ratios of 10, while this value can be as high as 65% for pressure ratio of 2. There were two main observations from these results, one emphasises the use of proper heat exchanger to improve the energy conversion efficiency, and the other one, with the support of evidences obtained from the energy density analysis of a CAES system, suggests the usefulness of flexible storage with variable volume can enhance the performance of the system. The second observation was the basis for development of a novel criteria to evaluate the performance of the energy storage systems.

The new proposed criterion targets the limited capacity of the energy storage systems in capturing abundant excess renewable energy due to their physical or technical limitations. On the other hand, by focusing on unique characteristics of the CAES system it was shown that with proper setup and system sizing, CAES system can store more energy than pumped hydro and battery energy storage systems investigated in the presented case study. These two energy storage systems were intentionally chosen because of their high energy conversion efficiency that always is considered as the main drawback of a CAE system. The result shows how a proper system sizing and control strategy can convert a low efficiency energy storage system such as CAES to a very attractive option in comparison to the two best energy storage systems and make it an economical viable option.

Another contribution of this study is developing a systematic approach to investigate the performance of wind turbines in a desired location. As it was shown in the presented case study, the wind turbine power curves can be obtained as function of the speed; and by using Monte-Carlo statistic simulation, the wind speed and load data can be regenerated with desired resolution and used for evaluation of the wind turbine performance in a specific location.

The following publication and conference presentations are outcomes of this study:

- H.SedighNejad, T.Iqbal and J.Quaicoe,” *Compressed Air Energy Storage System Control and Performance Assessment Using Energy Harvested Index*”, Electronics Special Issue on Renewable Energy Systems, 2014, 3, 1-21.
- H.SedighNejad, T.Iqbal and J.Quaicoe, “*Effect of the sizing of compressed air storage system on overall performance of Hybrid systems*”, poster presentation at CanWEA’s 26th Annual Conference and Exhibition, November 1-3, 2010, Montreal, Quebec.
- Hanif Sedighnejad, T. Iqbal, J. Quaicoe,” *Design Considerations for Compressed Air Energy Storage Systems*”, 2010, PKP Open Conference Systems, presented by IEEE Newfoundland and Labrador Section.
- H.SedighNejad, T.Iqbal and J.Quaicoe, “*Performance evaluation of a hybrid wind-diesel-compressed air energy storage system*”, 24th Canadian Conference on Electrical and Computer Engineering (CCECE), 8-11 May 2011, Niagara Falls, ON Page(s): 000270 – 000273.

- H.SedighNejad, T.Iqbal and J.Quaicoe, “*Design and dynamic modeling of a micro compressed air energy storage system*”, poster presentation at CanWEA’s 27th Annual Conference and Exhibition, October 3-6, 2011, Vancouver, BC.
- H.SedighNejad, T.Iqbal and J.Quaicoe, “*A compressed air storage system Design and Steady-State Performance Analysis of CAES*”, The Twentieth Annual Newfoundland Electrical and Computer Engineering Conference (NECEC), Nov. 1st, 2011.
- H.SedighNejad, and T.Iqbal, “*Simplified dynamic model for vane type air motor*”, The 21th Annual Newfoundland Electrical and Computer Engineering Conference (NECEC), Nov. 8th, 2012.

5.2 Suggested Future Work

Despite the development of a simple CAES system and some primary simulations and experiments, some aspects of the proposed system can be enhanced. The suggested future work can be divided into four categories: economical assessment of CAES sizing and scalability in comparison with the other energy storage systems, application of heat exchanger to improve the energy conversion efficiency, dynamic control of the CAES system in conjunction with another energy source, and evaluation of the system with capability of working in series/parallel configuration and its impact on round trip efficiencies and system power ratings.

References

- [1] S. M. Shaahid and M. A. Elhadidy, "Technical and economic assessment of grid-independent hybrid photovoltaic–diesel–battery power systems for commercial loads in desert environments," *Renewable and Sustainable Energy Reviews*, vol. 11, pp. 1794-1810, 2007/10/01/ 2007.
- [2] I. Das and C. A. Cañizares, "Renewable Energy Integration in Diesel-Based Microgrids at the Canadian Arctic," *Proceedings of the IEEE*, vol. 107, pp. 1838-1856, 2019.
- [3] E. Canada. (2020). Energy and Greenhouse Gas Emissions (GHGs). Available: <https://www.nrcan.gc.ca/science-data/data-analysis/energy-data-analysis/energy-facts/energy-and-greenhouse-gas-emissions-ghgs/20063>
- [4] S. Rehman, N. Natrajan, M. Mohandes, L. M. Alhems, Y. Himri, and A. Allouhi, "Feasibility Study of Hybrid Power Systems for Remote Dwellings in Tamil Nadu, India," *IEEE Access*, vol. 8, pp. 143881-143890, 2020.
- [5] G. P. f. Mobile, "Powering Telecoms: West Africa Market Analysis, Sizing the Potential for Green Telecoms in Nigeria and Ghana," 2013.
- [6] C. Kathirvel and K. Porkumaran, "Analysis and design of hybrid wind/diesel system with energy storage for rural application," in *2010 Conference Proceedings IPEC*, 2010, pp. 250-255.
- [7] J. Eyer and G. Corey, "Energy storage for the electricity grid: Benefits and market potential assessment guide," Sandia National Laboratories Report, SAND2010-0815, Albuquerque, New Mexico, 2010.
- [8] B. Bose, "Global energy scenario and impact of power electronics in 21st. Century," 2013.

- [9] P. Sullivan, W. Short, and N. Blair, "Modeling the Benefits of Storage Technologies to Wind Power," presented at the American Wind Energy Association (AWEA) WindPower 2008 Conference, Houston, TX, Jun. 1–4, 2008, NREL/CP-670-43510, Available: www.nrel.gov/analysis/pdfs/43510.pdf, Feb. 2010.
- [10] S. Succar and R. H. Williams, "Compressed air energy storage: Theory, resources, and applications for wind power," Princeton Environmental Institute Report, vol. 8, 2008.
- [11] I. Atzeni, L. G. Ordóñez, G. Scutari, D. P. Palomar, and J. R. Fonollosa, "Demand-side management via distributed energy generation and storage optimization," 2013.
- [12] V. H. Dong and X. P. Nguyen, "A strategy development for optimal generating power of small wind-diesel-solar hybrid microgrid system," in 2020 6th International Conference on Advanced Computing and Communication Systems (ICACCS), 2020, pp. 1329-1334.
- [13] A. J. Cavallo, "High-capacity factor wind energy systems," Transactions- American Society of Mechanical Engineering, Journal of Solar Energy Engineering, vol. 117, pp. 137-137, 1995.
- [14] I. P. Gyuk, "Energy Storage for Grid Connected Wind Generation Applications," EPRI, Palo Alto, CA, EPRI-DOE Handbook Supplement, 1008703, 2004.
- [15] T. Ackermann, Wind power in power systems vol. 140: Wiley Online Library, 2005.
- [16] P. Denholm, E. Ela, B. Kirby, and M. Milligan, "The role of energy storage with renewable electricity generation," National Renewable Energy Laboratory, Golden, CO, Technical Report, NREL/TP-6A2-47187, , Jan. 2010.

- [17] E. A. DeMeo, G. A. Jordan, C. Kalich, J. King, M. R. Milligan, C. Murley, et al., "Accommodating wind's natural behavior," *Power and Energy Magazine*, IEEE, vol. 5, pp. 59-67, December 2007.
- [18] H. Ibrahim, A. Ilinca, and J. Perron, "Energy storage systems—characteristics and comparisons," *Renewable and Sustainable Energy Reviews*, vol. 12, pp. 1221-1250, 2008.
- [19] H.-J. Bullinger, *Technology Guide*: Springer, 2009.
- [20] S. Teleke, "Energy Storage Overview: Applications, Technologies and Economical Evaluation," ed: Quanta Technology, Raleigh, NC, *Energy Storage White Paper*, 2009.
- [21] A. Ruddell, "Storage Technology Report: WP-ST6 Flywheel," *Investigation on Storage Technologies for Intermittent Renewable Energies (INVESTIRE-Network)*, 2003.
- [22] B. Roberts, "Capturing grid power," *Power and Energy Magazine*, IEEE, vol. 7, pp. 32-41, 2009.
- [23] J. Makansi and J. Abboud, "Energy storage, the missing link in the electricity value chain," *ESC (Energy Storage Council) White Paper*, 2002.
- [24] P. F. Ribeiro, B. K. Johnson, M. L. Crow, A. Arsoy, and Y. Liu, "Energy storage systems for advanced power applications," *Proceedings of the IEEE*, vol. 89, pp. 1744-1756, 2001.
- [25] M. Semadeni, "Energy storage as an essential part of sustainable energy systems," *The Centre for Energy Policy and Economics (CEPE), Zürich, Switzerland, CEPE Working Paper No. 24., May 2003.*
- [26] S. Tewari and N. Mohan, "Value of NAS Energy Storage Toward Integrating Wind: Results From the Wind to Battery Project," 2013.

- [27] I. P. Gyuk, "EPRI-DOE Handbook of Energy Storage for Transmission and Distribution Applications," EPRI, Palo Alto, CA, EPRI Report 1001834, Dec 2003.
- [28] X. Luo, J. Wang, M. Dooner, and J. Clarke, "Overview of current development in electrical energy storage technologies and the application potential in power system operation," *Applied Energy*, vol. 137, pp. 511-536, 2015/01/01/ 2015.
- [29] Z. Nie, X. Xiao, Q. Kang, R. Aggarwal, H. Zhang, and W. Yuan, "SMES-Battery Energy Storage System for Conditioning Outputs From Direct Drive Linear Wave Energy Converters," 2013.
- [30] A. M. Gee, F. V. Robinson, and R. W. Dunn, "Analysis of battery lifetime extension in a small-scale wind-energy system using supercapacitors," 2013.
- [31] M. Albu, A. Nechifor, and D. Creanga, "Smart storage for active distribution networks estimation and measurement solutions," in *Instrumentation and Measurement Technology Conference (I2MTC)*, 2010 IEEE, 2010, pp. 1486-1491.
- [32] M. Musio, P. Lombardi, and A. Damiano, "Vehicles to grid (V2G) concept applied to a Virtual Power Plant structure," in *Electrical Machines (ICEM), 2010 XIX International Conference on*, 2010, pp. 1-6.
- [33] L. Chunhua, K. T. Chau, W. Diyun, and G. Shuang, "Opportunities and Challenges of Vehicle-to-Home, Vehicle-to-Vehicle, and Vehicle-to-Grid Technologies," *Proceedings of the IEEE*, vol. 101, pp. 2409-2427, 2013.
- [34] D. J. Swider, "Compressed air energy storage in an electricity system with significant wind power generation," *Energy Conversion, IEEE Transactions on*, vol. 22, pp. 95-102, March, 2007.

- [35] J. Kaldellis, D. Zafirakis, and K. Kavadias, "Techno-economic comparison of energy storage systems for island autonomous electrical networks," *Renewable and Sustainable Energy Reviews*, vol. 13, pp. 378-392, 2009.
- [36] S. Eckroad, "Energy Storage for Grid Connected Wind Generation Applications," EPRI, DOE, Palo Alto, CA, Technical Report, 1008703, Dec. 2004.
- [37] H. Paloheimo and M. Omidiora, "A feasibility study on Compressed Air Energy Storage system for portable electrical and electronic devices," in *Clean Electrical Power, 2009 International Conference on*, 2009, pp. 355-362.
- [38] Y. A. Çengel, "Thermodynamics: an Engineering Approach," McGraw-Hill, ISBN: 0079116523 1994.
- [39] D. Villela, V. V. Kasinathan, S. De Valle, M. Alvarez, G. Frantziskonis, P. Deymier, et al., "Compressed-air energy storage systems for stand-alone off-grid photovoltaic modules," in *Photovoltaic Specialists Conference (PVSC), 2010 35th IEEE*, 2010, pp. 000962-000967.
- [40] U. Bossel, "Thermodynamic analysis of compressed air vehicle propulsion," 2009.
- [41] C. Maolin, T. Kagawa, and K. Kawashima, "Energy conversion mechanics and power evaluation of compressible fluid in pneumatic actuator systems," in *Energy Conversion Engineering Conference, 2002. IECEC '02. 2002 37th Intersociety*, 2002, pp. 438-443.
- [42] M. Cai, K. Kawashima, and T. Kagawa, "Power Assessment of Flowing Compressed Air," *Journal of Fluids Engineering*, vol. 128, pp. 402-405, 2005.

- [43] F. Creutzig, A. Papson, L. Schipper, and D. M. Kammen, "Economic and environmental evaluation of compressed-air cars," *Environmental Research Letters*, vol. 4, p. 044011, 2009.
- [44] A. Gonzalez, B. Ó. Gallachóir, E. McKeogh, and K. Lynch, "Study of Electricity Storage Technologies and Their Potential to Address Wind Energy Intermittency in Ireland " Sustainable Energy Research Group, Department of Civil and Environmental Engineering, University College Cork, Cork, MUS, Ireland, Technical report, RE/HC/03/001, May. 2004.
- [45] J. Taylor and A. Halnes, "Analysis Of compressed air energy storage," in *PCIC Europe 2010 Conference Record*, 2010, pp. 1-5.
- [46] R. Baxter, "Energy Storage: a Nontechnical Guide," PennWell publications, c2006, ISBN: 159370027X.
- [47] F. Crotogino, K.-U. Mohmeyer, and R. Scharf, "Huntorf CAES: More than 20 Years of Successful Operation " presented at the spring 2001 Meeting, Orlando, FL., 15-18 Apr. 2001.
- [48] I.-I. Irimie, S. Irimie, and I.-C. Tulbure, "Compressed Air Energy Storage," *Wiley Encyclopedia of Electrical and Electronics Engineering*, , Dec. 1999.
- [49] A. J. Giramonti, R. D. Lessard, W. A. Blecher, and E. B. Smith, "Conceptual design of compressed air energy storage electric power systems," *Applied Energy*, vol. 4, pp. 231-249, 10// 1978.
- [50] A. Sharma, H. H. Chiu, F. W. Ahrens, R. K. Ahluwalia, and K. M. Ragsdell, "Design of optimum compressed air energy-storage systems," *Energy*, vol. 4, pp. 201-216, 4 1979.
- [51] O. P. S. B. (OPSB), "Staff Investigation Report and Recommendation," Ohio Power Siting Board, Public Utilities Commission of Ohio, Columbus, OH., June 17 2011.

- [52] IAMU, "Site for ISEP Development is officially Announced," IOWA Association of Municipal Utilities Newsletter, Dec. 2006.
- [53] D. Thornley, "Texas Wind Energy: Past, Present, and Future," Texas Public Policy Foundation publications, Available: http://www.texaspolicy.com/publications.php?report_year=2008, Oct. 2008.
- [54] N. Desai, S. Gonzalez, D. J. Pemberton, and T. W. Rathjen, "The Economic Impact of CAES on Wind in TX, OK, and NM," Ridge Energy Storage & Grid Services L.P., Texas State Energy Conservation Office, June 27, 2005.
- [55] TXU, "Luminant and Shell Join Forces to Develop a Texas-Sized Wind Farm," Available: http://www.electricenergyonline.com/?page=show_news&id=71408., July, 2007.
- [56] Y. S. H. Najjar and M. S. Zaamout, "Performance analysis of compressed air energy storage (CAES) plant for dry regions," Energy Conversion and Management, vol. 39, pp. 1503-1511, 10// 1998.
- [57] L. Sang-Seung, K. Young-Min, P. Jong-Keun, M. Seung-II, and Y. Yong-Tae, "Compressed Air Energy Storage Units for Power Generation and DSM in Korea," in Power Engineering Society General Meeting, 2007. IEEE, 2007, pp. 1-6.
- [58] M. Nakhamkin, M. Chiruvolu, M. Patel, S. Byrd, R. Schainker, and J. Marean, "Second generation of CAES technology—performance, operations, economics, renewable load management, green energy," Proc. Power-Gen International, 2009.
- [59] V. d. Biasi, "New Solutions for Energy Storage and Smart Grid Load Management," Gas Turbine World, vol. 39, No. 2, pp. 21-26, Mar.-Apr. 2009.

- [60] M. Nakhamkin, M. Chiruvolu, and C. Daniel, "Available Compressed Air Energy Storage (CAES) Plant Concepts," Power-Gen Conference - MN, Dec. 2007
- [61] M. Nakhamkin. (2016). CAES Bottom Cycle Concept.
- [62] M. Nakhamkin, R. H. Wolk, S. v. d. Linden, and R. Hall, "New Compressed Air Energy Storage Concept Can Improve the Profitability of Existing Simple Cycle, Combined Cycle, Wind energy and landfill gas Combustion Turbine- based Power plants," ASME Turbo Expo, Vienna, Austria,, June 14-17 2004.
- [63] V. d. Biasi, "Fundamental Analyses to Optimize Adiabatic CAES Plant Efficiencies," GAS Turbine World, vol. 39, Sep- Oct. 2009.
- [64] E. Lerch, "Storage of fluctuating wind energy," in Power Electronics and Applications, 2007 European Conference on, 2007, pp. 1-8.
- [65] C. Bullough, C. Gatzen, C. Jabel, M. Koller, A. Nowi, and S. Zunft, "Advanced Adiabatic compressed Air Energy Storage for the Integration of Wind Energy " in proc. of the European Wind Energy Conference, EWEC, London, UK,, Nov. 22-25, 2004.
- [66] F. D. S. Steta, "Modeling of an Advanced Adiabatic Compressed Air Energy Storage (AA-CAES) Unit and an Optimal Model-based Operation Strategy for its Integration into Power Markets," Master Thesis, PSL1003, EEH Power Systems Laboratory, Swiss Federal Institute of Technology (ETH) Zurich, , 2010.
- [67] G. Grazzini and A. Milazzo, "Exergy analysis of a CAES with thermal energy storage," Università di Firenze, Italy, 2008.
- [68] G. Grazzini and A. Milazzo, "Thermodynamic analysis of CAES/TES systems for renewable energy plants," Renewable Energy, vol. 33, pp. 1998-2006, 2008.

- [69] H. Ibrahim, R. Younès, A. Ilinca, M. Dimitrova, and J. Perron, "Study and design of a hybrid wind–diesel-compressed air energy storage system for remote areas," *Applied Energy*, vol. 87, pp. 1749-1762, 5// 2010.
- [70] H. Ibrahim, A. Ilinca, R. Younes, J. Perron, and T. Basbous, "Study of a hybrid wind-diesel system with compressed air energy storage," in *Electrical Power Conference, 2007. EPC 2007. IEEE Canada, 2007*, pp. 320-325.
- [71] D. Shively, J. Gardner, T. Haynes, and J. Ferguson, "Energy Storage Methods for Renewable Energy Integration and Grid Support," in *Energy 2030 Conference, 2008. ENERGY 2008. IEEE, 2008*, pp. 1-6.
- [72] D. Flowers, "Pneumatic Energy Storage," US Department of Energy by the Lawrence Livermore National Laboratory, Livermore, CA , UCRL-ID- 122156, September 19 1995.
- [73] A. Rufer and S. Lemofouet, "Energetic performance of a hybrid energy storage system based on compressed air and super capacitors," in *Power Electronics, Electrical Drives, Automation and Motion, 2006. SPEEDAM 2006. International Symposium on, 2006*, pp. 469-474.
- [74] I. Cyphelly, A. Rufer, P. Brückmann, W. Menhardt, and A. Reller, "Usage of compressed air storage systems," Swiss Federal Office of Energy, Bern, Switzerland, DIS Project 240050 May 2004.
- [75] S. Lemofouet and A. Rufer, "Hybrid Energy Storage System based on Compressed Air and Super Capacitors with MEPT (Maximum Efficiency Point Tracking)," presented at the *IPEC 2005: Int. Power Electronics Conf., Niigata, Japan, April 4-8 2005*.
- [76] S. Lemofouet and A. Rufer, "Hybrid energy storage systems based on compressed air and supercapacitors with maximum efficiency point tracking," in *Power Electronics and Applications, 2005 European Conference on, 2005*, pp. 10 pp.-P. 10.

- [77] T. M. Weis and A. Ilinca, "The utility of energy storage to improve the economics of wind-diesel power plants in Canada," *Renewable energy*, vol. 33, pp. 1544-1557, 2008.
- [78] "Energy for the future: Energy planning for the Northwest Territories," ed. Yellowknife, NT: Government of the Northwest Territories
2006.
- [79] J. Beukes, T. Jacobs, J. Derby, R. Conlon, and I. Henshaw, "Suitability of compressed air energy storage technology for electricity utility standby power applications," in *Telecommunications Energy Conference*, 2008. INTELEC 2008. IEEE 30th International, 2008, pp. 1-4.
- [80] D. Zafirakis and J. Kaldellis, "Autonomous dual-mode CAES systems for maximum wind energy contribution in remote island networks," *Energy Conversion and Management*, vol. 51, pp. 2150-2161, 2010.
- [81] J. B. Greenblatt, S. Succar, D. C. Denkenberger, R. H. Williams, and R. H. Socolow, "Baseload wind energy: modeling the competition between gas turbines and compressed air energy storage for supplemental generation," *Energy Policy*, vol. 35, pp. 1474-1492, 2007.
- [82] "MATLAB R2012b," The MathWorks Inc.
- [83] J. Kaldellis, "The wind potential impact on the maximum wind energy penetration in autonomous electrical grids," *Renewable Energy*, vol. 33, pp. 1665-1677, 2008.
- [84] H. Sedighnejad, T. Iqbal, and J. Quicoe, "Performance evaluation of a hybrid wind-diesel-compressed air energy storage system," in *Electrical and Computer Engineering (CCECE)*, 2011 24th Canadian Conference on, 2011, pp. 000270-000273.

- [85] V. Vongmanee, "The renewable energy applications for uninterrupted power supply based on compressed air energy storage system," in *Industrial Electronics & Applications, 2009. ISIEA 2009. IEEE Symposium on*, 2009, pp. 827-830.
- [86] B. W. Power. (2011-2018). bergey excel-R & S power curve. Available: <http://bergey.com/products/wind-turbines/excel-7-5kw-wind-turbine>
- [87] X. W.-. Windenergy. (2018). Whisper 500. Available: <http://www.hardysolar.com/wind-turbine/whisper-500.html>
- [88] X. W.-. windenergy. (2010-2013). Skystream 3.7 Available: <http://www.windenergy.com/products/skystream/skystream-3.7>
- [89] Eoltec.Wind.Turbines. (2012). Eoltec Scirocco E5.6-6. Available: <http://www.aveco.gr/docs/Eoltec%20Scirocco%20Brochure%20V1.1-EN%20.pdf>
- [90] J. Marques, H. Pinheiro, H. Gründling, J. Pinheiro, and H. Hey, "A survey on variable-speed wind turbine system," *network*, vol. 24, p. 26, 2003.
- [91] J. Morren, J. Pierik, and S. W. H. de Haan, "Inertial response of variable speed wind turbines," *Electric Power Systems Research*, vol. 76, pp. 980-987, 7// 2006.
- [92] C. Tang, M. Pathmanathan, W. L. Soong, and N. Ertugrul, "Effects of inertia on dynamic performance of wind turbines," in *Power Engineering Conference, 2008. AUPEC'08. Australasian Universities*, 2008, pp. 1-6.
- [93] R. Prakash and R. Singh, "Mathematical modeling and simulation of refrigerating compressors," 1974.
- [94] M. Elhaj, F. Gu, A. Ball, A. Albarbar, M. Al-Qattan, and A. Naid, "Numerical simulation and experimental study of a two-stage

reciprocating compressor for condition monitoring," *Mechanical Systems and Signal Processing*, vol. 22, pp. 374-389, 2008.

- [95] V. Vongmanee and V. Monyaku, "A Modeling of Small-Compressed Air Energy Storage System (Small-CAES) for Wind Energy Applications," Presented at the GMSARN Int. Conf. on Sustainable Development: Issues and Prospects for the GMS, Kunming, China, November 12-14 2008.
- [96] H. Ibrahim, M. Dimitrova, A. Ilinca, and J. Perron, "Système hybride éolien-diesel avec stockage d'air comprimé pour l'électrification d'une station de télécommunications isolée," *Revue internationale de génie électrique*, vol. 12, pp. 701-731, 2009.
- [97] J. Pu, P. Moore, and R. Weston, "Digital servo motion control of air motors," *THE INTERNATIONAL JOURNAL OF PRODUCTION RESEARCH*, vol. 29, pp. 599-618, 1991.
- [98] B. Li, E. J. Barth, K. B. Fite, and M. Goldfarb, "Design of a hot gas vane motor," in 2004 ASME International Mechanical Engineering Congress and Exposition, IMECE, November 13, 2004, pp. 41-46.
- [99] Y.-D. Shen and Y.-R. Hwang, "Dynamic modeling and controller design for air motor," in SICE-ICASE, 2006. International Joint Conference, 2006, pp. 461-466.
- [100] Y.-R. Hwang and Y.-D. Shen, "Fuzzy MRAC Controller Design for the vane-type air motor," in SICE, 2007 Annual Conference, 2007, pp. 180-185.
- [101] M. Tokhi, M. Al-Miskiry, and M. Brisland, "Real-time control of air motors using a pneumatic H-bridge," *Control Engineering Practice*, vol. 9, pp. 449-457, 2001.
- [102] J. Wang, J. Pu, P. R. Moore, and Z. Zhang, "Modelling study and servo-control of air motor systems," *International Journal of Control*, vol. 71, pp. 459-476, 1998.

- [103] J. Wang, J. Pu, C. Wong, and P. Moore, "Robust servo motion control of air motor systems," 1996.
- [104] R. B. Van Varseveld and G. M. Bone, "Accurate position control of a pneumatic actuator using on/off solenoid valves," *Mechatronics, IEEE/ASME Transactions on*, vol. 2, pp. 195-204, 1997.
- [105] J. Pu, P. Moore, and H. WESTON, "High-gain control and tuning strategy for vane-type reciprocating pneumatic servo drives," *THE INTERNATIONAL JOURNAL OF PRODUCTION RESEARCH*, vol. 29, pp. 1587-1601, 1991.
- [106] M. Martinez, M. G. Molina, F. Frack, and P. E. Mercado, "Dynamic Modeling, Simulation and Control of Hybrid Energy Storage System Based on Compressed Air and Supercapacitors," *Latin America Transactions, IEEE (Revista IEEE America Latina)*, vol. 11, pp. 466-472, 2013.
- [107] H. I. Ali, S. B. B. M. Noor, S. Bashi, and M. Marhaban, "A review of pneumatic actuators (modeling and control)," *Australian Journal of Basic and Applied Sciences*, vol. 3, pp. 440-454, 2009.
- [108] S. R. Pandian, F. Takemura, Y. Hayakawa, and S. Kawamura, "Control performance of an air motor-can air motors replace electric motors?," in *Robotics and Automation, 1999. Proceedings. 1999 IEEE International Conference on*, 1999, pp. 518-524.
- [109] X. Luo, J. Wang, L. Shpanin, N. Jia, G. Liu, and A. S. Zinober, "Development of a mathematical model for vane-type air motors with arbitrary N vanes," in *Proceedings of the World Congress on Engineering*, 2008.
- [110] P. Beater, "Modelling and control of pneumatic vane motors," *International Journal of fluid Power*, vol. 5, pp. 7-16, 2004.
- [111] T. Baumeister and L. S. Marks, *Marks' standard handbook for mechanical engineers*: McGraw-Hill, 1978.

- [112] T. Guo-liang, W. Xuan-yin, and L. Yong-xiang, "Research on the continuous positioning control to servo-pneumatic system," *Journal of Zhejiang University SCIENCE A*, vol. 2, pp. 128-131, 2001.
- [113] J. F. Blackburn, G. Reethof, and J. L. Shearer, *Fluid power control: Technology Press of MIT*, 1960.
- [114] Q. Song, F. Liu, and R. D. Findlay, "Improved fuzzy neural network control for a pneumatic system based on extended kalman filter," in *Computational Intelligence for Modelling, Control and Automation, 2006 and International Conference on Intelligent Agents, Web Technologies and Internet Commerce, International Conference on*, 2006, pp. 76-76.
- [115] M. Carfagni, R. Furferi, and Y. Volpe, "A novel tool for pneumatic spindle design," *Proceedings of the IMProVe 2011, International conference on Innovative Methods in Product Design*, pp. 266-271., 2011.
- [116] R. Marumo and M. Tokhi, "Neural-model reference control of an air motor," in *AFRICON, 2004. 7th AFRICON Conference in Africa*, 2004, pp. 467-472.
- [117] M. Sorli, L. Gastaldi, E. Codina, and S. De las Heras, "Dynamic analysis of pneumatic actuators," *Simulation Practice and Theory*, vol. 7, pp. 589-602, 1999.
- [118] E. Twinning, "Modeling grid-connected voltage source inverter operation," *Proc. AUPEC'01*, pp. 501-506, 2001.
- [119] T. Vandoorn, B. Renders, F. De Belie, B. Meersman, and L. Vandeveldel, "A voltage-source inverter for microgrid applications with an inner current control loop and an outer voltage control loop," 2009.
- [120] D. M. Van de Sype, K. De Gussemé, A. P. Van den Bossche, and J. A. Melkebeek, "Duty-ratio feedforward for digitally controlled boost

- PFC converters," *Industrial Electronics, IEEE Transactions on*, vol. 52, pp. 108-115, 2005.
- [121] N. M. Abdel-Rahim and J. E. Quaicoe, "Analysis and design of a multiple feedback loop control strategy for single-phase voltage-source UPS inverters," *IEEE Transactions on Power Electronics*, vol. 11, pp. 532-541, 1996.
- [122] P. Pillay and R. Krishnan, "Modeling, simulation, and analysis of permanent-magnet motor drives. I. The permanent-magnet synchronous motor drive," *Industry Applications, IEEE Transactions on*, vol. 25, pp. 265-273, 1989.
- [123] M. Khan and M. Iqbal, "Simplified modeling of rectifier-coupled brushless DC generators," in *Electrical and Computer Engineering, 2006. ICECE'06. International Conference on*, 2006, pp. 349-352.
- [124] J. Khan, T. Iqbal, and J. Quaicoe, "Simplified parameter estimation technique of brushless dc generators," *Newfoundland Electrical and Computer Engineering Conf., NECEC2006*, October 2006.
- [125] T. Senjyu, N. Urasakt, T. Simabukuro, and K. Uezato, "Modelling and parameter measurement of salient-pole permanent magnet synchronous motors including stator iron loss," *Mathematical and Computer Modelling of Dynamical Systems*, vol. 4, pp. 219-230, 1998.
- [126] M. Torres and L. A. Lopes, "An optimal virtual Inertia Controller to support frequency regulation in autonomous diesel power systems with high penetration of renewable," in *Proc. Int. Conf. Renewable Energy & Power Quality (ICREPQ 11)*, La Palmas de Gran Canaria, Spain, 2001, pp. 13-15.
- [127] J. C. Neely, S. Pekarek, S. Glover, J. Finn, O. Wasynczuk, and B. Loop, "An economical diesel engine emulator for micro-grid research," in *Power Electronics, Electrical Drives, Automation and*

Motion (SPEEDAM), 2012 International Symposium on, 2012, pp. 175-179.

- [128] P. Tielens and D. Van Hertem, "Grid Inertia and Frequency Control in Power Systems with High Penetration of Renewables," status: published, 2012.
- [129] o. d and m. s, "Modeling an Isolated Hybrid Wind-Diesel Power System for Performing Frequency Control Studies. A Case of Study: San Cristobal Island, Galapagos–Ecuador," IEEE Latin America Transactions, vol. 17, pp. 775-787, 2019.
- [130] Y. Wang and N. C. Pahalawaththa, "Power system load modelling," in Power System Technology, 1998. Proceedings. POWERCON'98. 1998 International Conference on, 1998, pp. 725-729.
- [131] I. Hiskens and J. Milanovic, "Load modelling in studies of power system damping," Power Systems, IEEE Transactions on, vol. 10, pp. 1781-1788, 1995.
- [132] R. M. Rifaat, "On composite load modeling for voltage stability and under voltage load shedding," in Power Engineering Society General Meeting, 2004. IEEE, 2004, pp. 1603-1610.
- [133] W. Xu and Y. Mansour, "Voltage stability analysis using generic dynamic load models," Power Systems, IEEE Transactions on, vol. 9, pp. 479-493, 1994.
- [134] W. Price, S. Casper, C. Nwankpa, R. Bradish, H. Chiang, C. Concordia, et al., "Bibliography on load models for power flow and dynamic performance simulation," IEEE Power Engineering Review, vol. 15, p. 70, 1995.
- [135] N. K. Merzouk, "Wind energy potential of Algeria," Renewable energy, vol. 21, pp. 553-562, 2000.

- [136] A. Ilinca, E. McCarthy, J.-L. Chaumel, and J.-L. Réiveau, "Wind potential assessment of Quebec Province," *Renewable energy*, vol. 28, pp. 1881-1897, 2003.
- [137] "Atmospheric Environment Service," Environment Canada, http://climate.weather.gc.ca/index_e.html#access.
- [138] E. Canada, "The Simulation Results on Canada for the Mean Wind Speed at 50m," Available: http://www.windatlas.ca/en/EU_50m_national.pdf, Aug, 21st, 2008.
- [139] W. C. Cliff, "Effect of generalized wind characteristics on annual power estimates from wind turbine generators," Battelle Pacific Northwest Labs., Richland, WA (USA)1977.
- [140] "National Climatic Data Center," - <http://gcmd.nasa.gov/>.
- [141] T. Ayodele, A. Jimoh, J. Munda, and J. Agee, "Viability and economic analysis of wind energy resource for power generation in Johannesburg, South Africa," *International Journal of Sustainable Energy*, pp. 1-20, 2013.
- [142] A. S. Ahmed, "Wind energy as a potential generation source at Ras Benas, Egypt," *Renewable and Sustainable Energy Reviews*, vol. 14, pp. 2167-2173, 2010.
- [143] Z. Č, P. Mršić, B. Erceg, L. Đ, N. Kitić, P. Matic, et al., "A Monte Carlo Simulation Platform for Studying the Behavior of Wind-PV-Diesel-Battery Powered Mobile Telephony Base Stations," in *2020 International Conference on Probabilistic Methods Applied to Power Systems (PMAPS)*, 2020, pp. 1-6.
- [144] S. M. Kay, *Intuitive probability and random processes using MATLAB*: Springer New York, 2006.

- [145] G. Marmidis, S. Lazarou, and E. Pyrgioti, "Optimal placement of wind turbines in a wind park using Monte Carlo simulation," *Renewable energy*, vol. 33, pp. 1455-1460, 2008.
- [146] M. Hopkins and A. Pahwa, "Monte-Carlo simulation of energy production by a small wind generator," in *Power Symposium, 2008. NAPS'08. 40th North American*, 2008, pp. 1-6.
- [147] S. A. Khajehoddin, M. Karimi-Ghartemani, P. K. Jain, and A. Bakhshai, "DC-Bus Design and Control for a Single-Phase Grid-Connected Renewable Converter With a Small Energy Storage Component," *IEEE transactions on power electronics*, vol. 28, pp. 3245-3254, 2013.
- [148] C. Guillaud, "Making Full Use of Wind Power Potential in North America," *21st World Energy Congr., Montréal, QC*, pp 1-15, Sep. 12-16, 2010.
- [149] V. Valtchev, A. Van den Bossche, J. Ghijselen, and J. Melkebeek, "Autonomous renewable energy conversion system," *Renewable energy*, vol. 19, pp. 259-275, 2000.
- [150] R. Bansal, T. Bhatti, and D. Kothari, "On some of the design aspects of wind energy conversion systems," *Energy conversion and management*, vol. 43, pp. 2175-2187, 2002.
- [151] S. M. Schoenung, "Characteristics and technologies for long-vs. short-term energy storage," 2001.
- [152] R. A. Jackey, "A simple, effective lead-acid battery modeling process for electrical system component selection," *SAE Paper*, pp. 01-0778, 2007.
- [153] O. Tremblay, L.-A. Dessaint, and A.-I. Dekkiche, "A generic battery model for the dynamic simulation of hybrid electric vehicles," in *Vehicle Power and Propulsion Conference, 2007. VPPC 2007. IEEE*, 2007, pp. 284-289.

- [154] H. U. R. Habib, S. Wang, M. R. Elkadeem, and M. F. Elmorshedy, "Design Optimization and Model Predictive Control of a Standalone Hybrid Renewable Energy System: A Case Study on a Small Residential Load in Pakistan," *IEEE Access*, vol. 7, pp. 117369-117390, 2019.

Appendix 1 Wind turbine specifications

Excel-R rotor diameter	7m
Weight	477 kg
Nominal rotational speed	13m/s
Generator nominal speed	1800 rpm

Specifications

Wind Generator Specifications	
Rated Power Output	7,500 watts at 29 mph (13.0 m/s)
Cut-in Wind Speed	7.0 mph (3.1 m/s)
Maximum Design Wind Speed	120 mph (53.6 m/s)
Type	3 Blade Upwind
Rotor Diameter	23.0 ft (7.0 m)
Weight	1050 lbs (477 kg)
Generator	Permanent Magnet Alternator
Turbine Output Form	3 phase AC, variable frequency
System Output Form	120VDC, 240VDC, 48VDC nominal (with included battery charge controller)

Appendix 2 Simulation parameters values

Gaussian equation parameters for Cp approximation (Excel-S 10K)

Parameter	Value	Parameter	Value	Parameter	Value
a ₁	0.2	b ₁	5.963	c ₁	2.218
a ₂	0.1555	b ₂	3.825	c ₂	1.228
a ₃	0.2439	b ₃	10.06	c ₃	4.004
a ₄	0.1056	b ₄	15.59	c ₄	5.769

Gaussian equation parameters for Cp approximation (Excel-R 7.5 kW)

Parameter	Value	Parameter	Value	Parameter	Value
a ₁	0.1787	b ₁	8.564	c ₁	2.956
a ₂	0.0154	b ₂	21.5	c ₂	4.056
a ₃	0.1271	b ₃	12.21	c ₃	3.669
a ₄	0.2121	b ₄	5.577	c ₄	1.977

Excel-R dynamic response parameters

Parameter	Value	Parameter	Value	Parameter	Value
ω_{we}	1800	V_{nWT}	13	n_G	51
m_r	460	R_r	3.5	Je	2
BT	200	B_{we}	0.7	ρ	1.2 25

Gaussian equation parameters for Cp approximation (Excel-S 10K)

Parameter	Value	Parameter	Value	Parameter	Value
a ₁	0.2	b ₁	5.963	c ₁	2.218
a ₂	0.1555	b ₂	3.825	c ₂	1.228
a ₃	0.2439	b ₃	10.06	c ₃	4.004
a ₄	0.1056	b ₄	15.59	c ₄	5.769

Compressor dynamic model parameters

Parameter	Value	Parameter	Value	Parameter	Value
ω_{r-Comp}	240	K_{comp}	10	J_{T-Comp}	0.1
B_{T-Comp}	10	P_{Comp}	10	P_{in}	1

Linear equation parameters for the torque static model

Parameter	Value	Parameter	Value
C_{T11}	-0.0001382	C_{T01}	1.015
C_{T10}	1.981e-005	C_{T00}	0.1513

Quadratic equation parameters for output power static model

Parameter	Value	Parameter	Value	Parameter	Value
C_{PW22}	7.854e-010	C_{PW12}	-1.387e-006	C_{PW02}	-1.627e-08
C_{PW21}	-1.45e-008	C_{PW11}	9.507e-005	C_{PW01}	3.724e-005
C_{PW20}	-1.044e-5	C_{PW02}	0.003669	C_{PW00}	-0.01922

Quartic equation parameters for air consumption static model

Parameter	Value	Parameter	Value	Parameter	Value
C_{AF24}	-9.474e-8	C_{AF14}	0.000346	C_{AF04}	-0.2166
C_{AF23}	1.692e-06	C_{AF13}	-0.006139	C_{AF03}	3.991
C_{AF22}	-1.044e-5	C_{AF12}	0.03769	C_{AF02}	-25.43
C_{AF21}	2.578e-5	C_{AF11}	-0.08909	C_{AF01}	68.04
C_{AF20}	-2.031e-5	C_{AF10}	0.07823	C_{AF00}	-51.34

Air motor dynamic modeling

$$c = -\frac{1}{4}L_{AM} \left(e_{AM} r_{sAM} + \frac{\pi}{2} (r_{sAM}^2 - r_{rAM}^2) \right)$$

$$V_b(\phi) = \frac{1}{2}L_{AM} (r_{sAM}^2 - r_{rAM}^2) (\pi - \phi) - \frac{1}{4}L_{AM} e_{AM}^2 \sin 2\phi - L_{AM} e_{AM} r_{sAM} \sin \phi + c$$

$$C_0 = \sqrt{\frac{k}{R} \left(\frac{2}{k+1} \right)^{\frac{k+1}{k-1}}} = 0.040418 \quad , \quad C_r = \left(\frac{2}{k+1} \right)^{\frac{k}{k-1}} = 0.528$$

$$C_k = \sqrt{\left(\frac{2}{k-1} \right) \left(\frac{k+1}{2} \right)^{\frac{k+1}{k-1}}} = 3.864$$

Air parameters

Parameter	Value	Parameter	Value
k	1.4	R	287

Single phase synchronous Generator parameters

Parameter	Value	Parameter	Value	Parameter	Value
R_{SG}	0.218Ω	# of poles	2	S_{DEG}	6500 (W)
ω_n	3600 (rpm)	J_{DEG}	0.73176	B_{DEG}	0.36588
R_f	52.8Ω	τ_e	0.2 (s)	t_d	110 (ms)
t_{rm}	25°C	t_{mc}	90°C	L_{SG}	188mH

Single phase synchronous Generator flux equation

$$\phi(I_f) = 0.4545(I_f)^3 - 1.911(I_f)^2 + 2.554I_f - 0.01824$$

Diesel Generator dynamic parameters

Parameter	Value	Parameter	Value	Parameter	Value
H_{DEG}	2 (s)	<i>poles</i>	2	S_{DEG}	6500 (W)
ω_{nDEG}	3600 (rpm)	J_{DEG}	0.73176	B_{DEG}	0.36588
k_e	1	τ_e	0.2 (s)	t_d	110 (ms)
k_p	1.5	k_i	1.4	k_d	0.01

Rectifier dynamic parameters

Parameter	Value	Parameter	Value	Parameter	Value	Parameter	Value
R_{lrec}	0.4	L_{rec}	2.6 m	R_{Crec}	0.2	C_{rec}	66 μ

Inverter and its controller parameters

Parameter	Value	Parameter	Value	Parameter	Value	Parameter	Value	Parameter	Value
V_d	1V	V_{cf0}	230V	$\Delta V_{o[p-p]}$	1%	R_{Line}	50m Ω	L_f	1.5mH
r_{on}	0.88 m Ω	P_{inv}	3kw	$\Delta i_{o[p-p]}$	10%	L_{Line}	50mH	C_f	20 μ F
$Q_{tc}=Q_{rr}$	1 μ C	$t_{rr}=t_{tc}$	0.2 μ C	f_s	15kHz	v_G	230V	R_f	0.5 Ω

3rd order approximated Maximum power trajectory parameters

Parameter	Value	Parameter	Value	Parameter	Value	Parameter	Value
a_3	4.619	a_2	-64.6	a_1	548.4	a_0	1752

The approximated CDF for the first hour (12:00am – 1:00 am)

5th degree polynomial equation
 $p1_{h01} = -4.471e-009$; $p2_{h01} = 9.578e-007$; $p3_{h01} = -7.191e-005$;
 $p4_{h01} = 0.001886$; $p5_{h01} = 0.01327$; $p6_{h01} = 0.008685$;
 $App_CDF_WS_h01_2 = p1_{h01} \cdot x_{WS_h01}^5 + p2_{h01} \cdot x_{WS_h01}^4 + p3_{h01} \cdot x_{WS_h01}^3 + p4_{h01} \cdot x_{WS_h01}^2 + p5_{h01} \cdot x_{WS_h01} + p6_{h01}$

Hourly Weibull distribution equation:

$Wei_pdf_h01 = @(p,x)p(3) \cdot (x./p(1)).^{(p(2)-1)} \cdot \exp(-(x./p(1)).^{p(2)});$
 $coefEsts_h01 = nlinfit(binCtrs_h01, Prob_WS_h01, Wei_pdf_h01, startingVals)$
 $xgrid_h01 = linspace(0,Max_WS_h01,n_xgrid);$
 $We_PDF_h01=Wei_pdf_h01(coefEsts_h01, xgrid_h01);$

Appendix 3 wind box interface and inverter specifications

The AURORA WIND Interface specifications:

Description	Value
Input voltage range(no damaging)	0 Vac to 600 Vac
Input voltage range(MPPT operating range)	40 Vac to 400 Vac
Max. operating input current	15 A
Input overcurrent (fuse protected)	20 A
Max. output power (@400Vac, PFC \geq 0.7)	7 KW
V _{ax} voltage range	188Vac 288Vac
Stand-By Grid tare losses	1.3W
efficiency(@400Vac, PFC \geq 0.7)	99.4%
Output Voltage range	0-600Vdc
Max current in the brake resistor	30A
Operating ambient temperature	-25°C to +60°C (-13°F to 140°F)
Enclosure type	Nema 4X
Relative Humidity	0 – 100 % condensing
Audible Noise	< 40dBA
Size (height x width x depth):	29X 9.5X26 mm

PVI-3600- OUTD specifications:

Description	Value
Input voltage range (no damaging)	0 Vac to 400 Vac
Input voltage range (operating)	50Vdc to 530Vdc
Input frequency range	0Hz to 600Hz
Max. operating input current	Up to 16.6 A (rms)
Input over current (fuse protected)	Up to 20 A
Max. output power , (@400Vac, PFC \geq 0.7)	3600W
Maximum output current + diversion load current	20 A(rms) up to 20A _{dc} continuous / up to 30A _{dc} peak
Efficiency (@400Vac, PFC \geq 0.7)	99.4%
Output Voltage range	0-600 Vdc
Output Voltage range (@ full output power)	360-600Vdc (PVI-7200-W-I) *** 200-600Vdc (PVI-4000-W-I) ***
Operating ambient temperature	-25°C to +60°C (-13°F to 140°F)
Enclosure type	Nema 4X
Relative Humidity	0 – 100 % condensing
Audible Noise	< 40dBA
Size (height x width x depth):	420 x 310 x 144 mm

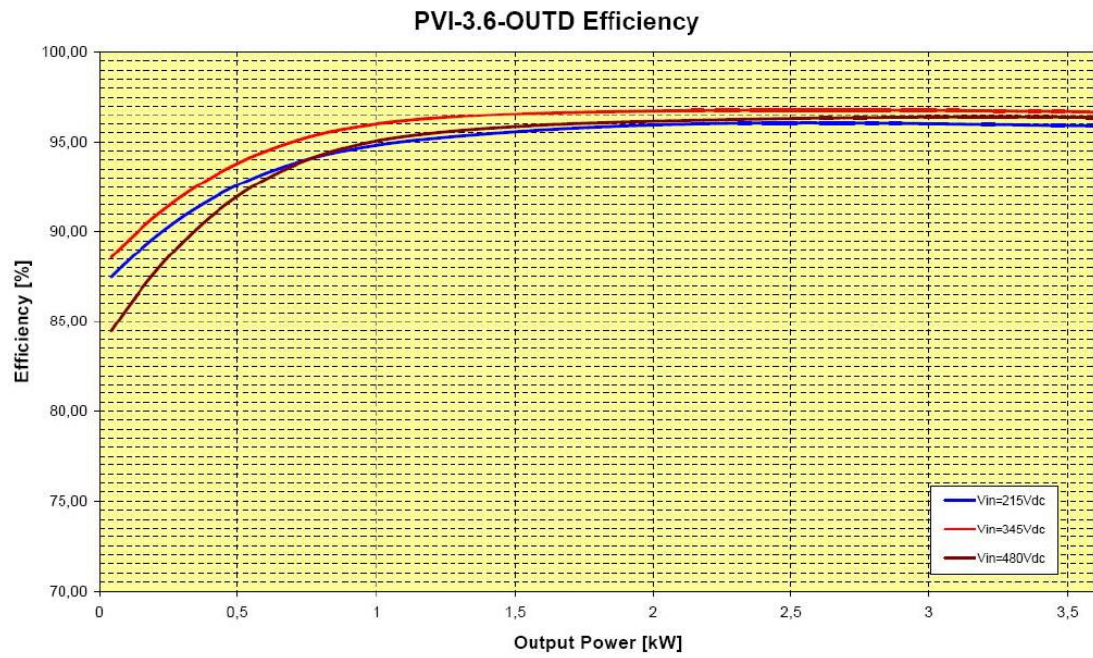


Fig. 28 – Efficiency curve PVI-3.6-OUTD

Appendix 4 Full bridge diode Rectifier

The DC voltage on the DC bus is the average over the period T of the output voltage of the rectifier:

$$V_{dc} = \frac{1}{T} \int_0^T (V_g(t) - V_f) dt \quad (A1)$$

where $V_g(t)$ is the generator output voltage and V_f is the voltage drop across the full bridge diode rectifier. Assuming the generator output voltage to be an ideal sinusoidal wave form its mathematical representative can be considered as the following:

$$V_g = V_m \sin \omega t \quad (A2)$$

Where V_m is the generated voltage amplitude. Including (A2) in (A1) and integrating over its non-zero values, the average dc voltage output of the full bridge diode rectifier can be obtained.

$$\begin{aligned} V_{dc} &= \frac{2}{T} \int_{t_0}^{T/2-t_0} (V_m \sin \omega t - V_f) dt = \frac{2}{T} \left[-\frac{V_m}{\omega} \cos \omega t - V_f t \right]_{t_0}^{T/2-t_0} \\ &= \frac{2}{T} \left[-\frac{V_m}{\omega} (\cos \omega t_0 - \cos \omega (\frac{T}{2} - t_0)) - V_f (\frac{T}{2} - 2t_0) \right] \end{aligned} \quad (A3)$$

Where t_0 is the conduction start time for diode bridge, when the input voltage is more than V_f , and its value can be calculated using (A4).

$$t_0 = \frac{\sin^{-1} \left(\frac{V_f}{V_m} \right)}{\omega} \quad (A4)$$

Using Trigonometric Identities (A5) and (A6), the average output voltage can be simplified as (A7), where

$$\cos\alpha - \cos\beta = -2\sin\left(\frac{\alpha + \beta}{2}\right)\sin\left(\frac{\alpha - \beta}{2}\right) \quad (\text{A5})$$

$$\sin^2\alpha = \frac{1 - \cos 2\alpha}{2} \quad (\text{A6})$$

$$V_{dc} = \frac{2}{T} \left[\frac{2V_m}{\omega} \left(\sin\left(\frac{\omega T}{2}\right) \times \sin\omega\left(\frac{T}{2} - t_0\right) - V_f \left(\frac{T}{2} - 2t_0\right) \right) \right]$$

for $V_m > 10V_f \longrightarrow T \gg t_0 \longrightarrow V_{dc} = \frac{2V_m}{\pi} - V_f \quad (\text{A7})$

$$V_{dc} = \frac{2V_m}{\pi} - V_f$$

The bridge rectifier ripple voltage which includes the load dynamics in model can be calculated using .:

$$V_{ripple} = \frac{I_{load}}{f \times C} \quad (\text{A8})$$

where I_{load} in Ampere is the dc bus current supplied to the inverter, f in Hertz is the frequency and C in Farad is the capacitance.